Characterization of electromagnetic fields in the *a*SPECT spectrometer and reduction of systematic errors

Dissertation
zur Erlangung des Grades
"Doktor der Naturwissenschaften"
am Fachbereich Physik, Mathematik und Informatik
der Johannes Gutenberg-Universität
in Mainz

vorgelegt von
Fidel Ayala Guardia
geboren in Valencia

Mainz, im October 2011

A mis padres,

Abstract

The *a*SPECT spectrometer has been designed to measure, with high precision, the recoil proton spectrum of the free neutron decay. From this spectrum, the electron antineutrino angular correlation coefficient a can be extracted with high accuracy. The goal of the experiment is to determine the coefficient a with a total relative error smaller than 0.3 %, well below the current literature value of 5 %.

First measurements with the *a*SPECT spectrometer were performed in the Forschungs-Neutronenquelle Heinz Maier-Leibnitz in Munich. However, time-dependent background instabilities prevented us from reporting a new value of a.

The contents of this thesis are based on the latest measurements performed with the *a*SPECT spectrometer at the Institut Laue-Langevin (ILL) in Grenoble, France. In these measurements, background instabilities were considerably reduced. Furthermore, diverse modifications intended to minimize systematic errors and to achieve a more reliable setup were successfully performed . Unfortunately, saturation effects of the detector electronics turned out to be too high to determine a meaningful result. However, this and other systematics were identified and decreased, or even eliminated, for future *a*SPECT beamtimes.

The central part of this work is focused on the analysis and improvement of systematic errors related to the *a*SPECT electromagnetic fields. This work yielded in many improvements, particularly in the reduction of the systematic effects due to electric fields. The systematics related to the *a*SPECT magnetic field were also minimized and determined down to a level which permits to improve the present literature value of a. Furthermore, a custom NMR-magnetometer was developed and improved during this thesis, which will lead to reduction of magnetic field-related uncertainties down to a negligible level to determine a with a total relative error of at least 0.3 %.

Zusammenfassung

Das *a*SPECT Spektrometer wurde entworfen, um das Spektrum der Protonen beim Zerfall freier Neutronen mit hoher Präzision zu messen. Aus diesem Spektrum kann dann der Elektron-Antineutrino Winkelkorrelationskoeffizient a mit hoher Genauigkeit bestimmt werden. Das Ziel dieses Experiments ist es, diesen Koeffizienten mit einem absoluten relativen Fehler von weniger als 0.3 % zu ermitteln, d.h. deutlich unter dem aktuellen Literaturwert von 5 %.

Erste Messungen mit dem *a*SPECT Spektrometer wurden an der Forschungsneutronenquelle Heinz Maier-Leibnitz in München durchgeführt. Jedoch verhinderten zeitabhängige Instabilitäten des Meßhintergrunds eine neue Bestimmung von *a*.

Die vorliegende Arbeit basiert hingegen auf den letzten Messungen mit dem *a*SPECT Spektrometer am Institut Laue-Langevin (ILL) in Grenoble, Frankreich. Bei diesen Messungen konnten die Instabilitäten des Meßhintergrunds bereits deutlich reduziert werden. Weiterhin wurden verschiedene Veränderungen vorgenommen, um systematische Fehler zu minimieren und um einen zuverlässigeren Betrieb des Experiments sicherzustellen. Leider konnte aber wegen zu hohen Sättigungseffekten der Empfängerelektronik kein brauchbares Ergebnis gemessen werden. Trotzdem konnten diese und weitere systematische Fehler identifiziert und verringert, bzw. sogar teilweise eliminiert werden, wovon zukünftige Strahlzeiten an *a*SPECT profitieren werden.

Der wesentliche Teil der vorliegenden Arbeit befasst sich mit der Analyse und Verbesserung der systematischen Fehler, die durch das elektromagnetische Feld *a*SPECTs hervorgerufen werden. Hieraus ergaben sich vielerlei Verbesserungen, insbesondere konnten die systematischen Fehler durch das elektrische Feld verringert werden. Die durch das Magnetfeld verursachten Fehler konnten sogar soweit minimiert werden, dass nun eine Verbesserung des aktuellen Literaturwerts von a möglich ist. Darüber hinaus wurde in dieser Arbeit ein für den Versuch maßgeschneidertes NMR-Magnetometer entwickelt und soweit verbessert, dass nun Unsicherheiten bei der Charakterisierung des Magnetfeldes soweit reduziert wurden, dass sie für die Bestimmung von a mit einer Genauigkeit von mindestens 0.3 % vernachlässigbar sind.

Contents

Chapter 1

Introduction

The Standard Model (SM) of Particle Physics describes the current understanding of the elementary particles and their fundamental interactions. The development of the SM, starting in the 1960's, became a great success in the 1970's when the current formulation was finalized upon experimental confirmation of the existence of quarks. The SM described all phenomena and observed particles so far and predicted multiple particles which were later detected. This theory divides the known elementary particles into two groups: quarks and leptons. Each group is divided in three generations containing two particles each, see table 1.1. Each particle has its anti-particle which has the same mass but opposite charge. The SM describes three of the four known interactions: the strong, the weak and the electromagnetic force. Thanks to the SM, the strong, the weak and the electromagnetic interaction are unified and can be described by a single Hamiltonian.

Type of particle	**Generation**			**Effective interactions**		
	$\mathbf{1}^{st}$	$\mathbf{2}^{nd}$	$\mathbf{3}^{rd}$	**El.magn.**	**Strong**	**Weak**
Leptons	e	μ	τ	yes	no	yes
	ν_{e}	ν_{μ}	ν_{τ}	no	no	yes
Quarks	u	c	t	yes	yes	yes
	d	s	b	yes	yes	yes

Table 1.1: The elementary particles and their interactions in the SM description.

Despite of its great success this model (SM) does not contain gravitation. Furthermore, it cannot explain, for example, the baryon asymmetry in the universe, the number of quark generations, and the observed symmetry breaking. One of the goals of modern physics is to test the SM in different systems. The results of such experiments provide information to search for new physics beyond the SM, like for example super symmetry. Additionally to experiments at high energy carried out in accelerators, neutron decay offers a different approach to physics beyond the SM in the low energy limit [1]. It is, for example, used in the search of CP-symmetry and time-reversal violations.

Although neutrons are stable in a nucleus, free neutrons are unstable and decay through the weak interaction with a mean life time of about 15 minutes into a proton p, an electron e^{-} and an electron antineutrino $\bar{\nu_{\mathrm{e}}}$:

$$n \rightarrow p + e^{-} + \bar{\nu_{\mathrm{e}}} + 782.3\,\mathrm{keV}. \tag{1.1}$$

The energy released in this process is given by the mass difference of the neutron compared to proton and electron [2].

Free neutron decay is the simplest form of the β^- decay and it is of great interest as no nuclear structure corrections are necessary. The life time of the free neutrons is one of the parameters which can be measured in neutron decay. There are ongoing disputes about the exact life time of the neutron. The present neutron lifetime world average is $\tau_n = 881.5 \pm 1.5\,\mathrm{s}$, where the error includes a scale factor of 2.7[2]. The scale factor is due the two last measurements of Serebrov et al.[3] and Pichlmaier et al.[4], which disagree considerably from the old average value given by the PDG[2]. New measurements of the neutron life time are therefore needed to clarify the situation. Further information on neutron life time experiments can be found in ref. [1] and [5].

In addition to the life time of the neutron, there is a large number of observables present in neutron decay. This makes it a strongly over-determined process. In the description of the three body decay of the neutron one can define angular correlations between the momenta and spins of the participating particles. The differential decay probability $dW(\vec{p}_\mathrm{e}, \vec{p}_{\bar{\nu}})$ can be expressed by [6]:

$$dW(\vec{p}_\mathrm{e}, \vec{p}_{\bar{\nu}}) \propto 1 + b\frac{m_\mathrm{e}}{E_\mathrm{e}} + a\frac{\vec{p}_\mathrm{e}\cdot\vec{p}_{\bar{\nu}}}{E_\mathrm{e}E_{\bar{\nu}}} + \frac{\vec{P}_\mathrm{n}}{P_\mathrm{n}}\cdot\left(A\frac{\vec{p}_\mathrm{e}}{E_\mathrm{e}} + B\frac{\vec{p}_{\bar{\nu}}}{E_{\bar{\nu}}} + D\frac{\vec{p}_\mathrm{e}\times\vec{p}_{\bar{\nu}}}{E_\mathrm{e}E_{\bar{\nu}}} + R\frac{\vec{p}_\mathrm{e}\times\vec{P}_\mathrm{e}}{E_\mathrm{e}}\right) + \ldots \quad (1.2)$$

where m_e is the mass of the electron, $\vec{p}_{\bar{\nu}}$, $\vec{p}_\mathrm{e}$, $E_{\bar{\nu}}$ and E_e the momenta and energies of antineutrino and electron, respectively. $\vec{P}_\mathrm{e}$ and $\vec{P}_\mathrm{n}$ are the polarizations of electron and neutron. The coefficients $a, A, b, B, D, R \ldots$ are defined as:

a: Electron-antineutrino angular correlation, A: Beta asymmetry, b: Fierz interference term, B: Neutrino asymmetry, D and R: Triple correlation coefficients.

These coefficients can be determined experimentally as well as theoretically. According to the SM, neutron beta decay can be described as a V-A type interaction and then, the Fierz interference term vanishes, $b = 0$ [7]. In the Standard Model time reversal invariance is fulfilled and thus D=0 and R=0. Hence, equation 1.2 reduces to the terms expressed by the correlation coefficients a, A and B which all depend on a single parameter, λ:

$$a = \frac{1 - |\lambda|^2}{1 + 3\,|\lambda|^2} \quad (1.3)$$

$$A = -2\frac{|\lambda|^2 + Re\ \lambda}{1 + 3\,|\lambda|^2} \quad (1.4)$$

$$B = 2\frac{|\lambda|^2 - Re\ \lambda}{1 + 3\,|\lambda|^2} \quad (1.5)$$

Measurements of these correlation coefficients offer three independent ways to determine λ with different systematic errors [7]. The combination of λ with the lifetime of

the neutron, τ_n, permits to determine the matrix element V_{ud} of the Cabibbo-Kobayashi-Maskawa (CKM) matrix (see chapter 2). According to the Standard Model the CKM matrix has to be unitary. One of the unitarity conditions for the first row is given by:

$$|V_{ud}|^2 + |V_{us}|^2 + |V_{ub}|^2 = 1 \tag{1.6}$$

V_{ud} can as well be determined from nuclear β-decay experiments. Together with measurements of $|V_{us}|$ from, for example, K-decays [8] [9] and $|V_{ub}|$ from B meson decays [10], unitarity can be tested. At present, there is an ongoing discussion whether or not unitarity is violated [7]. Furthermore, precision measurements of these angular coefficients permit to search for scalar and tensor contributions in the weak interaction.

To date, the highest accuracy on the determination of the angular correlation coefficient a is $\Delta a/a = 5\,\%$ [11] [12] and results in an average of $a = -0.103(4)$ [2]. This accuracy is still too poor to extract λ with an accuracy comparable to that of other correlation coefficients.

The aim of the spectrometer aSPECT is to improve the accuracy of the measurement of the coefficient a by one order of magnitude, i.e., $\delta a/a = 0.3\,\%$. Since the antineutrino can hardly be detected, we extract the correlation coefficient a from a precise measurement of the proton recoil spectrum in free neutron decay (see chapter 3). aSPECT is a retardation spectrometer based on the MAC-E filter concept, i.e., a **Magnetic Adiabatic Collimation** system followed by an **Electrostatic Filter**. This concept has been successfully applied on electron spectroscopy, [13] [14] [15], and is the basic principle in the KATRIN experiment intended to measure the neutrino mass, [16] [17] [18].

This thesis mostly focusses on the analysis of the electromagnetic field of the aSPECT experiment and the reduction of its systematic errors. The concept of the MAC-E filter and the realization of the electric and magnetic fields are discussed in detail in chapters 3, 4 and 5. A fundamental requirement of the aSPECT spectrometer is a precise determination and monitoring of the magnetic field. For this purpose, a precision magnetometer based on the principles of nuclear magnetic resonance has been built (chapter 6). Its special features permit to measure in ultra high vacuum and low temperature conditions.

Important systematics studied experimentally with different electromagnetic field configurations and results from the aSPECT beamtime, from November 2007 to June 2008, at the Institute Laue-Langevin (ILL) in Grenoble, France, are presented in chapter 7.

Chapter 2

Theoretical introduction

In this chapter the theoretical background of the experiment is introduced with particular emphasis on the decay of the free neutrons. Firstly, an historical overview of the development of the weak interaction, particulary on β-decay, is given. Following, it will be discussed its implementation into the Standard Model of the particle physics and the kinematics of the free neutron beta decay.

The theory of the weak interaction is properly described in several text books and articles. However, the contents in this work are mostly based on review articles from N. Severijns *et al.* [1] and H. Abele [5] as well as previous publications from our collaborators; [19], [20] and [7].

2.1 Theory of Beta Decay

The weak interaction was initially discovered and associated to the β-decay. It is the fundamental interaction responsible of the change of flavor of the quarks and therefore of the hadrons, as free quarks have not been observed. It is also the only interaction experienced by neutrinos. To date, bound states for this interaction have not been found.

Initially, weak decays were described by the theory of Fermi who assumed a point-like interaction. After the discovery of the parity violation on weak processes the theory had to be extended, finally resulting on the V-A theory. Still, the interaction was assumed to be point-like. Nowadays, it is well known that the weak interaction is mediated by the exchange of the $W^{\pm}$ and Z^0 bosons. The high mass of these bosons (about 80 and 91 GeV respectively) justifies the short range of the interaction (about 10^{-3} fm) and consequently explains the great succeed of the Fermi's theory.

2.1.1 Fermi's Theory

Enrico Fermi proposed the point-like theory for the β-decay in 1934. Due the big success of the quantum electrodynamics, QED, to explain the electromagnetic interaction, Fermi proposed to build up the Hamiltonian of the weak interaction in analogy to that of the electromagnetic interaction.

If we consider the electromagnetic scattering of an electron and a proton:

$$e^- + p \longrightarrow e^- + p \tag{2.1}$$

The conservation of the number of leptons and hadrons permits to describe the process as the interaction of two currents, via a virtual photon exchange. In the simplest case of the interaction of an electron with the electromagnetic field, figure 2.1, the Hamiltonian can be expressed as the contraction of two 4-vectors:

(a) (b)

Figure 2.1: Feynman graphs: (a) An electron-photon vertex. (b) Neutron decay in Fermi's presentation. The time arrow is pointing to the right.

$$\mathcal{H} = e j_\mu^{\mathrm{em}} \cdot A^\mu, \tag{2.2}$$

where $j_\mu^{\mathrm{em}} = \bar{\Psi}_{\mathrm{e}} \gamma_\mu \Psi_{\mathrm{e}}$ represents the electromagnetic current density and A^μ the 4-vector potential of the electromagnetic field. The function Ψ_{e} is the electron spinor and $\bar{\Psi}_{\mathrm{e}}$ the corresponding adjoint function[1]. The electric charge, e, is the coupling constant which characterizes the strength of the electromagnetic interaction.

In order to explain the neutron decay, figure 2.1, Fermi assumed a point like interaction between the participating particles and replaced the 4-vector potential by a leptonic current and the electromagnetic by the a hadronic current. The coupling constant for the weak interaction is now the constant G_{F}, which replaces the electric charge:

$$A^\mu(x) \rightarrow J^{\mu,\,\mathrm{lep}}(x) = \bar{\Psi}_{\mathrm{e}}(x)\gamma^\mu \Psi_{\bar{\nu}}(x) \tag{2.3}$$

$$j_\mu^{\mathrm{em}}(x) \rightarrow J_\mu^{\mathrm{had}}(x) = \bar{\Psi}_{\mathrm{p}}(x)\gamma_\mu \Psi_{\mathrm{n}}(x) \tag{2.4}$$

$$e \rightarrow \left(\frac{G_{\mathrm{F}}}{\sqrt{2}}\right) \tag{2.5}$$

The Fermi coupling constant has to be determined experimentally. For example, it can be determined with high accuracy from the decay of the muon[2]: $G_{\mathrm{F}}/(\hbar c)^3 = 1.16637(1)\ \mathrm{GeV}^{-2}$. In analogy to equation 2.2 the Hamiltonian density for the β-decay can now be written as:

$$\mathcal{H}_{Fermi}(x) = \frac{G_{\mathrm{F}}}{\sqrt{2}}(J_\mu^\dagger(x) \cdot J^\mu(x) + \mathrm{h.c.}) \tag{2.6}$$

[1] Ψ is the 4-vector Dirac spinor and $\gamma^\mu = (\gamma^0, \gamma^1, \gamma^2, \gamma^3)$ are the Dirac γ-matrices: $\gamma^0 = \begin{pmatrix} \mathbf{I} & 0 \\ 0 & -\mathbf{I} \end{pmatrix}$, $\vec{\gamma} = \begin{pmatrix} 0 & \vec{\sigma} \\ -\vec{\sigma} & 0 \end{pmatrix}$, $\gamma^5 = i\gamma^0\gamma^1\gamma^2\gamma^3 = \begin{pmatrix} 0 & \mathbf{I} \\ \mathbf{I} & 0 \end{pmatrix}$, $\vec{\sigma}$ are the Pauli matrices using the sum convention of Bjorken-Drell [21]

where h.c. is the hermitian conjugate and the current J_μ is the sum of the hadronic and the leptonic currents:

$$J_\mu = J_\mu^{\text{had}} + J_\mu^{\text{lep}}. \tag{2.7}$$

In most of the publications concerning experiments on neutron decay and, in general, weak interaction, the gamma matrices are represented in their covariant form, γ_5. This is the metric adopted by Severijns *et. al.* [1] and Jackson *et.al.* [6]. For simplicity, this will be the convention used in this work on the following.

2.1.2 Parity Violation

In 1956 Lee and Yang questioned the parity conservation on beta decay, which is explicitly conserved in Fermi's Theory. Lee and Yang, [22], examined the parity conservation in hyperon and meson decays and proposed possible experiments to test parity conservation in these interactions.

It was in 1957 when the violation of the parity on the nuclear beta decay of ^{60}Co was measured on the experiment of Wu *et al.* [23].

The study of the angular distribution of the electrons emitted by polarized ^{60}Co, confirmed experimentally that parity is not conserved on weak interactions. In the Wu's experiment, the atoms of cobalt were kept at low temperatures with their spins aligned along the direction of a strong magnetic field and the emission of the beta electrons was observed. It was measured an asymmetry on the spins of the emitted electrons with respect to the spin of the atoms of cobalt; about 70% of the electrons were emitted in a direction opposite to the nuclear spin.

Experimentally it has been also observed that neutrinos are always left-handed, i.e., their spin is antiparallel with respect to the momentum $\overrightarrow{p}$ of the particle, in contrast antineutrinos are always right-handed particles, see figure 2.2.

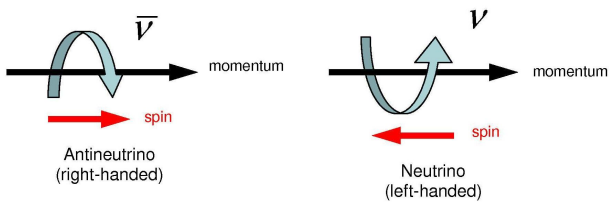

Figure 2.2: Helicity of the neutrino and antineutrino, defined as the projection of the spin onto the direction of the momentum of the particle.

So far parity was found to be maximally violated in weak interaction by all experiments. To include these experimental evidences in the theory of the weak interaction, it was necessary to search for a more general form of the Hamiltonian.

2.1.3 The *V-A* Theory of the Weak Interaction

The most general hamiltonian containing all possible interaction terms which accomplish invariance under Lorentz, parity and time-reversal transformation was proposed by Gamow

and Teller in 1936, [24], as an extension of the Fermi's Theory. Gamow and Teller demonstrated that it is possible to create 16 linear independent 4×4 matrices from the γ-matrices, see table 2.2.

Operator (Γ_i)	Name	Number of matrices
$\Psi\Psi$	Scalar (S)	1
$\Psi\gamma_\mu\Psi$	Vector (V)	4
$\Psi\sigma_{\lambda\mu}\Psi$	Tensor (T)	6
$-i\Psi\gamma_\mu\gamma_5\Psi$	Axial-vector (A)	4
$\Psi\gamma_5\gamma_\mu\Psi$	Pseudoscalar (P)	1

Table 2.2: List of possible current-current interactions. The tensor operator $\sigma_{\lambda\mu}$ is given by: $\sigma_{\lambda\mu} = -\frac{i}{2\sqrt{2}}(\gamma_\lambda\gamma_\mu - \gamma_\mu\gamma_\lambda)$

With these operators the hamiltonian which includes already the observed parity violation in weak decays can be written in its most general form [1]:

$$\begin{aligned}\mathcal{H}_\beta &= \left(\bar{\Psi}_{\mathrm{p}}\Psi_{\mathrm{n}}\right)\cdot\left(\bar{\Psi}_{\mathrm{e}}[C_S + C_S^{'}\gamma_5]\Psi_\nu\right) + \left(\bar{\Psi}_{\mathrm{p}}\gamma_\mu\Psi_{\mathrm{n}}\right)\cdot\left(\bar{\Psi}_{\mathrm{e}}\gamma_\mu[C_V + C_V^{'}\gamma_5]\Psi_\nu\right)\\ &+ \frac{1}{2}\left(\bar{\Psi}_{\mathrm{p}}\sigma_{\lambda\mu}\Psi_{\mathrm{n}}\right)\cdot\left(\bar{\Psi}_{\mathrm{e}}\sigma_{\lambda\mu}[C_T + C_T^{'}\gamma_5]\Psi_\nu\right) - \left(\bar{\Psi}_{\mathrm{p}}\gamma_\mu\gamma_5\Psi_{\mathrm{n}}\right)\cdot\left(\bar{\Psi}_{\mathrm{e}}\gamma_\mu\gamma_5[C_A + C_A^{'}\gamma_5]\Psi_\nu\right)\\ &+ \left(\bar{\Psi}_{\mathrm{p}}\gamma_5\Psi_{\mathrm{n}}\right)\cdot\left(\bar{\Psi}_{\mathrm{e}}\gamma_5[C_P + C_P^{'}\gamma_5]\Psi_\nu\right) + \mathrm{h.c.}\end{aligned} \tag{2.8}$$

where the subindex $i \in [S, V, T, A, P]$ refers to the operators defined in table 2.2. The coefficients C_i and C_i' determine the amplitude of each interaction. The Hamiltonian of equation 2.8 can be regrouped[25] in order to show separately the sum corresponding to the left-handed and right-handed currents:

$$\mathcal{H} = \frac{G_{\mathrm{W}}}{\sqrt{2}}\sum_i \left[L_i\left(\bar{\Psi}_{\mathrm{p}}\Gamma_i\Psi_{\mathrm{n}}\right)\cdot\left(\bar{\Psi}_{\mathrm{e}}\Gamma_i(1+\gamma_5)\Psi_\nu\right) + R_i\left(\bar{\Psi}_{\mathrm{p}}\Gamma_i\Psi_{\mathrm{n}}\right)\cdot\left(\bar{\Psi}_{\mathrm{e}}\Gamma_i(1-\gamma_5)\Psi_\nu\right)\right] + \mathrm{h.c.} \tag{2.9}$$

where the weak coupling constants C_i and C_i' are parametrized as:

$$C_i = \frac{G_W}{\sqrt{2}}(L_i + R_i), \qquad C_i^{'} = \frac{G_W}{\sqrt{2}}(L_i - R_i). \tag{2.10}$$

and $G_{\mathrm{W}} = G_{\mathrm{F}}V_{ud}$ is a general weak coupling constant also introduced in [25]. The coupling constants for the left-handed, L_i, and right-handed, R_i, contributions have to be determined experimentally. This Hamiltonian violates parity if $L_i \neq R_i$ and time reversal symmetry if the coupling constants have a relative complex phase. The introduction of parity violation inside the model implies that only left-handed components of vector and axial-vector couplings can contribute to the beta decay. In terms of the coupling constants: $C_V/C_V^{'} = 1$, $C_A/C_A^{'} = 1$, $C_S = C_S^{'} = C_T = C_T^{'} = C_P = C_P^{'} = 0$, and $Im(C_i) = 0$ for all

i [1].This leads to a simplification of the Hamiltonian of equation 2.9 to:

$$\begin{aligned}\mathcal{H} &= \frac{G_{\mathrm{W}}}{\sqrt{2}} \sum_{\mathrm{V,A}} L_i \left(\bar{\Psi}_{\mathrm{p}} \Gamma_i \Psi_{\mathrm{n}}\right) \cdot \left(\bar{\Psi}_{\mathrm{e}} \Gamma_i (1+\gamma_5) \Psi_{\nu}\right) + \mathrm{h.c.} \\ &= g_{\mathrm{V}} (\bar{\Psi}_{\mathrm{p}} \gamma_\mu (1 - \lambda\gamma_5) \Psi_{\mathrm{n}}) \cdot (\bar{\Psi}_{\mathrm{e}} \gamma_\mu (1+\gamma_5) \Psi_{\nu}) + \mathrm{h.c.}\end{aligned} \tag{2.11}$$

where g_{V} and g_{A} are the vector and axial vector coupling constants and λ their ratio:

$$g_{\mathrm{V}} = \frac{G_{\mathrm{W}}}{\sqrt{2}} L_{\mathrm{V}}, \quad g_{\mathrm{A}} = \frac{G_{\mathrm{W}}}{\sqrt{2}} L_{\mathrm{A}}, \quad \lambda = \frac{g_{\mathrm{A}}}{g_{\mathrm{V}}} = \frac{|g_{\mathrm{A}}|}{|g_{\mathrm{V}}|} \cdot e^{i\phi}. \tag{2.12}$$

with ϕ=180° in the SM. In β-decay, not all the transitions are allowed. The transitions where no orbital angular momentum is transferred to the leptons are called allowed transitions and are divided into Fermi and Gamow-Teller transitions. The spins of the electron and antineutrino are 1/2. Thus, they can couple to a total spin $\vec{S}$ equal to 0 or 1. Transitions mediated by the Scalar and Vector couplings are called Fermi transitions. They do not change the spin of the nucleus or nucleon and the spin of the leptons couple to a singlet state $S = 0$. Axial-Vector and Tensor couplings contribute to the Gamow-Teller transitions where the spin of the nucleus or nucleon is changed and the spin of the leptons couple to a triplet state $S = 1$:

$$\begin{aligned}\Delta J &= 0 \quad \text{Fermi decay} \\ \Delta J &= 0, \pm 1 \quad \text{Gamow-Teller decay} \\ &\quad (\text{except } 0 \rightarrow 0)\end{aligned} \tag{2.13}$$

Pure Fermi transitions (like $^{14}O \rightarrow {}^{14}N$) and Gamow-Teller transitions (like $^{6}He \rightarrow {}^{6}Li$) are experimentally observed, however, most of the decays are mixtures as the free neutron decay too.

2.1.4 The Standard Model and the CKM Matrix

The Hamiltonian of equation 2.11 is a generalization of the Fermi's theory and consequently considers a point-like interaction. Although it describes properly the parity violation in beta decay, produces a non re-normalizable theory, i.e., the cross section diverges for energies $E \rightarrow \infty$, see equation 2.19.

In analogy to the QED where the interaction is mediated by virtual photons, the Standard Model postulates that the interaction is mediated by the exchange of virtual particles called bosons. The interaction via boson exchange introduces a propagator term into the Hamiltonian in the form:

$$\frac{1}{Q^2 + M^2} \tag{2.14}$$

where Q is the momentum transfer and M the mass of the intermediate boson. If the momentum transfer is small compared to the boson mass the propagator can be considered to be constant. But it falls as $1/Q^2$ at very high momentum transfer. Now, equation 2.19

converges to 0 for very high energies, $E \to \infty$.

The fundamentals for this theory were developed by Glashow, Weinberg and Salam, [26], [27], [28], from the study of hadrons decays and neutrinos interactions. The theory predicts an spontaneous symmetry breaking and the existence of three intermediate vector bosons, $W^{\pm}$ and Z^0. Now, the interaction is not point-like but is produced due to the exchange of these virtual particles. The high mass of the virtual bosons is a consequence of the short range of the interaction. By Heisenberg's relation of uncertainty, $\tau < \hbar/M_{\mathrm{W,Z}}$ with $M_{\mathrm{W}} = 80,398(25)\,\mathrm{GeV}/c^2$ [2] and $M_{\mathrm{Z}} = 91,1876(21)\,\mathrm{GeV}/c^2$ and considering the speed of light as maximum speed, the interaction is found to have a range of $\sim 2.5{\cdot}10^{-18}\,\mathrm{m}$. Therefore, the point-like interaction of the V-A theory can be considered as a low energy limit of the Standard Model.

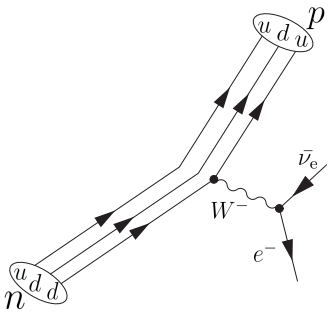

Figure 2.3: Feynman graph of neutron decay in the SM: A neutron (udd) decays into proton (uud), electron and antineutrino by the exchange of a $W^{\pm}$ boson.

Nowadays it is known that matter is composed by fermions (fundamental particles with spin 1/2) grouped into two categories: quarks and leptons. The standard model subdivides the known quarks into three families depending on their charges and masses:

$$\begin{pmatrix} u \\ d \end{pmatrix}, \quad \begin{pmatrix} c \\ s \end{pmatrix}, \quad \begin{pmatrix} t \\ b \end{pmatrix}. \tag{2.15}$$

The six type of quarks are known as flavors. Furthermore, each quark has three degrees of freedom called color. The attraction and repulsion of quarks charged with different combinations of the three colors is due to the strong interaction which is mediated by force carrying particles known as gluons. Quarks have spin=1/2 and baryonic number B=1/3. In addition to the electric charge, they present charges S, C, T and B plus the isospin I (where I_3 is the third component of the isospin). The three families of quarks and their properties are summarized in table 2.3.

To each lepton and quark, correspond as well its anti-particle. Quarks combine in groups of three to produce baryons and in groups of quark-antiquark to produce mesons. Nucleons are baryons and thus they are composed of three quarks. In a nut shell, atoms are composed by only two kind of quarks; protons are an ensemble of (u, d, u) whereas neutrons are composed by (u, d, d). This means, neutron beta decay occurs because of the quark transformation $d \longrightarrow u$, figure 2.3. However, weak decays between different families have been observed. Examples of such transitions are $K^+ \longrightarrow \mu^+\nu$ or $\Delta^0 \longrightarrow p\pi^-$. Due to the fact that in weak decays quarks from different families can interact, it is necessary to

QUARKS S=1/2, B=1/3	Q	I	I_3	C charm	S strange	T truth	B beauty
up	2/3	1/2	1/2	0	0	0	0
down	-1/3	1/2	-1/2	0	0	0	0
charm	2/3	0	0	1	0	0	0
strange	-1/3	0	0	0	-1	0	0
top	2/3	0	0	0	0	1	0
bottom	-1/3	0	0	1	0	0	-1

Table 2.3: Properties of the three quark families.

consider the weak quark eigenstates to be composed as a linear combination of the quarks mass eigenstates. For the first two quark families, the linear combination was formulated by Cabibbo in 1963 as a rotation matrix with rotation angle θ_c, the Cabibbo angle [29]. With the discovery of the third family of quarks, the matrix had to be extended to a 3×3 matrix, the Cabibbo-Kobayashi-Maskawa (CKM) matrix [30]:

$$\begin{pmatrix} |d'\rangle \\ |s'\rangle \\ |b'\rangle \end{pmatrix} = \begin{pmatrix} V_{ud} & V_{us} & V_{ub} \\ V_{cd} & V_{cs} & V_{cb} \\ V_{td} & V_{ts} & V_{tb} \end{pmatrix} \begin{pmatrix} |d\rangle \\ |s\rangle \\ |b\rangle \end{pmatrix} \tag{2.16}$$

where the primed values are the weak eigenstates, $|q'\rangle$, and the unprimed values the mass eigenstates $|q\rangle$. The coefficients $V_{i,j}$, of the matrix have to be determined experimentally. The up to date accepted coefficients of the CKM matrix are obtained combining the different measurements available with the constrains imposed by the Standard Model [2]:

$$(|V_{ij}|) = \begin{pmatrix} 0.97419 \pm 0.00022 & 0.2257 \pm 0.0010 & 0.00359 \pm 0.00016 \\ 0.2256 \pm 0.0010 & 0.97334 \pm 0.00023 & 0.0415^{+0.0010}_{-0.0011} \\ 0.00874^{+0.00026}_{-0.00037} & 0.0407 \pm 0.0010 & 0.999133^{+0.000044}_{-0.000043} \end{pmatrix}. \tag{2.17}$$

The elevated value of the diagonal coefficients in comparison to the rest shows that transitions between families are considerably suppressed. The Standard Model assumes the existence of only three quark generations and thus the transformation matrix, CKM, can be considered as a rotation matrix which has to be unitary. Nowadays, the most precise test of unitarity comprises the sum of the square roots of the matrix elements of the first row which should equal to one:

$$|V_{\mathrm{ud}}|^2 + |V_{\mathrm{us}}|^2 + |V_{\mathrm{ub}}|^2 = 1. \tag{2.18}$$

Its deviation from unitarity would point to physics beyond the Standard Model [31] [32] [1] [5].

2.2 Observables in neutron decay

2.2.1 Angular correlation coefficients

The so called Fermi's golden rule describes how to calculate the transition rate (probability of a transition per unit of time) from an initial state to a final state:

$$W_{i\to f} = \frac{2\pi}{\hbar} |\langle f|\mathcal{H}_{\rm fi}|i\rangle|^2 \cdot \rho'_{\rm e}(E_{\rm e}), \tag{2.19}$$

where $\rho'_{\rm e}(E_{\rm e})$ is the phase space density of the final states and $\mathcal{M}_{\rm fi} = \langle f|\mathcal{H}_{\rm fi}|i\rangle$ is the transition matrix element. So, the transition rate depends on the strength of the interaction between the initial and final state, $\mathcal{M}_{\rm fi}$, and the density of final states at a certain energy interval, $\rho'_{\rm e}(E_{\rm e})$.

The interaction matrix $\mathcal{M}_{\rm fi}$ can be calculated by using the Hamiltonian of equation 2.11. Consequently, the decay probability for a certain process can be calculated as a function of the coupling constants. Jackson *et al.* calculated in 1957[6] the distribution of electron and antineutrino energies ($E_{\rm e}$ and E_ν, respectively) and momenta ($\vec{p}_{\rm e}$, $\vec{p}_\nu$) for the case of the beta decay:

$$\frac{dW}{dE_{\rm e}d\Omega_{\rm e}d\Omega_\nu} = \frac{G_{\rm W}^2}{(2\pi)^4\hbar}\rho'_{\rm e}(E_{\rm e})\xi \cdot \left\{1 + a\frac{\vec{p_{\rm e}}\vec{p_\nu}}{E_{\rm e}E_\nu} + \frac{\vec{P}_{\rm n}}{P_{\rm n}} \cdot \left(A\frac{\vec{p_{\rm e}}}{E_{\rm e}} + B\frac{\vec{p_{\bar\nu}}}{E_{\bar\nu}}\right) + \dots\right\}. \tag{2.20}$$

In this work we are interested on the parameters (a, A and B). Thus, the complete expression derived by Jackson is not shown. ξ is the sum of the squares of the coupling constants as presented in [25]:

$$\xi = \left(|L_{\rm S}|^2 + |L_{\rm V}|^2 + |R_{\rm S}|^2 + |R_{\rm V}|^2\right) + 3\left(|L_{\rm A}|^2 + |L_{\rm T}|^2 + |R_{\rm A}|^2 + |R_{\rm T}|^2\right). \tag{2.21}$$

Equation 2.21 shows the mixture of Fermi and Gamow-Teller decays. The factor 3 indicates the triplet state of the Gamow-Teller decays in contrast to the singlet state of the Fermi transitions. Within the standard model the equation simplifies to

$$\xi = |L_{\rm V}|^2 + 3|L_{\rm A}|^2, \tag{2.22}$$

which, using the coupling constants of the weak interaction (equation 2.12) takes the form:

$$\xi = \frac{|g_{\rm V}|^2 + 3|g_{\rm A}|^2}{G_{\rm W}^2/2}. \tag{2.23}$$

Now, the parameters a, A and B (also known as angular correlation coefficients), can be expressed as a function of the coupling constants L_i and R_i. Within the Standard Model these coefficients depend only on the coupling constants of the weak interaction:

$$a = \frac{1-|\lambda|^2}{1+3|\lambda|^2}, \quad A = -2\frac{|\lambda|^2 + Re(\lambda)}{1+3|\lambda|^2}, \quad B = 2\frac{|\lambda|^2 - Re(\lambda)}{1+3|\lambda|^2}, \quad \lambda = \frac{g_{\rm A}}{g_{\rm V}} \tag{2.24}$$

The first coefficient a is named *Beta-neutrino correlation coefficient*. It represents the angular correlation between the decaying electron and the electron antineutrino. Coefficient A, also called *Beta asymmetry coefficient*, is the angular correlation between neutron spin and electron momentum. Finally, parameter B, the *Antineutrino asymmetry coefficient*, represents the correlation between the neutron spin and the momentum of the decay neutrino. The abBA Collaboration, [33], is preparing a detector that would be able to measure the correlations a, b, A and B, where b is the Fierz interference coefficient (not shown in equation 2.20). The Fierz interference term contains mixed S/V, and A/T terms, therefore, in the framework of the V-A theory b is zero. For more detailed information on the coefficients the reader is referred to [1], [5] and [25].

The best sensitivity on λ is obtained by measuring the β-asymmetry coefficient A, $dA/d\lambda = -0,374$. The most precise measurement on A was obtained by the Perkeo II experiment, [5]. The world average value of A is $A = 0.1173(13)$ [2]. A measurement of the coefficient a has a similar sensitivity to λ as the parameter A, $da/d\lambda = -0,298$. At present, the most accurate measurements of a was performed by Stratowa *et al.*, 1978 [11] and Byrne *et al.*, 2002 [12]. The present world average value is $a = -0.103(4)$ [2]. Consequently, the measurements of the angular correlation coefficient a has to be improved by almost one order of magnitude in order to be competitive with the measurements of A.

The aim of the aSPECT spectrometer is to measure the coefficient a with an accuracy of $\Delta a/a \approx 0.3\,\%$ in order to provide an independent test for the value of λ and to search for contributions of scalar and tensor interactions, [1].

The difficulties of detecting neutrinos forces us to search for an indirect measurement of the angular correlation coefficient. Similarly to previous measurements of a, [34], [11] and [12], aSPECT infers the coefficient a from the shape of the proton spectrum, see section 7.2.2. A different approach is used by the aCORN experiment. The aCORN experiment determines a by comparing the coincidence rates of electron and proton which presents an asymmetry proportional to a, [35] and [36].

2.2.2 Neutron Lifetime

Another fundamental observable on free neutron decay is the lifetime τ_n of the free neutron. τ_n can be obtained by integration of the differential decay probability, equation 2.20, and inversion (using natural units $\hbar$=c=1) [5]:

$$\tau_n = \frac{2\pi^3}{m_e^5 G_W^2 \xi f (1 + RC)}. \tag{2.25}$$

f is the phase space factor, which includes the Fermi function contribution [37]:

$$f = m_e^{-5} \int_{m_e}^{E_{0,e}} \rho_e' \mathrm{d}E_e = 1.6887$$

$(1+RC)$=1.03885 ± 0.00044 is an overall electroweak radiative correction factor which includes $\mathcal{O}(\alpha^2)$ [38].

In the V-A theory, equation 2.25 simplifies to:

$$\tau_n = \frac{2\pi^3}{m_e^5 f} \frac{1}{|g_V|^2 + 3|g_A|^2}. \tag{2.26}$$

It can also be expressed to show its dependency with λ and the first element of the CKM matrix, V_{ud} [2]:

$$|\mathrm{V_{ud}}| = \sqrt{\frac{4908.7(1.9)\quad \mathrm{sec.}}{\tau_\mathrm{n}\,(1+3|\lambda|^2)}} \tag{2.27}$$

The present neutron lifetime world average is $\tau_n = 881.5 \pm 1.5\,\mathrm{s}$, where the error includes a scale factor of 2.7[2]. The scale factor is due the two last measurements of Serebrov et al.[3] and Pichlmaier et al.[4], which disagree considerably from the old average value given by the PDG[2]. New measurements of the neutron life time are therefore needed to clarify the situation. Further information on neutron life time experiments can be found in ref. [1] and [5].

2.2.3 Proton spectrum

The proton energy spectrum for the specific case of the neutron decay was calculated by Nachtmann in 1968 [39]. A sign error was found by Habeck [40]. Neglecting Coulomb and radiative corrections, Nachtmann obtains for the differential proton energy spectrum:

$$\begin{aligned}\mathrm{d}w(T) = \frac{\Sigma\Delta^3 G_V^2}{2^4\pi^3(1+2\delta)}\Big(\frac{\sigma-x^2}{\sigma}\Big)^2\sqrt{1-\sigma}\Bigg\{\Big(1+\frac{x^2}{\sigma}-\sigma\Big)- \\ -\frac{1}{3}\frac{\sigma-x^2}{\sigma}(1-\sigma)+\lambda^2\Bigg[\Big(1+\frac{x^2}{\sigma}+\sigma\Big)-\frac{1}{3}\frac{\sigma-x^2}{\sigma}(1-\sigma)\Bigg]\Bigg\}\mathrm{d}T\end{aligned} \tag{2.28}$$

where T represents the kinetic energy of the proton, and λ the ratio of the coupling constants as defined in equation 2.12. The other quantities are defined as follows:

$$\begin{aligned}&\Delta = m_n - m_p, && \Sigma = m_n + m_p,\\ &x = m_e/\Delta, && \delta = \Delta/\Sigma,\\ &\sigma = 1 - \frac{2m_n}{\Delta^2}T.\end{aligned}$$

Now it is useful to rewrite equation 2.28 as a linear combination of two functions with the angular correlation coefficient a as parameter [41]. This form permits to show the dependency of the proton spectrum shape with the correlation coefficient a:

$$\frac{\mathrm{d}w(T)}{\mathrm{d}T} \propto g_1(T) + a g_2(T) \tag{2.29}$$

with $g_1(T)$ and $g_2(T)$ are functions of the kinetic energy of the proton, T:

$$g_1 = \Big(\frac{\sigma-x^2}{\sigma}\Big)^2\sqrt{1-\sigma}\Bigg[4\Big(1+\frac{x^2}{\sigma}\Big)-\frac{4}{3}\frac{\sigma-x^2}{\sigma}(1-\sigma)\Bigg] \tag{2.30}$$

$$g_2 = \left(\frac{\sigma - x^2}{\sigma}\right)^2 \sqrt{1-\sigma}\left[4\left(1 + \frac{x^2}{\sigma} - 2\sigma\right) - \frac{4}{3}\frac{\sigma - x^2}{\sigma}(1-\sigma)\right] \tag{2.31}$$

Both functions are plotted in figure 2.4 (a). Further, the effect of several hypothetical values of a on the proton spectrum profile is shown in figure 2.4 (b). A theoretical proton recoil spectrum including recoil-order, Coulomb and model independent radiative corrections, can be found in ref. [42].

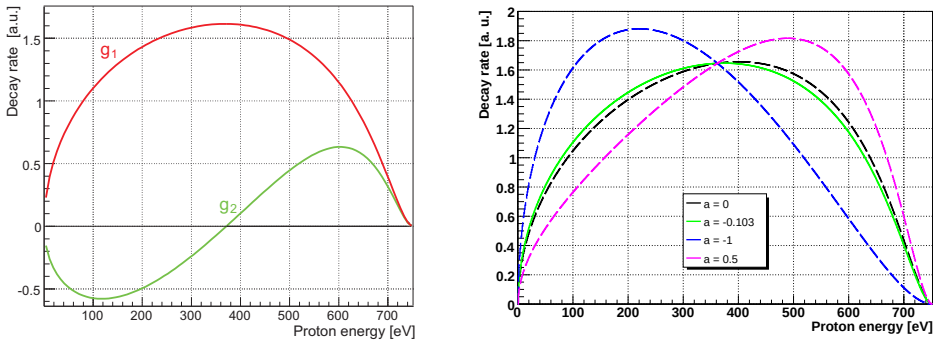

(a) (b)

Figure 2.4: (a) Functions g_1 and g_2 used for the decomposition of the proton spectrum, equations 2.30 and 2.31. (b) Proton spectra for different values of a. The proton spectrum for the world average value of $a = -0.103(4)$ [2] is displayed in green.

Chapter 3

Description of the spectrometer *a*SPECT

The *a*SPECT spectrometer has been designed in order to provide a precise measurement of the proton spectrum in free neutron beta decay. Its particular design allows a 4π acceptance of the decay protons and provides a wide variety of possibilities for carrying out systematic checks.

In this chapter, the working principle as well as the main features of the spectrometer are described. References to other papers will be given within the text.

3.1 Measurement principle

A beam of unpolarized cold neutrons passes through the *a*SPECT spectrometer which is essentially cylindrically symmetric, see figure 3.5. About 10^{-8} of the neutrons in the beam decay in the so called **Decay Volume** (DV). This region defines the origin of the coordinate system. Protons emitted into the upper hemisphere are guided by the strong magnetic field towards the proton detector placed on top of the spectrometer. A mirror electrode placed below the decay volume reflects all protons emitted into the lower hemisphere. Thus, these protons are redirected towards the proton detector and consequently a 4π acceptance is realized.

Protons traveling towards the detector are energy-selected by a potential barrier, U_A, created by the **Analyzing Plane** electrode (AP). Varying the potential applied at this electrode permits to scan the complete proton spectrum. In addition, background measurements can be performed for voltage settings $> 780\,\mathrm{V}$. Note that the maximum kinetic energy of the decay protons is $751.4\,\mathrm{eV}$.

Finally, protons able to overcome the potential barrier are focused onto the detector by a strong magnetic field. The high electric potential at which the detector electrode is held, typically $-15\,\mathrm{kV}$, accelerates the protons to a detectable energy.

Protons unable to cross the AP potential barrier are reflected and remain trapped between the mirror and the AP electrode. The $E \times B$ drift created by the dipole electrode named **Lower** $E \times B$ permits to remove the trapped protons out of the flux tube[1] of the spectrometer.

The high accuracy for the determination of a, reachable by such an spectrometer, comes from the MAC-E filter design which is explained next.

[1] The magnetic field lines connecting the decay volume and the detector define what we call a flux tube.

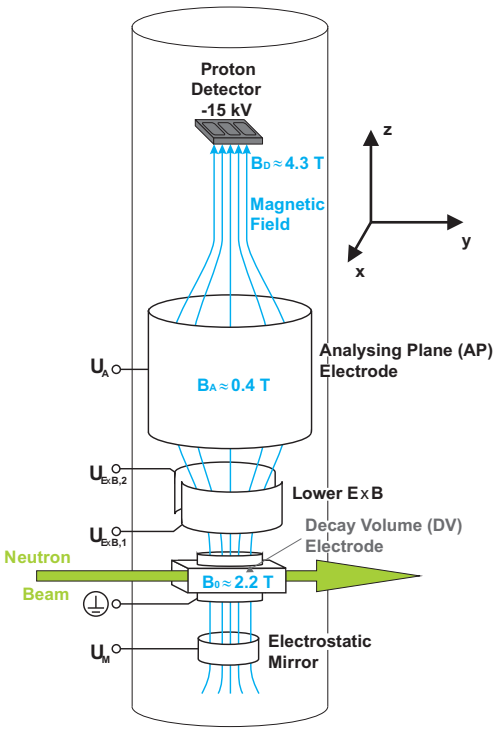

Figure 3.5: Scheme of the *a*SPECT spectrometer. Decay protons are guided by the magnetic field either towards the detector or in the opposite direction, where they are reflected by an electrostatic mirror. The protons are energy selected by the AP electrode. Protons able to cross the AP potential barrier are focused onto the detector.

3.2 MAC-E Filter

MAC-E filter refers to a **Magnetic Adiabatic Collimation** system followed by an **Electrostatic Filter**. This concept has been successfully applied on electron spectroscopy, [13] [14] [15], and is the basic principle in the KATRIN experiment (**Ka**rlsruhe **Tri**tium **N**eutrino experiment) intended to measure the neutrino mass, [16] [17] [18]

A scheme of the *a*SPECT MAC-E filter spectrometer is shown in figure 3.6. Decay protons in the DV region are guided by the magnetic field lines on a helical motion along the spectrometer. The drop of the magnetic field from the DV, $B_0 \approx 2.2\,\mathrm{T}$, to the AP $B_A \approx 0.4\,\mathrm{T}$ produces a conversion of the proton transversal momentum into longitudinal momentum, i.e, along the magnetic field axis. This effect is called Magnetic Adiabatic Collimation.

The collimation is followed by an electrostatic potential barrier which acts as a filter to the longitudinal component of the proton momentum; only protons with enough longitudinal energy component are able to cross the potential barrier. A remaining perpendicular energy momentum is therefore not analyzed. This circumstance will be discussed in detail in following section 3.3

The helical motion of charged particles inside an electromagnetic field arises from the

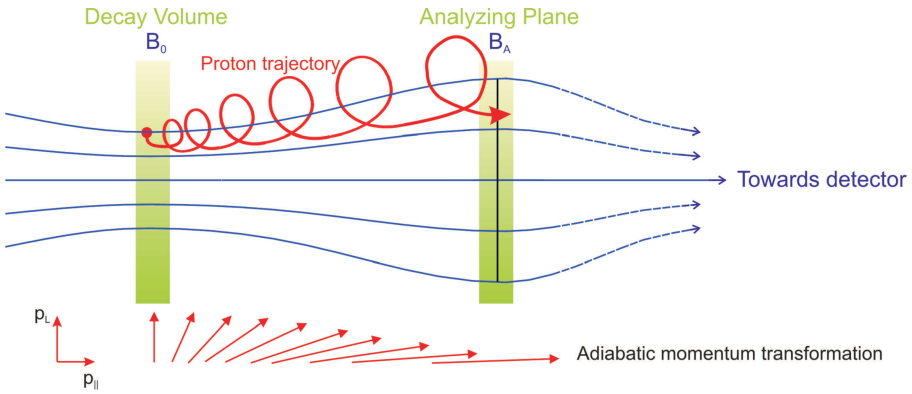

Figure 3.6: Scheme of the *a*SPECT MAC-E filter spectrometer. The MAC-E filter comprises the region from the decay volume to the analyzing plane. The magnetic field lines are plotted in blue. The blue dashed lines after the analyzing plane denote the steep increase of the magnetic field which focusses the protons onto the detector.

Lorentz force:

$$\vec{F} = q\vec{v} \times \vec{B} + q\vec{E} \tag{3.1}$$

where $\vec{v}$ and q represent the velocity and charge of the particle moving inside electric and magnetic fields $\vec{E}$ and $\vec{B}$, respectively.

A special consideration can be made to particles moving inside slowly changing magnetic fields. The helical motion induced by the Lorentz force is called adiabatic if the relative spatial changes of the magnetic and electric fields stay small during one particle gyration, $\Delta B/B \ll 1$ and $\Delta E/E \ll 1$. In this case, the magnetic flux through the particle orbit remains constant, [43]. This means that if B increases, the gyration radius of the particle decreases so that the product $B\pi r^2$ remains unchanged. The constancy of the magnetic flux through the particle orbit leads to the following adiabatic invariants:

$$\begin{aligned} &Br^2 \\ &p_\perp^2/B \\ &\gamma\mu \end{aligned} \tag{3.2}$$

where $p_\perp$ represents the component of the particle momentum perpendicular to the magnetic field and $\gamma = 1/\sqrt{1 - v^2/c^2}$ is the relativistic factor. The magnetic moment μ is defined as the current loop of the charged particle times the area enclosed by the loop:

$$\mu = I \cdot A = \left(\frac{qv_\perp}{2\pi r}\right)(\pi r^2) = \frac{q\omega r^2}{2} \tag{3.3}$$

where q is the charge of the particle gyrating around the magnetic field lines on an orbit of radius r with a speed $v_\perp$. The subindex $\perp$ indicates the component perpendicular to the magnetic field lines. ω is the cyclotron frequency given by:

$$\omega = \frac{qB}{\gamma m} \tag{3.4}$$

The magnetic moment can be rewritten as:

$$\mu = \frac{p_\perp^2}{2mB} \tag{3.5}$$

which, according to equation 3.2, is an adiabatic invariant where γ has been set to 1 due to the small velocity of the protons.

If only a slowly changing magnetic field is applied, the kinetic energy is conserved and so that the velocity is constant at any position along the z axis:

$$v_\parallel^2 + v_\perp^2 = v_0^2 = \text{constant} \tag{3.6}$$

v_0 is the initial velocity of the particle at $z = 0$ which can be decomposed into its longitudinal and perpendicular components, $v_\parallel^2$ and $v_\perp^2$. Since the field is slowly changing, the magnitude $p_\perp^2/B$ is an adiabatic invariant and we can write:

$$\frac{v_\perp^2}{B} = \frac{v_{\perp 0}^2}{B_0} \tag{3.7}$$

Then the parallel velocity along the field axis is given by:

$$v_\parallel^2 = v_0^2 - v_{\perp 0}^2 \cdot \frac{B(z)}{B_0} \tag{3.8}$$

In other words, the magnetic field gradient, $\vec{\nabla}\vec{B}$, from $z = 0$ to z transforms most of the cyclotron energy into longitudinal motion. This is due the Stern-Gerlach force ($\vec{F} = -\vec{\nabla}(-\vec{\mu}\vec{B})$) which for a constant magnetic moment $\vec{\mu}$ is $\vec{F} = \vec{\mu}(\vec{\nabla}\vec{B})$. The momentum transformation depends on the field gradient or equivalently on the ratio of the field at the starting position, B_0, and at the point $z > 0$. Only a ratio $B(z)/B_0 \longrightarrow 0$ produces a total momentum transfer. Contrary, an increasing magnetic field may reverse the longitudinal component of the particle momentum producing the so called magnetic mirror effect. This effect can be used to trap particles.

3.3 Transmission Function

The transmission function of the spectrometer, $F_{tr}(T_0)$ is defined as the probability that a proton with a given starting kinetic energy T_0 passes the potential barrier U_A applied at the analyzing plane. It is thus dependent on the electric potential difference between AP and DV, and the magnetic field ratio which determines the momentum conversion. The energy resolution of the spectrometer is therefore linked to these parameters. The derivation of the theoretical transmission function follows the previous works [25] and [44].

If the adiabatic condition is fulfilled all the way from the DV to the AP, the transmission function can be derived analytically. To do that, we can decompose the kinetic energy of the protons into its longitudinal and perpendicular components at any point z:

$$\begin{aligned} T_\perp &= T \sin^2\theta \\ T_{||} &= T \cos^2\theta \end{aligned} \tag{3.9}$$

θ is the angle between the momentum of the proton and the magnetic field lines. Within the adiabatic approximation the magnetic moment μ is invariant:

$$\mu = \frac{p_\perp^2}{2m_\mathrm{p}B} = \frac{T\sin^2\theta}{B} = \text{const} \tag{3.10}$$

where m_p is the mass of the proton and B refers to the magnetic field value at any point of the trajectory. Thus, the value of the magnetic moment at any point of the proton's trajectory is equal to the magnetic moment in the decay volume at the time of the decay:

$$\frac{T_0\sin^2\theta_0}{B_0} = \frac{T\sin^2\theta}{B} \tag{3.11}$$

The subindex 0 denotes the initial position in the DV. No sub-index refers to any point along the proton trajectory. Then, the angle of the proton momentum with respect the magnetic field line at a given position may be written:

$$\sin^2\theta = \frac{B}{B_0}\frac{T_0}{T}\sin^2\theta_0 \tag{3.12}$$

Combining equations 3.12 and 3.9, the longitudinal kinetic energy at any point of the trajectory can be written as:

$$T_{||}^{\mathrm{ad}} = T - \frac{B}{B_0}T_0\sin^2\theta_0 \tag{3.13}$$

where the index *ad*, refers to the adiabatic approximation. The total energy (E) of the proton is composed of a kinetic and a potential contribution $E = T + V$. The initial energy of the decay protons is fully kinetic: $E_0 = T_0$. As the proton travels towards the AP, part of the kinetic energy converts into potential energy. At any point of the trajectory, the proton has kinetic energy T and potential energy $V = e(U - U_0)$. At the same time, the inverse magnetic mirror effect converts the cyclotron or transverse kinetic energy into longitudinal energy. Then, combining equation 3.13 with the conservation of the energy inside electric and magnetic fields and using $E_0 = T_0$:

$$T_{||}^{\mathrm{ad}} = T_0 - e(U - U_0) - \frac{B}{B_0}T_0 sin^2(\theta_0) \tag{3.14}$$

A proton is able to cross the potential barrier only if $T_{||}^{\mathrm{ad}} > 0$ at any point of its trajectory. If $T_{||}^{\mathrm{ad}}$ becomes zero at some point, the proton is reflected. In the following we define T_{tr} as the minimum initial kinetic energy necessary to cross the potential barrier. Then, imposing the condition $T_{||}^{\mathrm{ad}} = 0$ at the analyzing plane for a proton with an initial kinetic energy $T_0 = T_{\mathrm{tr}}$, we obtain:

$$T_{\mathrm{tr}} = \frac{\mathrm{e}(U_\mathrm{A} - U_0)}{1 - \frac{B_\mathrm{A}}{B_0}\sin^2\theta_0} \tag{3.15}$$

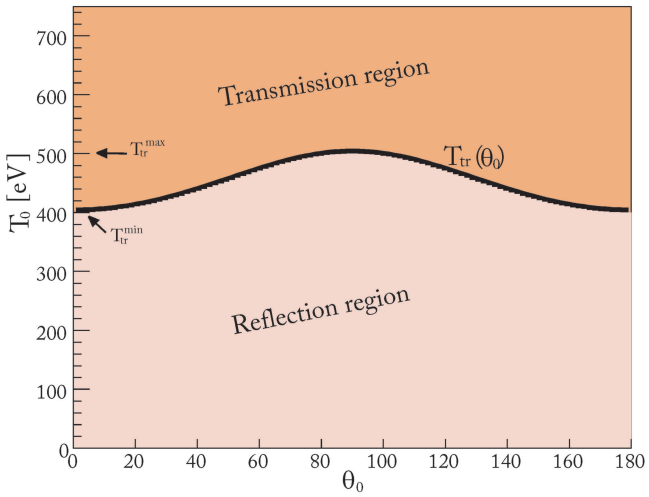

Figure 3.7: Angular dependence of the minimum initial kinetic energy, $T_{\mathrm{tr}}(\theta_0)$, needed for a proton to cross the potential barrier (equation 3.15). For the example given, a potential barrier $U_A - U_0 = 400\,\mathrm{V}$ is used. Only protons with an initial kinetic energy $T_0 \geq T_{\mathrm{tr}}(\theta_0)$ are transmitted.

This results implies that the minimum transmission kinetic energy T_{tr} is a function of the emission angle of the decay proton with respect to the magnetic field lines, see figure 3.7. On the extreme case of a proton emitted along the magnetic field axis, $\theta_0 = 0$:

$$T_{\mathrm{tr}}^{\mathrm{min}} = e(U - U_0) \tag{3.16}$$

the minimum transmission energy equals the electric potential energy. So each proton with $T_0 < T_{\mathrm{tr}}^{\mathrm{min}} = e(U - U_0)$ is reflected independently of its emission angle, i.e., $F_{\mathrm{tr}}(T_0 < T_{\mathrm{tr}}^{\mathrm{min}}) = 0$. On the other hand, for the case of $\sin\theta_0 = \pm 1$ (protons emitted perpendicular to the magnetic field lines), we obtain the transmission energy $T_{\mathrm{tr}}^{\mathrm{max}}$ above which all protons with higher initial kinetic energies, $T_0 \geq T_{\mathrm{tr}}^{\mathrm{max}}$, are transmitted independently of the angle, i.e. $F_{\mathrm{tr}}(T_0 \geq T_{\mathrm{tr}}^{\mathrm{max}}) = 1$ with

$$T_{\mathrm{tr}}^{\mathrm{max}} = \frac{T_{\mathrm{tr}}^{\mathrm{min}}}{1 - \frac{B_A}{B_0}} \tag{3.17}$$

In the intermediate energy range, $T_{\mathrm{tr}}^{\mathrm{min}} < T_0 < T_{\mathrm{tr}}^{\mathrm{max}}$, the transmission of the protons is strongly dependent on their initial angle, θ_0. In this case, it is needed to compare the rate of transmitted protons, $\rho_{\mathrm{tr}}(T_0)$, with respect to the rate of protons emitted into 4π ($\rho_{\mathrm{total}}(T_0)$):

$$\rho_{\mathrm{tr}}(T_0) = \int_0^{2\pi} d\varphi \int_0^{\theta_0^{\mathrm{max}}} \sin\theta_0 d\theta_0 w(T_0) \tag{3.18}$$

$$\rho_{\mathrm{total}}(T_0) = \int_0^{2\pi} d\varphi \int_0^{\pi/2} \sin\theta_0 d\theta_0 w(T_0) \tag{3.19}$$

$\theta_0^{\max}$ is the maximum angle at which a proton with an initial kinetic energy T_0 is transmitted through the potential barrier. $w(T_0)$ is the proton recoil spectrum. Since $w(T_0)$ has no angular dependence it can be taken out of the integral and we obtain:

$$\rho_{\mathrm{tr}}(T_0) = 2\pi w(T_0)(1 - \cos\theta_0^{\max}) \tag{3.20}$$

$$\rho_{\mathrm{total}}(T_0) = 2\pi w(T_0) \tag{3.21}$$

Consequently, the transmission probability for protons with initial kinetic energies in the interval $T_{\mathrm{tr}}^{\min} < T_0 < T_{\mathrm{tr}}^{\max}$ is:

$$F_{\mathrm{tr}}(T_0)|_{T_{\mathrm{tr}}^{\min}<T_0<T_{\mathrm{tr}}^{\max}} = \frac{\rho_{\mathrm{tr}}(T_0)}{\rho_{\mathrm{total}}(T_0)} = (1 - \cos\theta_0^{\max}) \tag{3.22}$$

In equation 3.15, the adiabatic transmission energy has been defined as the minimum kinetic energy needed to pass the potential barrier for a certain initial angle θ_0. Then, for the initial angle $\theta_0^{\max}$, the minimum initial kinetic energy T_0 necessary for the transmission is given by

$$T_0 = \frac{\mathrm{e}(U_{\mathrm{A}} - U_0)}{1 - \frac{B_{\mathrm{A}}}{B_0}\sin^2\theta_0^{\max}} \tag{3.23}$$

Replacing $\sin^2\theta_0^{\max}$ by $1 - \cos^2\theta_0^{\max}$ and using equation 3.16 we get

$$\cos\theta_0^{\max} = \sqrt{1 - \frac{B_0}{B_{\mathrm{A}}}\left(1 - \frac{T_{\mathrm{tr}}^{\min}}{T_0}\right)} = \sqrt{1 - \frac{B_0}{B_{\mathrm{A}}}\left(1 - \frac{\mathrm{e}(U_{\mathrm{A}} - U_0)}{T_0}\right)} \tag{3.24}$$

Finally the complete transmission function $F_{tr}(T_0)$ is given by

$$F_{\mathrm{tr}}(T_0) = \begin{cases} 0, & \mathrm{if} T_0 \leq T_{\mathrm{tr}}^{\min} \\ 1 - \sqrt{1 - \frac{B_0}{B_{\mathrm{A}}}\left(1 - \frac{T_{\mathrm{tr}}^{\min}}{T_0}\right)}, & \mathrm{if} T_{\mathrm{tr}}^{\min} < T_0 < T_{\mathrm{tr}}^{\max} \\ 1, & \mathrm{if} T_0 \geq T_{tr}^{max} \end{cases} \tag{3.25}$$

Figure 3.8 shows the transmission function $F_{\mathrm{tr}}(T_0)$, equation 3.25, for an electric potential difference of $U_{\mathrm{A}} - U_0 = 375\,\mathrm{V}$. The theoretical proton spectrum $\omega(T_0)$ for two different values of a is also shown .

3.4 Systematic effects

In the following section several possible sources of systematic effects are presented. The description will mostly follow the presentation given in the publication of F. Glück *et al.* in 2005 [19]. Citations for current studies or new results will be given.

The goal of the experiment aSPECT is to measure the coefficient a with a relative accuracy of $\delta a/a \approx 3 \cdot 10^{-3}$. Therefore, the systematics presented in the following are

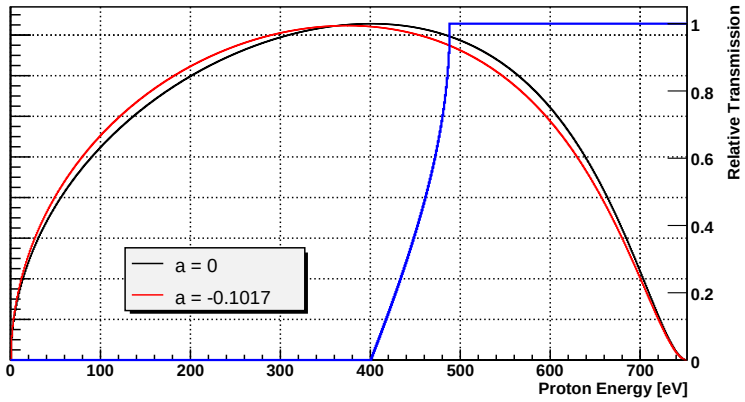

Figure 3.8: Proton spectrum for different values of the electron antineutrino correlation coefficient a and transmission function for a potential barrier of $U_{\mathrm{A}} - U_0 = 375\,V$, blue line.

studied in order to keep the uncertainties bellow $\delta a \approx 10^{-4}$.

The different sources of errors are related to:

1. Theoretical corrections (like Coulomb correction or radiative correction)
2. Transmission function (like electric and magnetic field characteristics, adiabaticity...)
3. Background
4. Detector efficiency
5. Edge effect

In this work, the most important sources of errors are treated. Background and detector studies can be found in [45] and [46]. A complete study of the aSPECT systematics by means of Monte Carlo simulations can be found in [38].

3.4.1 Adiabatic transmission function

The adiabatic transmissions function has been already presented in section 3.3. It is a function of the electric and magnetic fields at the DV and AP; U_0, B_0, U_A and B_A. Therefore, the accuracy on their determination affects the accuracy reachable by aSPECT.

Electric potential difference $(U_A - U_0)$**:**
An uncertainty in the potential difference $U_A - U_0$ of 10 mV would correspond to an uncertainty on a of 10^{-4}, see figure 3.9. In order to reach this goal, several demands on the electric potentials in the DV and AP are necessary.

1. The electrodes must provide a very *homogeneous field*. The electrodes have been specially produced with pure copper and coated with silver and a final layer of gold. The surfaces of all electrodes were polished and carefully cleaned. The DV electrodes and the AP electrode have been built with big diameters. In this configuration small work function differences may average out in the flux-tube region.

2. *Field penetration* by neighboring electrodes has to be minimized. This is done by the large length of the DV and AP electrodes and by setting the neighboring electrodes to the same potential. With this configuration, the electrostatic potential within the DV has been calculated to be smaller than 1 mV and the potential in the center of the AP is only by 2 mV smaller than at the surface of the electrode.

3. Factors which may *change the potential* like accumulation of negative charges over the surfaces of the electrodes have to be reduced. A good cleaning procedure of the electrodes and strict ultra high vacuum conditions permits to prevent from it.

Besides, the diameter of the electrodes has to be wide enough to ensure that they do not cut the magnetic *flux tube* of the decay protons.

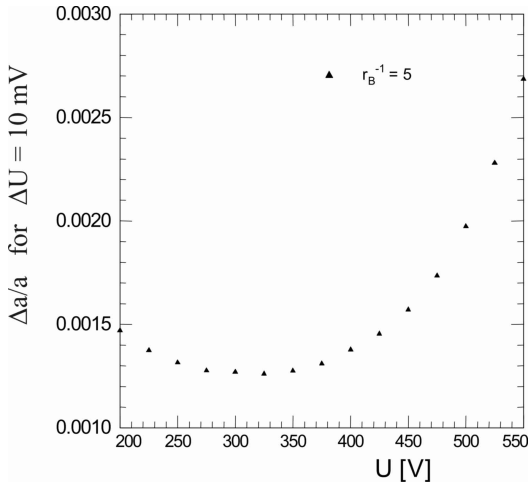

Figure 3.9: Relative accuracy of a for a relative uncertainty of 10^{-4} computed for different values of U.

These points and the complete electrode system setup will be discussed in detail in chapter 4. Measurements and undergoing studies of surfaces treatment will be as well presented.

Magnetic field ratio $r_B = B_A/B_0$:

In order to reach an absolute accuracy on the measurement of a of at least $3 \cdot 10^{-4}$, it is necessary to determine the magnetic field ratio $r_B = B_A/B_0$ with a relative accuracy of 10^{-4}[19]. This implies that we need to know the size of the magnetic field B_0 in the DV and B_A in the AP with a relative accuracy of 10^{-4}. In addition, the magnetic field gradient within the DV, $\Delta B_0/B_0$, and within the AP, $\Delta B_A/B_A$, should not be much larger than 10^{-4} in order to define a unique transmission function independently of the proton emission point. Otherwise, protons emitted at different positions in the DV have a slightly different transmission function. Then, it becomes necessary to know the neutron beam distribution inside the DV, $N_n(\vec{r})$, and the corresponding proton beam distribution at the AP, $N_p(\vec{r})$.

Another crucial point is the stability of the magnetic field. Since magnetic field measurements during the data taking are not feasible, it is necessary a good stability (small time dependence) of the magnetic field.

These points will be discussed in detail in chapter 5.

3.4.2 Deviation from adiabatic motion

In the adiabatic approximation the transmission function of the spectrometer can be calculated analytically, equation 3.25, and the orbital magnetic moment, $\mu = T_\perp/B$, is considered to be constant. Deviations from the adiabatic motion may cause the actual transmission function to be different from the calculated transmission function and therefore falsify the interpretation of the measured proton rates. The electric and magnetic fields of the *a*SPECT spectrometer have been designed to keep contributions of non-adiabatic proton motion negligible to first order, see figure 4.14. By using calculated electric and magnetic field maps within the flux-tube, an optimization procedure for suppression of non-adiabatic effects down to the required level was established [19].

In the adiabatic approximation the orbital magnetic moment, μ, is constant. However, in regions with high electric or magnetic field gradients, μ presents large oscillations. As described in [47], [48] and [49], when a proton moves from one homogeneous field region to another, its orbital magnetic moment can regain the starting value although between these two regions the field gradients are large. This permits to apply large field gradients between the DV and the AP without any significant effect on the transmission function, see figure 4.14. A magnetic field decay of about 1.5 T per 20 cm, is produced in this region. This correspond approximately to a relative field decay of $\sim 5 \cdot 10^{-2}\,\mathrm{cm}^{-1}$, much larger than the field decay within DV ($\sim 9 \cdot 10^{-5}\,\mathrm{cm}^{-1}$) and AP ($\sim 7 \cdot 10^{-6}\,\mathrm{cm}^{-1}$) regions. According to trajectory calculations, the deviations from adiabatic motion due to this gradient between the DV and the AP are reduced to a negligible level.

However, the influence of non-adiabatic effects is more severe for protons trapped between the AP and the mirror electrode than for transmitted protons. Protons with insufficient energy to pass the AP potential perform several oscillations between the two potential wells. The impact of non-adiabatic changes of the angle and of the orbital magnetic moment increases with the number of oscillations. The dipole field introduced by the lower ExB drift electrode removes trapped particles after a few oscillations. On the one hand, the efficiency of the ExB drift increases with the strength of the applied electric field gradient. On the second hand, the impact of the non-adiabatic effects gets amplified: protons are accelerated due to the electric field gradient and thus their gyration length becomes larger. As a consequence, the deviation from adiabatic approximation also increases. Trajectory calculations show that breakdown of the adiabatic approximation sets a limit of $-3\,\mathrm{kV}$ for the lower ExB [19].

The non-adiabatic effects on μ increase exponentially with decreasing magnetic field [49]. With a potential of $-3\,\mathrm{kV}$ on the lower ExB, the change of the extracted a value due to deviation from adiabatic motion has been calculated for several B_0, table 3.4. Above $B_0 = 1.5\,\mathrm{T}$, the systematic effect on a is negligible.

B_0	3 T	1.5 T	1.2 T	0.9 T	0.6 T
δa	10^{-6}	$4 \cdot 10^{-5}$	$5 \cdot 10^{-4}$	$4 \cdot 10^{-3}$	$2 \cdot 10^{-2}$

Table 3.4: Uncertainty δa due to deviations from adiabatic motion for different magnetic field values, B_0. The ratio $r_\mathrm{B} = B_A/B_0$ has been fixed to a value of 0.2. The dipole potential of the lower ExB is set to $U = -3\,\mathrm{kV}$.

For this reason, a rather homogeneous and strong magnetic field is provided in the

region of the lower ExB electrode, see figure 4.14. This permits to use a large potential difference without any significant influence on adiabaticity.

During the ILL beamtime, even lower voltages were applied at the ExB drift electrode: the configuration used during most of the time was -1000 V / -50 V, i.e., an electric field gradient of 950 eV and an averaged potential of -525 eV (on-axis). Different settings like -200 V / 0 V were also applied during some time for systematic tests, see section 7.2.3. Furthermore, supplementary systematic tests were performed with lower magnetic field values ($B_0 \approx 0.94\,\mathrm{T}$) in order to verify the impact on a (see section 7.2.6).

Nowadays, new studies of the adiabatic condition for the electromagnetic configurations used during the beamtime of 2008 at ILL are being carried out. Information about the status of these calculations can be found in reference [38].

3.4.3 Background

Background is mainly produced by the neutron beam and the environmental conditions (e.g., neighboring experiments, cosmic rays...). Some of the background components are considerably reduced thanks to the design of the spectrometer:

- *γ-radiation* is suppressed by the small opening angle to the detector.
- *Charged particles from outside the spectrometer* are "shielded" by the strong magnetic field of aSPECT.
- *Cosmic rays* make only a very small contribution to the spectra.
- *Ionization of residual gas* in the flux tube produces very low energetic ions of several eV. They are detected for AP voltage settings of $U_\mathrm{A} \approx 0\,\mathrm{V}$. But they are blocked applying a low AP potential if their origin is below the AP. Therefore, data was taken down to $U_\mathrm{A} = 50\,\mathrm{V}$ only.

Furthermore, thanks to the retardation principle of our spectrometer, the background can be easily measured and subtracted from the spectrum. The extraction of the correlation coefficient a from the measured proton spectra at different AP voltages and the subtraction of the background will be discussed in detail in chapter 7. Here we are going to summarize just the most important points.

1. The measurable obtained with aSPECT is the pulse height spectrum of events for a certain AP potential barrier.
2. Since the maximum kinetic energy of protons is about 751.4 eV, measurements at 800 V potential barrier are defined as background spectrum.
3. Subtracting the background spectrum (2) from the pulse height spectra measured for a certain AP voltage (1) gives us the pure proton events for different AP voltage settings.
4. Finally one can extract a from the pure proton event count-rate for different AP voltage settings as it will be described in section 7.2.2.

Problems arise if the background is not the same at different AP voltages as the background measured at 800 V. In this case, some background events will be identified as

proton events or viceversa. As a result, the proton recoil spectrum, and thus a, is modified.

During the first aSPECT beamtime at the research reactor FRM-II in Munich, a component of the background dependent on the AP potential was found. The possible sources of this background were identified as field emission at the high voltages electrodes of the detector, Penning discharges and particle traps [50].

From November 2007 to June 2008, aSPECT was set up at the cold neutron beam position PF1b at the Institute Laue-Langevin (ILL) in Grenoble, France. The main objective of this beamtime was a measurement of the correlation coefficient a with a relative error better than $\frac{\delta a}{a} \cong 5\,\%$ (see chapter 7). Several measures were taken in order to suppress these sources before the ILL beamtime, see chapter 4. If the AP voltage-dependence background is suppressed to a negligible level, the subtraction of background measured at 780 V is sufficient for the determination of a

Another problematic component of the background was identified during the ILL beamtime: *correlated background*. When a neutron decays in the DV, a proton and an electron are produced simultaneously. A fraction of the electrons may reach the detector in near coincidence with a proton from the same decay. Due to the high energy deposited by the electrons, proton events detected shortly after an electron may be masked. This effect may introduce an AP-voltage dependent background.

The most important background components identified during the ILL beamtime are be discussed in chapter 7. A detailed study of the complete aSPECT background can be found in [45].

3.4.4 Edge effect

The magnetic flux tube projects the proton detector surface into the neutron beam (see figure 3.5). Protons emitted inside the projected area should be able to reach the detector. However, protons also gyrate around the magnetic field lines with a gyration radius which depends on their transversal kinetic energy, $r_g \propto \sqrt{T_\perp}$. This may cause that protons emitted inside the projected area and which follows the magnetic field lines to the detector, still do not hit the detector due to the finite gyration radius. Contrary, protons emitted outside the projected area, may be detected, see figure 3.10. This effect would be balanced in the case of a perfectly homogeneous neutron beam profile. The problem arises when the neutron density distribution is not flat. In this case the probabilities for both situations are not equal. The probability of loosing or gaining a proton are no longer the same and depend on the kinetic energy and the emission angle.

Along the direction of the neutron beam, the neutron density is practically constant and the edge effect is negligible. However, along the direction perpendicular to the neutron beam, this effect has to be considered. It exists two possible ways to minimize this effect. One possibility is to collimate the neutron beam to fit completely inside the region where every proton is detected. In order to avoid the enormous lost of statistics that this would mean, we decided to increase the area of the neutron beam profile as much as possible in order to obtain a flat profile.

During the ILL beam time in 2007-2008 several measurements of the neutron beam profile were taken before and after the spectrometer, see chapter 7. These measurements permit to reconstruct the neutron beam density all along the DV. The reconstructed

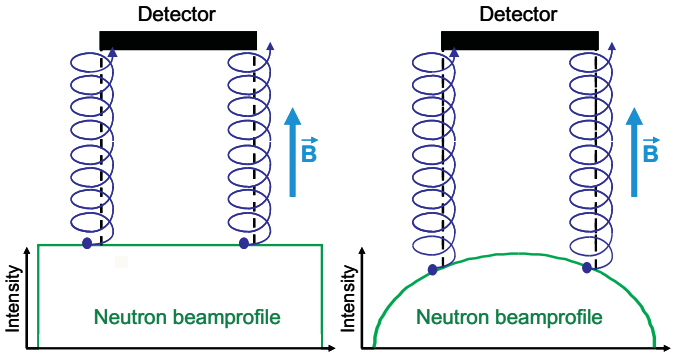

Figure 3.10: Illustration of the edge effect. Left: In the ideal case of a perfectly flat beam profile the edge effect is negligible. Right: For a inhomogeneous beam profile the value for a has to be corrected for the edge effect.

neutron beam density is used for the weighting of the transmission function (chapter 5) and to apply corrections due to the edge effect. The upper ExB was also used to center the proton beam on the detector in order to use the flattest region.

The inconvenient of using the ExB-drift is that it affects protons with different velocities in a different amount. This leads to a deformation of the *effective flux tube* (see chapter 4). Therefore, a simple projection of the detector through the magnetic field lines is not sufficient. Trajectory calculations using Montecarlo Simulations are needed. This point is treated in detail in reference [38].

3.4.5 Detector efficiency

The efficiency of the detector is another important systematic effect that has to be considered. Although the accuracy of the aSPECT spectrometer is determined by the MAC-E filter, it is necessary to determine the efficiency of the detector. Actually, not every proton is detected due to the dead layer and the response function of the detector. The detection efficiency has an angular and energy dependence of the incidence protons and also includes losses due to backscattering, dead time and DAQ system. These points are discussed in the PhD thesis of M. Simson [46] and only a short summary will be given here.

Detector efficiency

The finite efficiency of the proton detector just reduces the count rates and therefore drops out of the ratios of measured count rates. However, if a dependence on the energy or proton impact angle influences the ratio of count rates, has to be considered.

Protons which have passed the AP potential barrier with a finite kinetic energy ΔE, are then accelerated towards the detector by an electrostatic potential of $-15\,\mathrm{kV}$. Thus, the impact energy of the protons, E_p, may vary between $15\,\mathrm{keV} \leq E_p \leq 15.75\,\mathrm{keV}$. Since we have $\Delta E/E_p \ll 1$, we expect a small energy dependence of the detector efficiency given by:

$$\varepsilon_D \propto (1 + c_1 E_p)$$

where c_1 has to be a small number. With the required level of tolerance of $\delta a < 10^{-4}$, calculations show that the condition $|c_1| < 200\,\mathrm{ppm/keV}$ has to be fulfilled.

Similarly, we can investigate the dependence of the detection efficiency on the impact angle which goes:

$$\varepsilon_D \propto (1 - c_2/\cos\gamma)$$

where γ is the angle of the proton relative to the detector axis and c_2 is a constant which should be small too. Energy and impact angle, can be calculated by means of simulations of the detector properties. The results can then be used to correct the count rates. Details of the simulations of the *a*SPECT proton detector can be found in [46].

Dependence of the detector efficiency on backscattering

A fraction of the protons hitting the detector are scattered several times inside the detector and finally leave the detector again in backward direction. The negative voltage applied at the detector together with the magnetic flux tube avoids that the backscattered proton escapes. It will hit the detector again with the same energy and angle as initially. Due to the short time difference between the two hits of about $0.5\,\mu$s, it is not possible that a backscattered proton is counted as two separate events.

For each backscattered proton, it has to be considered if the energy deposited in the active layer of the detector is sufficient to be detected.

From the simulations [46], a relative amount of backscattered protons of 1.8 % at 10 kV and 1.0 % at 15 kV acceleration voltage is expected.

Chapter 4

Electric field design

The electric and magnetic fields are essential components of the MAC-E filter architecture of the *a*SPECT spectrometer and the detection system. Their design characteristics allow us to determine the correlation coefficient a with a final accuracy of $\delta a/a \approx 3 \cdot 10^{-3}$. For this purpose, several calculations have been performed [19] in order to reduce the systematics down to a negligible level (section 3.4). As a result of these calculations, the electrode system has been built as a complex assembly of cylindrical electrodes which fulfills three fundamental requirements:

- Adiabaticity of the electric field.
- High field homogeneity within DV and AP regions.
- Electrodes do not interfere the effective flux tube of the decay protons.

Besides, the experience acquired during the first *a*SPECT beamtime at the research reactor FRM-II in Munich [50], led to the implementation of several modifications on the electrode system construction, the manufactory process and the cleaning procedure.

This chapter focuses on the improvements performed on the electrode system. A detailed description of the different parts of the electrode system, their various usages and the voltage settings applied during the ILL beamtime will be discussed too.

4.1 Improvements of the electrode system

The main motivations for the improvement of the electrode system after the FRM-II beamtime were the following:

- A component of the background dependent on the AP potential was found during the first *a*SPECT beamtime (section 3.4.3). The suppression or minimization of this background component down to a negligible level was a fundamental goal for the ILL beamtime.
- The diaphragm used during the FRM-II beamtime to collimate the proton flux tube[50] was eliminated for future beamtimes. The usage of this diaphragm was perjudicial for the calculation of the edge effect and represented an extra source of background.

These two points are described in detail next.

4.1.1 Particle traps in the spectrometer

In section 3.4.3 it has been pointed out the existence of an APV-dependent (AP voltage) background component. This background component prevented us from presenting a value of the angular correlation coefficient a after the FRM-II beamtime [50]. The minimization of this background component down to a negligible level is fundamental for the determination of a with an accuracy of 10^{-4}.

The explanation for this background component could be related to particles traps in the spectrometer. The combination of magnetic and electric fields inside aSPECT form Penning traps [51] [52] (see figure 4.11). For example, protons which are not able to cross the AP potential barrier remain trapped between the AP and the Mirror potential, trap P-III. Moreover, the different potentials applied at the AP change the depth of this trap. The impact of non-adiabatic changes of the angle and of the orbital magnetic moment of trapped protons increases with the number of oscillations as well as the probability of collision with residual gas, see section 3.4. This would introduce an APV-dependent systematic error. To avoid that, the lower ExB drift electrode was installed with the aim to remove the decay protons and any other beam-related ionized background that is trapped between the AP and the Mirror electrodes after a few oscillations.

Measurements during the beamtime at the FRM-II reactor permitted to identify several particle traps and different filling mechanisms as possible sources of the unstable background [50]. The known traps configurations in aSPECT are numerated from I to IV in figure 4.11. Several mechanisms can be thought as possible sources of low energetic particles that can be confined in the traps of our spectrometer, for example:

- Field emission from the upper ExB and detector electrodes:

  Both electrodes are at high voltage. Irregularities on surfaces of these electrodes (tips, micro-points...) may create much larger local electric fields. Then, quantum tunneling can produce field emission [53].

- Penning discharges between those two electrodes [54]:

  In bad vacuum conditions (in the order of mbars), electrons created at the electrodes surface by some external source are accelerated by the electric field. They soon gain enough energy to ionize the rest gas atoms creating positive ions and secondary electrons. Those ions and electrons are then accelerated again creating a self sustained discharge (*Townsend discharge*). In good vacuum conditions like in our experiment ($\sim 10^{-9}$ mbar), the probability of electron collisions with rest gas is not enough to produce a self sustained discharge. However, if magnetic field lines are going from the upper ExB to the detector electrodes or viceversa, a penning trap may be formed. Then, the small ionization probability for a certain rest gas density is compensated by the large path lengths of the trapped electrons. Consequently, a self sustained discharge may be produced (Penning discharge). Then, some of the trapped particles can move perpendicularly to the magnetic field lines due to collision processes with the rest gas atoms and escape the trap.

These two processes can act as primary source of electrons which will travel through the spectrometer being accelerated by the high voltage applied at these electrodes. In turn, part of these electrons can create low energy secondary electrons from collisions to walls or rest gas atoms. The low energy electrons can then be trapped.

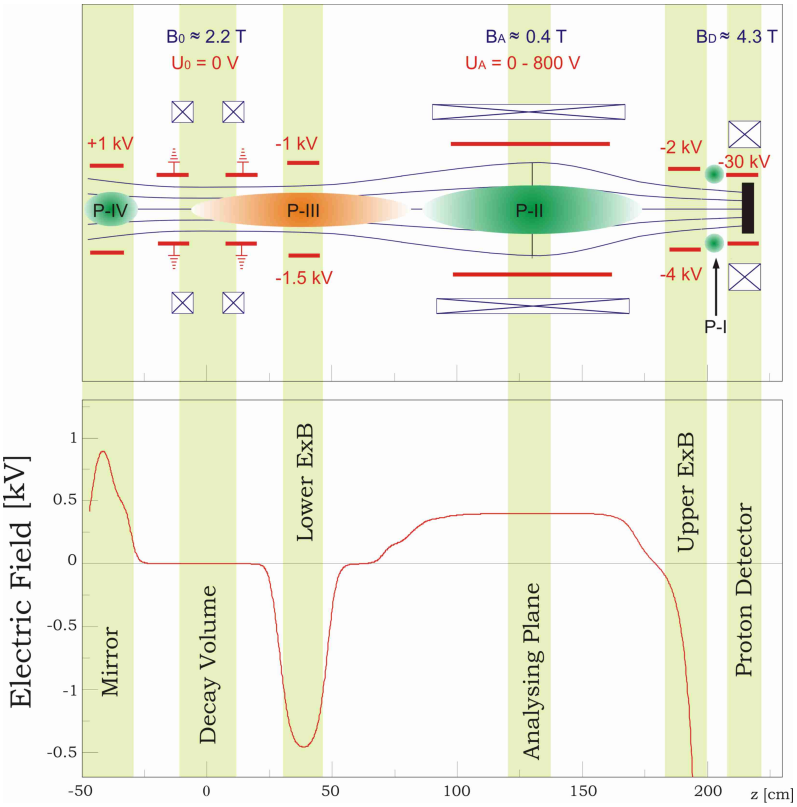

Figure 4.11: Scheme of the *a*SPECT spectrometer with its electric field design. Electrodes are shown in red whereas coils and magnetic field lines are shown in blue. The approximate region of the traps are highlighted with green and orange colors. Green/orange colors indicate traps for negative/positive particles respectively. The voltages shown correspond to the settings at the FRM-II beamtime.

As the path of the particles inside the spectrometer increases when they are trapped, so does the probability of particle collisions. In the collision process they can create ions (H^+ for example) which, if they are detected, would produce events undistinguishable from proton events. These events may be the source of the APV-dependent background contribution. As consequence, several modifications of the electrode system were carried out after the FRM-II beamtime for the reduction of particle traps as discussed in section 4.2.

4.1.2 Effective flux tube

In section 3.1 the flux tube was defined as the magnetic field lines connecting the decay volume and the detector. However, protons emitted outside the flux tube may reach the proton detector due to their gyration around the magnetic field lines (see edge effect in section 3.4.4). The outermost proton able to hit the proton detector is the one emitted at two times its gyration radius away from the flux tube (see figure 4.12). Therefore, it is useful to define an effective proton flux tube which includes the gyration of the protons around the magnetic field lines. The radius of the effective flux tube at any z position,

$r(z)$, is given by:

$$r_{\text{flux-tube}}(z) = \sqrt{\frac{B_{\text{det}}}{B(z)}} r_{\text{det}} + 2r_g(z) \tag{4.1}$$

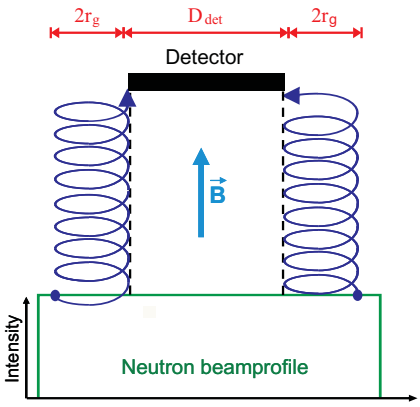

Figure 4.12: Effective flux tube

where r_{det} is the radius of the detector, $B_{\text{det}}/B(z)$ is the ratio of the magnetic field at the detector position with respect to the magnetic field at a given z position, and r_g is the gyrating radius of the protons around the magnetic field lines. The first term of equation 4.1 corresponds to the radius of the detector projected by the magnetic field, where the factor $\sqrt{B_{\text{det}}/B(z)}$ arises from the conservation of the magnetic field flux, $\phi = \vec{B} \cdot \vec{A}$. The gyration radius r_g is given by:

$$r_g(z) = \frac{m v_\perp(z)}{qB(z)} = \frac{\sqrt{2T_\perp(z)m}}{qB(z)} \tag{4.2}$$

where m and q are the mass and charge of the proton. The gyration radius can be written as function of the initial kinetic energy, i.e., at the DV. Due to the conservation of the orbital magnetic moment $\mu = T_\perp/B$, the kinetic energy at any z position is:

$$T_\perp(z) = \frac{B(z)}{B_0} T_{\perp 0} \tag{4.3}$$

and therefore the gyrating radius is:

$$r_g(z) = \frac{\sqrt{2T_{\perp 0}m}}{qB_0} \sqrt{\frac{B_0}{B(z)}} \tag{4.4}$$

From equations 4.1 and 4.4 we see that the effective flux tube is energy and angle dependent on the proton kinetic energy (note that $T_\perp = T \sin^2\theta$).

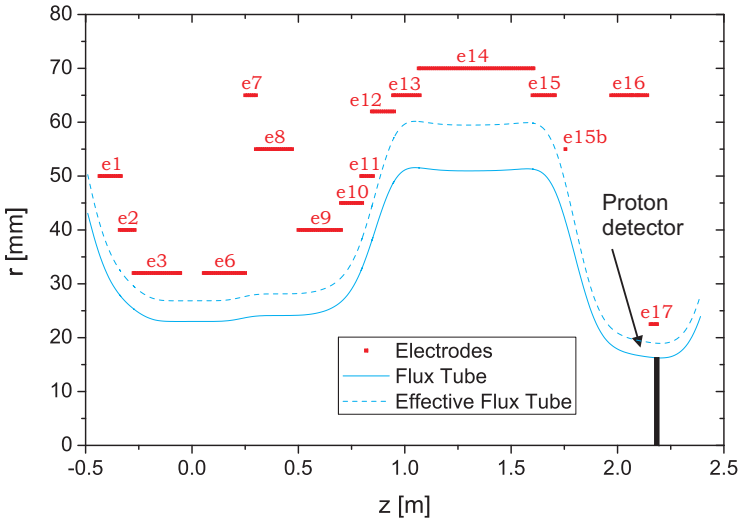

Figure 4.13: The effective proton flux tube (blue dashed line) of the spectrometer comprises the flux tube (blue line) plus two times the gyration radius of the protons (see figure 4.12). The surrounding electrodes, shown in red, should be such not to cut the effective flux tube.

During the beamtime at FRM-II, the size of the effective flux tube was defined by a thin diaphragm installed just above the DV electrode. Its function was to collimate the proton beam in order to reduce the edge effect; a diaphragm with a few microns thickness, compared to a gyration length of several millimeters, induces an edge effect (section 3.4.4) far bellow the required limit if the neutron beam density is homogeneous. This density should be determined to a few percent accuracy, in order that the edge effect contribution for the parameter a should not be larger than 10^{-4}[19]. However, this is only true if the detection efficiency of the detector does not depend on the detection position. Unfortunately this was not the case with the segmented PIN diode used during the FRM-II beamtime [50]. This circumstances together with the background introduced by the collimator motivated us to remove the diaphragm in future beamtimes. Now, the flux tube is determined by the size of the detector. As a result, the proton beam got widened and consequently some electrodes had to be modified in order not to cut the effective flux tube.

Figure 4.13 shows the flux tube, the effective flux tube and the position and radius of the electrodes. The effective flux tube has been calculated for the magnetic field at 70 % of its maximum strength, protons with starting kinetic energy $T_{\perp 0} = 751.4\,\text{eV}$ and for a maximum detector size of 32.6 mm[1]. The electrodes setup shown is the version already modified in order not to cut the effective flux tube. The modifications in the electrodes will be described in next section, section 4.2.

Some other factors may influence the size and shape of the flux tube. Protons at several radial positions experience different electric potentials at the ExB regions where the field varies transversally. These fields could alter the longitudinal or transversal components

[1]The proton detector used during the ILL beamtime is composed of three squared pads of 10.3 mm side placed in a row, thus, the half-diagonal (the outermost magnetic field line connecting the proton detector with the DV) has a length of 16.3 mm.

of the kinetic energy and thus the gyrating radius. Furthermore, the time the particles expend inside the ExB regions depends on their longitudinal kinetic energy and on the retardation potential. These factors create a deformation of the particles effective flux tube which can only be estimated by trajectory calculations. For edge effect calculations or backscattering this effect has to be considered [38].

4.2 Electrode system construction for the ILL beamtime

The basic conditions which have to be fulfilled by the electrode system in order to reach a final accuracy of a in the order of 10^{-4} have been already discussed in section 3.4.1. A summary of these conditions is given next:

- The adiabaticity of the electric field has to be accomplished all along the proton trajectory. For this reason the electric field has been calculated for several electrodes configurations in order to find the optimum one[19].
- The electrodes must provide a very *homogeneous field* at the DV and AP regions (The potential difference $(U_A - U_0)$ has to be known with an uncertainty $\leq 10\,\mathrm{mV}$):

  - The *DV* and *AP electrodes dimensions* should be wide enough such, within the effective flux tube, the local surface potential differences average out.

  - *Field penetration* by neighboring electrodes into DV and AP has to be minimized (According to the calculations, the influence of field penetration from neighboring electrodes is $< 1\,\mathrm{mV}$ and $< 2\,\mathrm{mV}$ within DV and AP, respectively).

  - Factors which may *change the potential* like accumulation of negative charges over the surfaces of the electrodes have to be reduced. Surface studies will be presented in section 4.3.

Further, the modifications described in section 4.1 have to be accomplished:

- Some electrodes had to be rebuilt in order to reduce the influence of *particle traps*.
- The diameter of the electrodes has to be wide enough to ensure that they do not cut the *effective flux tube* of the decay protons.

In this section, the complete electrode system used during the ILL beamtime of 2008 is described. The different parts of the electrode system, their various usage and the applied settings in the ILL beamtime will be discussed too.

The original *a*SPECT electric field design was presented by Glück *et al.* in the publication of 2005 [19]. The PhD Thesis of Muñoz [50] describes the construction of this electrode system. Experiences with that system and problems raised during the FRM-II beamtime are described in detail there.

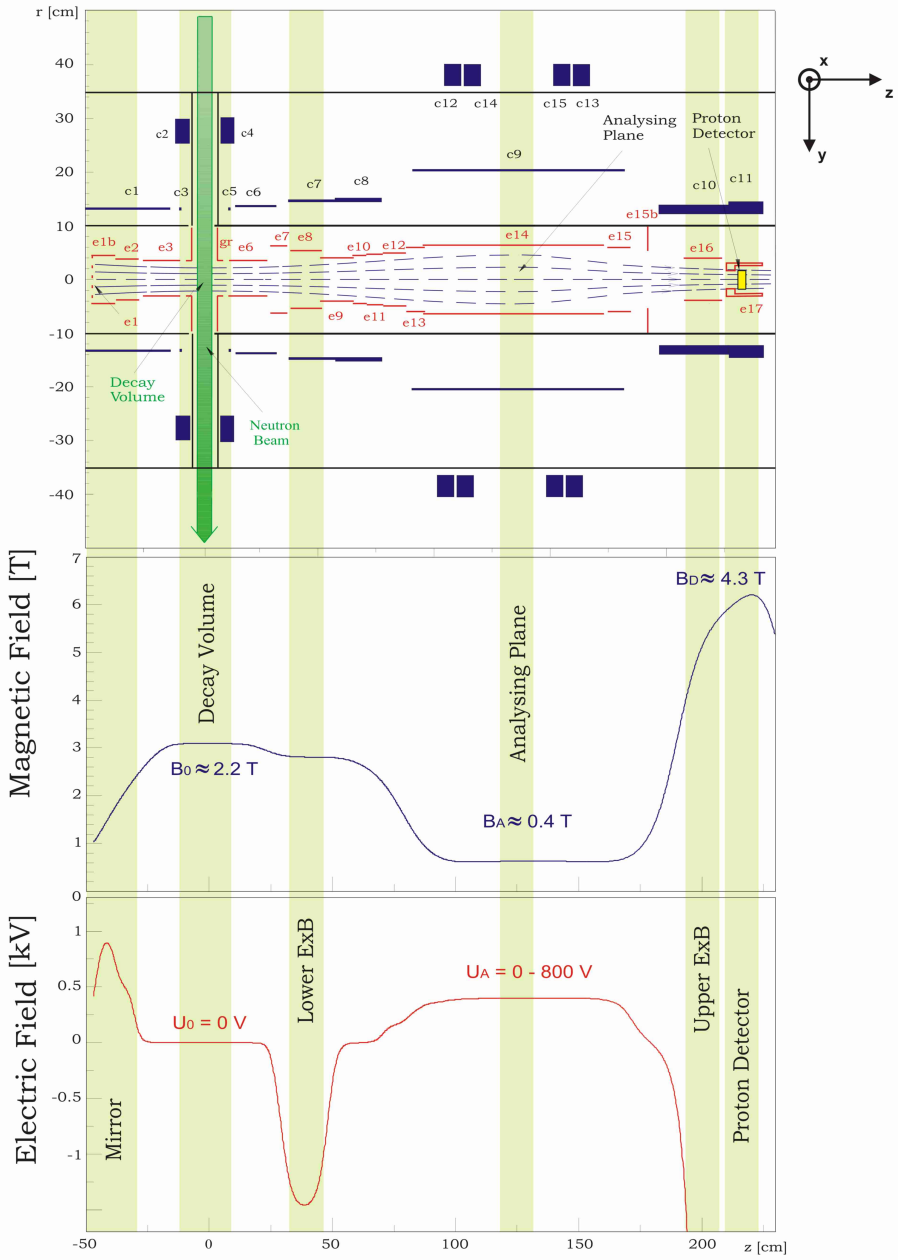

Figure 4.14: Sketch of the *a*SPECT spectrometer with its magnetic and electrostatic field profile along the z-axis of the spectrometer. Coils and magnetic field lines are shown in blue. The electrodes and the electrostatic potential are shown in red. The most remarkable regions are highlighted with a green background bar.

Figure 4.14 shows a sketch of the spectrometer together with the magnetic and electric field profiles. Electrodes and electric fields are shown in red. The system of coils and the magnetic field lines are presented in blue. The neutron beam is represented by a green arrow going through the spectrometer. The most important regions that will be explained in the following are highlighted with green bars. The radius of the spectrometer is approximately 70 cm, so the coils c12 to c15 are external coils installed at the height of

the AP in order to modify the shape of the magnetic field at that position.

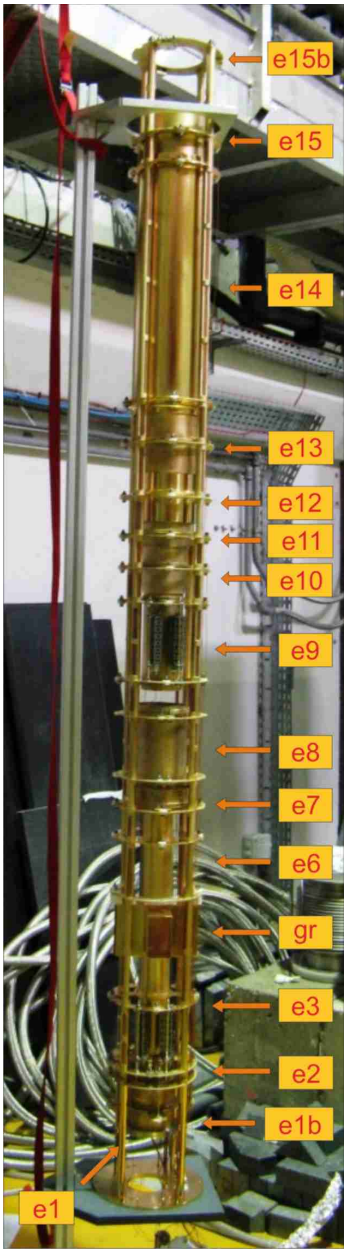

Figure 4.15: Electrode system before insertion into the cold bore tube of the *a*SPECT magnet.

The sketch of the spectrometer already contains the final configuration used for the ILL beam time. In some publications of the *a*SPECT collaboration, [7] [19] [45] [46], the same scheme has been shown partly uncomplete for simplicity. In this work the complete configuration is shown following the notation established in [55].

Figure 4.15 shows a picture of the *a*SPECT electrode system as it was constructed for the ILL beamtime. The electrode system is 2.4 m long and has a maximum diameter of 14 cm (AP electrode). Electrodes and holders are completely made out of OFHC[2] copper, coated with silver ($\sim 10\,\mu$m) and a final layer of gold ($\sim 1\,\mu$m). This treatment provides a good surface quality and preserves ultra-high vacuum conditions (UHV).

The electrodes are wired with Kapton wire, KAP1, which is insulated by a layer of UHV compatible material. The thickness of the KAP1 wire is only 0.25 mm (diameter). The small diameter helps to limit the thermal heat load transferred from room temperature to the cryostat. The wires are connected to a custom insulating feedthrough made of Macor[3]. There, the wires are glued to male pins (made of gold-coated copper alloy) inserted in the Macor feedthrough (figure 4.17). The glue used for this purpose was EPO-TEK H27D, a two component silver-filled epoxy adhesive designed for electrical applications with very low outgassing rate. The epoxy has demonstrated to work at the low temperatures of the main vacuum chamber of *a*SPECT (about 70 K, see appendix A.2). ExB electrodes are connected with thicker Kapton wires, Kap2 $\phi = 1$ mm, in order to stand the high voltage applied there.

The wiring system of the electrodes has been duplicated. This permits to have a test of the connection of the cables once the electrode system has been installed inside the cryostat and offers a second connection in case one connection brakes. The voltage difference between DV and AP was

[2]Oxygen-Free High Conductivity copper (OFHC) is produced under carefully controlled conditions to prevent contamination of the pure oxygen-free metal during processing. The method of producing OFHC copper ensures extra high grade of metal with a copper content of 99.99%.

[3]Macor and its homolog Vitronit have been used indistinctly in the system.

permanently monitored by a calibrated Agilent 3458A multimeter which has a temporal stability of $< 5\,\text{mV}$ at an applied voltage of 1000 V.

The wire connection to the electrode system is made by means of titanium screws which are UHV compatible and non-magnetic (every material used in the electrode system is non-magnetic). The titanium screws also attach the electrodes to the holding rings. The electrodes are insulated from the holding rings via custom made Macor pieces. The rings are attached to four long rods that hold together the complete electrode system. Due to the length of these rods, they are not gold coated. The distance between the rings gets fixed by coated copper tubes which act as distance holders.

The electrode system at the top ends with a thin plate which provides stability to the system and shields it from the high electric potential applied at the detector electrodes. At the bottom, see figure 4.17, a thick plate ("bottom plate") holds the complete electrode system. The electrode system is inserted into the spectrometer through its lower opening and then attached to the cryostat via this bottom plate (see appendix A.2). Thus, the complete electrode system, with the exception of the electrodes itself, is electrically connected to the cryostat and share the same ground.

The construction of the electrode system demonstrated to be stable and reliable during the ILL beamtime. Furthermore, no problems in the electrical connections were detected. The different parts of the electrode system are described next in detail.

Decay Volume electrode (e3, gr and e6):

The Decay Volume is defined as the region in which emitted protons can hit the detector if they are able to cross the AP potential barrier. The DV electrode surrounds this volume and defines the ground potential for the DV with respect to the potential applied at the AP electrode. The rectangular shape of the central part ($110 \times 70\,\text{mm}$), gr, is designed in order to permit the flight of the neutrons through the spectrometer (see figure 4.15 and 4.16). A third side opening permits a fast pumping in the main volume of the spectrometer [4]. At the other side of this opening, a NMR-Magnetometer sensor can be installed for monitoring the magnetic field, see chapter 6. Upper and lower openings, cylindrical electrodes e3 and e6 (220 mm length and inner diameter of 64 mm), permit the protons to travel along the z-axis. The three parts of the DV electrode are separated by a gap of 5 mm.

In order to define a unique transmission function for all protons independently of their emission position, the homogeneity of the electric field inside DV and AP is a prerequisite [19]. For that purpose, electrodes have been designed in order to create a very flat electric field profile at both places, see figure 4.14. Furthermore, the aimed accuracy of $3 \cdot 10^{-4}$ for a requires to know the potential difference $(U_A - U_0)$ with an uncertainty of 10 mV (section 3.4.1). To achieve these goals, three factors have to be considered: the quality of the surfaces (*homogeneous work function*), the *dimensions of the electrodes* and the *field penetration by neighboring electrodes.*

[4] The vacuum chamber containing the electrode system is called Main Vacuum. The vacuum chamber containing the superconductive coils is normally referred to as Insulating Vacuum

Small inhomogeneities of the *work function* of the electrodes can create deviations from a constant electric potential. The work function is strongly dependent on the crystal structure of the surface and surface contaminations. The manufacturing process (bending, welding and polishing) creates mechanical stress which degrade the crystal structure. Also impurities inside the material affect the work function and are very difficult to avoid. These inhomogeneities at the DV may create local Penning traps. Protons emitted at a local minimum of the electric field may be trapped if they do not have sufficient longitudinal kinetic energy to overcome the field inhomogeneities. This would create an energy dependent trap since the longitudinal kinetic energy depends on the energy and angle of emission. These traps would seriously limit the accuracy reachable by the spectrometer. The gold layer of the electrodes provides a more constant work function. Studies of the work function of the electrodes surfaces by means of a Kelvin Probe will be discussed at the end of section 4.3.

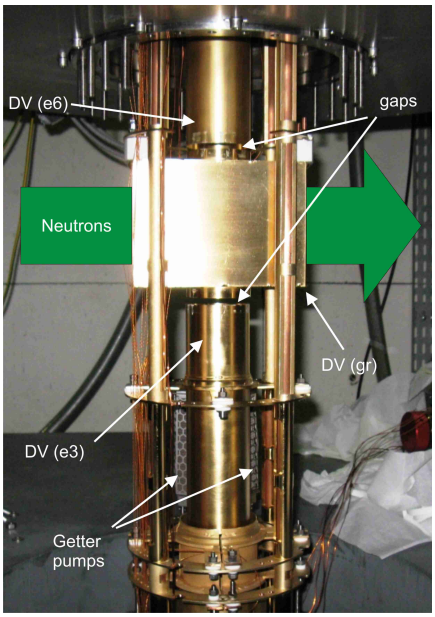

Figure 4.16: Decay Volume electrodes.

The *dimensions of the electrodes* have been thought in a way not to reach inside the effective flux tube. But, furthermore, the effective flux tube should not be "close" to the DV and AP surfaces in order not to experience the local surface potential differences. By "greater" distances they will be smoothed out. On contrary, large electrode sizes causes *field penetration* from other electrodes. At the end, our task was to find an appropriate size which takes into account both boundary conditions. Electrodes e3 and e6 help to shield the central part of the DV electrode and additionally, electrode e7 is set at ground potential to shield from the large field applied at the lower ExB drift electrode, e8.

The lower cylinder e3 had to be shortened in comparison to its original design for the FRM-II beamtime [50]. At that, time the DV was composed of one unique piece. Calculations showed an influence of the potential of neighboring electrodes into the decay volume of less than 1 meV, [19]. At present, the new design shows a similar shielding factor from the penetration of electric potentials from neighboring electrodes. However, new studies [38] have shown that some insulating materials close to the DV (mostly the neutron collimation system, see chapter 7) charged by ionizing radiation can influence the potential

inside the DV. As it will be seen in chapter 7, the analysis of the data acquired during the ILL beamtime showed a large influence of the charging of the collimation system on a.

The construction of the Decay Volume electrode in three independent parts permits to apply different voltages at each part. This leads to a position dependence of the initial potential $U_0(z)$ that may be used for systematic checks of the transmission function or to remove/create Penning Traps in order to study its influence on the measured spectrum. During the ILL beamtime, all the measurements for the extraction of the coefficient a were done without field gradients at the DV.

Mirror electrodes (e1, e1b and e2):

The Mirror electrodes (figure 4.17) are designed to reflect protons emitted into the lower hemisphere with respect to the detector. Decay protons have a maximum kinetic energy of 751.4 eV. Thus, a mirror potential of 1 kV ensures the reflection of every proton independently of its initial kinetic energy and angle. The reflection has to fulfill the adiabatic condition. In this case, they are reflected by 180° maintaining their original kinetic energy at the emission point and are kept on their trajectories relative to the magnetic field lines.

Without Mirror electrode the amount of neutrons emitted towards the detector would have to be known very accurately, see section 3.4 and chapter 5. Then, the accuracy would be limited by the knowledge of the magnetic field gradient and the neutron beam density distribution.

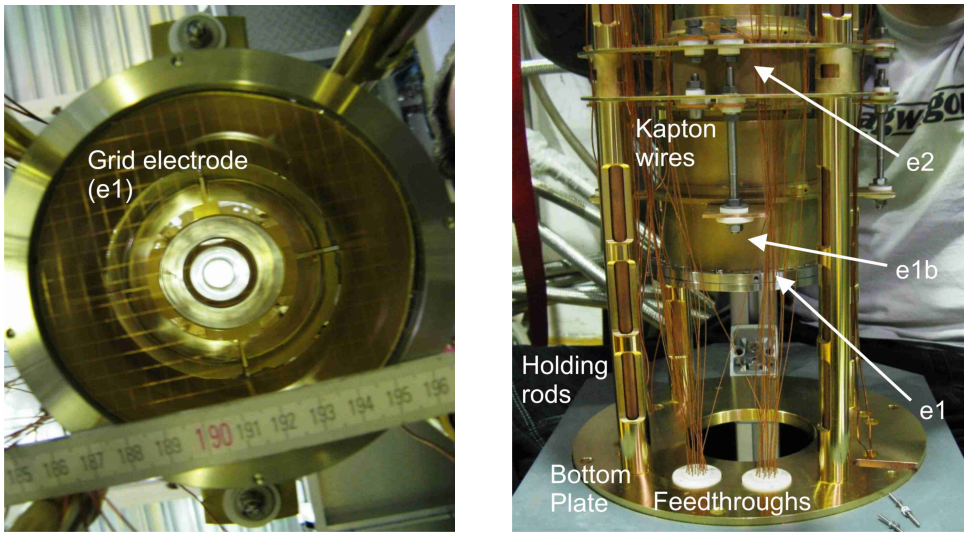

(a) Grid electrode. (b) Mirror electrodes.

Figure 4.17: Mirror electrodes. Composed of two cylindrical electrodes plus a grid electrode closing the bottom of the electrode system.

The mirror potential was originally produced by two electrodes. This permits to increase the electric field gradually in order to fulfil the adiabatic condition. The original dimensions of the electrodes were not wide enough not to cut the effective flux tube. Thus,

both electrodes were replaced by electrodes with bigger diameter. Due to the lack of time and the high cost of new electrodes, electrode e1 was used as e2 and a spare electrode with a diameter of 100 mm was used instead of e1. This combination translated into a shift of the position of these electrodes along the z-axis. In order to keep a small overlap between electrodes e2 and e3, electrode e3 had to be shortened on 2.5 cm to a final length of 20.5 cm. Electrode e2 is a quadrupole planned for the use of a calibration source which can be installed at the bottom entrance of *a*SPECT [45]. e2 could be used to shift the ion beam in the transversal plane $(x - y)$ by the application of asymmetric potentials. Additionally, a grid was added at the bottom of the lowest electrode (e1b) (see figures 4.14 and 4.17).

The grid helps to shape the reflective mirror potential and removes negative particles which may be trapped in between the DV and the Bottom Plate, trap P-IV. Both, BP and DV electrode are grounded, so the positive potentials at the Mirror electrodes create a trap for negative particles. A full plate would remove much faster the particles oscillating between the bottom plate and the DV, but high energetic decay electrons would be backscattered and some of them may be redirected to the detector. This fact would introduce a systematic error on the correlated events, see section 3.4 and chapter 7. In order to find a compromise between fast removing of trapped particles and low probability of electron backscattering the grid was constructed with non-insulated wires of 0.125 mm of diameter spaced at a distance of 5 mm.

Unfortunately, the measurements carried out during the ILL beamtime in 2008 have shown systematic effects which are related to non-adiabatic proton reflection at the mirror potential and to possible Penning discharges in the bottom of the spectrometer which may be produced due to the new electric mirror potential (see section 7.2.4).

Lower ExB electrode (e8):

Protons which are not able to overcome the potential barrier remain trapped and oscillate between AP and Mirror electrodes; see trap P-III in figure 4.11. These protons can collide with rest gas inside the spectrometer, creating a background dependent on the AP potential; the depth of the Penning trap increases with increased AP potential. In order to prevent from that, a dipole electrode is introduced, see figure 4.18 and 4.19. The direction of the drift is independent of the direction of movement of the particle and only depends on the direction of the electric and magnetic field and their strength. After a few oscillations the protons are shifted till they collide with an electrode and get neutralized creating H-atoms. The lower ExB electrode has been mounted in such a way that it produces an ExB drift along the direction of the incident neutron beam (figure 4.19) which is also the orientation of the three pads of the *a*SPECT detector. Calculations of proton trajectories through the ExB region give upper limits on the acceptable strength of the dipole field not to break the adiabatic condition, see section 3.4. With a magnetic field of about 2.2 T, a potential difference of −3 kV would introduce an uncertainty on a of $< 4 \cdot 10^{-5}$. Measurements during the ILL beamtime with several potential differences showed that a potential difference of only 200 V is already sufficient to remove trapped particles, see chapter 7, so we can neglect any influence on a.

The ExB electrode is surrounded by two electrodes, e7 and e9, at the same ground potential as the DV electrode. These electrodes shield the DV and AP electrodes from

the high transversal electric field created by the dipole electrode.

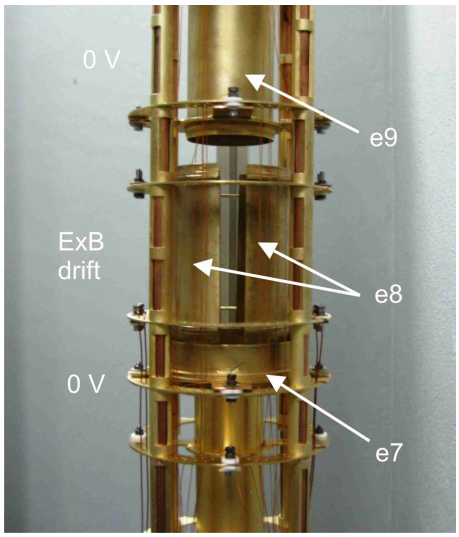

Figure 4.18: Dipole electrode e8, lower ExB. Its function is to remove trapped particles by means of an ExB drift.

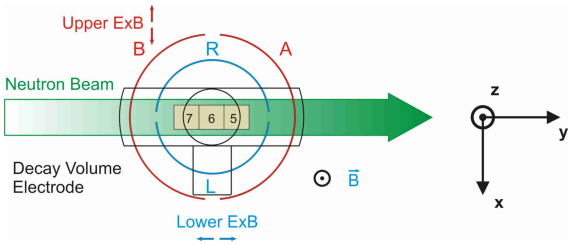

Figure 4.19: Sketch of the ExB-drift electrodes and their orientation with respect to the neutron beam trajectory. Lower ExB is shown in blue. The upper one in red. The proton detector, composed of three pads (7, 6, 5), is aligned along the direction of the neutron beam (green). The DV electrode is shown on the picture as well (black).

Analyzing plane electrode (e14):

The AP electrode provides the potential barrier U_A that filters the protons by their energy. Since the maximum proton kinetic energy is 751.4 eV, the AP electrode is held on voltages between 0 and +800 V. It is designed as the longest and widest electrode (length of 620 mm and diameter of 140 mm). The big diameter is necessary to cover the expanded effective flux tube at that low magnetic field region, B_A. The length of 620 mm ensures a very homogeneous electric field. The region of about ±4 cm around the center of the electrode presents the highest homogeneity. There, the plane perpendicular to the z-axis containing the maximum electric field defines the Analyzing Plane. Electrodes e9 to e13 are connected in series by a set of resistances that define the potential of the electrodes. The electric potentials have been selected to vary slowly from ground potential, electrode e9, to the AP potential, electrode e14. This way, a slow (adiabatic) increase of the electric field is ensured for every selected value of potential barrier. After the analyzing plane, electrodes e15 and e16 avoid the penetration of the post-acceleration potential. Calcula-

tions showed an influence of the potential of neighboring electrodes into the AP of less than 2 meV [19]

In order to give enough space for the wider effective proton flux to travel along the spectrometer (section 4.1.2), electrode e12 had to be redesigned, see figure 4.13. The diameter of electrode e12 was chosen as big as possible (diameter of 124 mm) but still keeping a safe distance to electrode e13. The AP electrode e14 was completely reconstructed taking especial care on the polishing, coating and cleaning in order to obtain a good surface quality, which is of particular importance in the AP- and the DV-region. Details will be given in section 4.3.

Upper ExB electrode (e16):

The potential applied at electrode e16 is part of the post-acceleration potential. Post acceleration of the protons is necessary to overcome the mirror effect of the increasing magnetic field towards the detector, which otherwise would reflect part of the protons. It has been designed as a dipole electrode for its use as ExB-drift electrode. One function of electrode e16 is the centering of the proton beam onto the detector (see figure 4.19). It may be also used to perform several systematic checks, e.g. edge effect or angular sensitivity of the detector[46][38]. The ExB electrode is oriented to cause a shift of the proton distribution in the direction perpendicular to the neutron beam. This permits to scan the proton beam intensity in order to center it with respect to the detector.

In its first version, the upper ExB consisted of two parallel stainless steel plates with a surface of $10 \times 10\,\mathrm{cm}^2$ separated by 4 cm. During the FRM-II beamtime, instabilities on the count rates were found. The analysis of the data showed that this problem came from unstable background[50]. One of the components of this background showed to be higher at the edges of the detector than at its center. This anomalous background could be produced by trap P-I, which would explain the specific spatial profile of this background component[50].

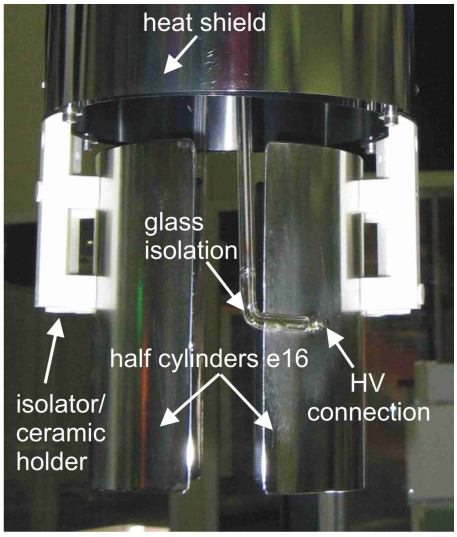

Figure 4.20: View of the upper ExB drift electrode and heat shield around the detector electrode (not shown in the picture).

Electric field simulations[38] indeed demonstrated the existence of a trap (P-I) between upper ExB electrode, e16, and detector electrode, e17. Therefore, the upper ExB electrode was shifted upwards to reduce the gap between electrodes e16 and e17 and redesigned as a cylindrical electrode (130 mm of diameter and a length of 160 mm) divided in two half cylinders, see figure 4.20. New simulations[38] have shown that a trap could still be there but clearly reduced in its impact. The trap has been shifted radially to positions further away from the detector. At this position, trapped particles are outside the effective flux tube and should not reach the detector. Furthermore, electrones emitted by field emission at the edges of the ExB electrode could not directly reach the detector since the ExB electrode is now placed outside of the flux tube. Additionally, we took care that sharp edges were reduced in order to reduce field emission. The measurements carried out during ILL beamtime have not shown this background anymore (see chapter 7).

The new ExB electrode was tested to work up to a voltage difference of 20 kV without discharges. The maximum voltage difference applied in the ILL beamtime was 4 kV (-4.2/ -0.2 kV). Most of the time it was not used as drift electrode and a symmetric voltage was applied (-2/-2 kV).

To avoid thermal heating of the detector (and therefore reduce the thermal noise, see chapter 7), two thin plates made of stainless steel, bent into coaxial cylinders, have been installed surrounding the detector (see figure 4.20). The heat shield is grounded to the spectrometer. The heat shield and the upper ExB electrode, are fixed at a its position whereas the detector can be moved vertically to extract it from the main vacuum chamber. Then, a mechanical valve permits to close the main vacuum chamber so the detector can be repaired or exchanged during the course of the beam-time.

High Voltage electrode (e17):

A front view of the proton detector and the cup of the detector electrode can be seen in figure 4.21 (a). The cup has an inner diameter of 45 mm and an outer diameter of 109.4 mm. The walls of the cup are filled with lead to reduce background caused by gamma radiation (section 3.4.3). The side view, (b), shows the long high voltage detector electrode (e17) which is separated from the spectrometer (at ground potential) by a cylindrical insulator. For detailed information on the detector electronics and its mechanical setup the reader is referred to M. Simson [46]

During the ILL beamtime, the electrode was held on acceleration voltages between -10 and -15 kV. These high voltages are necessary to accelerate the protons to energies higher than the energy threshold of the detector. High voltages are also recommendable to produce a good separation between the electronic noise of the detector and the energy of the proton signal (see section 7.2.2).

The opening of the detector cup had to be increased not to cut into the flux tube. Table 4.5 summarizes the features of all the electrodes.

4.3 Surfaces studies

Additionally to the modifications of the electrodes described in the last section, the manufacturing of the electrodes and the cleaning procedure were improved in order to get clean surfaces with a very homogenous work function. Furthermore, two new sets of get-

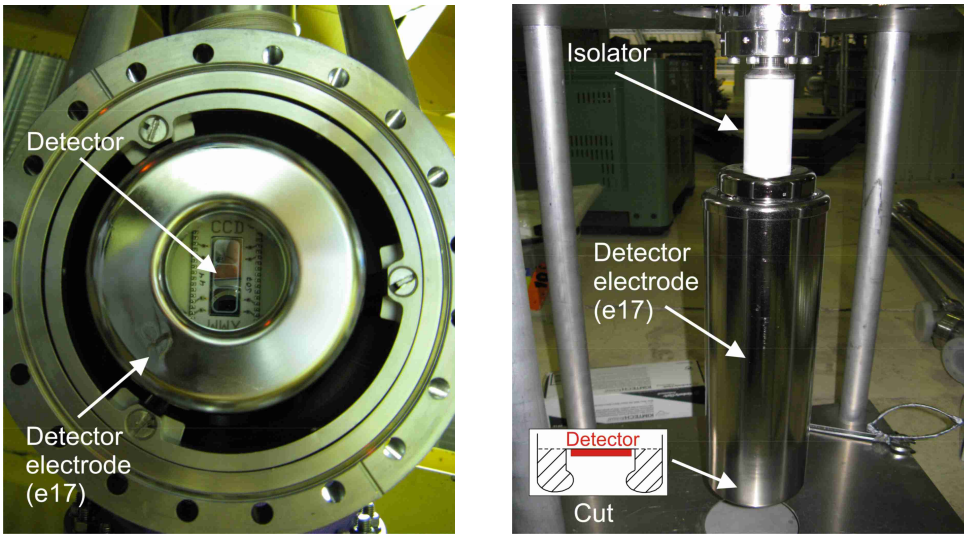

(a) Grid electrode. (b) Mirror electrodes.

Figure 4.21: High voltage detector electrode. Left, front view of the SDD detector composed of three pads and the detector cup which shields from background radiation. Right, side view of the detector electrode. The detector is placed at the lowest side of the stainless steel electrode. A ceramic insulator separates the high voltage applied at the detector from the rest of the system which has electric contact with the complete spectrometer.

Electrode	Voltage [V]	Comments
e1	800	mirror (new, increased diameter, grid)
e1b	800	mirror (new, increased diameter, grid holder)
e2	1000/ 820	mirror (quadrupole electrode, used as a cylinder)
e3	grounded (U_0=0 V)	DV electrodes (wired individually, shortened)
gr1 to gr5	grounded (U_0=0 V)	DV electrodes (wired individually)
e6	grounded (U_0=0 V)	DV electrodes (wired individually)
e7	grounded	useable for systematic checks (same ground than DV)
e8	mostly -1000/ -50 or -200/ 0	lower $E \times B$ electrodes (two half cylinders)
e9	grounded	(same ground than DV)
e10	0,435331 $\times U_A$	variable
e11	0,683960 $\times U_A$	variable
e12	0,892352 $\times U_A$	variable
e13	0,991040 $\times U_A$	variable
e14	U_A	AP electrode; variable
e15	0,985094 $\times U_A$	variable
e15b	grounded	grounded to the spectrometer, not the DV ground
e16	mostly -2/ -2 or -3.7/ -4.2 [kV]	upper $E \times B$ electrode (two half cylinders)
e17	-10/ -12/ -15 [kV]	detector HV

Table 4.5: Typical voltage settings at the electrodes.

ter pumps were added to the electrode system. The getters improved the quality of the vacuum hence reducing background caused by rest gas ionization. All these measures improved the performance of the setup at the ILL beamtime considerably: particle traps where enormously reduced and no discharges were observed at the detector high voltage electrodes. Results of the beam time will be discussed in chapter 7.

The manufacturing and the cleaning procedure of the electrodes described in appendix A.1 are improved versions of the treatment carried out for the first *a*SPECT beamtime at the FRM-II reactor [50]. At the end of the FRM-II beamtime the quality of the electrodes surfaces was found to be quite low. Apparently, the silver layer (2 μm) below the gold coating (1 μm) was too thin and after some months, the gold started to diffuse and spots appeared on the surfaces of the electrodes. In addition, for the preparation of the FRM-II beamtime a ultrasonic bath was used to clean the electrodes. The ultrasonic bath removed part of the gold layer and therefore increased the degradation of the surface quality too.

Due to the high cost and the time needed to produce a completely new electrode system, not all electrodes were reconstructed. Nevertheless, the "bad" quality of the surfaces of those electrodes which were not reconstructed is not so important for *a*SPECT since their surface properties do not enter in the transmission function. The new electrodes (DV, AP and e12) were coated with a thicker layer of silver, 10 μm, and 1 μm of gold. The ultrasonic bath was suppressed and the cleaning was performed by alternating baths with iso-propanol, Mucasol and distilled water (see appendix A.1).

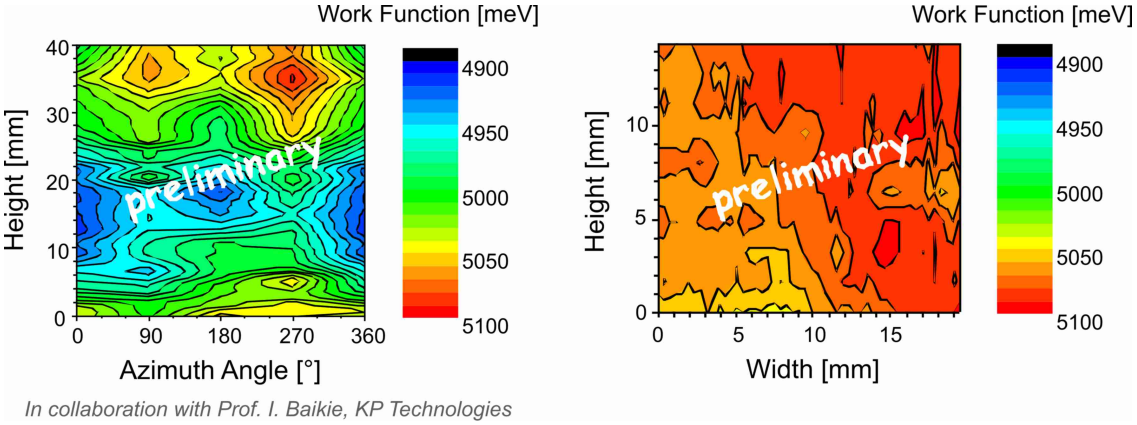

Figure 4.22: Left: Work function measured at the surface of a original *a*SPECT electrode (2005) with a Kelvin probe. Right: Work function measured on new samples with an improved polishing and cleaning procedure.

As explained in section 3.4.1, in order to reach the final accuracy on the determination of the coefficient a, we have to be sure to determine $U_A - U_0$ with an accuracy of 10 mV. For that reason, surfaces studies are under way. Figure 4.22 left, shows the potential at the surface of one test electrode, measured with a Kelvin probe. Inhomogeneities of about 100 meV in the root mean squared (RMS) of the work function were found. As an example, an uncertainty of ± 75 meV on the potential difference $(U_A - U_0)$ would prevent an absolute precision in a better than 1.13 %. Figure 4.22 right, shows the same measurement of a test sample following the improved manufacturing and cleaning procedure. The measurement showed differences of 21 meV and 15 meV on the RMS work function across the sample surface. The result shows the right way to go. More measurements are needed

still in order to ensure the reproducibility of the results. Further studies with different coating methods and different materials are under way [38].

Additionally, the potential difference $(U_A - U_0)$ can be determined by using a mono-energetic calibration source which could be installed below the aSPECT cryostat or inside the DV. It would also permit to measure the aSPECT transmission function F_{tr}. A prototype ion source is described in [45], furthermore, studies to build up a calibration electron source are also under way.

Chapter 5

Magnetic field design

As introduced in chapter 3, the magnetic field is a fundamental component of MAC-E filter spectrometers. In aSPECT, its special design allows to measure the angular correlation coefficient a keeping the systematic uncertainties well below $\delta a \approx 3 \cdot 10^{-4}$. In this chapter, the features of the magnetic field design of aSPECT, as well as its measurement procedure with a high accuracy Hall probe are discussed in detail. Finally, the magnetic field mapping obtained with this Hall probe will be presented.

5.1 Magnetic field requirements

The magnetic field of the aSPECT spectrometer has been designed for two main purposes: To guide the decay protons towards the proton detector and to convert adiabatically the transversal component of the proton momentum into longitudinal, before reaching the AP. Furthermore, the magnetic field provides a good shielding from external charged background. In order to achieve a measurement of a with an absolute accuracy of $\delta a \approx 3 \cdot 10^{-4}$, the magnetic field has to fulfill the following conditions:

1. The adiabatic condition has to be satisfied all along the proton trajectory.
2. The position and extension of the DV and AP regions have to be rigorously defined, as well as the shape of the magnetic field profile within them.
3. The ratio of the magnetic field at the DV and at the AP, $r_{\mathrm{B}} = B_A/B_0$, has to be large enough to provide the sensitivity necessary to the spectrometer to extract a with the desired accuracy.
4. r_{B} has to be known with a relative accuracy of $\delta r_{\mathrm{B}}/r_{\mathrm{B}} \approx 10^{-4}$.
5. Every proton has to "see" the same transmission function independently of their emission position. This implies that the relative magnetic field gradient has to be $\Delta B/B < 10^{-4}$. Otherwise, the neutron and the proton beam density distribution have to be known.

5.1.1 Adiabatic condition

As it was introduced in chapter 3, the adiabatic approximation is accomplished if $\Delta B/B \ll 1$ and $\Delta E/E \ll 1$ during one particle gyration. Breakdown of the adiabatic approxima-

tion would cause the transmission function to be different from the adiabatic transmission function defined in 3.25. Calculations for given field maps of the electric potential and of the magnetic field permit us to determine this effect and to optimize the field profiles to suppress non-adiabatic effects down to a negligible level [19]. A simple comparison of the measured field along the z-axis with the simulated field permits to check the validity of the adiabatic approximation inside our spectrometer (see figure 4.14).

5.1.2 DV and AP regions

The DV is defined as the region of the neutron beam were decay protons have the possibility to reach the proton detector if they are able to cross the AP potential barrier. As it was explained in chapter 4, due to the edge effect in the proton detector, the width of the proton flux tube depends on the energy and angle of emission of the decay protons. Consequently, the width of the DV region depends on the the energy and angle of emission of the decay protons too. Expression 4.1 permits to calculate the width of the flux tube at the DV by using $B(z) = B_0$.

Along the ***x*-axis**[1] (which is perpendicular to the neutron beam and to the detector pads alignment), the x-dimension of the the DV extents from -12.5 to $+12.5\,\mathrm{mm}$, see figure 5.23.

Along the ***y*-axis** (which corresponds to the direction of flight of the neutrons and to the alignment of the detector pads), the size of the DV is determined by the number of working pads. Since during the ILL beamtime of 2008 only the central pad was working, the y-dimension of the DV extents from -12.5 to $+12.5\,\mathrm{mm}$.

With regard to the ***z*-axis**, every proton is able to reach the detector independently of their emission position along this axis. Therefore, the height of the DV is only determined by the size of the neutron beam profile along the z-axis. As can be seen in figure 5.23 (right), the DV in the z-axis extents from -40 to $+40\,\mathrm{mm}$

The aSPECT magnetic field was foreseen to contain a local maximum in the DV at $z \approx 0\,\mathrm{cm}$, see figure 5.24. Since the neutron beam is also centered at this height, approximately half of the decay protons would be emitted into the lower hemisphere. Protons emitted at $z < 0$ with very low longitudinal kinetic energy, after being reflected at the mirror electrode, can be reflected again by the magnetic mirror effect produced at the magnetic field maximum, at $z \approx 0$. Hence, these protons are permanently trapped between the mirror electrode and the DV. A set of two coils at the height of the DV region, trim coils c3 and c5 (see figure 4.14 and 5.24), permit to create a small magnetic field gradient across the DV in the z-direction, displacing the local maximum out of the DV, towards the mirror electrode. In this way, no protons can be trapped due to this effect. Furthermore, due to the inverse mirror effect of the magnetic field gradient, the longitudinal kinetic energy of the protons slightly increases. This helps protons to overcome small inhomogeneities of the electric field.

Trim coils c3 and c5, may be used for systematic checks too. Changing the magnetic field gradient across DV it is possible to study its impact on a. A gradient in opposite

[1] The definition of the coordinate system, the neutron beam direction and the alignment of the three pads of the proton detector are shown in figure 4.19

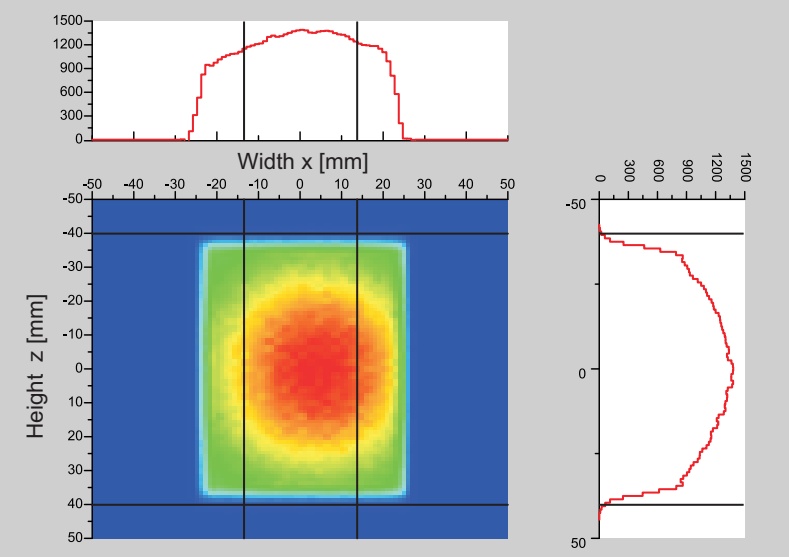

Figure 5.23: Neutron beam profile at the center of the DV (y=0) for full beam configuration, see chapter 7. The boundaries of the DV in the x and z axis are marked with black lines.

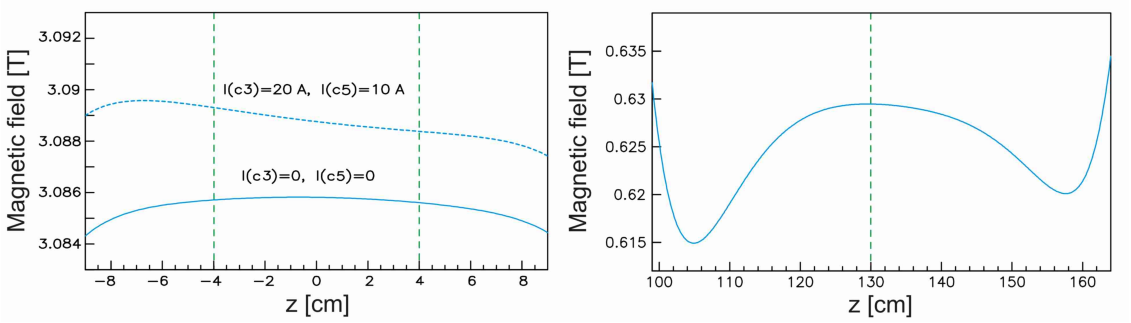

(a) DV region (b) AP region

Figure 5.24: Simulated magnetic field profile within DV and AP regions according to the calculations of 2005 [19].

direction may be used to trap protons due to the magnetic mirror effect and again study the effect on a.

The AP is defined as an imaginary plane (perpendicular to the z-axis) at the position of the local maximum of the magnetic field. This position should coincide with the maximum of the electric field created by the AP electrode, see figure 4.14 and 5.24. The extension of the AP in the x and y axis is determined by the width of the flux tube in these directions. Since the flux tube is energy and angle dependent, see equation 4.1, the AP dimensions are as well dependent on these parameters. Thus, the AP has a maximum size of 54 mm (from -27 to $+27$ mm) in x and y direction.

The reason to create a local maximum of the magnetic field at the AP region is related to the transmission function. Close to the AP, the electrostatic potential is nearly constant, $U \approx U_A$. If the magnetic field had a minimum there, it would have to be extremely

shallow in order to fulfill the transmission condition. By creating a local maximum of the magnetic field there, the adiabatic condition is automatically fulfilled[19]. This can be seen from the following argument: protons created at the DV will overcome the potential barrier only if their longitudinal kinetic energy, $T_{\parallel}^{\mathrm{add}}$, is positive at any point of their trajectory. We have defined in equation 3.15 the adiabatic transmission energy T_{tr} as the minimum kinetic energy necessary to overcome the potential barrier. Thus, the adiabatic transmission condition requires $T_{\parallel}^{\mathrm{add}}(T_{\mathrm{tr}}) > 0$. Combining equation 3.14 and 3.15, the following condition is derived:

$$\frac{B_0 - B\sin^2\theta_0}{B_0 - B_A\sin^2\theta_0} > \frac{U - U_0}{U_A - U_0} \tag{5.1}$$

Close to the AP, $U < U_{\mathrm{A}}$ and consequently the right side of this equation is smaller than unit. Hence, the inequality is automatically fulfilled if the left side is larger than 1, that is if $B < B_{\mathrm{A}}$. This also implies that the reflection of protons unable to overcome the potential barrier may happen before to reach the maximum of the magnetic field. For this reason and due to the uncertainties in the position of the electric and magnetic field maxima, the AP is defined as a volume with a height (z-axis) of $\pm 2\,\mathrm{cm}$ around the position of the electric field maximum, at approximately 132 cm according to the latest electric field calculations [38].

5.1.3 Resolution of the spectrometer

The observable measured with aSPECT is the ratio r_h of count rates at a AP voltage setting U_A with respect to the measured count rates at $U_{\mathrm{Amin}} = 0\,\mathrm{V}$. Note that for background reasons (section 3.4.3) we have chosen $U_{\mathrm{Amin}} = 50\,\mathrm{V}$. So we have:

$$r_h(U_A, r_{\mathrm{B}}) = \frac{\rho(U_A, r_{\mathrm{B}})}{\rho(U_{\mathrm{Amin}} = 50V, r_{\mathrm{B}})} \tag{5.2}$$

Thus, the sensitivity of the observable r_h on a, given by the derivative $\mathrm{d}r_h(U_A, r_{\mathrm{B}})/\mathrm{d}a$, depends on U_A and r_{B}. In figure 5.25 $\mathrm{d}r_h/\mathrm{d}a$ as a function of U_A for different r_{B}^{-1} values is shown. Calculations show that for $r_{\mathrm{B}}^{-1} \approx 5$, the sensitivity does not change that much anymore.

Furthermore, the main parameters which determine the spectrometer size are the ratio of the magnetic field $B(z)/B_0$ and the radius of the detector, r_{det}, see equation 4.1. Thus, a small ratio r_{B} requires a bigger diameter at the AP region. For a small value of r_{B} also the length of the spectrometer has to be large to fulfill the adiabatic condition, see section 3.4.2. Therefore, in aSPECT it has been chosen $r_{\mathrm{B}} \approx 0.2$ as good compromise between the dimensions of the spectrometer and its resolution[20].

5.1.4 Required accuracy of the magnetic field ratio

The objective of the aSPECT experiment is to improve the uncertainty in the correlation coefficient a to 0.3 %. In order to meet this target all systematic effects must be kept below $\Delta a/a \approx 0.1\,\%$ (see section 3.4.1).

The error in the determination of the magnetic field ratio r_{B} introduces an error in a which is correlated to the electrostatic potential difference $(U_A - U_0)$, since it also enters

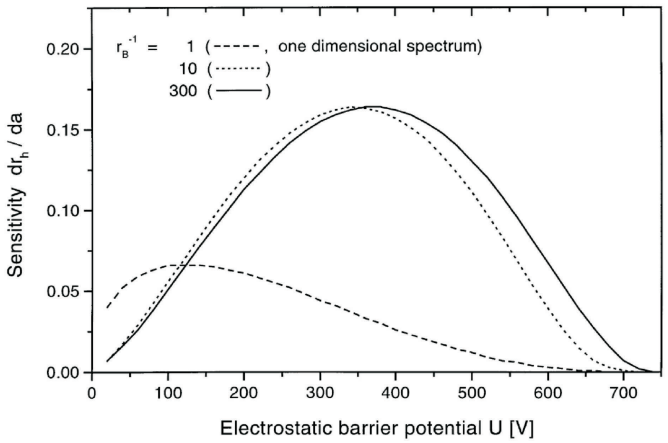

Figure 5.25: Sensitivity of $r_h(U, r_\mathrm{B})$ to the coefficient a for three different values of the ratio r_B. Picture from [20]

in the transmission function (see equation 3.8). Therefore, we can write the uncertainty that the magnetic field ratio r_B introduces in a as a function of these two parameters[20]:

$$\delta r_\mathrm{B} = c(U_A, r_\mathrm{B})\delta a \tag{5.3}$$

where it has been considered $U_0 = 0\,\mathrm{V}$. This function is represented in figure 5.26 for a fixed value of $r_\mathrm{B} = 0.2$. As can be seen, a ratio $r_\mathrm{B} = 0.2$ determined with a relative accuracy of $\delta r_\mathrm{B}/r_\mathrm{B} = 10^{-4}$ is sufficient to keep $\delta a/a$ smaller than $\sim 2 \cdot 10^{-3}$ for all AP electric potentials U_A.

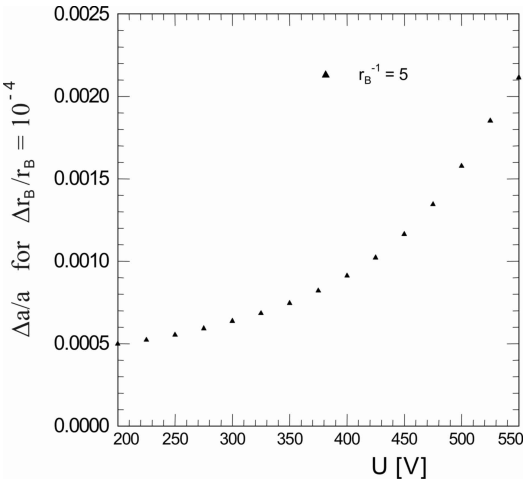

Figure 5.26: Relative change of a for a fixed $\Delta r_\mathrm{B}/r_\mathrm{B} = 10^{-4}$, computed for different values of U_A.

However, the uncertainty in a depends strongly on the barrier voltage chosen. Therefore, for measurements of the integral proton spectrum $N_p(U_A)$ (see equation 7.5), we have to choose a suitable set of barrier voltages. As an example, the barrier voltages used during the ILL beamtime (see chapter 7) were $U_A = 50, 250, 400, 500, 600\,\mathrm{V}$.

If we consider the relative change of a introduced by a shift of the magnetic field ratio by adjusting equation 7.5 with the input data: $B_A/B_0 = 0.203$, $U_A = 50$, 250, 400, 500, 600 V, and the recommended value for $a = -0.103$, we obtain figure 5.27. The exact values of the data points displayed in figure 5.27 are written in table 5.6. Figure 5.27 shows the relative change of the angular correlation coefficient a for a certain relative variation of the ratio r_B. As a first approximation, we can consider the relation between $\Delta a/a$ and $\Delta r_\mathrm{B}/r_\mathrm{B}$ as linear:

$$\Delta r_\mathrm{B}/r_\mathrm{B} \approx 1.09 \cdot 10^{-1} \Delta a/a \tag{5.4}$$

Equation 5.4 permits to estimate the error introduced in a due to an uncertainty in the magnetic field ratio r_B. For example, for an a measurement with a relative accuracy of $\delta a/a \cong 5\,\%$, we have to keep the systematic uncertainties in the order of $\delta a/a \approx 1\,\%$. Therefore, according to equation 5.4, the ratio r_B has to be determined with a relative accuracy of $\delta r_\mathrm{B}/r_\mathrm{B} \approx 1 \cdot 10^{-3}$.

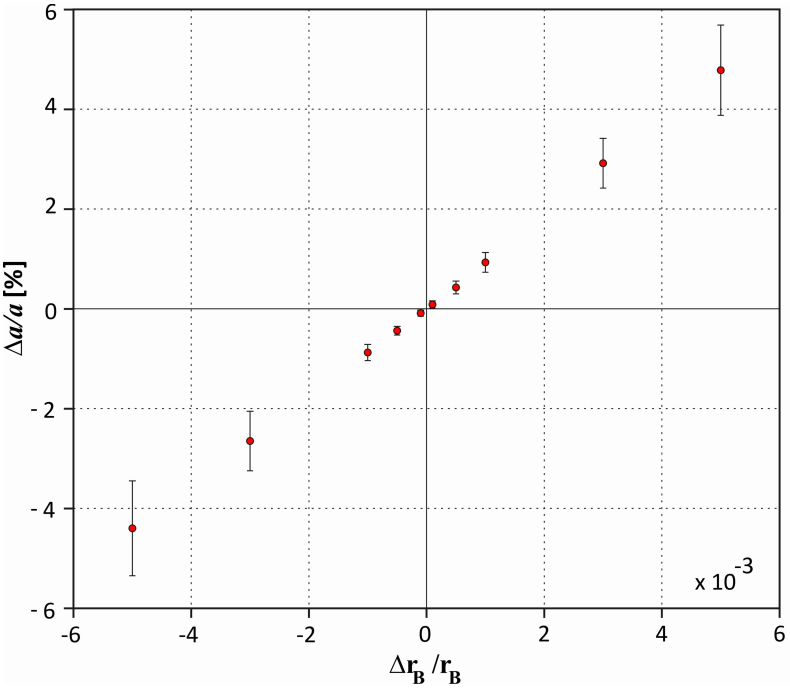

Figure 5.27: Relative variation $\Delta a/a$ vs $\Delta r_\mathrm{B}/r_\mathrm{B}$. The values have been calculated assuming a linear field gradient and a flat neutron beam profile (see section 5.1.5). Input data for the simulation: $B_A/B_0 = 0.203$, $U_A = 50$, 250, 400, 500, 600 V, and the recommended value for $a = -0.103$.

Table 5.27 indicates that the magnetic field ratio has to be known with a relative accuracy of $\delta r_\mathrm{B}/r_\mathrm{B} \approx 10^{-4}$ in order to obtain a with an accuracy of $\delta a \sim 10^{-4}$. For that, it is necessary to determine the value of the magnetic field at the DV and AP regions with a relative accuracy of $\delta B/B \approx 10^{-4}$, independently of the field inhomogeneity (see section 5.1.5).

$\Delta r_B/r_B$ ($\times 10^{-3}$)	$\Delta a/a$ [%]
-5	-4.4(9)
-3	-2.7(6)
-1	-0.88(16)
-0.5	-0.44(9)
-0.1	-0.09(6)
0.1	0.09(4)
0.5	0.43(13)
1	0.9(2)
3	2.9(5)
5	4.8(9)

Table 5.6: Relative shift $\Delta a/a$ vs $\Delta r_B/r_B$. Values corresponding to the points of figure 5.27.

5.1.5 Required homogeneity of the magnetic field

In order to define a unique transmission function for each proton independently of their emission position (see section 3.4.1), the magnetic field has to be kept constant all over the DV and AP. The drawback of the magnetic field gradient produced by trim coils c3 and c5 (discussed in section 5.1.2) is that the transmission function is no more independent of the proton emission point inside the DV. With the gradient created by the trim coils, protons emitted at different positions in the DV have a slightly different transmission function. Then, it becomes necessary to know the neutron beam distribution inside the DV, $N_n(\vec{r})$, and the corresponding proton beam distribution at the AP, $N_p(\vec{r})$. Thus, a more general definition of the ratio r_B has to be introduced:

$$r_B \equiv \frac{B_A^W}{B_0^W} = \frac{\int^{AP} N_p(\vec{r}) B_A(\vec{r}) d^3\vec{r} / \int^{AP} N_p(\vec{r}) d^3\vec{r}}{\int^{DV} N_n(\vec{r}) B_0(\vec{r}) d^3\vec{r} / \int^{DV} N_n(\vec{r}) d^3\vec{r}} \tag{5.5}$$

The superscript W indicates that the magnetic field profile is weighted with the neutron/proton beam distribution. Assuming a homogeneous neutron beam profile at the DV and a correspondingly homogeneous proton beam profile at the AP, the ratio is given by:

$$r_B = \frac{\int^{AP} B_A(\vec{r}) d^3\vec{r}}{\int^{DV} B_0(\vec{r}) d^3\vec{r}} \tag{5.6}$$

Then, r_B is determined by the accuracy the fields could be measured inside the DV and AP. If the neutron and proton beam profiles are not homogeneous inside the DV and AP, then, they will not affect our accuracy ($\delta r_B/r_B \approx 10^{-4}$) in case the relative field gradients inside DV and AP are $\Delta B/B < 10^{-4}$:

$$\begin{aligned} r_B &= \frac{\int^{AP} N_p(\vec{r}) B_A(\vec{r}) d^3\vec{r} / \int^{AP} N_p(\vec{r}) d^3\vec{r}}{\int^{DV} N_n(\vec{r}) B_0(\vec{r}) d^3\vec{r} / \int^{DV} N_n(\vec{r}) d^3\vec{r}} \\ &= \frac{\int^{AP} N_p(\vec{r}) (\overline{B}_A + \Delta B_A(\vec{r})) d^3\vec{r} / \int^{AP} N_p(\vec{r}) d^3\vec{r}}{\int^{DV} N_n(\vec{r}) (\overline{B}_0 + \Delta B_0(\vec{r})) d^3\vec{r} / \int^{DV} N_n(\vec{r}) d^3\vec{r}} \end{aligned} \tag{5.7}$$

Using $\Delta B_{\mathrm{A}}(\vec{r}) < 10^{-4}\overline{B}_{\mathrm{A}}$ and $\Delta B_0(\vec{r}) < 10^{-4}\overline{B}_0$, equation 5.7 leads to:

$$r_{\mathrm{B}} = \frac{\overline{B}_{\mathrm{A}}(1 \pm 10^{-4})}{\overline{B}_0(1 \pm 10^{-4})} \simeq \frac{\overline{B}_{\mathrm{A}}}{\overline{B}_0}(1 \pm 10^{-4}) \simeq \overline{r}_{\mathrm{B}} \pm \delta r_{\mathrm{B}} \tag{5.8}$$

As a result, if the relative field gradients are $\leq 10^{-4}$, then the knowledge on the neutron and proton beam profiles is not necessary and we get an additional uncertainty of $\delta r_{\mathrm{B}}/r_{\mathrm{B}} \simeq 10^{-4}$. Note that this uncertainty is independent of the error of the magnetic field measurements.

If the beam profiles were known exactly, there would not be any additional error to the error of the magnetic field measurements.

In our case, the neutron and proton beam distributions and the magnetic field profiles are not measured exactly but with a certain accuracy. Thus, both accuracies contribute in the uncertainty of r_{B}. However, according to magnetic field simulations (see appendix C.5), the relative magnetic field gradient within the AP region is $\Delta B_A/B_A \approx 1 \cdot 10^{-4}$ (in beamtime configuration, see section 5.4) and then equation 5.5 reduces to:

$$r_{\mathrm{B}} \equiv \frac{B_{\mathrm{A}}^{\mathrm{W}}}{B_0^{\mathrm{W}}} = \frac{\overline{B}_{\mathrm{A}}(1 \pm 10^{-4})}{\int^{\mathrm{DV}} N_n(\vec{r})B_0(\vec{r})d^3\vec{r} / \int^{\mathrm{DV}} N_n(\vec{r})d^3\vec{r}} \tag{5.9}$$

Considering that the relative magnetic field gradient within the DV region (in beamtime configuration, see section 5.4) is much bigger in the z-axis ($(\Delta B_0/B_0)_{z-\mathrm{axis}} \sim 10^{-3}$) than in x and y direction ($(\Delta B_0/B_0)_{x-y-\mathrm{plane}} \sim 10^{-4}$):

$$B_0^{\mathrm{W}} = \frac{\int^{\mathrm{DV}} N_n(\vec{r})B_0(\vec{r})d^3\vec{r}}{\int^{\mathrm{DV}} N_n(\vec{r})d^3\vec{r}} \approx \frac{\int^{\mathrm{DV}} N_n(z)B_0(z)dz}{\int^{\mathrm{DV}} N_n(z)dz} \tag{5.10}$$

The neutron beam profile shown in figure 5.23 can be idealized to a trapezoid parametrized with δ_i, W and N_{M}, as shown in figure 5.28:

$$N_{\mathrm{n}}(z) = \begin{cases} \frac{N_{\mathrm{M}}}{\delta_1}(z - z_1) & \text{for } z \in [z_1, z_2] \\ N_{\mathrm{M}} & \text{for } z \in [z_2, z_3] \\ -\frac{N_{\mathrm{M}}}{\delta_2}(z - z_4) & \text{for } z \in [z_3, z_4] \end{cases} \tag{5.11}$$

with $\delta_1 = z_2 - z_1 > 0$, $\delta_2 = z_4 - z_3 > 0$ and $W = z_4 - z_1 > 0$. The magnetic field is approximated to a straight line with $B(z = 0) = B_0$:

$$B_0(z) = -\frac{\Delta B}{z_4 - z_1}z + B_0 \tag{5.12}$$

With equations 5.11 and 5.12 we can calculate B_0^{W} (equation 5.10). The dividend of 5.10 is calculated integrating over the three regions defined in equation 5.11:

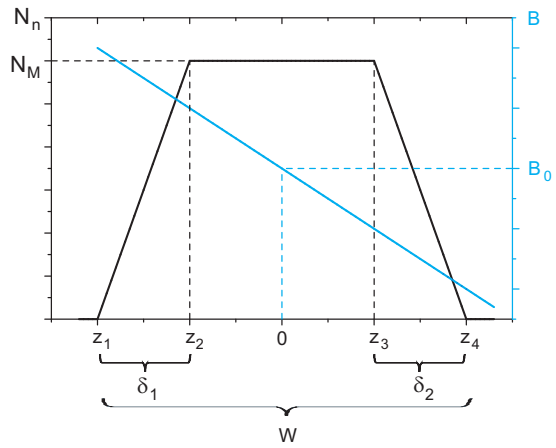

Figure 5.28: Weighting of the magnetic field at the DV with the neutron beam profile. In blue, magnetic field. In black, neutron beam.

$$\int_{z_1}^{z_4} N_n(z)B_0(z)dz = \int_{z_1}^{z_2} \frac{N_\mathrm{M}}{\delta_1}(z-z_1)\left(B_0 - \frac{\Delta B}{z_4-z_1}z\right)dz + \\ + \int_{z_2}^{z_3} N_\mathrm{M}\left(B_0 - \frac{\Delta B}{z_4-z_1}z\right)dz + \int_{z_3}^{z_4} -\frac{N_\mathrm{M}}{\delta_2}(z-z_4)\left(B_0 - \frac{\Delta B}{z_4-z_1}z\right)dz \quad (5.13)$$

Resolving the integration 5.13:

$$\begin{aligned}&\int_{z_1}^{z_4} N_n(z)B_0(z)dz = \\ &= \frac{N_\mathrm{M}}{\delta_1}\left[-\frac{\Delta B}{3W}\left(z_2^3 - z_1^3\right) + \frac{z_1\Delta B + B_0 W}{2W}\left(z_2^2 - z_1^2\right) - z_1 B_0\left(z_2 - z_1\right)\right] + \\ &+ N_\mathrm{M}\left[-\frac{\Delta B}{2W}\left(z_3^2 - z_2^2\right) + B_0\left(z_3 - z_2\right)\right] + \\ &+ \frac{N_\mathrm{M}}{\delta_2}\left[\frac{\Delta B}{3W}\left(z_4^3 - z_3^3\right) - \frac{z_4\Delta B + B_0 W}{2W}\left(z_4^2 - z_3^2\right) - z_4 B_0\left(z_4 - z_3\right)\right]\end{aligned} \quad (5.14)$$

The divisor of equation 5.10 is the area contained by the the neutron beam profile:

$$\int_{z_1}^{z_4} N_n(z)dz = N_\mathrm{M}\left(W - \frac{\delta_1}{2} - \frac{\delta_2}{2}\right) \quad (5.15)$$

In the case of a symmetric profile centered at $z = 0$:

$$\begin{aligned} z_1 &= -z_4 \quad , \delta_1 = \delta_2 \equiv \delta \\ z_2 &= -z_3 \quad , W = 2z_4 \end{aligned} \quad (5.16)$$

Equation 5.10 is then independent of the field gradient and the neutron beam profile:

$$B_0^\mathrm{W} = \frac{\int^\mathrm{DV} N_n(z)B_0(z)dz}{\int^\mathrm{DV} N_n(z)dz} = \frac{N_\mathrm{M}(B_0\delta + 2B_0 z_3)}{N_\mathrm{M}(W-\delta)} = B_0 = \overline{B}_0 \quad (5.17)$$

And therefore, the ratio results:

$$r_{\mathrm{B}} \simeq \frac{\overline{B}_{\mathrm{A}}}{\overline{B}_0}(1 \pm 10^{-4}) \simeq \overline{r}_{\mathrm{B}} \pm \delta r_{\mathrm{B}} \tag{5.18}$$

In the case of a non symmetric profile (figure 5.29 (a)), the magnetic field ratio r_{B} is shifted to higher or lower values. For an asymmetry bigger than $(\delta_1 - \delta_2) > 30\,\mathrm{mm}$, the relative shift of the ratio with respect to a symmetric beam profile is in the order of 10^{-4}. Similarly, in case of an asymmetric neutron beam, a change of the field gradient produces a shift of the ratio r_{B} with respect to a constant field, see figure 5.29 (b). For the beam profile used in figure 5.29 (b), the relative gradient of the field, $\Delta B_0/B_0$, has to be larger than $3 \cdot 10^{-3}$ in order to produce a shift on r_{B} in the order of $\Delta r_{\mathrm{B}}/r_{\mathrm{B}} \sim 10^{-4}$.

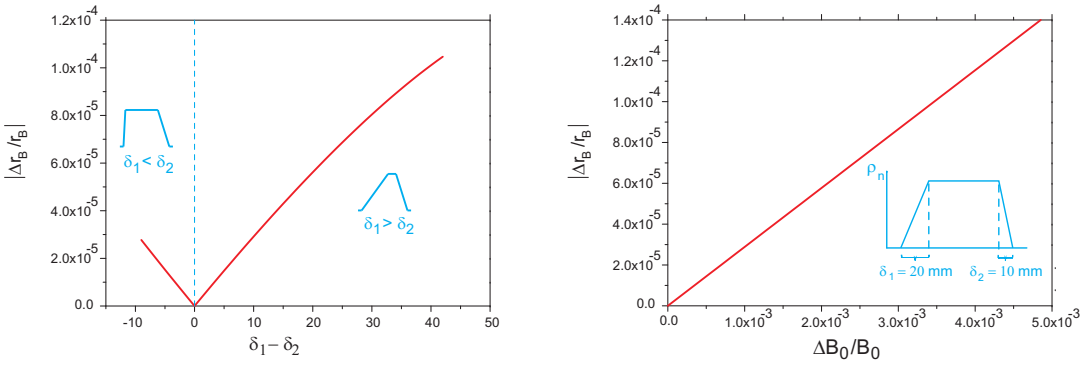

(a) Asymmetric neutron beam

(b) Different magnetic field gradients

Figure 5.29: (a) Effect of the asymmetry of the neutron beam to the ratio of the magnetic fields. Calculated for $\delta_2 = 10\,\mathrm{mm}$, $\Delta B_0/B_0 = 1 \cdot 10^{-3}$. (b) Effect of the gradient of the magnetic field, $\Delta B_0/B_0$, for an asymmetric neutron beam with $\delta_1 = 10\,\mathrm{mm}$ and $\delta_2 = 20\,\mathrm{mm}$.

A possible shift of the neutron beam profile with respect to $z = 0$ would produce an effect equivalent to an asymmetric beam profile. This effect has been calculated for the neutron beam profile measured during the ILL beam time of 2008 (figure 5.23) and the magnetic field configuration as measured for this beamtime (section 5.4), see figure 5.30. This permits to estimate the error in the weighted magnetic field within the DV ($\pm 0.2\,\mathrm{G}$), B_0^{W}, due to a misalignment of the neutron beam profile of $\pm 1\,\mathrm{mm}$, i.e., a relative uncertainty of $\left(\delta B_0^{\mathrm{W}}/B_0^{\mathrm{W}}\right)_{\mathrm{z}} = \pm 9 \cdot 10^{-6}$, which is negligible for the calculation of the ratio r_{B}.

The value of the magnetic field weighted with the neutron beam distribution is determined to be $B_0^{\mathrm{W}} = 2.17843(2)\,\mathrm{T}$, which differs from the result obtained weighting with a flat neutron beam profile (equivalent to average the field within the DV) in the sixth decimal, i.e., $\left(\Delta B_0^{\mathrm{W}}/B_0^{\mathrm{W}}\right)_{\mathrm{z}} \sim 10^{-6}$. As a result, only large asymmetries in the neutron beam profile produce a substantial change on the magnetic field ratio, r_{B}.

We can perform the same test for the effect of the magnetic field gradient in radial direction. For that, we have to weight the transmission function with the neutron- and pro-

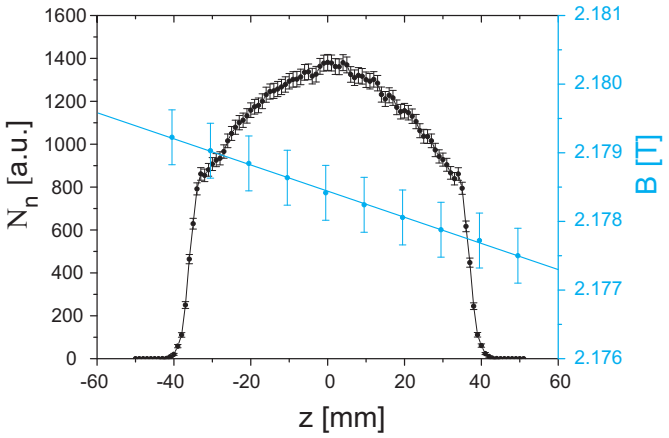

Figure 5.30: Calculated neutron beam profile inside the DV along the z-axis. The neutron beam profile has been calculated from the neutron profile measurements at the entrance and the exit of the aSPECT spectrometer, see section 7.1.2.

ton beam- profiles ($N_n(x)$ and $N_p(x)$) at the DV and AP , respectively. The x-dimension[2] of the DV and AP regions extent from -12.5 to +12.5 mm and from -27 to +27 mm, respectively (section 5.1.2). As a rough approximation, we can consider the proton beam profile at the AP to have the shape than the neutron beam profile at the DV, projected by the magnetic field lines.

Then, we can estimate the shift of B_0^{W} by averaging the neutron beam profile at the DV in the x-direction (see figure 5.23) with the simulated magnetic field profile (figure C.105) and comparing with the result obtained by averaging with a flat neutron beam profile. In this case, a relative shift of $\mid \left(\Delta B_0^{\mathrm{W}}/B_0^{\mathrm{W}}\right)_{\mathrm{radial}} \mid = 2 \cdot 10^{-8}$ is observed. Similarly, at the AP the result is $\mid \left(\Delta B_A^{\mathrm{W}}/B_A^{\mathrm{W}}\right)_{\mathrm{radial}} \mid = 1.3 \cdot 10^{-8}$. Both shifts introduce a negligible error on the calculation of the ratio r_{B}.

As it has been proved, only large asymmetries in the neutron beam profile produce a substantial change on the magnetic field ratio, r_{B}. Thus, as a result, the accuracy in the measurement of the neutron beam profile is not crucial as long as its shape is approximately known. With the measurement of the neutron beam density distribution performed in the ILL beamtime of 2008, the error resulting for the magnetic field ratio, r_{B}, is negligible, $\delta r_{\mathrm{B}} \ll 1 \cdot 10^{-4}$. Thus, the most crucial error is the one of the magnetic field measurement.

The effect of the magnetic field gradient in the correlation coefficient a is shown in figure 5.31. The figure has been obtained by fitting equation 7.5 with input parameters $B_A/B_0 = 0.203$, $U_A = 50, 250, 400, 500, 600$ V, and the recommended value for $a = -0.103$. A linear magnetic field gradient and a flat neutron beam profile have been considered for the calculation. As an example, a magnetic field gradient of $(B_{\max} - B_{\min})/B_0 = 8 \cdot 10^{-4}$, weighted whit a flat neutron beam profile corresponds to a shift in a of $\Delta a/a = -0.001(50)\,\%$, which is completely negligible for a measurement of a with the aimed accuracy.

[2]Note that the neutron beam profile is approximately constant along the y-axis and therefore its effect on the weighted magnetic field is negligible.

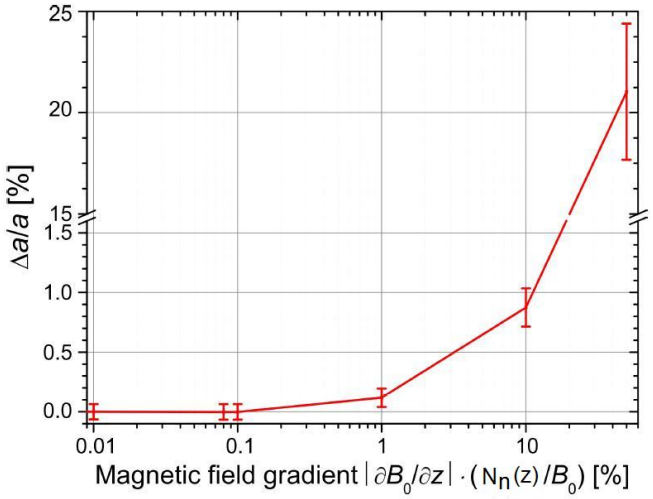

Figure 5.31: Relative change of the angular correlation coefficient a for different magnetic field gradients, $\partial B_0/\partial z$, in the decay volume (DV), assuming a uniform neutron beam density. For better visibility, the y-axis is broken at $\Delta a/a = 1.6\,\%$. Input data for the simulation: $B_A/B_0 = 0.203$, $U_A = 50,\ 250,\ 400,\ 500,\ 600$ V, and the recommended value for $a = -0.103$. The error bars, in the order of $0.05\,\%$, represent the error by fitting equation 7.5 to the simulated proton count rates only. Picture taken from [38].

5.1.6 Required magnetic field measurements

In summary, we need to map the complete magnetic field of the *a*SPECT spectrometer in order to compare it with the simulations, specially within DV and AP. Since mapping of the magnetic field is not possible during beamtimes, it is fundamental to study the reproducibility and stability of the field and to implement an on-line magnetic field monitoring suitable to be used simultaneously to the a measurements. For this reason we have developed different magnetic field measurements procedures:

- A complete mapping of the field with a high accuracy Hall-probe to check if the requirements described in section 5.1 are fulfilled. These measurements permit to study the shape, reproducibility and stability of the magnetic field, specially within DV and AP, and to tune it to our needs with correction coils. These measurements have to be carried out before or after the beamtime, therefore, they are off-line measurements.

- To provide an online monitoring of the field during beamtimes, a NMR-magnetometer which uses hyperpolarized ^{3}He as resonant material has been developed. This system and the results obtained with it will be discussed in detail in chapter 6.

- With the experience acquired during the measurements with hyperpolarized ^{3}He, the on-line monitoring of the field via a NMR-system has been simplified and improved by modifications of the electronics and by using protons as resonant material instead of ^{3}He. These improvements are discussed in chapter 6.

The results obtained with these magnetic field measurements are essential to extract a from the proton spectra measured during the ILL beamtime of 2008 and for the study of different systematics, see chapter 7.

5.2 Studies of the Hall-probe

In this section, the properties of the Hall-probe MPT-141 manufactured by Group 3 Technologies are studied in order to characterize its accuracy and stability for an accurate measurement of the magnetic field of the *a*SPECT spectrometer.

5.2.1 Accuracy of the magnetic probe

A Group 3 Technologies (model MPT-141) Hall probe providing a relative accuracy of about 10^{-4}, has been used to map the magnetic field along the spectrometer. The MPT-141 probe incorporates a temperature sensor to correct for temperature drifts in the working range from 0 to 50 °C. The probe is only sensitive to one component of the field. In our case, it was set to measure the z component since radial components at the DV and AP regions are completely negligible, with $B_r/|B| < 10^{-5}$. A detailed description of the Hall probe used for the mapping of the field and preliminary measurements can be found in [44].

According to the specifications of the company, there are three contributions that affect the accuracy of the MPT-141 Hall probe: the calibration error, the temperature- and the time-stability. Their contributions to the total error at the two magnetic field values of interest in the *a*SPECT spectrometer are listed in table 5.7.

	DV [G]	AP [G]
Accuracy:	$B_0 \sim 21800$	$B_A \sim 4400$
±0.006 % of full scale	±1.3	±0.36
±0.01 % of reading	±2.2	±0.44
Temperature stability:		
Calibration: ±10 [ppm of reading/°C]	±0.44	±0.09
Zero drift: ±(1 μT + 0.0003 % of full scale)/°C	±0.15	±0.06
(*)Shift:-3 [ppm of reading/°C m of cable]	−1.3	−0.26
Time stability:		
±0.1 % max over 1 year	±0.003/hour	±0.0005/hour
Total:	±4	±0.8

Table 5.7: Specifications of the MPT-141 Hall probe, calculated in the scales of 2.2 and 0.6 T. The maximum temperature change at the probe is estimated to be below 2 °C and a cable length of 10 meters was used. (*) This is not an error but a drift of the measurement due to temperature changes which has to be subtracted to the measurement.

The calibration of the probe has to be specially considered in our case. The probe was calibrated before its delivery in 2002 and again in 2006. The calibration is incorporated to the software in such a way that the value displayed is already corrected. The last calibration resulted in a relative correction in the order of $5 \cdot 10^{-4}$ (or 10 G) at the DV and $8 \cdot 10^{-4}$ (or 4 G) at the AP with respect to the first calibration. Since the measurements described here correspond to 2008, an increase of the error bars is necessary. As a rough estimation (conservative), the deviation during the period 2006 to 2008 was assumed to be of the same order as the deviation between the previous calibrations in 2002 and 2006.

Furthermore, the direction of the deviation can be different. Therefore, the error was estimated to be similar as the deviation observed between the calibration of 2002 and 2006:

DV: $\pm 10\,\mathrm{G}$
AP: $\pm 4\,\mathrm{G}$

Such calibration error does not have to be applied in case the probe is recently calibrated. However, the error due to the lack of a new calibration **is not used** here since the main objective of the present analysis is to study the accuracy reachable in the magnetic field measurements, the stability of r_B and the field gradients. However, the final result of the magnetic field ratio r_{B} will be presented with and without the calibration error contribution (table 5.11).

5.2.2 Corrections

The value displayed by the DTM-151 teslameter needs several corrections originated by two different factors: the temperature drift and the magnetic field drift.

The **first correction** can be written as follows:

$$B_{\mathrm{c1}} = B_{\mathrm{displayed}} - \mathrm{offset} - \mathrm{Temperature\ correction}(\Delta T) \tag{5.19}$$

Where "offset" is the offset of the Hall probe after its zeroing and ΔT is the change of temperature from the moment of the zeroing to the measurement. For example, for 10 meters of cable and a variation of the temperature of $+2\,^{\circ}\mathrm{C}$, the correction is -1.3 and $-0.26\,\mathrm{G}$ for the values of the field at the DV and AP regions, respectively (see table 5.7).

The **second correction** that has to be applied arises from the magnetic field drift. During operation of the magnet in persistent mode[3] a small magnetic field drift has been observed. This drift has been accurately measured with the NMR-magnetometer described in chapter 6. The drift is due to the power dissipation produced by the small resistance of the superconducting coils.

The main coils (from c1 to c11 with the exception of c3 and c5, see figure 4.14) are superconducting coils which are energized and switched to persistent mode. The external (12 to c15) and internal correction coils (c3 and c5) are energized independently[4]. Since they are not superconducting, they do not have persistent mode option. Their currents are highly constant whereas the current of the superconducting coils is slightly decreasing as function of time. As a result, the magnetic field ratio, r_{B}, is no more constant since we have the superposition of the magnetic fields from the superconducting coils plus the correction coils.

[3] In persistent mode the power supplies are disconnected from the superconducting coils. Then, the current introduced to the superconducting coils remains confined. This permits to avoid fluctuations of the field due to current instabilities originated in the power supplies.

[4] The coil system and the cryostat of the *a*SPECT spectrometer are described in section 5.4 and appendix A.2

Assuming we have only the field from the superconducting coils:

$$r_{\mathrm{B}} = \frac{B_{\mathrm{A}}(t)}{B_0(t)} = \frac{K_{\mathrm{A}} \cdot I(t)}{K_0 \cdot I(t)} = \frac{K_{\mathrm{A}}}{K_0} = \text{constant} \tag{5.20}$$

where $I(t) = I_0 - (\Delta I/\Delta t)t$ and therefore $B_i(t) = B_i - (\Delta B_i/\Delta t)t$. The variation of the main field (the field created by the superconducting/main coils) has been estimated to be $\Delta B_0/\Delta t = -2.81 \pm 0.07\,\mathrm{G/day}$ and $\Delta B_{\mathrm{A}}/\Delta t = -0.571 \pm 0.014\,\mathrm{G/day}$. The values given for the drift are a result from chapter 6. In case the correction coils are energized:

$$r_{\mathrm{B}} = \frac{B_{\mathrm{ACC}} + B_{\mathrm{A}}(t)}{B_{0\mathrm{CC}} + B_0(t)} = \frac{B_{\mathrm{ACC}} + K_{\mathrm{A}} \cdot I(t)}{B_{0\mathrm{CC}} + K_0 \cdot I(t)} = f(t) \tag{5.21}$$

or equivalently:

$$r_{\mathrm{B}} = \frac{B_{\mathrm{ACC}} + B_{\mathrm{A}}(t)}{B_{0\mathrm{CC}} + B_0(t)} = \frac{B_{\mathrm{ACC}} + B_{\mathrm{A}} - \frac{\Delta B_{\mathrm{A}}}{\Delta t}\Delta t}{B_{0\mathrm{CC}} + B_0 - \frac{\Delta B_0}{\Delta t}\Delta t} = f(t) \tag{5.22}$$

Note that at the field maximum $B_{0\mathrm{CC}} \approx 88\,\mathrm{G}$ and $B_{\mathrm{ACC}} \approx 12\,\mathrm{G}$ (in the standard configuration used during the beamtime of 2008) and decreases to approximately $B_{0\mathrm{CC}} \approx 50\,\mathrm{G}$ and $B_{\mathrm{ACC}} \approx 0\,\mathrm{G}$ at the center of the DV ($z = 0\,\mathrm{cm}$) and at the AP ($z = 132\,\mathrm{cm}$), respectively. The change of the ratio r_{B} as a function of time is shown in figure 5.32.

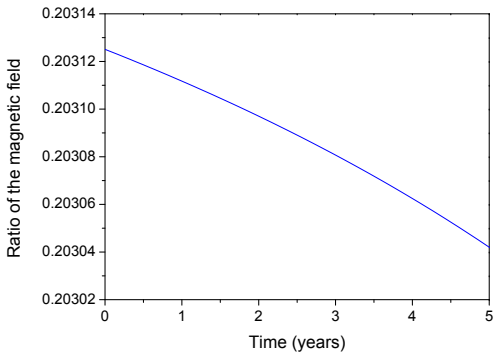

Figure 5.32: Change of the ratio r_{B} as a function of time, equation 5.21.

The relative change of the ratio is $4 \cdot 10^{-8}\,\mathrm{day}^{-1}$ and can be neglected. However, for long measurement periods this variation has to be controlled. For that purpose, the NMR-magnetometer described in chapter 6 was developed.

Another effect is due to the lapse of time between measurements at the DV and the AP. The time difference between the measurement at the DV and at the AP is approximately half an hour. During this time, the magnetic field decreases $-0.06\,\mathrm{G}$ at the DV and $-0.012\,\mathrm{G}$ at the AP, i.e., the field at the AP at the moment we measure there, corresponds to a field in the DV which is now about $-0.06\,\mathrm{G}$ lower than what we measured before. However, this affects the calculation of the ratio r_{B} only on a negligible level $\delta r_{\mathrm{B}}/r_{\mathrm{B}} = 3 \cdot 10^{-6}$.

Nevertheless, the effect is much stronger when measuring the radial homogeneity of the field (the time lapse is large [5]) or when comparing measurements taken on different days. For example, after 18 hours the field has drifted in total $\Delta B/B = 1 \cdot 10^{-4}$.

The field drift can be corrected by using the values $\Delta B_0/\Delta t$ and $\Delta B_A/\Delta t$ measured in chapter 6. Note that although the current varies as $I(t) = I_0 e^{-t/\tau}$, τ is so large that, as a first approximation, $I(t)$ can be considered as linear. The implementation of an accurate correction is complicated since the drift occurs only in the main coils whereas the measured field is the total field. However, a first order correction, i.e. correcting only the total field, is sufficient:

$$B_{c2}(t = t_0) = B_{c1} - B_{c1} C \Delta t \tag{5.23}$$

where $(\Delta B_0/B_0)/\Delta t = (\Delta B_A/B_A)/\Delta t = -1.292(2) \cdot 10^{-4}\text{day}^{-1} \equiv C$ and $\Delta t = t - t_0$.

5.2.3 Stability of the magnetic probe

The error bars of relative measurements can be reduced to the instability of the measurement (probe instability plus external factors) as absolute values are not necessary. Therefore, a specific study of the relative stability of the measurements may lead to higher accuracy than in absolute measurements.

In order to study the stability of the Hall probe, it was fixed at a certain position for longtime measurements with constant and variable temperature and in different magnetic field strength regions. The test measurements planned were:

- Longtime measurements with constant temperature and magnetic field.
- Measurements with constant magnetic field and variable temperature.
- Measurements in a zero field region (inside a μ-metal box) with constant and variable temperature.

During these tests, important fluctuations of the magnetic field reading were observed, see figure 5.33.

The measurements showed that the fluctuations of the magnetic field reading are independent of temperature variations and magnetic field strength, although the probability of fluctuations to appear increases during periods of temperature changes. Furthermore, the sign of the temperature variation does not determine the direction of the magnetic field drift (see figure 5.33 (a) and (b)). The fact that this effects were also observed inside a zero magnetic field region (figures 5.33 (c) and (d)) indicates that the fluctuations of the field reading are due to intrinsic instabilities of the probe. From the study the field drift at different magnetic field strengths (e.g., figure 5.33 (a)), the magnitude of the field fluctuations during large periods of time can be estimated.

[5] Note that for homogeneity measurements, the field has to be measured at least at four different angles and at two different radial positions (1.5 cm at the DV and 3.5 cm at the AP). Therefore, it takes more than eight hours to complete one set of measurements.

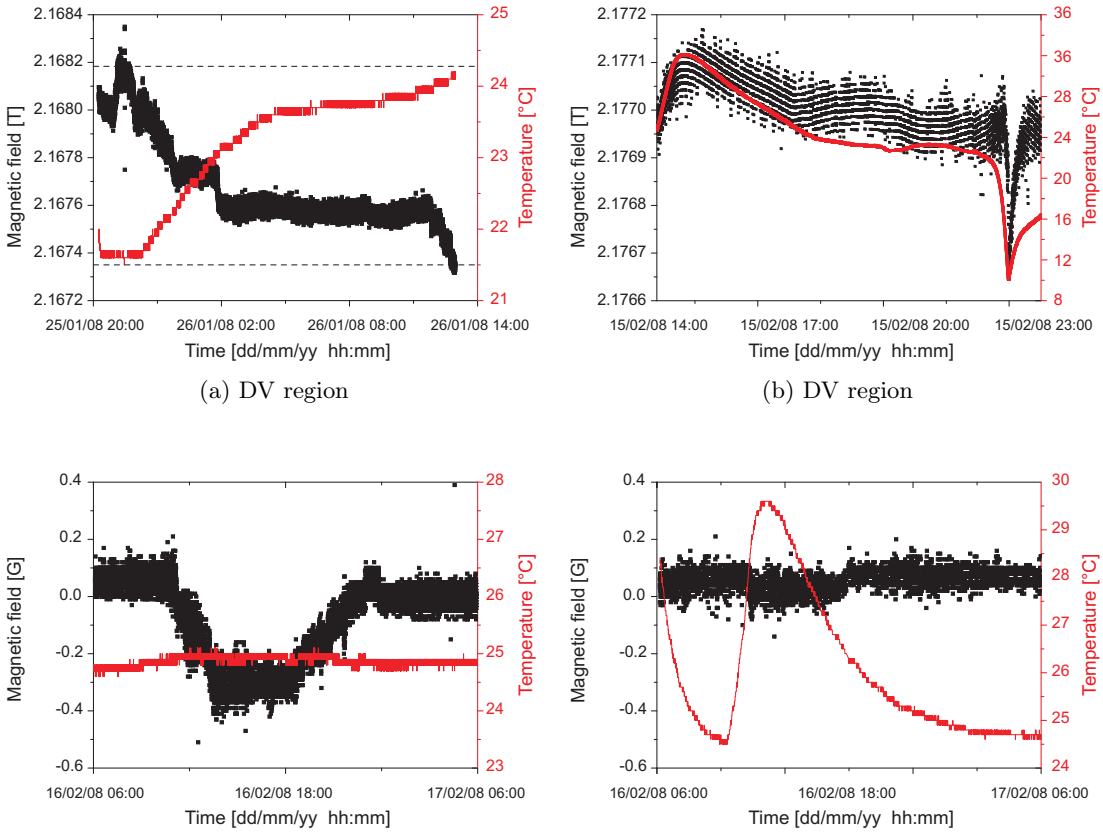

(a) DV region

(b) DV region

(c) Inside a μ-metal box (zero field)

(d) Inside a μ-metal box (zero field)

Figure 5.33: Stability of the field reading of a MPT-141 Hall-probe at a fix position inside the cryostat (magnet in persistent mode) and inside a μ-metal box, for large periods of time. The values have been corrected for the variation of the temperature and for the drift of the field, see section 5.2.2. The temperature measured by the thermal sensor of the Hall probe is shown in red.

The drift of the probe has been found to be ± 0.5 and $\pm 0.11\,\mathrm{G/hour}$ in the DV and AP, respectively. From these values we can infer two points:

- The relative field gradient along the radial direction is expected to be better than 10^{-4} while a change of $0.5\,\mathrm{G/hour}$ at the DV represents already a relative variation in the order of $2 \cdot 10^{-5}\,\mathrm{hour}^{-1}$. Therefore, only fast and consecutive measurements can be used to study the gradient of the magnetic field within DV and AP
- These random variations of the field could make the magnetic field ratio to jitter on a level $\Delta r_\mathrm{B}/r_\mathrm{B} \leq 5 \cdot 10^{-5}/\mathrm{h}$. Therefore, longtime measurements in the DV or AP cannot be used to study the stability of the ratio r_B.

5.3 Error sources and measurement procedure

The **error sources** on the magnetic field measurement can be classified as: intrinsic to the probe, i.e., the accuracy and stability already discussed, and factors external to the

probe which are described next:

- **Reproducibility of the probe position:** The magnetic field measurements are performed in steps of one centimeter along the z-axis. In radial direction, the measurements are taken at 0, 1.5 and 3.5 cm from the z-axis. The position of the probe in the $x - y$ plane is precisely determined by the tube holders (see section 5.3.1). However, since the active material of the Hall probe is located off-axis at the probe holder, rotations affect the radial position considerably. By repetition of the measurement, the error is averaged out and an estimation of the accuracy is possible. The accuracy on the positioning of the probe is estimated to be of about ± 1 mm along the z-axis and ± 1.5 mm along the radial direction. The results obtained give an estimation of the error due to misplacing of ± 0.2 G and ± 0.019 G at the DV and AP respectively.

- **Fluctuations of the correction coils current intensity:** due to the small contribution of them to the total field, fluctuations of the currents as large as 0.5 A would affect the main field at about 0.007 % at the DV and 0.005 % at the AP. This translates into an effect of 0.008 % on the magnetic field ratio which is negligible for our purpose.

- **Superconductor Hysteresis:** Superconductors of type II (like NbTi) behave as an "ideal" superconductor below a certain critical field H_{c1}. Above this field, vortices of material in normal state coexist surrounded by superconducting regions. This allow the magnetic field to penetrate the material. The magnetic flux lines penetrate the material in normal state creating a super-current loop around the vortex. Structural imperfections or chemical impurities prevent flux lines from moving freely through the crystal; this is called flux pinning [56]. In superconductors, hysteresis arises from flux pinning. This effect was studied by Scott *et. el.* [57] to characterize the reproducibility of the magnetic field after several energizing proceses in niobium-tin magnets. In their article, they describe the "Equilibrium" hysteresis effect as the one arisen from current redistributions in the superconductor in which the magnetic field distribution depends on the previous magnetic history. The "Dynamic" hysteresis effects have their origin in the time constant which characterizes the current redistribution from the stabilizing normal metal to the superconductor.

  Every time the *a*SPECT magnet is ramped up, internal current loops are formed around the normal metal cores created inside the superconducting materials. These current loops depend on the intensity of the field and the previous history. Therefore, the final magnetic field reached after several energizing process may differ by several Gauss. The proof that hysteresis effects are present in our superconducting coils comes from remanent currents observed in the *a*SPECT spectrometer at zero nominal current. The field produced by these currents can be seen in figure 5.34. The magnetic field profile shown was measured at two different days with no current applied to the coils. The remaining field is not homogeneous and has about 3 G in both the DV and AP region.

  The remaining currents after ramping down the coils can be avoided by warming up the coils over the superconducting temperature. The reproducibility of the field

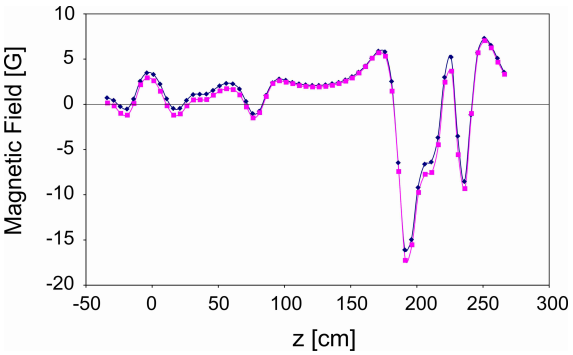

Figure 5.34: Magnetic field produced by the remanent currents due to the hysteresis present on the superconducting coils. Measurements taken on two consecutive days.

distribution can be anyway limited by slightly different current distributions created during the energizing process. This effect has to be characterized experimentally. According to the measurements discussed in section 5.4.4 and 6.4, this effect is negligible compared to the accuracy of our measurements.

- **Other factors:** The magnetization of materials in the spectrometer or near to it, or magnetized materials in the magnetic field measurement setup can affect the field or its measurement. Field measurements have shown this effects to be constant and negligible. The influence of the huge amount of steel of the ILL crane in the magnetic field was checked as well and no effects were observed. Finally, stray fields form other experiments, or other external factors, can influence the magnetic field. Reproducibility measurements have shown this effect to be below the accuracy of our Hall probe.

Considering these factors, the following **measurement procedure** has been established in order to minimize the different sources of error:

1. Select the appropriate scale for the region to measure (3 T scale for the DV and 0.6 T scale for the AP)
2. Zero the probe inside a zero field region (μ-metal box)
3. Measure the remaining offset after the zero inside the μ-metal box
4. Measure the field in steps of 1 cm at the regions of interest recording *field reading*, *temperature* and *time*
5. Measure the drift of the probe (offset) inside the μ-metal box
6. Apply the first and second correction described in section 5.2.2

5.3.1 Errors summary

As a consequence of the accuracy and stability studies described in sections 5.2.1 and 5.2.3, different error bars are applied for absolute measurements and relative measurements.

Absolute measurements

Measurements at DV cannot be considered relative with respect to the measurements at the AP (or vice versa) due to the different scale used in the two regions and due to the new probe zeroing necessary when changing the scale. Furthermore, the errors in each scale are different. As a result, it is necessary to use absolute values with the total accuracy of the measurement for the extraction of the magnetic field ratio r_{B}. Additionally, trajectory calculations also make use of absolute magnetic field values. Table 5.8 summarizes all relevant errors in absolute measurements of the magnetic field with the Hall-probe.

Total Error (absolute measurements)			
	DV [G]	AP [G]	Comment
Accuracy of the Hall probe	±4	±0.8	max (depends on ΔT)
Positioning	±0.2	±0.019	
Field drift	±0.07	±0.014	per day, first order correction

Table 5.8: Summary of the errors on the magnetic field measurements.

Relative measurements

Only relative variations of the field are necessary for the study of the relative field gradient within DV and AP regions. Thus, in principle may be enough to use only the instability of the measurement as error bar.

Measurements along the z-axis within DV and AP regions are fast and thus generally very stable. In such cases the instability of the measurement can be used as error bar. However, the time lapsed in between different scans along the z-axis is too large to consider that the Hall probe was not drifting. As a consequence, the error bars of the instability do not justify the different strengths of the field at different off-axis positions (see section 5.4.2). Then, the radial field gradient cannot be studied with instability error bars.

A possible solution for this problem will be discussed at the end of this chapter. Table 5.9 summarizes the errors in relative (and fast) measurements of the magnetic field with the Hall-probe.

Instability Error (only for longitudinal field gradient)			
	DV [G]	AP [G]	Comment
Stability of the Hall probe	±0.6	±0.15	max (depends on ΔT)
Positioning	±0.2	±0.019	
Field drift	±0.07	±0.014	per day, first order correction

Table 5.9: Contributions to the instability of the measurements.

5.4 Mapping of the *a*SPECT magnetic field

The *a*SPECT spectrometer consists of a set of fifteen axially symmetric coils. Nine of these coils are superconducting coils made of NbTi and connected in series, see figure 4.14. They create the variable magnetic field between the DV, the AP and the proton detector region. This is an important advantage since, then, the ratio r_B is independent of the exact value of the current. The trim coils c3 and c5 at the height of the DV region are powered independently to provide a small correction field of up to 1 % of the main field. These permit to modify the shape of the field at the DV. Coils c12 to c15 are external coils that were added a posteriori to modify the shape of the magnetic field at the AP and to change the ratio of the field r_B for systematic checks. The critical current density of the superconducting wires limits the maximum current applicable in the main coils to 100 A. The magnetic field at 100 A is $B_0 \approx 3\,\mathrm{T}$ in the DV, $B_A \approx 0.6\,\mathrm{T}$ in the AP and $B_{\mathrm{det}} \approx 6\,\mathrm{T}$ at the proton detector. Since the adiabatic condition is already fulfilled at currents above 50 A, see section 3.4, and higher currents increase the risk of a quench[6], a current intensity of 70 A was chosen as a good compromise.

The region of interest for the magnetic field measurements is the cold bore tube which houses the electrode system. To provide the necessary conditions for the Hall probe measurements, an inverted Dewar was built[7]. It consist of a non-magnetic aluminium tube covered on its outside by multiple layers of super-insulating foil. The dewar fits inside the bore tube of the spectrometer and is attached to the cryostat with two vacuum flanges which create a closed vacuum chamber. This chamber can be pumped to insulating vacuum conditions, $\approx 10^{-3}\,\mathrm{mbar}$, to permit the cool down of the cryostat to about 4 K. The size of the inner part of the dewar, which is now at room temperature, limits the maximum off-axis position where the magnetic field can be measured. The Hall probe is guided by an aluminium tube which centers the probe and permits measurements along the z-axis. The aluminium tube can be centered on the z-axis and at several distances and angles off-axis. An sketch of the cryostat can be found in appendix A.2 as well as more details of the coil system and the ramping up procedure of the magnetic field.

The knowledge acquired during the studies of the *a*SPECT magnetic field and the characterization of the field profile for the Munich beamtime of 2005 at the FRM-II reactor lead to several improvements:

- A second power supply was incorporated to the correction coils c3 and c5 in such a way that different currents in parallel or antiparallel direction can be applied. This offers a better optimization of the field gradient and allows different configurations which may be used for systematic checks.
- The two set of external correction coils c12/c13 and c14/c15 were added after the measurements of 2005. Coils c12 and c13 are used to correct the position of the

[6] A quench is an abnormal termination of magnet operation that occurs when the superconducting coil enters the resistive state. This can occur because the field inside the magnet is too large, the ramping rate of the field is too large or due to an anomalous increase of the temperature. If this happens, the region where the quench is originated is subject to rapid Joule heating. Thus, the temperature of the surrounding regions raises fast, also entering into the normal conducting state. Therefore, the entire magnet rapidly becomes resistive. The abrupt decrease of the high magnetic field to zero produces strong forces which can affect the position of the coils inside the cryostat.

[7] Note that the Hall-probe is not UHV compatible and its minimum working temperature is 0 °C.

local maximum of the magnetic field at the AP [44]. Coils c14 and c15, create an homogenous field which changes the ratio of the magnetic field, r_{B}, for systematic tests of the transmission function.

- Neighboring experiments at the ILL neutron guide can be distorted by the strong stray magnetic field produced by *a*SPECT. To avoid that, an anti-magnetic screen was built, which confines the field inside a restricted area and prevents interferences with other experiments, see figure 7.76. For details of the construction of the anti-magnetic screen the reader is referred to [38].

- An automatic readout of the magnetic probe was implemented for a proper longtime study of the stability of the probe and the *a*SPECT magnetic field (see previous sections: section 5.2.1 and 5.2.3). It also permits to take several measurements rapidly at each probe position.

5.4.1 Magnetic field profile

The magnetic field configuration used during the beamtime at ILL in 2008 is described and studied in the following. For simplicity, the field is given in units of the coil current. For example, 70 A coil current corresponds to a magnetic field of about $B_0 \approx 2.2\,\mathrm{T}$, $B_A \approx 0.4\,\mathrm{T}$, and $D_{\mathrm{Det}} \approx 4.3\,\mathrm{T}$ at the proton detector region. All coils except external correction coils, c12 to c15, and trim coils, c5 and c6, are connected in series, see figure 4.14. The field created by the coils connected in series is referred as "main field". The field settings where only the main field is energized will be referred as "main field configuration". The current applied at the other coils is explicitly given in each case. The field settings for most of the beamtime were $I = 70\,\mathrm{A}$ for the main field, $I(c3) = 35\,\mathrm{A}$ and $I(c5) = 15\,\mathrm{A}$ for the internal correction coils and $I(cc) = 25.5\,\mathrm{A}$[8] for the external correction coils (c12 and c13). These settings will be named "beamtime configuration". Also systematic checks were performed with different settings of the field gradients at the DV. Further, the ratio r_{B} was artificially modified by the external correction coils, c14 and c15. These coils were used in Helmholtz configuration in order to modify the main field at the AP on a level of 1 %, by applying a current of 50 A to them. Finally, also measurements at low field, 30 A for the main field coils, were performed for systematic checks of the adiabatic condition and the edge effect, see chapter 7.

The original configuration of the magnetic field inside the *a*SPECT spectrometer is described in [19]. Preliminary studies of the field are given in [44] and the measurements of the magnetic field for the Munich beamtime at the FRM-II are summarized in [50].

The result of the complete field mapping at the ILL beamtime in 2008-2009 together with the simulated field profiles are shown in figure 5.35. The figure shows the case of the 70 A main field without correction coils. Simulation and measurement agree properly except for the detector region, where the difference between measurement and simulation is due to the calibration of the Hall probe which is valid only up to 2.2 T.

[8] These values are the ones used in our magnetic field simulations and the ones selected in the power supplies. The values reached by the power supplies according to their display was: $I = 69.9\,\mathrm{A}$ for the main field, $I(c3) = 34.9\,\mathrm{A}$ and $I(c5) = 14.92\,\mathrm{A}$. The display of the power supply for the external correction coils c12 and c13 was drifting with time from $I(cc) = 25.5$ to $25.7\,\mathrm{A}$.

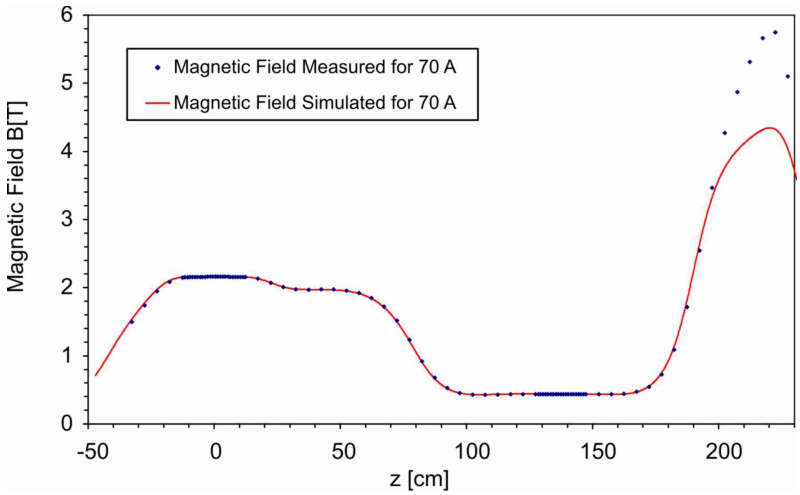

Figure 5.35: Simulated and measured magnetic field profiles along the complete spectrometer. Measurements on-axis with a main field of 70 A. The external correction coils and trim coils, c5 and c6, are off.

The slope of the measured field reproduces properly the simulated magnetic field profile. This ensures that motion of the particles inside the varying fields fulfils the adiabatic condition. It essentially follows the configuration as discussed in chapter 3 and section 5.1, already. This again permits us to use the transmission function as defined in section 3.3.

The flat magnetic field region at the lower ExB electrode position (between ~ 40 and ~ 60 cm) permits to apply large electrical potential differences without any significant influence on the adiabaticity [19]. The measurements showed a small local minimum present at this flat region. However, since no protons are emitted there, they cannot be trapped. A trap filled with ions from rest gas would be extremely shallow and the ExB drift would remove the ions quickly (see section 4.1.1). Consequently, no significant systematic effect is expected from there.

At the height of the proton detector ($z = 2.211(5)$ m) the field focuses the proton beam into the detector surface. At this region it is important to know the value of the magnetic field for trajectory calculations. From these calculations one can infer the angle and the energy of incidence, which are necessary for studies of the detector efficiency [46]. Also for the determination of the diameter of the protons flux tube (equation 4.1) the ratio of the magnetic field at the detector and at the DV region has to be known. Since the Hall probe is not calibrated for fields bigger than 2.2 T, it was necessary to perform the magnetic field measurements at low field and then to scale the result afterwards. With this procedure, the field at the position of the proton detector ($z = 2.211(5)$ m) is estimated to be 4.3606(12) T at 70 A main field.

The most critical field regions are the DV and AP. This regions are studied in detail below. The stability and reproducibility of the field and its ratio is also crucial and has to be determined with high accuracy.

5.4.2 Absolute magnetic field (stability vs. accuracy)

Figure 5.36 shows different sets of magnetic field measurements taken at different days in the DV region. The measurements correspond to "beamtime configuration" and magnet in persistent mode. Figure (a) shows the raw data before corrections. Figure (b) shows the same data after corrections (section 5.2.2) with instability error bars (table 5.9). Since time- and temperature-drift effects are corrected (figure (b)), the measurement sets are shifted to higher values and grouped to a smaller dispersion. The smoothness of the field profile is explained by the high stability of the probe during short time periods. Note that the instability error bars are larger than the field fluctuations within one measurement set. The different field strength observed between different measurement sets (up to $\sim 8\,\mathrm{G}$) is due to the large time difference between sets. For large periods of time the probe is not that stable anymore and therefore the absolute magnetic field values fluctuate within the total error bar: $\pm 4\,\mathrm{G}$ at the DV (table 5.8).

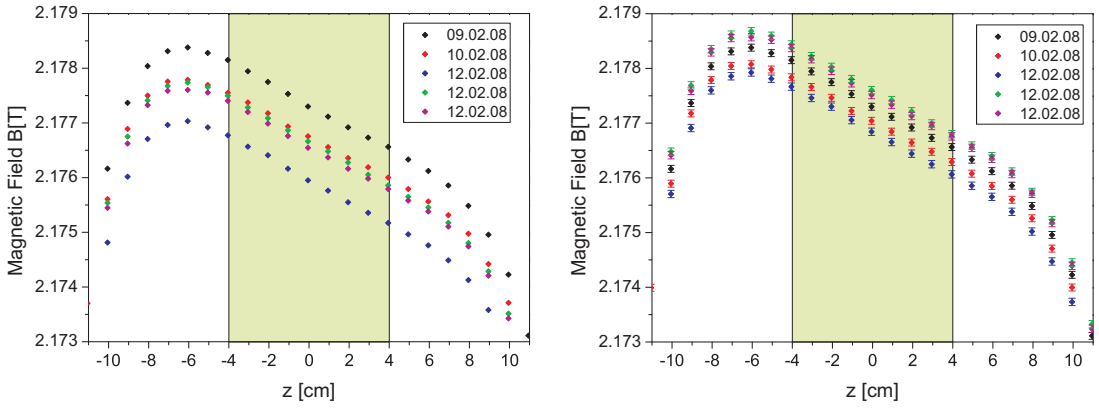

(a) Raw measurements (b) Corrected measurements

Figure 5.36: Magnetic field measurements carried out in "beamtime configuration" and persistent mode. (a) Raw data. (b) Corrected measurements (section 5.2.2) shown with instability error bars (section 5.3.1). Measurements taken on-axis, $r = 0\,\mathrm{cm}$.

The same measurement sets at the DV and AP, after corrections are shown in figure 5.37 with total error bars (table 5.8). We can observe that the spread between different sets is now justified by the size of the error bars.

Measurement sets along the complete length of the spectrometer (z-axis) take less than one hour. Although the Hall probe may remain stable during this period, the change of scale between the DV and AP regions makes the measurements at both positions independent and, thus, the total error bar has to be used. As an example, figure 5.39 shows that only the total error bar can explain the different ratios obtained from different measurement sets.

As a result, we can state that:

- The high stability of the Hall probe permits to "see" precise details of the magnetic field profiles, e.g. the smoothly variation of the field within the DV and the AP.
- The accuracy of the probe permits to compare measurement sets taken at different days.

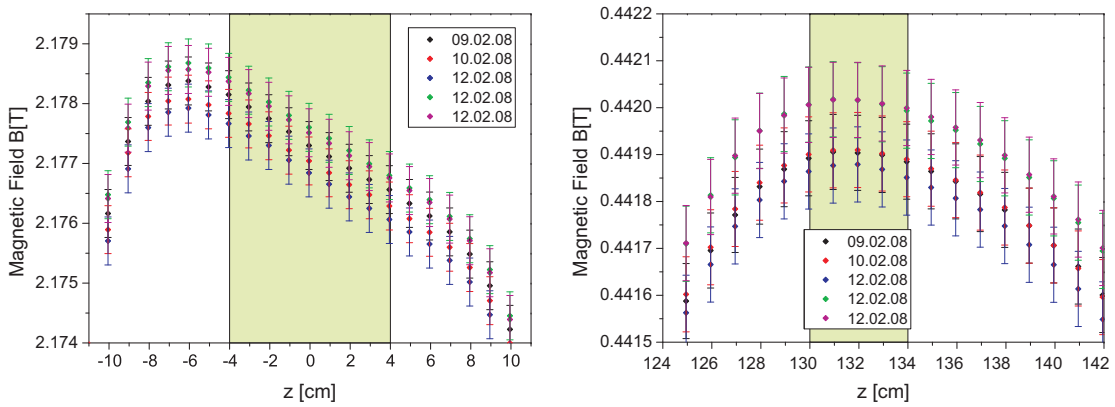

(a) DV (b) AP

Figure 5.37: Magnetic field measurements carried out in "beamtime configuration" and persistent mode. The measurements are corrected (section 5.3.1) and shown with total error bars (section 5.2.2). Measurements on-axis, $r = 0$.

- The fluctuations of the magnetic field strength observed between measurement sets is justified by the accuracy of the probe and is mostly due to the instability of the probe, as seen in section 5.2.3. This result is confirmed by the high accuracy measurements performed with our custom NMR-Magnetometer specially developed for the *a*SPECT experiment (see chapter 6). Measurements with the NMR-magnetometer allow us to set an upper limit to the fluctuations produced by external factors and possible field fluctuations.
- Measurements with different scales (even consecutive) have to be compared with total error bars.

5.4.3 Magnetic field distribution inside DV and AP regions

The mapping of the magnetic field within DV and AP regions has been performed by measuring along the z-axis direction at different radial positions. In the DV, the measurements were taken at $r = 0$ and $r = 1.5\,\text{cm}$. At the AP region the measurements were also taken at $r = 3.5\,\text{cm}$ due to the larger diameter of the flux tube (see section 5.1.2).

Measurements on- and off-axis were taken within three days. The measurements shown in figure 5.38 correspond to the 10.02.08 (DV) and to the 12.02.08 (AP). The measurements have been corrected fixing the origin of time as the beginning of the first measurement: 10.02.08 12:37. The measurements are shown with stability error bars only.

In both graphs the dispersion of the measurement sets is narrower than in figure 5.37. This is due to the shorter period of time between measurements and the smaller temperature variations. However, the dispersion of the measurements is higher than the error bars due to the instabilities. This is due to the time lapsed between measurements (which is much larger than the time spent during one scan within the DV or the AP region) and to the change of scale. Note that the slightly different field profile observed at 90° in the AP presents a higher offset, $7 \cdot 10^{-7}\,\text{T}$, than the others, $2 \cdot 10^{-6}\,\text{T}$, indicating a period of high instability of the probe.

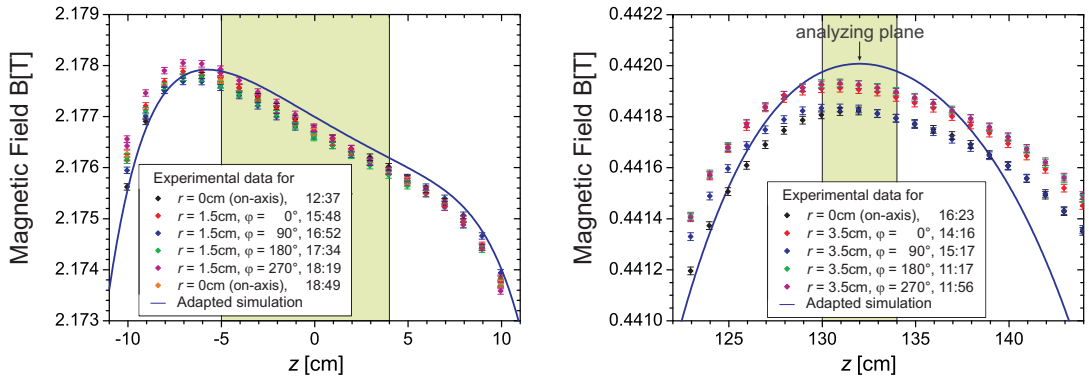

(a) (b)

Figure 5.38: Magnetic field measurements (on-axis and off-axis) at the DV and AP, (a) and (b) respectively. The measurements are corrected and drawn with error bars corresponding to the instability. The magnetic field simulation is shown in blue.

The **longitudinal field gradient** (along the z-axis) is calculated from every independent set of measurements and the result is averaged over all the sets. The systematic error, calculated using the error bar corresponding to the instability, is much better than required, see table 5.10.

The gradient of the field in the DV agrees precisely with our expectations according to the magnetic field simulations (see figure 5.38). Its maximum is well below the DV region to avoid trapping protons. In addition, the constant gradient in the DV gives a very linear field profile, which permits easy corrections in the calculation of a (section 5.2.2). The small magnetic field gradient amounts to approximately $(\Delta B_0/\Delta z)/B_0 = 1 \cdot 10^{-4}\,\mathrm{cm}^{-1}$ (table 5.10). This corresponds to a field gradient of $(B_{\max} - B_{\min})/B_0 = 8 \cdot 10^{-4}$ in the complete DV volume, out of our tolerance of $1 \cdot 10^{-4}$ (see section 5.1.5). Consequently, we have to weight the transmission function with the neutron beam intensity distribution $N_n(z)$ (section 5.1.5). The measured magnetic field gradient corresponds to a shift in a of (see figure 5.31):

$$\Delta a/a = -0.001(50)\% \tag{5.24}$$

Hence, the influence of the present magnetic field gradient on the neutrino-electron correlation coefficient a is negligible at the level of 0.1 %.

The maximum of the field in the AP region is centered at about $z = 131.5\,\mathrm{cm}$, close enough to the position where the most homogeneous region of the electric field is situated according to the latest electrostatic field calculations, $z = 132\,\mathrm{cm}$ [38]. The measurements off-axis at the AP show that the maximum of the field is at a slightly lower z position than for the measurements at $r = 0$. However, since both maxima are in the region of $\pm 2\,\mathrm{cm}$ around the maximum of the electric field, this shift does not introduce any serios problem. In any case, the different positions of the maxima are considered when calculating the ratio r_B weighting with the neutron beam profile.

Relative Field gradient		
Region	z-axis (longitudinal)	x/y-plane (radial)
DV	$7.4(3) \cdot 10^{-4}$	$4(3) \cdot 10^{-4}$
AP	$3(3) \cdot 10^{-5}$	$3(3) \cdot 10^{-4}$

Table 5.10: Relative magnetic field gradient within DV and AP regions.

The simulation of the magnetic field is performed by using the design characteristics of the cryostat provided by the company. However, the simulated field profile does not coincide at the AP region with the measured one [44]. To solve this, the simulation was modified by introducing different coil currents at the AP into the calculations in order to get a profile which describes the measured magnetic field configurations. This solution permits us to correct the position of the maximum of the field at the AP region but does not reproduce the field shape. A more precise profile is necessary for trajectory calculations [38]. A better result may be obtained by shifting the coils position in the simulation as well.

The **field gradient in radial direction** can not be resolved with the Hall probe since the stability of the probe does not permit to distinguish fluctuations in the reading from changes due to the gradient of the field along radial direction. For this reason, the maximum spread (measurements on-axis, figure 5.37) has to be considered for the estimation of the radial field gradient. The gradient is calculated for every z position (over r and φ) and then averaged for every z position, see table 5.10. The result is completely dominated by the instabilities of the probe and therefore the calculated field gradient is in the order of the error bar. This shows that the accuracy in measuring the radial homogeneity necessary for aSPECT ($\approx 10^{-4}$), is not feasible with our Hall probe if the measurements cannot be done fast enough to avoid instabilities. However, this results represent an upper limit for the homogeneity. An alternative measurement procedure which may allow us to perform accurate measurements of the radial field gradient is proposed at the end of this chapter.

We can study the effect of the radial magnetic field gradient given in table 5.10 on the ratio r_{B} as it was done in section 5.1.5. For that, we have to weight the transmission function with the neutron- and proton beam- profile ($N_n(x)$ and $N_p(x)$) at the DV and AP, respectively. As a rough approximation, we can consider that the proton beam intensity distribution at the AP has the shape of the neutron beam profile at the DV, projected by the magnetic field lines.

The limited stability of the Hall probe does not permit to know the magnetic field profile in the radial direction. Thus, we have to make a reasonable guess. We consider the radial magnetic field gradient has the profile obtained with the magnetic field simulation (figure C.105) and we scale it in order to obtain the field gradients of table 5.10.

Now, we can estimate the shift of B_0^{W} when weighting with the measured neutron/proton beam profiles and when weighting with a flat neutron/proton beam profiles:
$\left(\Delta B_0^{\mathrm{W}}/B_0^{\mathrm{W}}\right)_{\mathrm{radial}} = 5 \cdot 10^{-6}$ and $\left(\Delta B_A^{\mathrm{W}}/B_A^{\mathrm{W}}\right)_{\mathrm{radial}} = 4 \cdot 10^{-6}$.

This result indicates that a rough knowledge of the neutron and proton beams within DV and AP regions is sufficient for the weighting and thus the dominant error is the accuracy in the magnetic field measurements.

Since an accurate mapping of the radial magnetic field distribution is not possible with the accuracy of the Hall probe, we cannot calculate the effect of the radial magnetic field gradient on a as we have done for the longitudinal magnetic field gradient in the DV (figure 5.27). However, we can make a rough approximation. We consider the radial magnetic field gradient of table 5.10 as an error for the magnetic field value. Then, by using error propagation we find an estimation of the error introduced on r_B due to this assumption: $\delta r_B / r_B = 3 \cdot 10^{-4}$. This error, according to figure 5.27, implies a $\delta a/a = 0.3\,\%$. This is however a very rough approximation. For precise a precise determination of the ratio, trajectory calculations are necessary to obtain the proton beam profile at the AP. Furthermore, the actual field distribution within the complete DV and AP have to be measured with higher accuracy. However, this rough calculation provides an stimation of the accuracy reachable with the present magnetic field measurements.

5.4.4 Magnetic field ratio

Due to the small field gradient in the AP ($< 10^{-4}$ in the z-axis and $\sim 1 \cdot 10^{-4}$ in the radial direction according to the magnetic field simulations) and to the limitations to compare measurement sets off-axis, it is enough to evaluate the ratio of the magnetic field by weighting only in the DV. The result is shown in figure 5.39.

The measurements off-axis give slightly higher values due to the lower z position of the magnetic field maximum. However, the error bars cover this difference.

The error used for this calculation has been the total error bar since the time difference and the change of scale makes impossible to use only the error bar corresponding to instabilities. As expected, the instability error bar cannot explain the shift between the calculated ratios. Note that the error on the ratio r_B due to a possible misalignment of the neutron beam with respect the center of the DV (± 1 mm, see section 5.1.5) has been used but it is negligible with respect to the error in the magnetic field measurement.

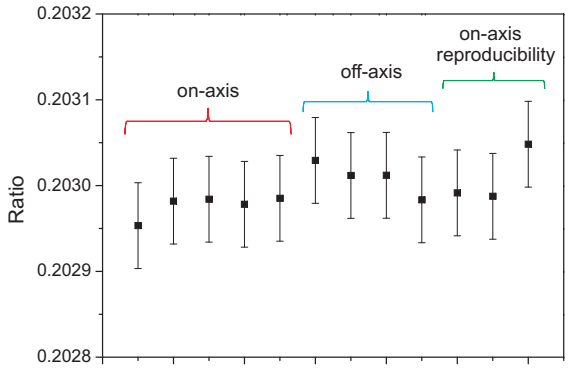

Figure 5.39: Stability and reproducibility of the magnetic field ratio r_B. The ratio has been calculated from every scan along the $z-axis$ with total error bar. The last three values correspond to measurements on-axis after ramping up the field for reproducibility tests.

Reproducibility of the field

In addition to the accuracy and stability of the Hall probe (sections 5.2.1 and 5.2.3) to measure the magnetic field and the external factors discussed in section 5.3, also the reproducibility of the field itself has to be considered. Several factors influence the field reached after the ramping up procedure of the magnet. One of the biggest is due to the stabilization of the current once the power supply reaches its selected value: it takes about six hours to reach a considerably field stability. The change of the field during that time is still about 30 G at the DV. Other factors influencing the reproducibility of the field have been discussed in section 5.3. A detailed study of the reproducibility of the *a*SPECT magnetic field can be found in appendix B.1.

Measurements after several ramping up procedures were performed in order to estimate the reproducibility of the field in situ. The maximum difference observed in the absolute value of the magnetic field after different ramping up procedures was 11 G at the DV. The fluctuations between measurements taken in different days, figure 5.37, are also in the same order, ~ 8 G. Therefore, this difference of 11 G can be explained by the probe uncertainty plus a slightly different field.

The magnetic field profile is reproducible after each ramping up procedure and the ratios calculated from all the measurements give approximately the same value, see figure 5.39. In conclusion, the ratio is reproducible after every ramping up and measurable with a relative accuracy of $3 \cdot 10^{-4}$. The final value given for the ratio r_{B}, in table 5.11, is the average of all the ratios from figure 5.39. The result calculated considering the error due to the lack of calibration indicates the accuracy reached with the present measurements. The result obtained without considering the lack of calibration shows the maximum accuracy reachable with the Hall probe.

Calibration error	Ratio	$\Delta r_{\mathrm{B}}/r_{\mathrm{B}}$	Relative error on a $\Delta a/a$ [%]
No	0.20300(5)	$\pm 3 \cdot 10^{-4}$	± 0.3
Yes	0.2030(2)	$\pm 1.1 \cdot 10^{-3}$	± 0.9

Table 5.11: Ratio of the magnetic field r_{B} and relative error introduced on a.

5.4.5 Magnetic Field configurations for systematic tests on a

The *a*SPECT magnetic field has been designed in a way that permits to study different systematics related to the transmission function and to the working principle of the spectrometer. These tests are necessary in order to calibrate our spectrometer for an accurate measurement of the correlation coefficient a (see section 3.4). Two fundamental systematic tests with different magnetic field configurations are briefly discussed next. A detailed analysis of the data can be found in appendix B.2.

Low field configuration

A field configuration with low magnetic field values permits to study important systematics of the *a*SPECT spectrometer. On the one hand, a low magnetic field increases the uncertainty of a due to the fact that the adiabatic approximation does not hold anymore (see section 3.4.2). On the other hand, although the ratio of the magnetic field B_{det}/B_0 is conserved (see chapter 5), the lower B field produces an increase of the gyration radius (equation 4.4). This translates into a larger effective flux tube diameter and, thus, in an increase of the impact of the edge effect on a (section 3.4.4). Furthermore, the larger diameter of the flux tube may increase the influence of other systematic effects like the charging of the collimation system (see section 4.2). The study of proton spectra measurements with low field configuration brings helpful information to understand and calculate the influence of these systematics on a (see section 7.2.6).

For these tests, the standard magnetic field configuration ($I(\mathrm{main})$=70 A, $I(c3)$ = 35 A, $I(c5)$ = 15 A, $I(cc)$ = 25.5 A) was scaled down to $I(\mathrm{main})$=30 A, $I(c3)$ = 15 A, $I(c5)$ = 6.4 A, $I(cc)$ = 11 A. The magnetic field profile measured with low field configuration can be found in appendix B.2. The ratio of the magnetic field obtained with this configuration is shown in table 5.12.

Increased magnetic field ratio (r_{B})

A different magnetic field ratio r_{B} permits to test the influence on the coefficient a of a possible error on the determination of r_{B}. For this test, the external Helmholtz coils c14 and c15 were energized with a current intensity of 50 A[9] while the magnet was set in beamtime configuration. This produces an increase of the magnetic field at the AP region of about 1 %. The ratio of the field was increased by 1.01 %. The ratio of the magnetic field obtained with this configuration is presented in table 5.12.

	Ratio (r_{B})	$\delta r_{\mathrm{B}}/r_{\mathrm{B}}$
Low field configuration	0.20296(5)	$3 \cdot 10^{-4}$
Increased ratio r_{B}	0.20515(5)	$3 \cdot 10^{-4}$

Table 5.12: Ratio of the magnetic field r_{B} for two magnetic field configurations intended for systematics tests on the correlation coefficient a. The ratios are calculated without including the error due to the lack of calibration.

Outlook

In this chapter, it has been demonstrated that the magnetic field of the *a*SPECT spectrometer fulfills the design requirements described in section 5.1. Furthermore, it has been demonstrated that the ratio of the magnetic field r_{B} is stable and reproducible at least up to the level of accuracy reachable with our Hall probe: $\Delta r_{\mathrm{B}}/r_{\mathrm{B}} = \pm 3 \cdot 10^{-4}$ (table 5.11).

The effect of weighting the magnetic field mapping with the neutron beam intensity distribution has been studied. It introduces a small correction on a which can be

[9] Coils c14 and c15 are referred to as HC

determined with high accuracy (see table 5.13) and hence can be considered negligible. Unfortunately, the magnetic field gradient in radial direction could not be determined with sufficient accuracy for a study of its effect on a. However, the error contribution due to the radial magnetic field gradient has been roughly estimated (table 5.13).

The ratio of the magnetic field has been measured with an accuracy of $\delta r_{\mathrm{B}} = \pm 2 \cdot 10^{-4}$ ($r_{\mathrm{B}} = 0.2030(2)$, table 5.11) which introduces an error on the determination of the coefficient a of only $\delta a/a = 0.9\,\%$ (including the error due to the lack of calibration). Furthermore, it has been proved that with a proper calibration of the Hall probe, the magnetic field ratio can be measured with an accuracy of $\delta a/a = 0.3\,\%$. These errors are sufficiently small for a determination of the correlation coefficient a with a total accuracy better than $\delta a/a = 5\,\%$, objective of the aSPECT beamtime at ILL in 2008 (chapter 7).

A summary of the errors and corrections introduced in a due to the uncertainties on the magnetic field is shown in table 5.13. Note that for a precise study it is necessary to measure accurately the magnetic field profile within the complete DV and AP regions and to perform trajectory calculations in order to estimate the proton beam intensity distribution within the AP region. Then, the calculation shown in figure 5.31 can be generalized for a 3D magnetic field profile.

For a precise measurement of the correlation coefficient a, the two fundamental limitations encountered during the analysis of the data have to be overcome:

- The measurement of the radial field gradient could be measured with an accuracy of only $\pm 3 \cdot 10^{-4}$, which is insufficient for our aimed accuracy of a.
- The relative accuracy reachable (i.e. without calibration error) in the measurement of the magnetic field ratio, $\Delta r_{\mathrm{B}}/r_{\mathrm{B}} = \pm 3 \cdot 10^{-4}$, is slightly higher than required $\Delta r_{\mathrm{B}}/r_{\mathrm{B}} \approx \pm 1 \cdot 10^{-4}$.

Both limitations mainly come from the Hall probe instabilities and, in the case of the ratio r_{B}, from the change of scale too. Both circumstances forces us to use absolute measurements instead of relative.

From the measurements studied in this chapter, we are able to propose solutions to the limitations.

- The radial field gradient can be measured with higher accuracy by fastening up the measurement procedure in order to reduce the effect of the probe instabilities. This may be done by means of a two steps measurement procedure. First, a measurement set along the z axis at one off-axis position is performed. Afterwards, measurements off-axis at the four azimuthal angles at a fixed z position are performed (this is equivalent to measure a transversal cut of the flux tube) and repeated for all z positions. These "transversal cuts" are then normalized with the field profile off-axis measured in the first step. Then, a complete 3D map with only instability error bars is obtained.
- The NMR-magnetometer developed during this thesis can be used for absolute magnetic field measurements with higher accuracy than the Hall probe, see chapter 6.

An adaption of this probe for B-field mappings is trivial and would permit to determine the ratio, r_B, with the necessary accuracy. The NMR-magnetometer could also be used jointly with Hall probe mappings. In this case, the values measured with the NMR-magnetometer would be used to normalize the scans performed with the Hall probe.

The development of the NMR-magnetometer and improved studies of the magnetic field reproducibility and stability are described in chapter 6. The NMR-magnetometer described there is designed to be implemented during an aSPECT beam time for a constant monitor of the magnetic field ratio.

Effect on the angular correlation coefficient a	Relative correction [%]	Relative error [%]	Relative error (MC) [%]
longitudinal B field gradient	+0.001		0.05
radial B field gradient		0.3	0.1
B field ratio		0.3	0.1
B field ratio (with calibration error)		0.9	0.2

Table 5.13: Corrections and uncertainties on the antineutrino-electron angular correlation coefficient a due to the magnetic field measurements.

Chapter 6

The *a*SPECT on-line NMR-Magnetometer

In this chapter the Nuclear Magnetic Resonance (NMR) magnetometer designed for the on-line monitoring of the *a*SPECT magnetic field is described. Magnetic field measurements via NMR presents several advantages respect the Hall probe measurements presented in chapter 5. On the one hand, it provides a much higher accuracy than the Hall probes. On the other hand, it can work even in the low pressure and temperature range existing inside our spectrometer, what permits to monitor the magnetic field during measurements of the decay proton spectra.

The fundamentals of this technique as well as the results obtained measuring the *a*SPECT magnetic field are discussed in detail in this chapter. Latest improvements and conclusions are presented too. The basics of the NMR are briefly discussed next, for a more detailed description the reader is referred to the following monographs [58] [59] [60] [61].

6.1 Theory of the Nuclear Magnetic Resonance

Nuclear Magnetic Resonance (NMR) is a phenomenon that occurs when isotopes which are composed of nucleons such that the overall nuclear spin $I \neq 0$ are brought into a static magnetic field. These isotopes have an associated nuclear magnetic moment, $\overrightarrow{\mu}$, which is proportional to the spin angular momentum $\overrightarrow{I}$,

$$\overrightarrow{\mu} = \gamma \hbar \overrightarrow{I} \tag{6.1}$$

where γ is the gyromagnetic ratio and $\hbar = h/2\pi$ the Dirac's constant. In the presence of an external magnetic field, the magnetic dipole energy (in the classical frame) can be written as:

$$E_m = -\overrightarrow{\mu}\overrightarrow{B_0} \tag{6.2}$$

This formula indicates that the magnetic dipole energy depends on the relative direction of the vectors $\overrightarrow{B_0}$ and $\overrightarrow{\mu}$. The negative sign indicates that the energy is minimum if

the magnetic moment is parallel to the field. In the framework of quantum physics, the Zeeman Hamiltonian, i.e., the magnetic dipole energy is written:

$$E_m = \mathcal{H}_Z = -\gamma\hbar \overrightarrow{I}\,\overrightarrow{B_0} \tag{6.3}$$

The gyromagnetic ratio γ can be expressed as $\gamma = g\mu_N/\hbar$, where g is the so called g-factor and μ_N is the nuclear magneton. The sign of the g factor determines the orientation of the spin that produces minimum magnetic dipole energy. For example, the minimum magnetic dipole energy of particles or nuclei with $g > 0$ corresponds to an antiparallel alignment of the spin $\vec{I}$ and the magnetic field $\vec{B_0}$, and the maximum magnetic dipole energy to an antiparallel alignment.

If the direction of the magnetic field is chosen along the z-axis in the laboratory frame, $\vec{B_0} = (0, 0, B_0)$, the different energy levels are:

$$E_m = -m\gamma\hbar B_0 \tag{6.4}$$

where the magnetic quantum number m can take the values $m = -I, -I+1, ..., I-1, I$, hereby defining the number of energy levels.

As a result a nucleus with spin quantum number I has $2I + 1$ discrete energy levels if the degeneracy is lost by $\overrightarrow{B_0}$. In this work only nuclei with spin $I = 1/2$ are considered, therefore only two such energy levels or spin projections exists (*up* and *down*). In this case, the distance between these two energy levels is given by

$$\Delta E = E_{1/2} - E_{-1/2} = \gamma\hbar B_0 \tag{6.5}$$

which corresponds to a frequency

$$\omega_0 = \frac{\Delta E}{\hbar} = \gamma B_0 \tag{6.6}$$

This frequency ω_0 is called the Larmor frequency.

In a more general treatment, the Hamiltonian of such a quantum mechanical system can be written as

$$\mathcal{H} = \mathcal{H}_Z + \mathcal{H}_{rf} + \mathcal{H}_{DD} \tag{6.7}$$

where $\mathcal{H}_Z$ refers to the Zeeman splitting due to the magnetic field and $\mathcal{H}_{rf}$ refers to an external radio frequency field used to manipulate the spin ensemble. These two first terms correspond to external spin interactions. The Hamiltonian $\mathcal{H}_{DD}$ refers to the direct dipole-dipole coupling interaction due to magnetic interactions of nuclear spins with each other. This last term correspond to internal spin interactions. For the case of NMR experiments with ^{3}He and ^1H in our particular experimental conditions this term can be safely neglected.

6.1.1 External spin interactions

If a short and strong, time-dependent magnetic field, $\overrightarrow{B_{rf}}$, is applied in the x-direction by means of a r.f. coil with a phase ϕ and frequency ω_1, the field will be given by

$$\overrightarrow{B_{rf}} = B_{rf}\cos(\omega_1 t + \phi)\overrightarrow{e_x} \tag{6.8}$$

where B_{rf} is the amplitude. It is convenient to visualize this oscillating field as two counter rotating vectors representing the resonant and nonresonant components. The resonant component rotates with the Larmor precession and the non-resonant component in the opposite direction:

$$\overrightarrow{B_{rf}^{res}} = \frac{B_{rf}}{2}[\cos(\omega_1 t + \phi)\overrightarrow{e_x} + \sin(\omega_1 t + \phi)\overrightarrow{e_y}] \tag{6.9}$$

$$\overrightarrow{B_{rf}^{non-res}} = \frac{B_{rf}}{2}[\cos(\omega_1 t + \phi)\overrightarrow{e_x} - \sin(\omega_1 t + \phi)\overrightarrow{e_y}] \tag{6.10}$$

The non-resonant component has almost no influence on the spins and may be neglected. Then, the corresponding Hamiltonian for the r.f. excitation is:

$$\mathcal{H}_{rf} \approx -\gamma\hbar B_1[\cos(\omega_1 t + \phi)\overrightarrow{I_x} - \sin(\omega_1 t + \phi)\overrightarrow{I_y}] \tag{6.11}$$

where $B_1 = \frac{1}{2}B_{rf}$. From now on, we will concentrate only on the resonant component of the r.f. pulse that will be referred to as $\overrightarrow{B_1} \equiv \overrightarrow{B_{rf}^{res}}$.

6.1.2 Semi-classical picture

In the semi-classical picture, the spin states are not examined individually on a microscopic quantum mechanical basis, but the time evolution of the macroscopic sum of all the magnetic moments, the so-called magnetization vector $\overrightarrow{M}$, is described. Within this picture, simple experiments are easier to understand and to visualize.

When an ensemble of N spins with $I = 1/2$ (like ^{3}He or ^{1}H) is placed inside a magnetic field, the spins will align parallel or anti-parallel to the field, see figure 6.40, on the two energy levels described by equation 6.4. The population of the two levels is very similar, because the energy difference is small compared to the thermal energy of the system at ambient temperature and normal magnetic fields. The ratio of the population in thermal equilibrium at a certain temperature T is then given by the Boltzmann distribution

$$\frac{N_-}{N_+} = e^{-\Delta E/k_B T} = e^{-\gamma\hbar B_0/k_B T} \tag{6.12}$$

with k_B the Boltzmann constant. The polarization P is then defined as the excess population of the two energy levels:

$$P = \frac{N_+ - N_-}{N_+ + N_-} \tag{6.13}$$

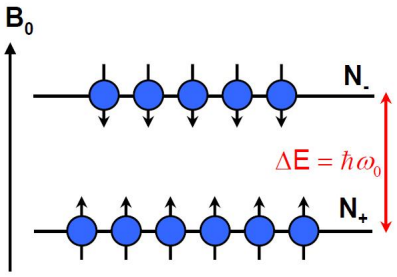

Figure 6.40: Energy levels population in a spin $I = 1/2$ system inside a magnetic field B_0.

Using equation 6.12 and the high temperature approximation $\gamma\hbar B_0 \ll k_B T$, the thermal polarization of the ensemble can be written as

$$P = tanh\left(\frac{\gamma\hbar B_0}{2k_B T}\right) \approx \frac{\gamma\hbar B_0}{2k_B T} \tag{6.14}$$

As a result, the sum of all nuclear magnetic moments $\vec{\mu_i}$ gives rise to a total macroscopic equilibrium magnetization $\overrightarrow{M_0}$ along the direction of the magnetic field $\overrightarrow{B_0}$, i.e., a *longitudinal* magnetic moment $\overrightarrow{M_0} = (0, 0, M_0)$

$$\overrightarrow{M_0} = \sum \overrightarrow{\mu_i} = \frac{N\gamma\hbar P\overrightarrow{e_z}}{2} \tag{6.15}$$

where $N = N_+ + N_-$ is the total number of spins.

In a classical picture the total magnetic moment experiments a torque $\tau = \overrightarrow{M_0} \times \overrightarrow{B_0}$ which makes the total magnetic moment to precess around the $\overrightarrow{B_0}$ field. A quantum description of the spin precession shows that the frequency of precession is the Larmor frequency ω_0 given in equation 6.6.

The longitudinal magnetic moment is almost undetectable. NMR spectroscopy takes thus a different approach. Instead of measuring the nuclear spin magnetization along the field, the magnetization perpendicular to the field is measured. This is achieved by an external r.f. magnetic field $\overrightarrow{B_1}$ (section 6.1.1). When the spins are excited by a r.f. magnetic field with a frequency close to the Larmor frequency, the number of spins in the respective energy levels change according to the Hamiltonian $\mathcal{H}_{rf}$. The evolution of the magnetization was described first by Felix Bloch by the following equation of motion

$$\frac{d\overrightarrow{M}}{dt} = \gamma\overrightarrow{M(t)} \times \overrightarrow{B(t)} - R \cdot [\overrightarrow{M(t)} - \overrightarrow{M_0}] \tag{6.16}$$

where $\overrightarrow{B}$ consist of both, the static magnetic field $\overrightarrow{B_0}$ and the oscillating r.f. field $\overrightarrow{B_1}$, which is applied in a direction perpendicular to the holding field $\vec{B_0}$

$$\overrightarrow{B(t)} = \begin{pmatrix} B_1 \cos(\omega t) \\ B_1 \sin(\omega t) \\ B_0 \end{pmatrix} \tag{6.17}$$

and R denotes the relaxation matrix

$$R = \begin{pmatrix} 1/T_2 & 0 & 0 \\ 0 & 1/T_2 & 0 \\ 0 & 0 & 1/T_1 \end{pmatrix} \tag{6.18}$$

The components of R are called relaxation rates and are shortly described in the following: T_1 is the so-called *longitudinal relaxation time* and specifies the time for the magnetization to return into its thermal equilibrium state along the direction of the static magnetic field after the r.f. excitation. T_2 is called *transverse relaxation time* and describes the loss of phase coherence of the spin ensemble in the transverse plane due to spin-spin interactions and field inhomogeneity while rotating around the axis of the main field with the frequency ω_0.

In a coordinate system rotating with the frequency of the r.f. field ω around the z-axis the equations simplifies, as the time dependence in $\overrightarrow{B}$ vanishes for an effective field $\overrightarrow{B_{eff}}$ in the rotating frame. The effective field is calculated to be

$$\overrightarrow{B_{eff}} = \overrightarrow{B_o} + \frac{\omega}{\gamma} + \overrightarrow{B_1} = \frac{\omega_0 - \omega}{\gamma}\overrightarrow{e_z} + \overrightarrow{B_1} \tag{6.19}$$

For the resonance condition $\omega = \omega_0$, $\overrightarrow{M_0}$ rotates only around $\overrightarrow{B_1}$ (in the rotating coordinate system). In case of a finite pulse, the duration τ_p of the r.f. pulse determines the resulting angle α between $\overrightarrow{M_0}$ and $\overrightarrow{B_0}$. It is given by

$$\alpha = \omega \cdot t_p \tag{6.20}$$

where α is referred to as the nutation or flip angle and the nutation frequency ω depends on the amplitude of the r.f. pulse

$$\omega = \gamma B_1 = \frac{1}{2}\gamma B_{rf} \tag{6.21}$$

6.1.3 Relaxation times

The return to the thermal equilibrium of the net magnetization after a perturbation is dominated basically by two characteristics processes: the first process is called Longitudinal Relaxation (or Spin-Lattice Relaxation) while the second one is called Transversal Relaxation (or Spin-Spin relaxation).

Longitudinal Relaxation (Spin-Lattice Relaxation)

In the absence of a an external magnetic field, the spin polarizations are uniformly, pointing in all possible directions. The total magnetic moment is close to zero. If a magnetic field is turned on, all protons spins start to precess at the Larmor frequency ω_0. The energy exchange with the surroundings leads eventually to a stable anisotropic distribution of the sin polarizations, called thermal polarization (equation 6.12). The time

constant of this process, T_1, is known as *longitudinal relaxation time constant* or *spin-lattice relaxation time constant*. The use of the term "lattice" derives from the early days of the NMR when the theoretical effort concentrated in solids and the thermal equilibrium was explained in terms of the interactions between the nuclear spins and the crystal lattice.

Another example of a process relaxing with the time constant T_1 is after the application of a $\pi/2$ pulse. The $\pi/2$ pulse perturbs the spins from their thermal equilibrium causing the net magnetization $\overrightarrow{M_0}$ to rotate into the $x-y$ plane, while the longitudinal component M_z becomes zero. After the application of the pulse, the spins tend to return back to equilibrium by exchanging energy with their surrounding neighborhood. Again, the longitudinal relaxation time constant T_1 describes the restoration of M_z back to its initial value M_0 after the application of the $\pi/2$ pulse. From Bloch equation 6.16, the relaxation rate of M_z can be described by

$$\frac{dM_z}{dt} = -\frac{M_z(t) - M_0}{T_1} \tag{6.22}$$

with the solution

$$M_z(t) = M_0(1 - e^{-t/T_1}) \tag{6.23}$$

In the case of laser polarized gases (see section 6.1.4), T_1 is also the characteristic time of the ensemble to recover thermal equilibrium. However, as for optical pumped gas the magnetization exceeds the thermal one, T_1 does not describe a magnetization recovery, but a loss of hyperpolarization back to thermal equilibrium. In other words, it can be described as a polarization decay to the Boltzmann magnetization, M_0:

$$M_z(t) = M_0 e^{-t/T_1} \tag{6.24}$$

This work is mainly concerned about gases, therefore, we will focus in the discussion of the longitudinal relaxation mechanisms in gases. The longitudinal relaxation time T_1 for gases depends on several relaxation mechanisms, see [62], in this thesis we will comment only the most important ones in our operating conditions:

$$\frac{1}{T_1} \approx \frac{1}{T_1^{Grad}} + \frac{1}{T_1^{Wall}} \tag{6.25}$$

- Gradient relaxation (T_1^{Grad}): In the presence of a magnetic field gradient, a moving atom will experience different magnetic field strengths. If the field fluctuations seen by the atoms in their rest system are close to the transition frequency $\omega = |\Delta E|/\hbar$ between the Zeemann levels of equation 6.4, then spin flips can be induced, resulting in a destruction of polarization. Early papers of groups working on ^3He, [63] and [64], derived a remarkably simple formula for the field gradient induced spin-relaxation rate, T_1^{Grad}. Their result is however only valid for sufficiently large pressures and magnetic field values so that the precession time is short compared to the diffusion time. Another important paper from the 80th written by Cates et al. [65] provides

more general expressions for the longitudinal and transversal spin-relaxation times due to field inhomogeneities over a wider pressure range. For our experimental conditions:

$$\frac{1}{T_1} \approx D\frac{|\overrightarrow{\nabla} B_x|^2 + |\overrightarrow{\nabla} B_y|^2}{B_0^2} \longleftarrow \text{ for } p \text{ so that } \omega_0 R^2/D \gg 1 \tag{6.26}$$

where R is the radius of the spherical cell, D is the diffusion coefficient which will be discussed in section 6.1.5.1, γ is the gyromagnetic ratio and $|\overrightarrow{\nabla} B_x|^2 + |\overrightarrow{\nabla} B_y|^2$ is the transversal field gradient of the holding field B_0. The limit of high pressure is fixed by Cates with the condition

$$\omega_0 R^2/D \gg 1 \tag{6.27}$$

This result shows that for high pressures the relaxation rate is proportional to the diffusion coefficient or equivalently inversely proportional to the gas pressure, whereas at low pressure the results shows the inverse dependence with D and p

- Wall Relaxation (T_1^{Wall}): The microscopic surface relaxation mechanisms of gases are complex. The general formula for $1/T_1^{Wall}$ rate, however, can be written:

$$\frac{1}{T_1^{Wall}} = \frac{1}{\eta}\frac{S}{V} \tag{6.28}$$

where S/V is the surface-to-volume ratio of the gas container and η is the relaxivity, a coefficient which dependes on the surface properties, the temperature, and the magnetic field strength.

Spin-Spin Relaxation and Free Induction Decay (FID)

Directly after a $\pi/2$ pulse, the spins flipped in the transverse $x-y$ plane have phase coherence but soon they move out of phase. This loss of phase coherence is called transverse relaxation (or pin-spin relaxation) and it is characterized by the relaxation time T_2. This process is described by the equation:

$$\frac{dM_{xy}}{dt} = -\frac{M_{xy}}{T_2} \tag{6.29}$$

resulting in

$$M_{xy} = M_{xy}(0)e^{-t/T_2} \tag{6.30}$$

We can distinguish two main contributions to the relaxation time:

$$\frac{1}{T_2^*} = \frac{1}{T_2} + \frac{1}{T_2'} \tag{6.31}$$

- Coherence decay time constant (T_2) due to homogeneous decay: The microscopic magnetic fields oscillate slightly due to several proceses like spin-spin interaction, wall interactions or extensive diffusion in homogeneous fields. Due to these oscillations, the precessing spins gradually get out of phase with each other producing a decrease of the net transversal magnetization. This decay process cannot be reversed by 180° pulses.

- Inhomogeneous broadening (T_2'): In an inhomogeneous magnetic field nuclear spins precess at different Larmor frequencies. Then, the spins precessing at different Larmor frequencies get out of phase producing a decrease of the net transversal magnetization. The inhomogeneous broadening is a process which can be reversed by a 180° pulse[1] (see figure 6.41).

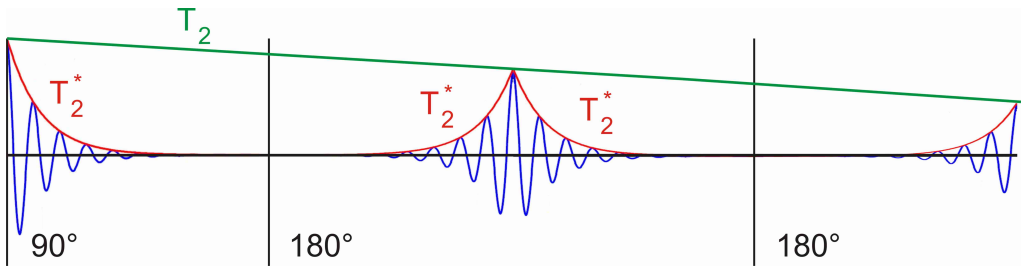

Figure 6.41: Measurement of T_2 and T_2^* by means of a pulse sequence called echo: 90° pulse followed by 180° pulses.

In the static approximation, the atoms are considered static during the length of the experiment. In this circumstance, all terms are negligible in comparison to the inhomogeneous broadening and one can approximate:

$$\frac{1}{T_2^*} = \gamma \Delta B = \Delta\omega \tag{6.32}$$

In solids, internuclear dipole-dipole interactions are large and they cause very strong relaxation resulting in a short T_2, while in liquids and gases these interactions are usually averaged out due to the Brownian movement of the particles. In gases, dipole dipole interaction is negligible. The most important contribution is due to inhomogeneous

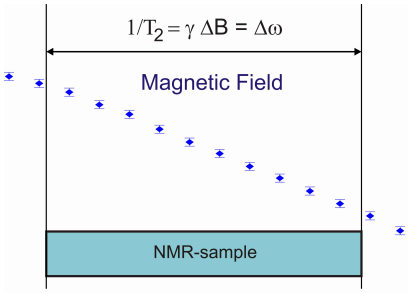

Figure 6.42: Definition of T_2^* in the particular case of the static approximation.

[1] This procedure is called spin echo. The concept works as follows: After the 90° flip pulse, the magnetic moment precess on the $x-y$ plane around the z axes. For instance, due to field inhomogeneities, some protons in lower fields slow down while some speed up due to higher field strength and get ahead of the others. Then, at a time τ a 180° pulse is applied gyrating the net magnetic moment by 180°. Now the slower protons lead ahead of the main moment and the fast ones trail behind. After 2τ a complete refocusing has occurred.

broadening. Then, the decay of the FID-signal can be approximated to an exponentially decaying signal with relaxation time T_2^*, see figure 6.43.

$$M_{xy}(t) = M_0 e^{-t/T_2^*} \cos(\omega_0 t) \tag{6.33}$$

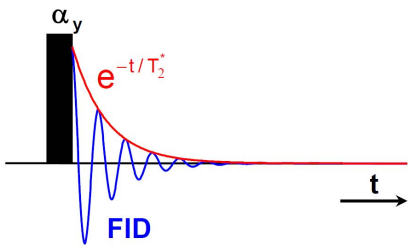

Figure 6.43: NMR pulse sequence to detect a Free Induction Decay (FID). The signal is detected after a r.f. pulse with flip angle α along the y-axis and is decaying with an exponential function.

However, special care has to be taken for the effect of rapid diffusion (e.g. in gases) in inhomogeneous fields on T_2'. Depending on the ratio of the diffusive length, relative to the size of the sample. If big enough the process can average out such inhomogeneities, causing the so called motionally narrowed signals and hence increased T_2^* values. Furthermore, it is clear that the random motion of spins diffusing in inhomogeneous fields cannot be refocussed by 180°-pulses. However, this is only true if the duration between the pulses is much longer than the dephasing due to diffusion. The specific case of our NMR-signals is discussed in section 6.3.3.

For some special cases the value of T_2^* in gases due to field inhomogeneities has been derived theoretically. This has been done by Cates for the case of an spherical cell [65]. The particular case of a cylindrical cell, as it is also the case for our experimental setup, is considered by McGregor [66]. McGregor considers the transverse relaxation to be caused by polarized atoms in various positions precessing at slightly different frequencies. Following the notation of McGregor, we consider the cross section of the cylindrical cell to be circular in the plane $y-z$ with a radius a and length L and with the holding field, B_0, pointing along the z direction:

$$\frac{1}{T_2^*} = \frac{1}{2T_1} + \frac{\gamma^2 L^4}{120D}\left(\frac{\partial B_z}{\partial x}\right)^2 + \frac{7\gamma^2 a^4}{96D}\left(\frac{\partial B_z}{\partial y}\right)^2 \tag{6.34}$$

In the case of a spherical cell with radius R and subjected to a gradient on the z axis, McGregor finds the same result as Cates for the high pressure limit.

6.1.4 Hyperpolarized ^3He

The main disadvantage of typical NMR materials is the lack of signal intensity due to the low thermal spin polarization at ambient temperatures, see section 6.1.2. In recent years several polarization techniques have been developed to overcome the thermal Boltzmann polarization of spins. In certain systems the NMR sensitivity can be greatly enhanced

via optical pumping. This is done by transferring the angular momentum from laser photons to electron spins and finally via magnetic coupling (hyperfine interaction) to nuclear spins. Thereby the nuclear spin polarization is temporally enhanced by about five orders of magnitude. Two common methods to achieve optical pumping of nuclear spins of noble gases are alkalimetal spin exchange optical pumping, (used for $^{1}29$Xe or ^{3}He), [67] and metastability exchange optical pumping, (used for ^{3}He) [68]. In our experiment we used the second method. The polarization method is however not the topic of this thesis and will not be treated here.

6.1.5 Diffusion and edge enhancement

The present section focuses on the basics of mass transport, self-diffusion and its effects on NMR.

6.1.5.1 The diffusion coefficient

Diffusion is usually defined as the transport of matter (gas, liquid or solid mixtures) by relative movement of the particles.

The classical description of diffusion is given by Fick's laws (diffusion at constant temperature and pressure):

$$\vec{J}(\vec{r},t) = -D\vec{\nabla}c(\vec{r},t) \tag{6.35}$$

$$\frac{\partial c(\vec{r},t)}{\partial t} = \vec{\nabla}D\vec{\nabla}c(\vec{r},t) \tag{6.36}$$

Equation 6.35 is the Fick's first law. It states that the induced flux of matter $\vec{J}(\vec{r},t)$ is proportional to the gradient of concentrations $\vec{\nabla}c(\vec{r},t)$, where $\vec{r}$ is the position of the particle at the time t. The proportionality factor is the diffusion coefficient, D, or more generally the diffusion tensor. It is a tensor because matter can diffuse differently depending on the direction. The Fick's second law, equation 6.36, describes the temporal evolution of the concentration.

Unfortunately Fick's laws do not give a good description of a particle moving in the absence of a concentration gradient, i.e., the so called self-diffusion.

The kinetic theory of gases permits to obtain an simple expression for the self-diffusion coefficient. For that purpose we have to consider a particle spreading in small steps with random direction. The general approach to describe the motion of particles of a perfect gas is considering that the only contribution to the energy of the gas is from the kinetic energies of the particles on such chaotic trajectories.

Calculating the particles flow which cross an imaginary plane on positive and negative direction, Atkins and de Paula [69] derive an expression for the self-diffusion coefficient as follows:

$$D = \frac{1}{3}\lambda\overline{v} = \frac{1}{3}\frac{k_B T}{\sigma p}\sqrt{\frac{4RT}{\pi M}} \tag{6.37}$$

where R is the gas constant, T the absolute temperature, M the molecular mass of the particle, λ is the mean free path of the particles or molecules between collisions, $\overline{v}$ is the averaged velocity of the ensemble, σ is the collision cross-section of the gas molecules and p the pressure.

A more detailed theory was presented by Chapman and Enskog and named after them [70]. The expression of the self-diffusion coefficient obtained from this theory and a brief discussion can be found in appendix C.2.

6.1.5.2 Edge enhancement

The rapid diffusion of the gas atoms during an NMR-experiment can make the nuclear spins experience different magnetic field values during the free induction decay. This certainly affects the recorded signal. It is well known that diffusion tends to attenuate the signal. However, close to a boundary there is less diffusion and the signals are thus less attenuated. In certain circumstances, the edges of a region may be enhanced during an NMR-experiment. This was predicted by numerical simulations, [71] and [72], and demonstrated by Callaghan et al. [73].

The edge enhancement with hyperpolarized ^3He has been measured by [74] and its application to resolution enhancement on MRI by [62].

The paper of T.M. de Swiet [75] presents a comprehensive quantitative theory for the shape of the spectrum in the case of edge effect as well as the limiting conditions of this effect. de Swiet introduces two limit situations; the slow- and the fast-exchange limit. To define both regimes we must introduce three length scales.

- The diffusion length during the lifetime of the experiment, $l_D = \sqrt{2nDt}$, where n is the number of dimensions in which the particle is allowed to move and D is the diffusion coefficient [60].
- The characteristic length scale of the vessel or structures inside it, l_s.
- The length scale associated with the field gradient, $l_g = (D/\gamma g)^{1/3}$, were $g = \left(\frac{\partial B_z}{\partial i}\right)_{i=x,y,z}$.

The slow-exchange regime is defined as $l_s >> l_g$, l_D, and the fast exchange regime is its opposite.

In the fast-exchange regime, the spins diffuse through the ^3He cell and are reflected at the walls during the lifetime of the experiment. The shape of the spectrum is then motionally narrowed and we obtain a simple Lorentzian. In the slow-exchange regime, the length scale is much bigger than the diffusion length and most of the spins do not contact a wall during the duration of the experiment. In this case the diffusive distortion is confined to a boundary layer of spins near the wall. The spins in the middle of the cell do not have time to reach the wall before the signal decays. Therefore the center of the cell will suffer from unrestricted diffusion, producing a flat profile. At the edges, the effective diffusion length is smaller and therefore there is less attenuation. There the result is an asymmetric peak which is not a Lorentzian (see figure 6.44).

de Swiet estimates a ratio of $l_s/l_g = 20$ for the slow-exchange limit and therefore pure edge enhancement at the boundaries and $l_s/l_g = 2$ for the fast-exchange limit or motional narrowing.

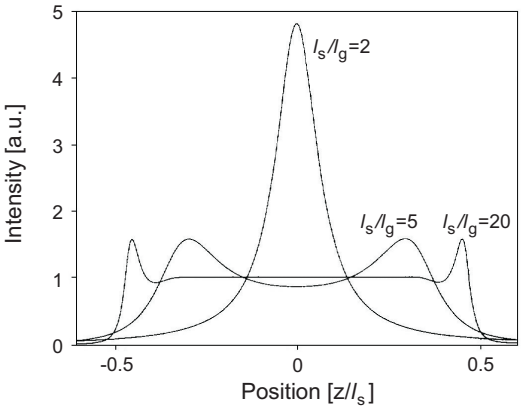

Figure 6.44: The graph shows the calculated profile (intensity versus position) for three different gradient strengths: $l_s/l_g = 20, 5, 2$. Note that in the presence of a constant magnetic field gradient, to talk in terms of position is equivalent to frequencies. Picture taken from [75].

In NMR-Magnetometry with gases (rapidly diffusing samples), this effect translates into an enhancement of the frequency components (magnetic field values) present on the boundaries of the NMR-probe. This produces a distortion of the frequency spectrum of the magnetic field distribution.

6.2 Experimental setup

The *a*SPECT NMR-Magnetometer is designed to measure and constantly monitor the ratio r_B of the magnetic field of the *a*SPECT spectrometer at the DV and AP regions (see chapter 5). For that purpose, two NMR-probes are installed at specified positions inside the spectrometer. The electronic setup is designed (i) to send r.f. pulses which flip the spins of the NMR-sample and (ii) to acquire the resulting FID-signal. The electronics are controlled via a computer which allows us to vary the characteristics of the flipping pulse and tho acquire the raw data as well as presenting a preliminary on-line analysis of the frequency distribution.

The relation between the holding field B_0 and the Larmor frequency ω_0 at which the spins are precessing (equation 6.6) provides a direct measure of the magnetic field at the sample's position.

Furthermore, the decay time of the signal T_2^* gives extra information on the magnetic field distribution within the sample cell. As it will be explained in section 6.3.3, in our experimental conditions, it can be approximated that the transversal relaxation time T_2^* is produced due to the field inhomogeneities within the sample value (equation 6.38). Thus, the length of the signal permits a direct estimation of the field variation within the NMR-sample.

$$\frac{1}{T_2^*} \approx \gamma \Delta B_0 = \Delta\omega_0 \tag{6.38}$$

This section describes the experimental setup of the NMR-Magnetometer designed for

the study and the monitoring of the *a*SPECT magnetic field. Firstly, the design and construction of the NMR-probes are presented. Secondly the electronics are described in detail.

6.2.1 NMR sample

An adequate material for the NMR-probe has to fulfil several conditions. On the one hand, the atoms of the material should have a spin ($I = 1/2$) that allows for the complete ensemble of atoms to present a net magnetization. On the other hand, since the NMR-sample has to be placed inside our cryostat (see chapter 5), it has to be UHV compatible and it has to permit measurements at temperatures around 70 K.

At such a low temperature most of the usual materials become solid. In solids, the internal spin interactions become dominant, producing a very short FID. The shortening of the signal translates into a broadening of the frequency components of the signal and therefore a loss in resolution and sensitivity. For these reasons, as well as the lack of time to search for new materials, it was decided to proceed with hyperpolarized ^{3}He. Due to non equilibrium polarization, this sample choice ensures high sensitivity with a narrow spectrum dependent on the magnetic field inhomogeneities, even at 70 K.

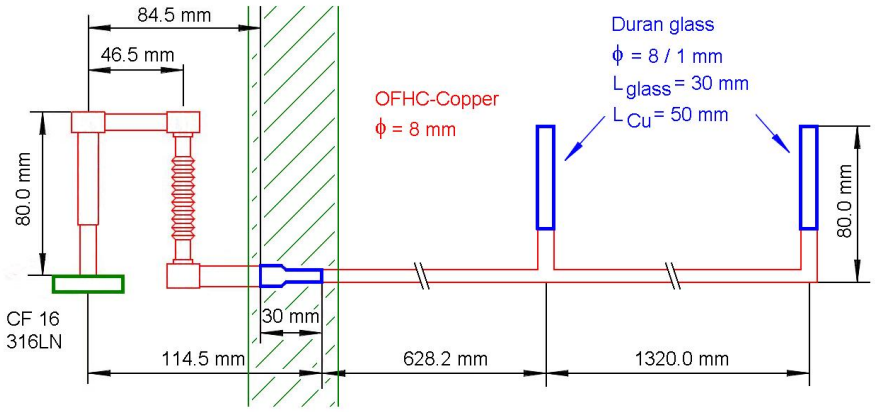

Figure 6.45: Copper tube system for the introduction of hyperpolarized ^{3}He into the NMR-sample volume (blue cells). The sketch is shown in horizontal whereas it is installed in vertical direction. The green dashed area corresponds to the transition from room temperature (left) to the inside of the electrode system chamber (right). The CF16 flange connects to the outside of the cryostat, giving access to the introduction of the helium into the system. The two glass cells correspond to the DV (left) and AP (right) positions, see figure 6.46.

The main disadvantage of the helium as a resonant material is the difficulty in introducing it inside the samples without damaging vacuum conditions and limiting the heat load introduced in the cryostat. For this purpose an OFHC-copper tube system was designed (see figure 6.45). This system is suitable for UHV conditions, however, the high thermal conductivity of the copper makes for difficulty in insulating the system thermally. For this reason copper-glass joint transitions were used to bridge that part of the system at room temperature (left side of the picture shown in figure 6.45) with the vacuum chamber at about 70 K (right side of the picture). The big change of temperature that occurs when the cryostat cools also required that the system be prepared for length adjustments that

come with temperature variations. The copper bellow placed below the transition region is designed to absorb the dilatation and compression of the material.

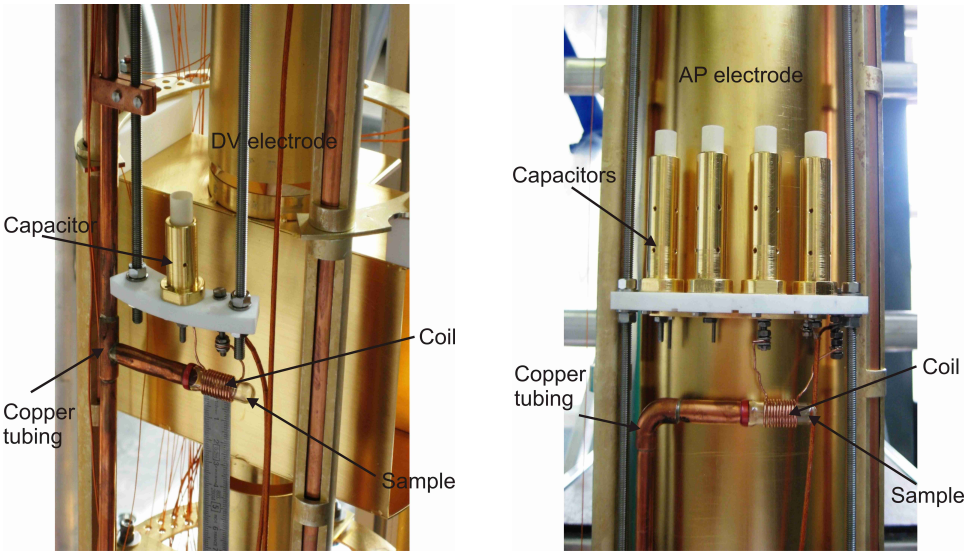

(a) (b)

Figure 6.46: Duran glass cells for the NMR-sample plus resonant circuit. (a) DV electrode, (b) AP electrode

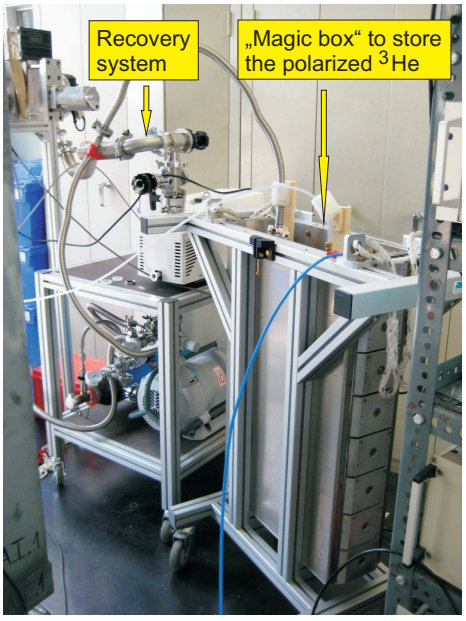

Figure 6.47: Storage and recovery system.

The LC resonant circuit for the r.f. pulse and the signal acquisition have to be UHV compatible as well (see figure 6.46). For this reason many parts have to be custom built to match these conditions. The coils are produced with special OFHC copper wire. The capacitors are cylinders made from OFHC-copper and gold coated in order to preserve a clean surface. The inner and outer cylinders are separated by a thin layer of insulating material (Degussit) which can be partially or totally removed in order to change the value of the capacitance. This permits a rough tuning of the LC circuit to the Larmor frequency of ^{3}He before installing it inside the spectrometer (see section 6.2.2).

The helium is polarized and kept inside a glass cell specially designed for storage purposes. The cell is placed inside a “Magic Box”, a magnetic box with a very homogeneous low field. This box permits the storage of helium while keeping its polarization for several hours or even days.

The cell is connected through a valve system to the outer flange of the copper tube-system of the NMR-Magnetometer. The valves permit the evacuation of the copper tube-system before introducing the helium. For an NMR experiment a valve is opened to allow the helium to fill the evacuated sample volume. After the measurement, the recovery system evacuates the NMR-sample volume and stores the recovered helium in a pressurized vessel. After each helium filling, the polarization of the helium decays fast due to several relaxation mechanisms (T_1) (see section 6.1.3). In less than one minute the polarization is completely destroyed. For this reason, consecutive measurements with identical configuration are made in order to acquire statistics before the polarization is lost. These consecutive measurements are called sets. Experimental measurements of the ^{3}He T_1 in the NMR-samples can be found in appendix C.1

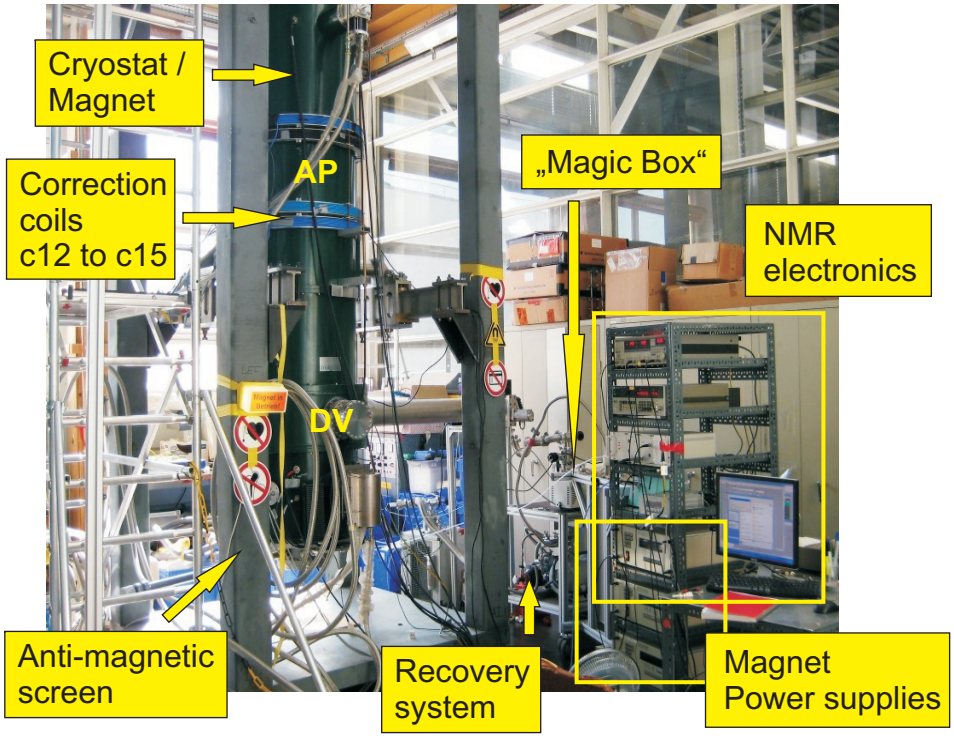

Figure 6.48: NMR-setup and *a*SPECT spectrometer.

6.2.2 Electronics

The electronic setup has to be able to produce a r.f. pulse of a controlled length in order to produce a $\pi/2$ spin-flip and to receive and record the resulting FID signal.

For this purpose, a radio **frequency generator** produces a sinusoidal signal which is divided by a **splitter** (see figure 6.49). One of the two signals is used to produce the spin-flip whereas the other is used as a reference for the detection system.

The first sinusoidal signal is mixed in a 3 dB **switch** with a squared pulse. The result is a squared r.f. pulse with a length that can be controlled via **computer**. This pulse is amplified by a **custom made amplifier**. Two different amplifiers have been built for

the two different frequencies used in our system: about 14 MHz for the 0.4 T field at the AP and 70 MHz for the 2.2 T field at the DV. The amplifiers may be set to work at full amplification or at half of it. Half of the amplification was used during our experiments. By changing the amplitude or the length of the pulse it is possible to control the flip angle, see equations 6.20 and 6.21. During the experiment, the pulse amplitude was fixed (316 mV in the r.f. generator) and the flip angle was varied by the length of the pulse. The pulse length corresponding to a spin flip of $\alpha = \pi/2$ was determined by searching the pulse length that results in the maximum NMR-signal amplitude ($\tau = 20\,\mu$s).

After the amplification, a set of **antiparallel diodes** removes the low amplitude ringing of the amplifier in order to keep a clean and sharp pulse. A **duplexer** guides the incoming pulse directing it to the **LC circuit** inside the cryostat. The coil of inductance L (**pick-up coil**) wrapped around the NMR-sample (see figure 6.46) is responsible for generating the B_1 field which produces the net magnetization to flip an angle $\alpha = \pi/2$ (see section 6.1.2).

The duplexers are made from spare parts of a Bruker MSL200 spectrometer. Two duplexers are available for the two frequencies used in *a*SPECT. Since the resonant circuit is not accessible once the electrode system is installed inside the cryostat, a **variable capacitor** and a **cable of variable length** connected outside the cryostat allow a fine matching and tuning of the circuit.

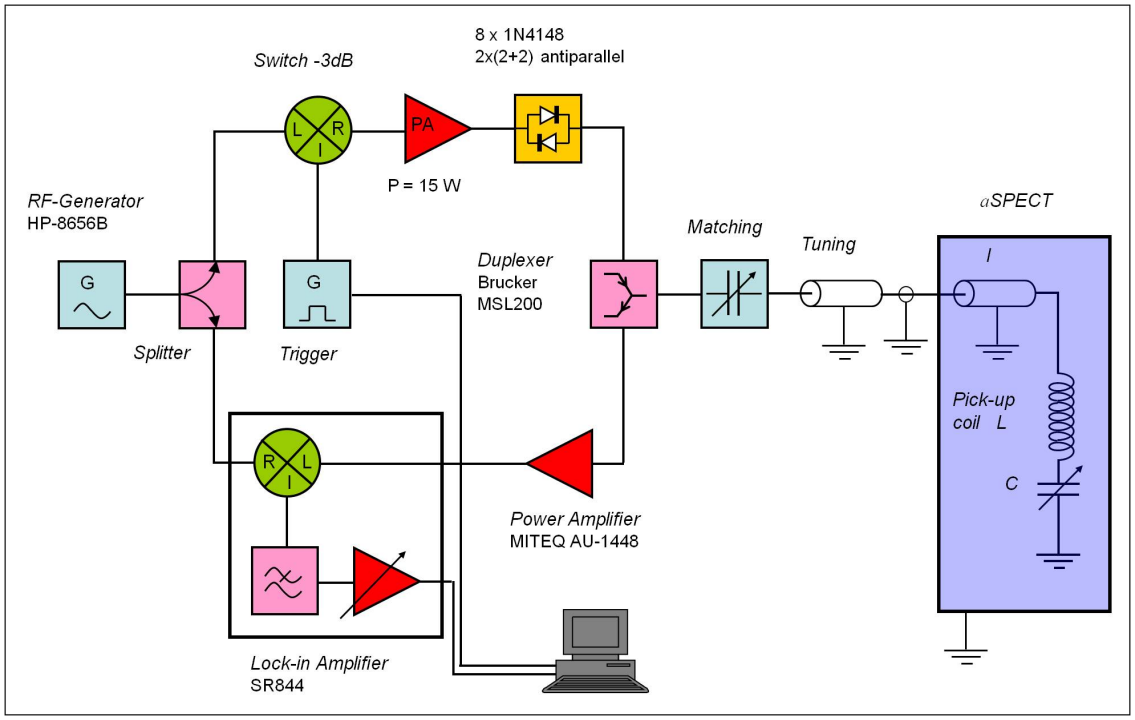

Figure 6.49: Sketch of the electronic setup of the *a*SPECT NMR-Magnetometer. The spectrometer is represented in blue on the right side of the picture.

Matching and tuning

In general, a resonant circuit must be tuned to the frequency of the corresponding nucleus and matched to the standard impedance of the connecting lines, i.e., 50 Ω. This is usually achieved by adjusting variable capacitors or inductances in the circuit. Tuning and matching reduces reflected power and increases the quality factor Q.

In electronics the resonance frequency of a LC circuit can be written as:

$$\omega_0 = \frac{1}{\sqrt{LC}} \tag{6.39}$$

where L represents the inductance and C the capacitance of the components. Tuning consists of varying the values of L and C to set the resonance frequency of the circuit to the Larmor frequency of the nuclei. Impedance matching is the practice of designing the input or output impedance of an electrical load to 50 Ω in order to maximize the power transfer and minimize reflections from the load.

In the case of *a*SPECT the rough tuning is made with the LC circuit installed inside the spectrometer. The fine tuning is done outside of the spectrometer by changing the length of a piece of cable. Once the tuning is finished, the variable capacitor permits the match of the impedance of the LC circuit to 50 Ω, thus minimizing reflections.

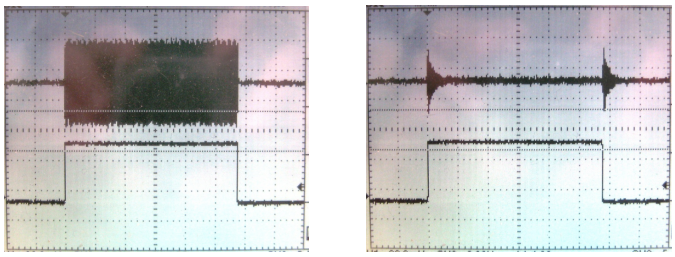

(a) (b)

Figure 6.50: Matching of the resonance LC circuit to a certain frequency. (a) Reflection at the LC circuit of a pulse with $\omega \neq \omega_0$. (b) Reflection at the LC circuit of a pulse with $\omega = \omega_0$. The rising and falling edges of the pulse alter the frequency components, producing a mismatch of the frequency and, thus, reflections.

Typically, the matching of a circuit to a specific frequency is done by means of a network analyzer. This is a very expensive device which was not available for our experiment. Therefore, we proceeded in a simple but effective alternative way. When the LC circuit is matched to a certain frequency, all the power sent to it at this specific frequency will be emitted and no reflections will be observed. Such reflections can be measured by a bidirectional coupler. This device permits one to monitor the amplitude of both the incoming and the reflected signals. Figure 6.50 shows a picture of a pulse reflected at the LC circuit ($\omega \neq \omega_0$, (a). Picture (b) shows the reflection at the LC circuit of a r.f. pulse matched to the resonance frequency of the LC-circuit, $\omega = \omega_0$. The matching is achieved when the reflections are minimized such that only the rising and falling edges of the pulse are

observed (figure 6.50 (b)).

The characteristics of the LC circuits installed inside the spectrometer to detect the FID signal are indicated in table 6.14. This circuit is roughly tuned to the Larmor frequency of the ^{3}He atoms at the corresponding magnetic field. To the values shown in table 6.14 one has to add the contributions of the internal capacitance and inductance of the coaxial cable inside the spectrometer (1.25 and 2.55 m for the DV and AP respectively). The fine tuning and matching is achieved with a variable capacitor and a cable of variable length connected directly outside the spectrometer. Cables of about 27 and 10 cm long are used to tune the DV and AP pick-up LC circuits, respectively, to the corresponding resonance frequency. The matching to create a real impedance of 50 Ω is achieved by a variable capacitor with a capacitance varying from 4 to 30 pF for the DV sample and from 37 to 63 pF for the AP sample.

	L (nH)	C (pF)
DV	480	47
AP	480	256

Table 6.14: Characteristics of the LC circuit installed inside the spectrometer.

The quality factor of the LC circuits for the DV- and AP-samples is discussed in appendix D.1. This value is necessary to calculate the expected signal and gives the bandwidth of frequencies "visible" with our setup.

After the $\pi/2$ pulse, the net magnetization precessing around the holding field induces a FID signal in the same coil of inductance L (see figure 6.46), which now acts as a **pick-up coil**. The received FID signal is now **pre-amplified** (MITEQ AU-1148) with a 55 dB gain and directed by the **duplexer** to the detection system, a **Lock-in amplifier** model SR844 (Stanford Research Systems).

Lock-in amplifier (LA)

Lock-in amplifiers are used to detect and measure very small AC signals. Accurate measurements may be made even when the small signal is obscured by noise sources many thousands of times larger.

Lock-in amplifiers use a technique known as phase sensitive detection to single out the component of the signal at a specific reference frequency and phase. Noise signals at frequencies other than the reference are rejected.

Typically an experiment is excited at a fixed frequency and the lock-in amplifier detects the response from the experiment at the reference frequency. The lock-in amplifier multiplies the signal with the reference $V_R \sin(\omega_R t + \phi_R)$ using a mixer

$$\begin{aligned} V_{M1} &= V_S V_R \sin(\omega_R t + \phi_S) \sin(\omega_R t + \phi_R) \\ &= \frac{1}{2} V_S V_R \cos(\phi_R - \phi_S) + \frac{1}{2} V_S V_R \sin(2\omega_R t + \phi_R + \phi_S) \end{aligned} \tag{6.40}$$

where V is the amplitude and ω and ϕ the frequency and phase of the signal respectively. The subindexes R and S refer to *detected* and *reference* signal. If the two inputs are exactly at the same frequency, the first term in the mixer output is a DC value and the second term is at a frequency $2\omega_R$ and easily removed by low pass filter. The result after the filter is

$$V_{M1+FILT} = \frac{1}{2} V_S V_R \cos(\phi_R - \phi_S) \tag{6.41}$$

A second mixer does the same operation with the reference input 90° out of phase

$$V_{M2+FILT} = \frac{1}{2} V_S V_R \sin(\phi_R - \phi_S) \tag{6.42}$$

By combining the results from both mixers the amplitude and phase of the input signal can be determined

$$R = \frac{2}{V_R} \sqrt{(V_{M1+FILT})^2 + (V_{M2+FILT})^2} \tag{6.43}$$

$$\phi_R - \phi_S = \tan \arctan \left(\frac{V_{M1+FILT}}{V_{M2+FILT}} \right) \tag{6.44}$$

In case of measurements off-resonance the result after the filters is

$$\begin{aligned} V_{M1+FILT} &= \frac{1}{2} V_S V_R \cos((\omega_R - \omega_S)t + \phi_R - \phi_S) \\ V_{M2+FILT} &= \frac{1}{2} V_S V_R \sin((\omega_R - \omega_S)t + \phi_R - \phi_S) \end{aligned} \tag{6.45}$$

Therefore, measurements off-resonance permit one to obtain a clean and amplified signal with a frequency which is the difference between the signal of the FID minus the reference. A Fourier analysis allows for the extraction of the central frequency as well as the study of the frequency distribution of the FID signal[2], i.e., the magnetic field distribution over the sample volume.

6.3 Data treatment and analysis

This section focuses on the treatment of the raw data as well as the analysis and characterization of the NMR-signals and their frequency distribution obtained by Fourier analysis. The first step is to consider the proper way to treat the signal in order to differentiate between noise and signal. Afterwards we will concentrate on the adequate procedure needed to characterize our signal, in order to ultimately extract the parameters of interest.

[2] Assuming homogeneous excitation.

6.3.1 Raw data analysis

A typical NMR-signal obtained at the *a*SPECT DV region, around 70 MHz (2.2T), is shown in figure 6.51. The FID signal is mixed by the lock-in amplifier with the reference signal. The reference frequency was set such that a signal with a few kHz is obtained as output of the Lock-in amplifier. The advantages of getting a low frequency signal from the lock-in amplifier are to maximize the amplification, which decays rapidly as moving away from the reference signal (see figure 6.70 in section 6.5.1), and keeping a high sampling ratio compared to the frequency of the signal (see *"Resolution of the Fast Fourier Transform"* later in this section).

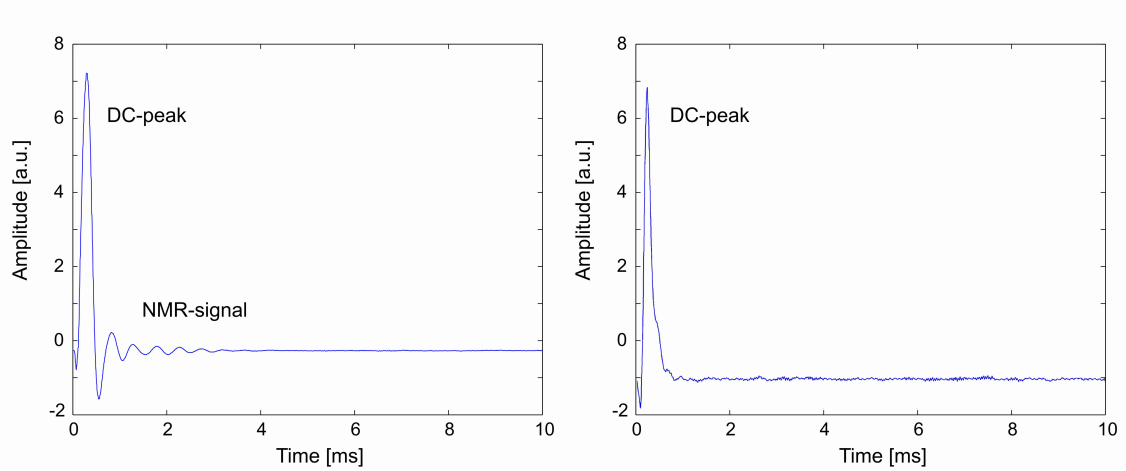

(a) (b)

Figure 6.51: (a) Original NMR signal produced at the Decay Volume region. (b) Signal detected without ^3He (background). The high peak observed early in the first millisecond is produced by leakage of the r.f. pulse into the detection system.

To extract the frequencies at which the spins are precessing around the holding field, an analysis of the recorded NMR-signal in the frequency domain is indicated. For that reason we will make use of the Fourier transformation to pass from the time domain to the frequency domain.

A raw signal as the one shown in figure 6.51 (a) has several components which obscure the pure FID signal and the power spectrum obtained via a Fourier Transform (FT). For this reason a preliminary treatment of the data is necessary. The first step is to remove the effect that the r.f. pulse has on the detected signal. For that purpose, the signal has to be truncated.

Time truncation

Although most of the r.f. pulse is blocked by the duplexer and lasts only 20 μs, its amplitude is still big enough to be detected by the lock-in amplifier. Since its frequency is exactly that of the reference signal, it results in a high DC peak which masks the first few tenths of a millisecond (see figure 6.51 (b)). This DC peak translates into low

frequency components when passing to the frequency domain via a FT[3]. Truncation of the signal permits the removal of this fast decaying DC-peak and thus the low frequency noise created by it in the power spectrum (see figure 6.52). Note that the DC peak is not stable and, hence, cannot be subtracted. Although the truncation alters the information contained in the signal, the benefits of removing the DC peak prevail. Figure 6.52 shows a comparison of the power spectrum obtained with the original signal and the truncated signal.

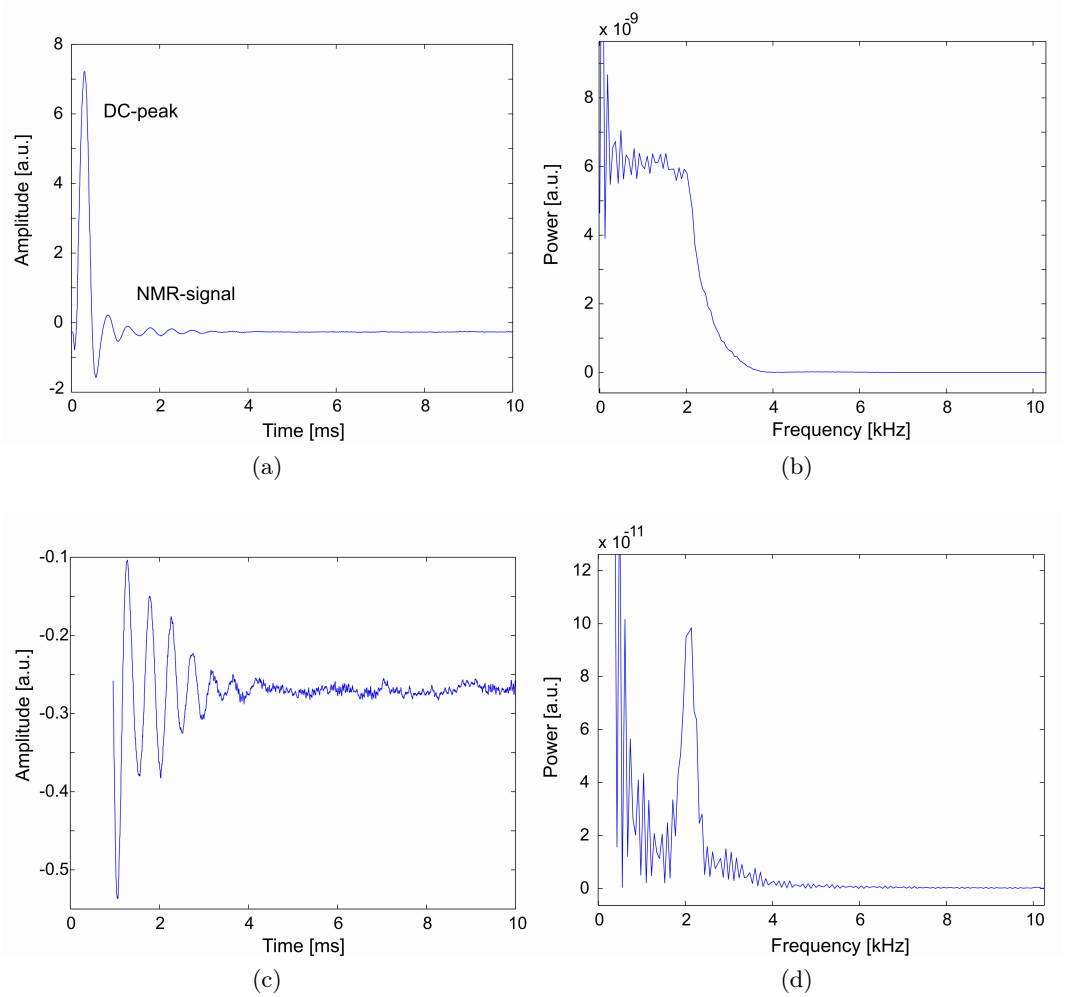

Figure 6.52: Comparison of the result of the FT with a complete signal and a truncated signal. (a) Complete NMR signal. (b) Power spectrum of signal (a). (c) Same NMR signal with its first tenths of a milliseconds truncated. (d) Power spectrum of signal (c).

Mathematically, the short time truncation is basically a change of amplitude and a time shift of the FID signal. A change on the amplitude of the signal only affects the height of the FT: $s'(t) = as(t) \Rightarrow \mathcal{F}(s'(t)) = a\mathcal{F}(s(t))$. A time or a phase shift produces a change of phase in the frequency domain. Defining $t' = t - t_0$:

[3]From now on we will refer to the Fourier Transform and to the Fast Fourier Transform (FFT) interchangeably unless otherwise indicated

$$\begin{aligned}\mathcal{F}(s(t-t_0)) &= \int_{-\infty}^{+\infty} s(t-t_0)e^{-i\omega t}dt = \int_{-\infty}^{+\infty} s(t')e^{-i\omega(t'+t_0)}dt' \\ &= = e^{-i\omega t_0}\int_{-\infty}^{+\infty} s(t')e^{-i\omega t'}dt' = e^{-i\omega t_0}S(\omega) = e^{-i\varphi}S(\omega) \qquad (6.46)\end{aligned}$$

However, physically the truncation of the signal produces the loss of the information contained in the truncated part of the signal. An actual NMR signal is typically composed of several frequencies with different T_2^* times (see section 6.3.3). If the signal contains some fast decaying components (i.e., with short T_2^* times), removing the first data points also removes these components. The truncation can be considered as a dead-time on the signal acquisition system.

There are two ways to avoid the truncation of the signal. One possibility is to apply a specific sequence of pulses called echo (see figure 6.41 in section 6.1.3). By applying a 90°-180° spin echo technique it is possible to start measurement from the exact moment at which the spins are all aligned and without the influence of a close pulse. In this way the complete signal can be measured, avoiding the need for truncation.

The second possibility would be a modification of the electronics, either by improving the shielding from the r.f. pulse or by employing a mixer (which does not integrate the signal) instead of the lock-in amplifier.

Signal offset (DC-artifact)

After the truncation another correction has to be applied to the raw signal. This correction is due to the DC-offset of the signal which via the FT translates into a dominant peak at zero frequency and other low frequency noise.

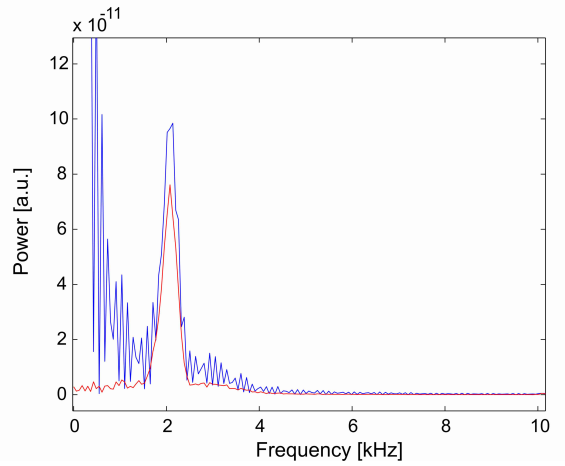

Figure 6.53: Blue curve, power spectrum of a signal without offset correction. Red curve, power spectrum of the same signal with offset correction.

This low frequency noise can completely mask the NMR peak or modify its shape, leading to false effects on the magnetic field determination (see figure 6.53).

To correct for this effect, the offset is calculated by averaging the recorded signal after the FID has completely decayed. The averaged offset is then subtracted from the complete signal.

Resolution of the Fast Fourier Transform (FFT)

Following, we have to consider how the Fourier Transform is calculated and the implications of the latter. The way LabView, Matlab and several other programs calculate the FFT is with a Discrete Fourier Transformation (DFT):

$$S_k = \sum_{n=0}^{N-1} s_n e^{-i\frac{2\pi kn}{N}} = \sum_{n=0}^{N-1} s_n \left[\cos(\frac{2\pi kn}{N}) - i\sin(\frac{2\pi kn}{N})\right] \quad \text{for } k = 0, 1, ..., N-1 \quad (6.47)$$

where N is the number of sampled points in both the discrete-time and the discrete-frequency domains, s_n is the input sequence (the NMR-signal) and S_k is its DFT. If we make $k = 0$, the sine vanishes and the cosine equals one for every n. The $S_{k=0}$ is then the sum of all sampled values s_n, i.e., the first point of the FFT contains the DC offset of the NMR-signal. If the values of s_n are equally distributed around zero, like in a sine wave, they will cancel each other out. A deviation from this cancelation is produced by a DC offset component added to the signal. Therefore, $S_k = 0$ corresponds to the DC component as observed in the previous point *"Signal offset (DC-artifact)"*.

Other important parameters which have to be understood when working with a DFT are summarized in table 6.15.

T	Measurement time interval
Δt	Time increment per sample
$f_s = 1/\Delta t$	Samples per unit of time
$\Delta f = f_s/N = 1/T$	Frequency increment
$f = (0 : N-1)(f_s/N)$	Frequency range
$f_s/2$	Nyquist frequency

Table 6.15: FFT parameters

The frequency resolution obtained from the FFT is linked to the sampling rate, f_s, and the total number of sampled points, N. Therefore, the longer the measurement takes (high N, T) the better the resolution on the FFT (smaller Δf). The frequency range is related to the frequency sampling rate; the higher the sampling frequency the higher the frequency range, i.e, higher frequencies can be seen. The highest frequency which can be seen when sampling with a frequency f_s is the Nyquist frequency, $f_N = f_s/2$. Nevertheless, higher frequencies can be observed shifting back to lower frequency values, a result of aliasing. Aliasing is an effect of finite sampling frequency, which mirrors frequencies higher then $f_s/2$ into the frequency range of interest.

The NMR-signals are sampled at two different stages in our detection system. The first sampling occurs in the lock-in amplifier (as it is a digital device). The second sampling takes places in the NI-card that reads the output signal of the lock-in amplifier and digitalizes it before storing in the computer. The aliasing effects due to this double sampling

are properly discussed in section 6.5.1. For the rest of the work, we will not take aliasing effects into consideration.

The frequency resolution of the FFT is determined by the NI-card which offers a maximum sampling rate of 250 kHz. During the first measurements, 5000 points were sampled at a frequency of 250 kHz, which results in a resolution of 50 Hz and a sampling interval of 20 ms (much longer than the signal length).

6.3.2 Power spectrum

After the first treatment of the raw data, the parameters which characterize the *a*SPECT magnetic field have to be extracted. These parameters are the center and the width of the spectrum. The center of the spectrum is assigned as the value of the magnetic field at the position of the NMR-sample (see equation 6.6) whereas the width of the spectrum gives information about the magnetic field distribution over the volume of the sample. The use of the power spectrum instead of the amplitude spectrum presents two important advantages. On the one hand, it allows one to neglect the phase of the recorded signal and thus to work directly without any further phase correction. On the other hand, in a simple NMR experiment, the NMR-signal can be approximated to an exponentially decaying oscillation (see figure 6.43). The power spectrum (PS) of such a signal has the shape of a Lorentzian. Consequently, a fit of the PS to a Lorentzian allows one to extract directly the center and width of the spectrum.

6.3.2.1 Linear and quadrature detection (phase of a signal)

The NMR signal has to be digitalized in order to be fed into the computer. This task is accomplished by an analogue to digital converter (ADC). However, oscillations in the order of MHz are too fast for typical ADCs. Therefore, it is necessary to mix the NMR-signal with a reference signal in order to obtain a signal oscillating at $\omega' = \omega_R - \omega_0$ in the order of kHz. This mixed signal can then be easily digitalized. This task is accomplished by a mixer or a more elaborated electronic device like the LA described in section 6.2.2. If a typical mixer is used in the experiment, one single output signal is obtained. This case is called *"linear detection"*. The LA used in this experiment supplies two mixed output signals with a phase difference of 90°. If both signals are used, the detection system is named *"quadrature detection"*.

Fourier transforming of a single oscillating signal gives peaks at $-\omega_0$ and $+\omega_0$ because the FT[4] cannot distinguish in between both cases, i.e. clockwise and anticlockwise rotation (see figure 6.54). The FT of a complex signal composed of the two output signals of the LA permits us to distinguish between negative and positive frequencies. Figure 6.54 shows the case of an anticlockwise rotation. In case of a clockwise rotation: $s(t) = \cos(\omega_0 t) - i\sin(\omega_0 t)$ and the FT would give $\mathcal{F}(s(t)) = S(\omega) = 2\delta(\omega + \omega_0)$ as a result. In linear detection, the acquisition of two signals with different reference frequencies, ω_R, allows us to solve this ambiguity.

However, linear detection either needs a careful adjustment of the phase difference between excitation and detection or subsequent phase correction by software [60] (see figure

[4] Actually this is called a cosine or a sine transformation.

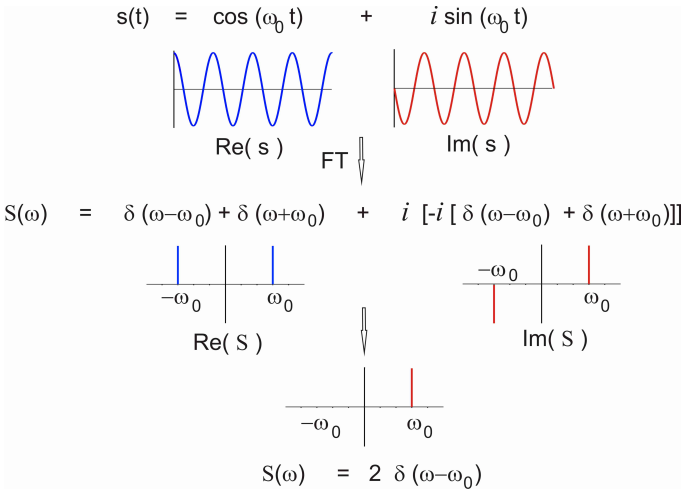

Figure 6.54: Fourier Transform of a cosine and a sine wave. The addition of both signals permits to distinguish between negative and positive frequencies, i.e., clockwise and anticlockwise rotation.

6.55). Nevertheless, this is not necessary in our setup because we are only interested in the position and distribution of the spectra, which is provided by the modulus of the spectrum (or the power spectrum) while the phase of the signal contains no useful information and is canceled when calculating the modulus (or the power spectrum):

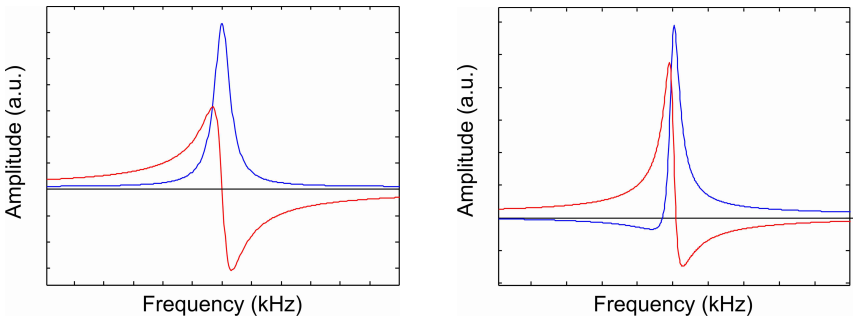

Figure 6.55: (a) FT of $s(t) = e^{-t/T_2^*}[\cos(\omega_0 t) + i\sin(\omega_0 t)]$. (b) FT of s(t) with an extra phase of $\varphi = 45$. Blue represents $\mathrm{Re}(S(\omega))$, called *absorption Lorentzian*, whereas red $\mathrm{Im}(S(\omega))$, is called *dispersion Lorentzian*.

$$|\mathcal{F}(e^{i\varphi}s(t))|^2 = |e^{(i\varphi)}|^2|S(\omega)|^2 = |S(\omega)|^2 \tag{6.48}$$

The FT of two typical NMR-signals in our experiment is shown in figure 6.56. The advantages of using the power spectrum instead of modulus are that the power spectrum is narrower than the modulus of the FT and it presents a direct relation with T_2^* which permits the extraction of the transversal relaxation time directly from the width of the Lorentzian.

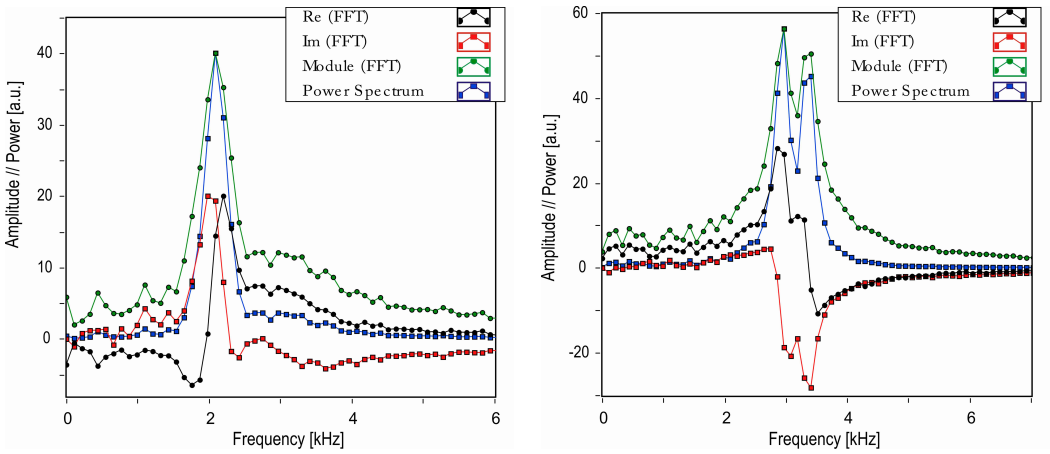

Figure 6.56: Result of the FT for a typical NMR signal at the DV, (a), and at the AP, (b). The original signal has no phase correction.

6.3.2.2 Lorentzian profile of the power spectrum

Consider the function below as an ideal NMR signal oscillating at ω_0 and decaying with a single decay factor T_2^*:

$$s(t) = e^{-t/T_2^*}\left[\cos\omega_0 t + i\sin\omega_0 t\right] \tag{6.49}$$

Equation 6.49 is composed of the real and imaginary components provided by the lock-in amplifier (quadrature detection). A more realistic model for a NMR-signal would be composed of several frequencies, amplitudes and T_2^*. If we now calculate the FT of the signal in equation 6.49, making use of the property of the Convolution theorem of the FT $\mathcal{F}(f(t)g(t)) = F(\omega) \otimes G(\omega)$, where $\otimes$ is the convolution:

$$\mathcal{F}(s(t)) = S(\omega) = \frac{1}{\frac{1}{T_2^*} + i\omega} \otimes \delta(\omega - \omega_0) \tag{6.50}$$

Defining $\lambda = 1/T_2^*$ and developing to obtain real and imaginary parts, we obtain:

$$S(\omega) = \frac{\lambda - i(\omega - \omega_0)}{\lambda^2 + (\omega - \omega_0)^2} = \left(\frac{\lambda}{\lambda^2 + (\omega - \omega_0)^2}\right) - i\left(\frac{(\omega - \omega_0)}{\lambda^2 + (\omega - \omega_0)^2}\right) \tag{6.51}$$

where the real part is the absorption Lorentzian and the imaginary part is the dispersion Lorentzian. The module of $S(\omega)$ is:

$$|S(\omega)| = \frac{1}{\lambda^2 + (\omega - \omega_0)^2}\sqrt{\lambda^2 + (\omega - \omega_0)^2} = \frac{1}{\sqrt{\lambda^2 + (\omega - \omega_0)^2}} \tag{6.52}$$

and finally the power:

$$|S(\omega)|^2 = \frac{1}{\lambda^2 + (\omega - \omega_0)^2} \tag{6.53}$$

Equation 6.53 is a Lorentzian curve obtained from the FT of an ideal FID (equation 6.49). The center of the spectrum is given by ω_0 and the width by λ. Thus, in an ideal situation, the width of the Lorentzian permits a direct determination of T_2^*. In case of a clockwise rotation, $s(t) = \cos(\omega_0 t) - i\sin(\omega_0 t)$, the same results are obtained but with $(\omega + \omega_0)$, i.e., centered at negative frequencies. If the power spectrum is calculated from only the real or the imaginary part of equation 6.49 (linear detection) the result is also equation 6.53 (but twice, one centered at $+\omega_0$ and the second centered $-\omega_0$). Equation 6.48 also confirms these results.

6.3.3 Signal characteristics

Now it is useful to estimate the mean path a particle travels during a certain time. The mean path is also known as the mean square displacement and is given by the Einstein-Smoluchowski equation [60]:

$$\langle \vec{r}(t)^2 \rangle = 2nDt \tag{6.54}$$

where n is the number of dimensions, D is the self-diffusion coefficient and t is the time. The self-diffusion coefficient has been calculated by using the Chapman-Enskog kinetic theory of gases (appendix C.2). Its value depends on the pressure and temperature conditions[5] of the helium gas inside the sample cell and is comprised in the range from $2.15\,\mathrm{cm}^2/\mathrm{s}$ to $12.17\,\mathrm{cm}^2/\mathrm{s}$.

If we consider the duration of the NMR experiment as the time the signal takes to vanish, the mean path a particle can move in during this time varies approximately between 1 to 3 mm in the DV- and 1 to 4 mm in the AP-sample (depending on pressure and temperature conditions and T_2^*). Consequently, the static approximation (see section 6.1.3) does not apply in our experimental conditions. However, the movement of the helium atoms is not fast enough to travel all along the NMR-sample cell during the duration of the experiment. Thus, a pure motional narrowing is also not applicable.

This result agrees with the observations given by de Swiet in his paper (discussed in section 6.1.5.2). The three length scales defined by de Swiet, l_s, l_g and l_D have been calculated for our working temperature and pressure range (appendix C.2) and the coefficient l_s/l_g has been found to vary from 3.1 (at low pressure and high temperature) to 11.2 (at high pressure and low temperature). A coefficient $2 < l_s/l_g < 20$ indicates that our experimental conditions are neither within the slow-exchange (pure edge enhancement) nor fast-exchange limit (pure motional narrowing).

In order to understand how this affects the NMR-signal, we can imagine the NMR-sample cell divided in small volumes of approximately 4 mm length[6], i.e. approximately the mean path of the helium atoms during the duration of the experiment (see figure 6.57 (a)). Inside these volumes, the helium atoms move freely such that motional narrowing

[5] Note that the pressure falls in each helium filling, and the temperature decreases during the measurements of a set due to heat dissipation.

[6] Note that the dimensions of the cell are $\phi_{\mathrm{inner}} = 6$ mm and a length of about 1.5 cm, considering only the length of the pick-up coil. Actually, the efficiency of the coil needed to flip the spins and to pick-up the signal created by the transversal component of the magnetization varies at the borders of the coil. Thus, a definition of the "effective" cell size is not trivial.

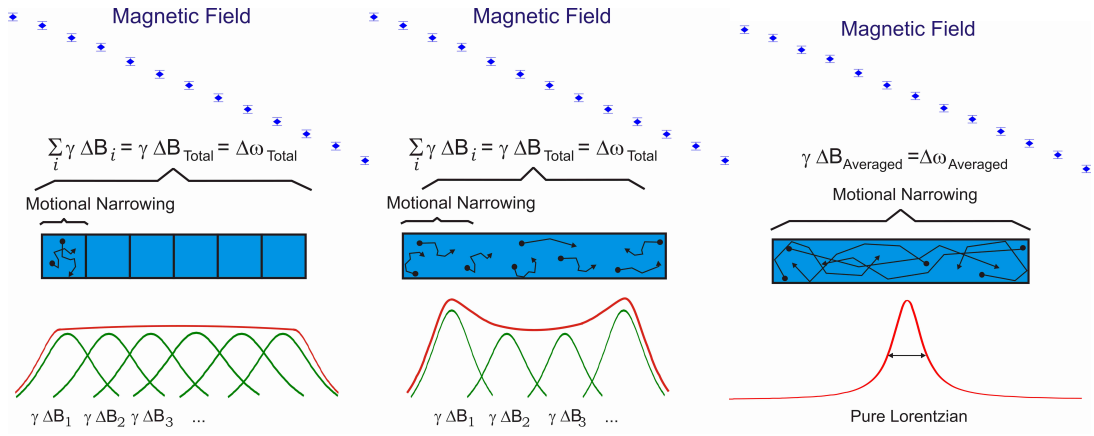

(a) $l_s/l_g \approx 20$ (b) $2 < l_s/l_g < 20$ (c) $l_s/l_g \approx 2$

Figure 6.57: Example of spectra composed by the sum of several Lorentzians motionally narrowed.

gives rise to a narrowed Lorentzian spectrum. In this picture, the particles cannot move from one volume to the next. As a result, the Lorentzians obtained from each volume sum up to a complicated spectrum. This example represents a slow-exchange situation where l_s/l_g is close to 20.

In figure (b), the walls have been removed so the particles can move larger distances and thus increasing motional narrowing. However, the diffusion coefficient is not so large that the helium atoms can travel all across the sample cell. This situation is equivalent to a cell divided by imaginary walls at a distance equal to the maximum diffusion length. That corresponds to a ratio $2 < l_s/l_g < 20$. In addition, particles close to the cell walls will travel a shorter "effective" mean path, resulting in an edge enhancement effect. As a result, the motion of the particles produces an averaging of the B field in such a way that every Lorentzian is narrowed. The result is a narrowed spectral width which slightly underestimates the actual B field distribution within the sample.

Lastly, figure (c) shows a situation in which the diffusion coefficient is so large that the particles can move across the complete cell during the duration of the experiment. This results in pure fast-exchange limit ($l_s/l_g \approx 2$) and therefore produces a narrowed Lorentzian profile. The width of the Lorentzian corresponds to an $\Delta\omega = \gamma\Delta_{\text{Averaged}}B$ were $\Delta B_{\text{Averaged}}$ is the averaged field seen by the particles due to their motion during the duration of the experiment. It is, therefore, an underestimation of the actual B field distribution within the sample.

Our experimental conditions are close to situation (b). The resulting spectrum is the addition of Lorentzian curves produced in individual volumes (of a length approximately equal to the maximum diffusion length), or equivalently, the final NMR-signal is the addition of all the exponentially decaying signals coming from the different volumes (each of them with its particular T_2^*). As a consequence, the width of the resulting spectra (or equivalently, the longest (total) T_2^*) corresponds, as a first approximation, to the total

field gradient within the sample volume:

$$\frac{1}{T_2^*} \approx \sum_i \gamma \Delta B_i = \gamma \Delta B_{\text{Total}} = \Delta\omega_{\text{Total}} \tag{6.55}$$

Where it has to be noticed that ΔB_{Total} is a field distribution which has been narrowed due to the motion of the atoms and therefore $\Delta\omega_{\text{Total}}$ is an underestimation of the actual spectral width. The fastest the movement the larger the underestimation ($l_s/l_g \to 2$). Therefore, we are interested in measuring with large values of the coefficient l_s/l_g. An estimation of the actual spectral width is necessary in order to properly define a "representative" frequency of the spectrum as the magnetic field value within the cell. As it will be seen later in this section, the choice of the "representative" frequency as the value at the spectrum maximum is not the ideal option.

Lastly, the arguments given here allow us to understand two effects observed in the measurement:

- The lower the pressure (larger D and consequently larger mean path), the smaller the value of the quotient l_s/l_g and, therefore, the narrower the peak (motional narrowing). This has been experimentally observed, see appendix C.4.
- Since the quotient l_s/l_g is larger at the DV than at the AP, the experimental conditions at the DV are closer to the slow-exchange limit than at the AP. Therefore, the DV spectra are broader, and equivalently present shorter T_2^*, than at the AP. This will be experimentally observed later in this section.

6.3.3.1 Signal characteristics at the DV

The NMR-signals recorded at the DV region (figure 6.58) show a clear exponential decay. This is the simplest model which can be considered: a sinusoidal wave decaying exponentially, due to the field inhomogeneities, with a time constant T_2^*. A signal corresponding to the DV region with beamtime configuration has been fitted to such a signal. The first graph, (a) shows the complete signal where the first 0.4 ms have been truncated to eliminate the DC-peak located at the beginning of the signal (see section 6.3). At 0.4 ms the DC peak is not completely removed but strongly reduced: the remaining DC peak has only 0.2 V of height whereas the signal amplitude is still 1.5 V.

The model does not adjust properly for the complete length of the signal (see figure 6.58 (a) and (b)). Therefore, a second fit was done for times longer than 1 ms. This indicates that the signal is composed of several exponentially decaying components with different T_2^* which add together producing a broadening of the Lorentzian profile (figure 6.58 (c)). After some time (~ 1 ms) those components with small T_2^* are vanished leaving only the components with longer T_2^* (figure 6.58 (d)), i.e., a narrower Lorentzian curve. This "double-peak" profile agrees with the picture described in section 6.3.3.

In order to extract the center and width of the spectrum, the complete spectrum (figure 6.58 (a)) is fitted to a double Lorentzian. The center of the spectrum is calculated as the center of mass of the spectrum (of the two Lorentzians), and the spectral width is the total width resulting from the addition of the two Lorentzians.

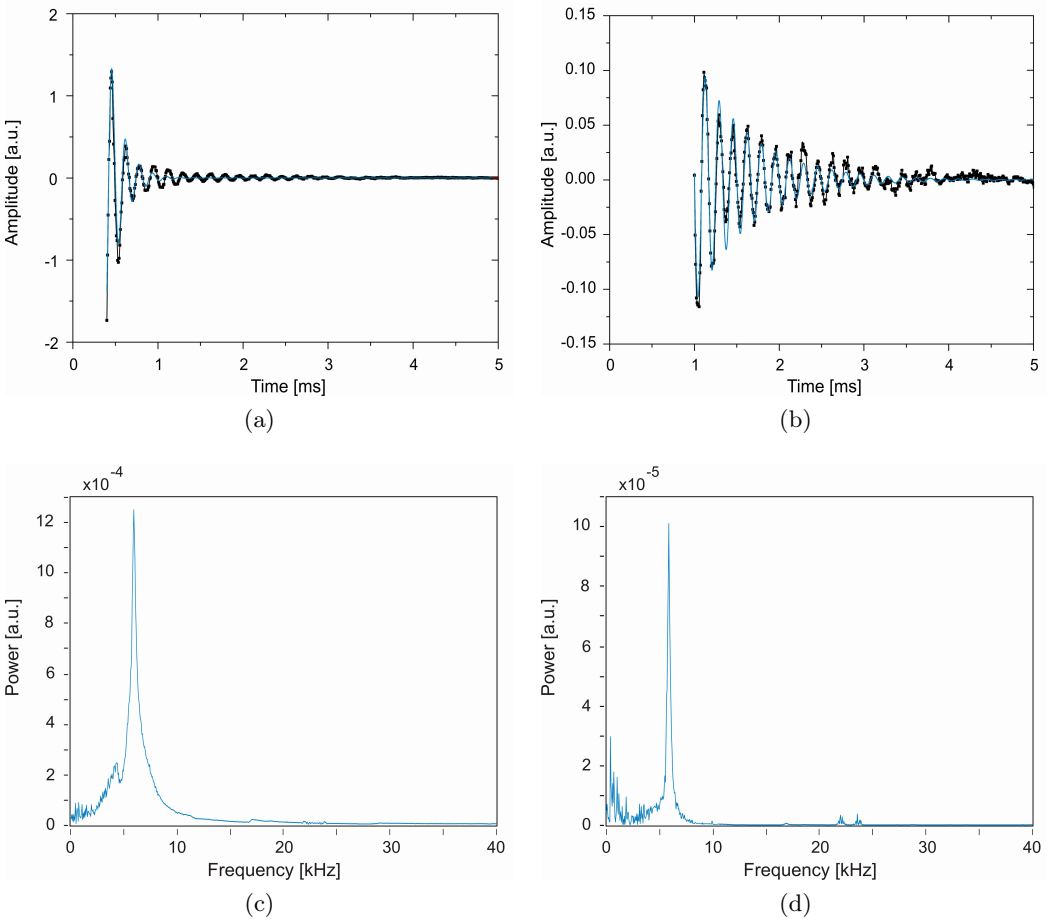

Figure 6.58: (a) and (b) NMR signal produced in the DV-sample in beamtime configuration (chapter 5). The signal has been truncated up to the first 0.4 and 1 ms respectively. The fit of the signal to an exponentially decaying sinusoidal wave is shown in blue. (c) and (d) are the power spectra of signal (a) and (b) respectively.

We can also check that the data obtained from the fit and from the width of the spectrum are coherent and give expected results. For the case of the signal shown in figure 6.58 (d), the complete width of the spectrum results in 1100 Hz, which implies a T_2^* of around 0.9 ms. If the complete signal is used, (c), the spectrum shows a width of around 6200 Hz, i.e., a T_2^* of 0.16 ms. Both values of T_2^* agree with the fits (b) and (a) which provide values of 0.6 and 0.15 ms. Making use of the relation 6.55 and the value of $\gamma_{^3He} = 32.436\,\mathrm{MHz/T}$, the inhomogeneity of the field in the complete volume of the sample turns out to be $\Delta B_0 = 1.9\,\mathrm{Gauss}$. In a magnetic field of $\approx 2.17\,\mathrm{T}$ this ΔB_0 represents an inhomogeneity of $\Delta B_0/B_0 = 9 \times 10^{-5}$, a result which agrees in the order of magnitude with the magnetic field simulation (see appendix C.5).

The case of main field configuration (chapter 5) is shown in figure 6.59. Similarly to the previous case, the signal in figure 6.59 present fast decaying components which are gone after less than 2 ms. The resulting T_2^* are on the same order of magnitude than that of the beamtime configuration, see table 6.16. The fact that the secondary peak remains even after a large truncation permits a better estimation of the width of the complete

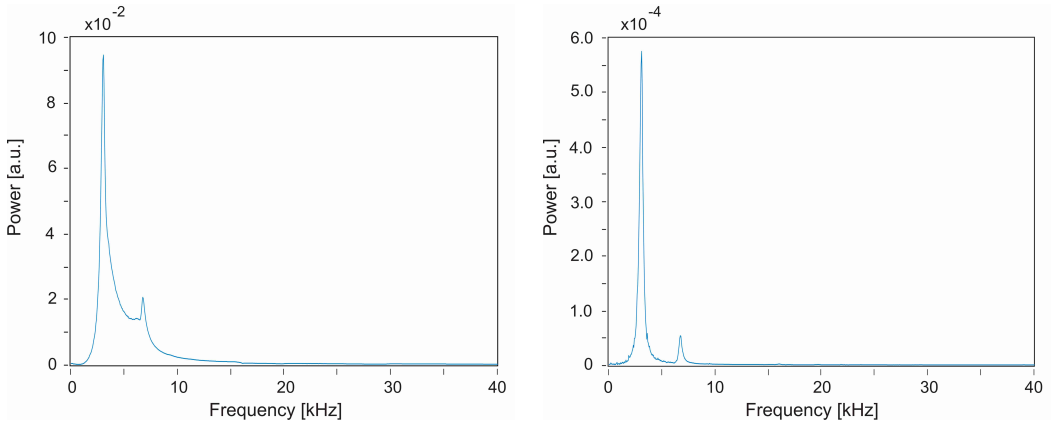

(a) (b)

Figure 6.59: Power spectrum of the signal obtained in the DV region with main field configuration. (a) and (b) are obtained after a truncation of 0.2 ms and 1 ms respectively.

spectrum, in contrast with the beamtime configuration where the truncation produces a considerable narrowing of the signal.

It is important to note that the shape of the power spectrum is not completely trustworthy due to the filters of the lock-in amplifier. The lock-in amplifier possesses several filters which attenuate frequencies far away from the resonance (see figure 6.70). In the case of the DV ($\omega_0 \approx 70.4\,\text{MHz}$), a complete attenuation of the signal at around 11 kHz away from the resonance has been experimentally measured. Therefore the second peak observed at about 7 kHz is already considerably attenuated. Measurements shifting the reference frequency, ω_R, demonstrated that both peaks have approximately the same height if they are compared at the same frequency, $(\omega_R - \omega_S)$ (see section 6.2.2), and so they experience the same amplification/attenuation from the lock-in amplifier.

From the analysis of the NMR-signals at the DV we can conclude:

- The fact that the signal contains fast decaying components implies that the truncation of the signal affects the resulting spectra and therefore the estimation of the width and center of the field distribution.
- Most of the NMR-signals measured at the DV present an amplitude in the same order of magnitude, or even smaller, than the height of the DC-peak (see section 6.3.1). This demands the application of a truncation as large as $0.7-1$ ms. Together with the small T_2^* values of the DV signals, the loss of information is considerable, producing a large modification of the spectrum profile and low signal to noise ratio.
- For the largest truncations, only one peak of the spectrum remains visible. In these cases we are forced to fit the spectra to one Lorentzian and the width of the field distribution is, thus, an underestimation of the real value.

6.3.3.2 Signal characteristics at the AP

The model of a FID-signal discussed above is a simple construction which makes possible to understand the DV-sample signals. Nevertheless, the signals generated at the AP region are more complicated (see figure 6.60), and thus a more elaborated model has to be built.

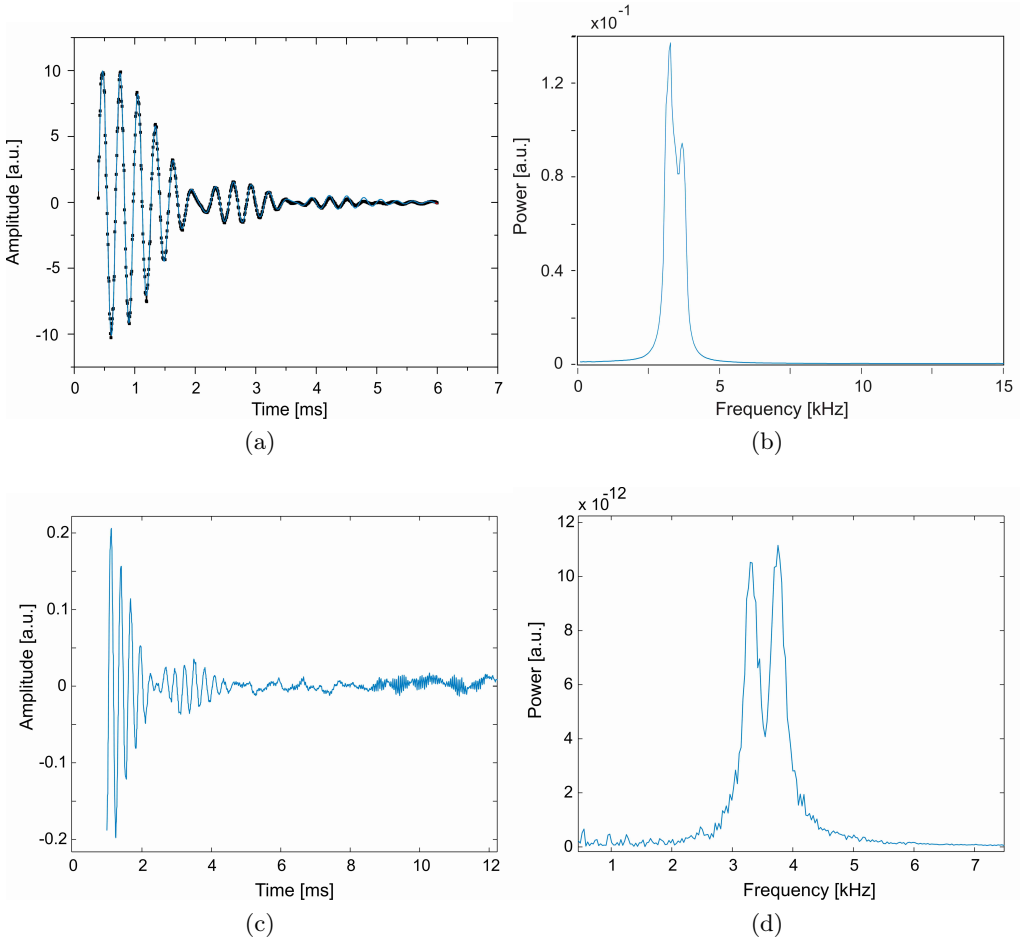

Figure 6.60: Typical signal produced at the AP region and its power spectrum. (a) and (b) represent a high amplitude signal where a short truncation length is sufficient. (c) and (d) show the narrowing of the individual Lorentzian peaks when a large truncation length is necessary.

The shape of the signals observed in figure 6.60 can be reproduced if, instead of a single frequency component, the total signal is considered as the superposition of a frequency (field) distribution. Calculations of the signal induced by a magnetic field distribution can be found in appendix C.3.

The best result is obtained by constructing a signal composed of two main frequency components with a frequency distribution around each of them. The power spectrum of such a signal results in two Lorentzian curves centered each of them around the respective central frequency and broadened due to the frequency distribution. With these considerations, the measured signal shown in figure 6.60 (a) has been fitted to the following

function:

$$s(t) = M_1 e^{-t\lambda_1} \frac{\sin\left(\frac{\Delta\omega_1}{2}t\right)}{\frac{\Delta\omega_1}{2}t} \cos(\omega_1 t) + M_2 e^{-t\lambda_2} \frac{\sin\left(\frac{\Delta\omega_2}{2}t\right)}{\frac{\Delta\omega_1}{2}t} \cos(\omega_2 t) \tag{6.56}$$

where $\lambda = \frac{1}{T_2^*} \approx \gamma\Delta B = \Delta\omega_0$. The center of the spectrum is defined as the center of mass of the two Lorentzians and the complete width of the spectrum is defined as the addition of half of the width of the Lorentzians plus the distance between them. This permits the estimate of complete T_2^* of the signal from a "global" $\Delta\omega_0$, or vice versa. The result obtained for figure 6.60 is a power spectrum with a width of 1200 Hz which corresponds to a T_2^* of 0.8 ms. This result agrees with theoretical calculations (see tables 6.16 and 6.17). The inhomogeneity of the field according to the magnetic field simulations (appendix C.5), around 0.4 Gauss, at the region of the NMR-sample cell also produces a spectral width in the order of 1.4 kHz. Note that in this case the fit is adjusting properly to the complete signal providing one unique T_2^* for the complete signal length. This illustrates that all the frequency components of the signal have a similar T_2^*.

The external correction coils at the AP intended to correct the position of the local maximum of the magnetic field are not supposed to change the homogeneity of the field to an important degree. Therefore, results similar to those obtained with main field configuration are expected (see table 6.16).

From the analysis of the NMR-signals at the AP we can conclude:

- Although T_2^* is similar in the DV and AP samples, the amplitude of the signal is much bigger in the AP sample. This permits us to apply much shorter truncation lengths and still conserve a good signal to noise ratio, even for long truncation times.
- The AP-sample PS is always composed of two visible peaks. Therefore, the width of the spectra is always obtained from the widths of the two Lorentzians plus the distance between them.

A summary of the results of the fits to the signals obtained in the DV- and AP-samples can be found in table 6.16. The first value corresponds to the shortest T_2^*, i.e., to the broadest peak and, thus, it contains the information of the width of the complete field distribution. The second value (in brackets) is important since it tells us how long the signal lasts before vanishing and contains the frequency information of the narrowest peak of the spectrum.

T_2^*	DV	AP
main field configuration	0.17 (0.7) ms	0.8 ms
beam-time configuration	0.15 (0.6) ms	0.8 ms

Table 6.16: Summary of the T_2^* obtained from the fits to the calculated induced signal. In the DV two values are given; the first value is the shortest T_2^*. It explains the broad width of the spectrum. The second value, in brackets, indicates the longest T_2^*, and therefore the duration of the complete signal. This is the part of the signal which produces the narrow component of the spectra. At the AP the fit function adjusts to the complete signal length, therefore only one T_2^* value is given.

The results obtained here have been compared with the theoretical prediction following the expression developed by McGregor, equation 6.34, for a cylindrical shaped cell. The results (table 6.17) are in good agreement with the measurements. This is a clear indication of the goodness of the magnetic field simulation. Note that the values of T_2^* obtained from McGregor correspond to the total width of the magnetic field distribution and therefore have to be compared with the smallest values obtained from the fit; the values without brackets in table 6.16.

	T_1 s	D cm^2/s	$\partial H_z/\partial L$ Gauss/cm	$\partial H_z/\partial r$ Gauss/cm	T_2^* ms
DV (main field conf.)	20.3	2.15	0.2	1.1	0.09
DV (beam-time conf.)	15.3	2.15	0.3	1.9	0.05
AP	1.81	2.15	0.08	0.5	0.6

Table 6.17: Calculation of the T_2^* according to equation 6.34. T_2^* is calculated for a cell dimensions: $a = 0.3\,cm$ and $L = 1.5\,cm$. The magnetic field inhomogeneity has been obtained from magnetic field simulations, appendix C.5.

6.3.4 Dead-time truncation

In cases where the amplitude of the signal is in the order of magnitude or lower than the height of the DC-peak, the signal gets masked during its first oscillations, producing a deformation of the signal spectrum (see section 6.3.1). This can be considered as a dead-time during which the signal cannot be "used". The dead-time is different for the DV and AP regions since the amplitude of the signals is different in both regions. Furthermore, the decrease of the helium density after every filling leads to different dead-time truncations as well. These facts introduce a dependence of the truncation length on the amplitude of the signal which has to be studied separately in the DV- and AP-samples.

Signal in the DV-sample

During the analysis of the data the truncation length was varied and a dependence of the center and width of the spectrum was found. As it can be seen in figure 6.61 (a), in signals with small amplitude, the center of the spectrum decreases for increasing truncation lengths, but converges to a constant value at about 1 ms. This is because the DC-peak produces low frequencies components which modify the shape of the spectrum, shifting its center to lower values. Once the truncation length is long enough to remove the DC-peak, the actual spectrum center can be seen.

Signals with large amplitude, (c), show a constant value of the spectrum center independently of the truncation length. In these signals, the low frequency components of the DC-peak are negligible compared to the spectrum height and therefore the truncation does not affect considerably the spectrum center.

A similar phenomenon occurs with the width of the spectrum (see figures (b) and (d)). However, signal components with short T_2^* may have been removed due to the truncation, hence, producing a narrowing of the spectrum. In signals with large amplitudes (figure (d)) the real spectral width can be seen for short truncation times. For longer truncation

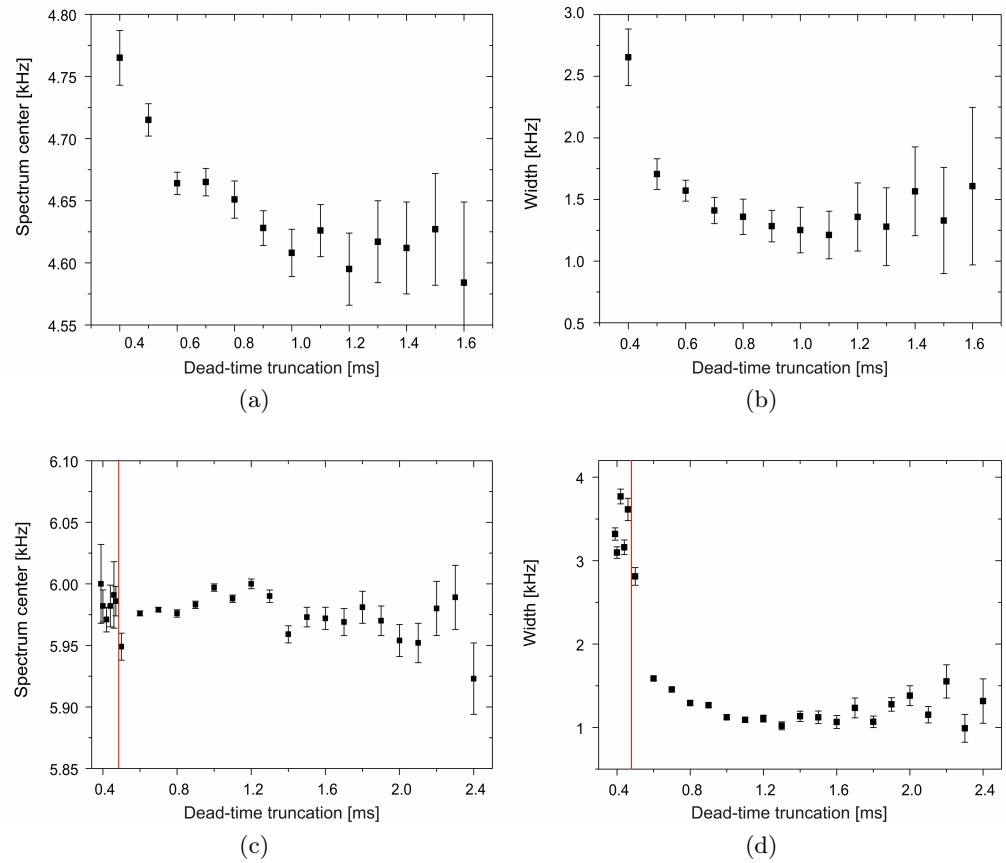

Figure 6.61: Spectrum center and width of the power spectrum in the DV-sample for different truncation lengths with beamtime configuration. (a)-(b) Standard signal. (c)-(d) Signal with high amplitude. The width for origin time cuts shorter than 0.5 ms has been scaled by a factor 0.5 in order to fit in the graph scale.

lengths, a drop of the width value is seen once the fast decaying components have vanished (marked with a red line). Note that this moment coincides approximately with the length of the signals components with small T_2^* values (broader components, table 6.16). In signals with small amplitude the real width gets masked by the DC-peak and cannot be estimated.

A decrease in the error bars as the truncation length increases is also observed. This occurs as a result of the lower noise introduced by the DC peak (see figure 6.61). Once the DC-peak has been eliminated, the error bars increase again with the truncation length as the signal to noise ratio decreases.

Sets of measurements with equal conditions but decreasing amplitude (due to the longitudinal relaxation time) show that the center of the spectrum remains constant independently of the amplitude of the signal for a fixed truncation length in the interval between 0.8 to 1.4 ms (figure 6.62). The error bars and the dispersion of the measurement increase with every new measurement due to the lower polarization and therefore lower signal to noise ratio.

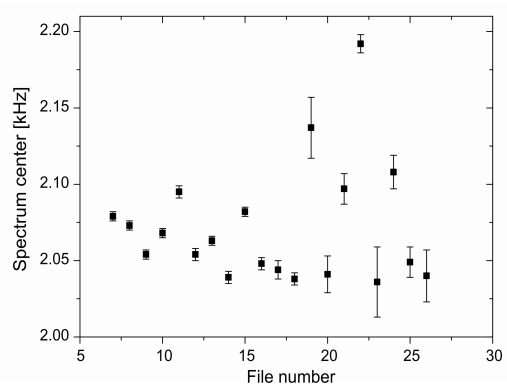

Figure 6.62: Spectrum center in a set of consecutive measurements with decreasing polarization. The truncation length is fixed for all the measurements.

As a conclusion, the center of the spectrum can be extracted from every measurement by just following the restriction of using a truncation length in between 0.8 to 1.4 ms, approximately. The width can only be extracted from a very few measurements with especially high amplitude. These measurements correspond to the first measurements taken with a new storage cell, i.e., with high polarization and high pressure.

Signal in the AP-sample

Due to the double peak structure of the power spectrum in the AP-sample, the spectrum is fitted to the sum of two Lorentzian functions. The center of the spectrum is defined as the center of mass and the width as the full width at half maximum of the complete spectrum (calculated from the individual widths of the peaks plus the distance between them). This model adjust properly to the measurements producing a very good fit and permits a direct estimation of the center and width of the spectrum.

The center of the spectrum calculated for different truncation lengths shows a constant value (figure 6.63 (a)). The error bars are large for short truncation times due to the noise introduced by the DC-peak. As the truncation increases, the error bars and the dispersion of the measurements increase again as the signal to noise ratio gets worse. As in the case of the DV-sample, signals with small amplitude need a longer truncation time, however, in the AP-sample the signals present much higher amplitude making the analysis easier.

In section 6.3.3.2, one single T_2^* for the complete signal length was found in the AP-sample signals (see table 6.17). This illustrates that all the frequency components of the signal have a similar T_2^*. The lack of fast decaying components makes the spectral width constant even for large truncation times. The periodic variation of the spectral width observed in figure 6.63 (b) is a mathematical artifact produced by the power spectrum (see appendix C.4). This can be corrected, as explained in the appendix, and the real width of the spectrum can be reconstructed.

6.3.5 Limits of the fit

The next step is to consider the stability of the fit with respect to variations in different parameters. On the one hand, the initialization of the fit parameters (offset, amplitude,

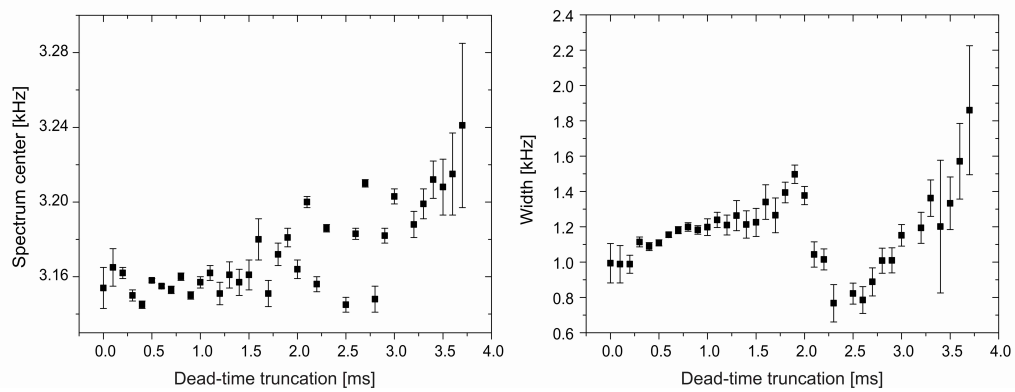

(a) Maximum Position (b) Width

Figure 6.63: Spectrum center and width of the power spectrum in the AP-sample for different truncation lengths.

width, etc.) has shown no effect. A poor initialization of the parameters does not give a wrong fit or big error bars but makes the fit procedure fail. An initialization of:

Threshold [a.u.]	$2 \cdot 10^{-6}$
Amplitude [a.u.]	0.01
Width (λ) [Hz]	400

Table 6.18: Fit parameters initialization.

has proven to be a good convergence for both cases, DV and AP. The maxima position is initialized with the values obtained from a maxima search algorithm. The rest of the parameters are set as fixed. Note that the width (λ) is the width of the Lorentzian as defined by LabView. The spectral width and the width of the magnetic field distribution over the sample volume has to be calculated by using:

$$\pi\lambda = \Delta\nu_0 = \gamma\Delta B_0 \qquad \text{with } \gamma = 32.436\,\text{MHz/T} \tag{6.57}$$

On the other hand, the fit limits, i.e. the range of frequencies used for the fit, have to be specially considered for two reasons. First of all, the highest amount of noise is grouped around 0 Hz and decreases strongly with the frequency (section 6.3.1). The inclusion of this noise in the fit limits has to be avoided as much as possible. However, the high attenuation of the lock-in amplifier (section 6.5.1) for high frequencies push one to always work with the spectra centered at low frequencies, which in turn forces us to work with a low value for the lower fit limit.

Secondly, thought it is advisable to use a high frequency value for the upper fit limit as the noise is minimal in this region, the power spectra present an extra peak at around 10 kHz produced by the lock-in amplifier. The upper limit, thus, has to be set below the 10 kHz peak in order to avoid influences on the fit result.

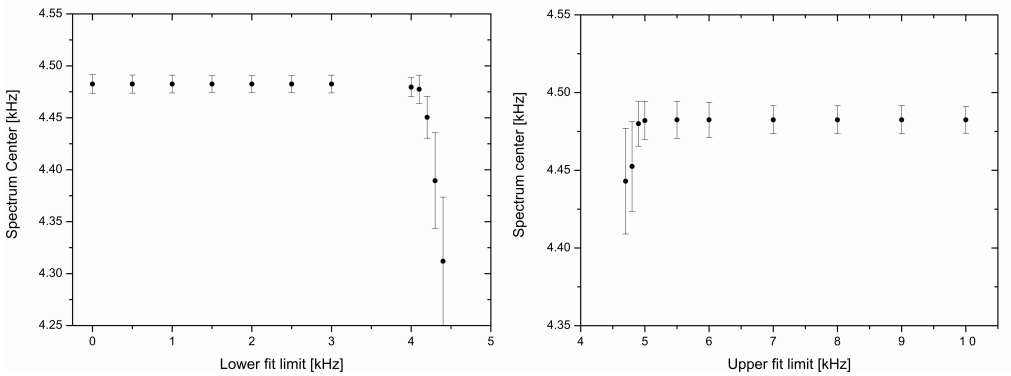

(a) (b)

Figure 6.64: Center of the power spectrum for different fit limits.

Figure 6.64 shows the center of the spectrum for different limits. The values are practically constant for fit limits far away of the spectrum and drift when part of the spectrum is cut. In cases with low signal to noise ratio, larger error bars and larger fluctuations of the center of the spectrum are observed. In this case, the center of the spectrum is slightly shifted and the error bars decrease as the lower fit limits increases due to the distancing from the low frequency noise. When the upper fit limit increases, the center of the spectrum remains constant while the error bars decreases. In this case, the information of the Lorentzian offset increases, hence, improving the quality of the fit and reducing the offset which converges to the noise level. The error bars shown in the figure correspond to the errors of the fit.

The shift of the maximum center due to the fit limits is approximately ± 10 Hz, which is negligible compared to the dispersion of the measurements itself. For the data analysis the upper fit limit was established as the highest possible, 9.5 kHz, and the lower limit was chosen to be in between 0.3 to 0.8 kHz depending on the position of the NMR-spectrum and the level of the low frequency noise.

The same study has been performed for the spectral width of signals originating in the AP-sample. The error due to the fit limits has been estimated to be ± 30 Hz. Due to the small amount of data from which the spectral width of signals originating in the DV-sample can be extracted, such an analysis is not necessary. Instead, the width is estimated from the small amount of useful data (high amplitude signal) and the error bars are conservatively estimated to a safe range (see section 6.3.6).

6.3.6 Error estimation

The three systematic errors present in our NMR-Magnetometer are described next and summarized in table 6.19:

1. **Dead-time truncation:**

   Due to the different signal to noise ratios in each measurement, the truncation length has to be selected independently for every measurement. In the case of the

DV-sample the truncation length needed to obtain the spectrum center has to be selected in the flat region in figure 6.61 (a), i.e., between 0.8 and 1.4 ms. The error corresponds to the dispersion of the measurements in this region: ±100 Hz. In some specific cases we have been forced to use even lower value. In such a cases a specific error bar has been selected.

The width of the spectrum in the DV-sample signals is determined with a high uncertainty due to a dearth of measurements with quantifiable signal amplitude. For this reason, we have been forced to make a conservative guess of the error bar which ensures all the values obtained for the width are covered: ±900 Hz.

In the case of the *AP-sample*, the error in the determination of the spectrum center has been set to ±40 Hz because the signal to noise ratio is better there and, therefore, the dispersion of the values is smaller.

The width of the spectrum can be accurately determined here thanks to the high amplitude of the signals. However, a positive shift to higher values of the width is produced for any truncation length (see appendix C.4). In such a case, an offset correction is applied. The offset correction for the width at the AP is tabulated in table C.38.

2. **Fit limits:**

   In order to take into account the small variations of the center and width of the spectrum due to the fit limits, an error of ±10 Hz for the center and ±30 Hz for the width of the spectrum is chosen for the AP region. At the DV region we also assign an error of ±10 Hz to the center of the spectrum.

3. The strongest effect on the final error bar comes from the **accuracy of the radio frequency generator**. The accuracy according to the manual of the radio frequency generator, is ±2 ppm/year of aging rate plus ±10 ppm due to temperature effects in the internal time base (valid from $0 - 55\,^{\circ}\mathrm{C}$). Since the date of the last calibration is unknown, we have to make a reasonable estimation of the present accuracy.

   The objective of these measurements is to prove the working principle of the *a*SPECT NMR-magnetometer and to study the stability and reproducibility of the ratio of the magnetic field. At present, the ratio of the magnetic fields at the NMR-samples position is not necessary. For this reason, we are interested in estimating the errors as they would occur for a beamtime, i.e., after a recent calibration. Therefore, we assume that the generator had been calibrated a few months before a beam time, i.e., ±2 ppm (per one year) plus ±10 ppm. In order to be conservative both components have been added linearly. Still, twelve parts per million correspond to a relative error of $1.2 \cdot 10^{-5}$, a value better than necessary for *a*SPECT.

	Error summary [Hz]			
	Decay Volume		Analyzing Plane	
	Spectrum center	Width	Spectrum center	Width
Statistical	±1 to ±130	±500	±1 to ±130	±2 to ±430
Dead-time truncation	±100		±40	(tab. 6.20)
Fit Limits	±10		±10	±30
Frequency Generator	±850	—	±170	—

Table 6.19: Statistical and Systematic errors.

truncation length [ms]	0.5	0.6	0.7	0.8	0.9	1.0
error [Hz]	±130	±150	±160	±170	±200	±240

Table 6.20: Error of the offset correction for the width of the spectrum at the AP.

The three systematic errors presented are independent and have to be added in quadrature. For the calculation of the magnetic field ratio systematic and statistic errors can be Gauss propagated independently, in such a way that the final result can also be presented with differentiated error bars.

6.4 Determination and characterization of the *a*SPECT magnetic field

In this section the analysis procedure explained previously is used to determine the absolute magnetic field values at the DV- and AP-sample positions. The ratio of the magnetic field r_B is calculated and its stability and reproducibility characterized. The analysis of the data will also permit to distinguish between the stability and reproducibility of the magnetic field (and its ratio) and that of the NMR-Magnetometer.

6.4.1 Absolute magnetic field (drift of the field)

The drift of the main magnetic field (chapter 5) at the DV-region due to power dissipation (section 5.2.2) is shown in figure 6.65. The error bars in figure (a) are not visible due the large scale of the plot. Figure (b) shows a zoom into one single day. The error bars do not include the accuracy of the r.f. generator in order to illustrate the high stability of the radio frequency generator (much better than its accuracy) and the robustness of the data analysis procedure.

These measurements have been fitted, obtaining a magnetic field drift of 1.8 and 9.2 kHz per day at the AP and DV regions respectively. That drift represents a relative change of about 0.013% per day. The effect of such a small drift in r_B has been already discussed in chapter 5. In simultaneous measurements at the DV and AP regions,

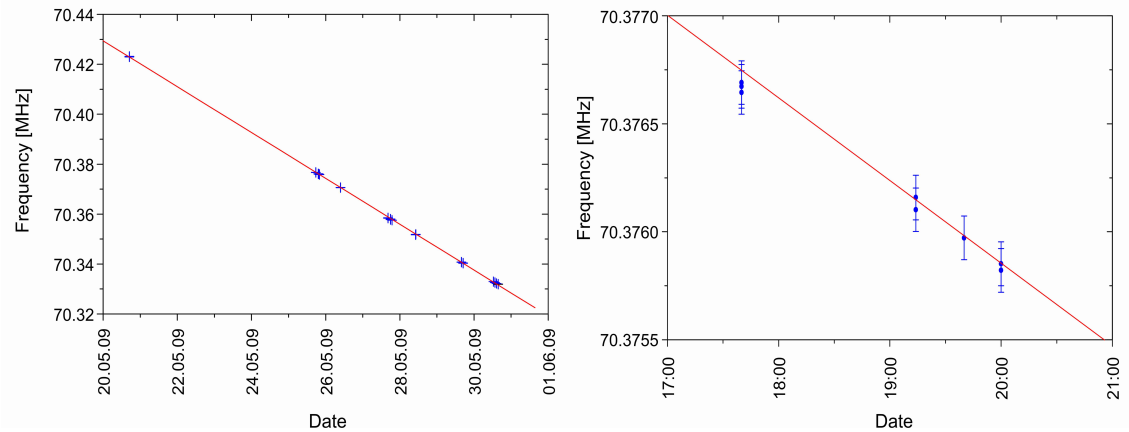

(a) (b)

Figure 6.65: Drift of the magnetic field at the DV region in main field configuration. (a) Complete set of measurements. Due to the large scale the error bars are not visible. (b) Zoom to the 25.05.2009. The error bars do not include the accuracy of the radio frequency generator.

the effect of the drift on r_{B} is negligible, therefore, only simultaneous measurement will be used for its calculation.

Similar measurements have been performed for beamtime configuration. As seen in chapter 5, the main magnetic field decreases slightly due to energy dissipation while the correction coils produce a constant field. This produces a change of r_{B} which is negligible for the duration of the measurements, about 10 days. Hence, the drifts measured in beamtime and main field configuration are very similar (see table 6.21). Three factors contribute to obtaining bigger error bars in beamtime configuration: the smallest signal amplitude, a shorter measurement period, and the effect of the constant field of the correction coils.

It is more useful to present the value of the magnetic field drift in relative terms: $(\Delta B/B)/\Delta t = -1.292 \cdot 10^{-4} \pm 2 \cdot 10^{-7}\mathrm{day}^{-1}$. This result has been obtained from the measurements in beamtime configuration (table 6.21). Note that $(\Delta B_A/\Delta t)/(\Delta B_0/\Delta t = r_{\mathrm{B}}$, however, this calculation is less precise than the calculation of r_{B} from simultaneous measurements, mostly due to the r.f. generator instabilities (see section 6.4.2). For this reason, the value $(\Delta B/B)/\Delta t$ has been calculated as an average of the combinations of the field drift values from table 6.21 with the ratio, r_{B}, in main field configuration from table 6.22.

	Main field configuration		Beamtime configuration	
	drift	error	drift	error
	MHz/day	MHz/day	MHz/day	MHz/day
AP	$-1.839 \cdot 10^{-3}$	$6 \cdot 10^{-6}$	$-1.84 \cdot 10^{-3}$	$3 \cdot 10^{-5}$
DV	$-9.18 \cdot 10^{-3}$	$5 \cdot 10^{-5}$	$-9.10 \cdot 10^{-3}$	$1.4 \cdot 10^{-4}$

Table 6.21: Magnetic field drift due to power dissipation.

6.4.2 Stability of the magnetic field ratio r_B

The magnetic field ratio r_B has been calculated from simultaneous measurements only. The error bars have been calculated considering all the errors listed in table 6.19.

The result (figure 6.66) shows a very stable r_B value during the complete measurement period. The dispersion of the measured r_B is completely covered by the error bars, being the systematical error of the dominant term. The biggest contribution to the systematical error proceeds from the accuracy of the radio frequency generator. Here we have to consider as well a possibly different stability and reproducibility of the r.f. generator at the two frequencies involved in the measurements (DV and AP). These measurements provide good evidence of the high stability of the ratio r_B during large periods of time and of the reliability of the measurement procedure and data analysis. As a result, the value of r_B is stable and its measurement is reproducible at a level better than necessary for the aSPECT spectrometer (see chapter 5). The final value, after averaging the measurements, is given in table 6.22.

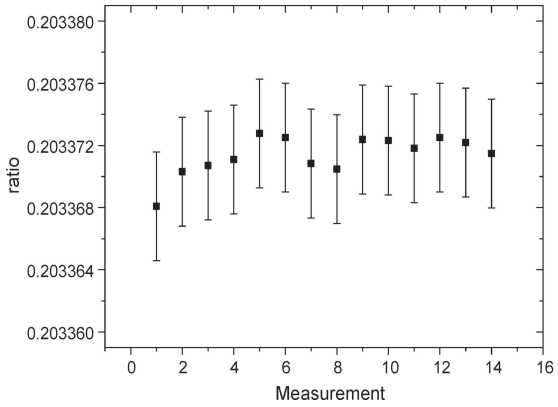

Figure 6.66: Magnetic field ratio represented with total error bars for the measurements with main field configuration.

The magnetic field ratio obtained with main field and beamtime configuration differs at a 0.19% level. This illustrates the strong influence of the correction coils on the magnetic field ratio. The stability of the ratio r_B demonstrated here permits the use of the same transmission function during the complete duration of an aSPECT beamtime, a fundamental requirement to obtain the aimed for accuracy in the measurement of the correlation coefficient a (chapter 5). However, since these measurements have not been performed in the running conditions of aSPECT (i.e. in the ILL experimental zone with neighboring experiments), this result has to be validated during a beamtime as well.

Configuration	ratio (r_B)	statistical error	systematical error	$\Delta r_B / r_B$
Main field	0.203371	$9 \cdot 10^{-7}$	$4 \cdot 10^{-6}$	$1.8 \cdot 10^{-5}$
Beamtime	0.202989	$9 \cdot 10^{-7}$		

Table 6.22: Magnetic field ratio

6.4.3 Reproducibility of the magnetic field ratio r_B

The reproducibility of the magnetic field (and its ratio, r_B) after every ramping up procedure is also a fundamental requirement in order to ensure that the off-line magnetic field measurements (chapter 5) are valid during the beamtime. Otherwise, two main problems appear: the actual transmission function during the beamtime is unknown and accurate proton trajectory calculations (e.g. for edge effect.) are not possible.

Several factors which can affect the reproducibility of the field have been discussed in chapter 5. The high accuracy, stability and reproducibility of the measurements performed with the NMR-magnetometer permits us to characterize the reproducibility of the *a*SPECT magnetic field accurately and to distinguish it from the instabilities of the Hall probe.

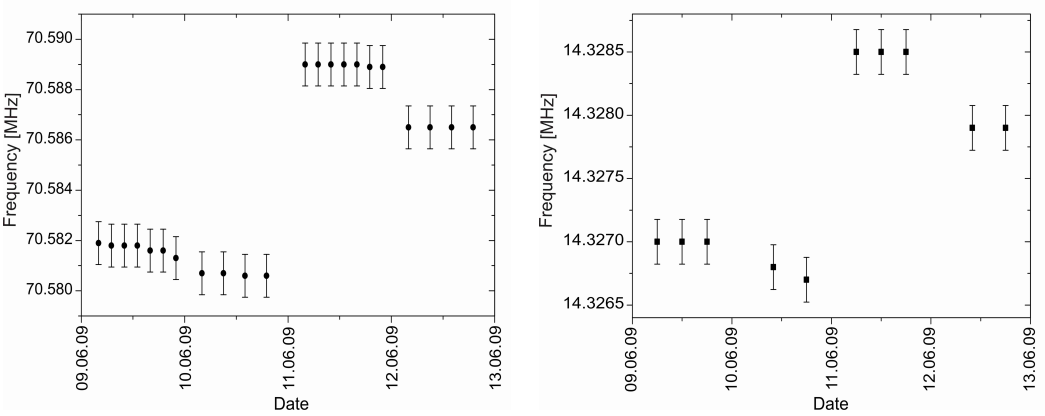

(a) Measurements at the DV (b) Measurements at the AP

Figure 6.67: Reproducibility of the magnetic field at DV and AP after several ramping up procedures. Measurements with beamtime configuration.

Similarly to the reproducibility tests performed with the Hall probe, a warming up procedure over the critical temperature is applied before every new ramping up procedure in order to remove hysteresis. In addition, the persistent mode was switched on after several hours (normally a complete night) in order to ensure that the power supply had reached the stable regime (see appendix B.1). This study has been carried out using the beamtime magnetic field configuration.

Figure 6.67 shows the magnetic field strength at the DV and AP-samples after several ramping up procedures. The error bars indicate that the different magnetic field strengths are not produced by the instabilities of the NMR-magnetometer. The maximum difference observed of 8 kHz (at the DV) corresponds to 2.5 G ($\Delta B/B \approx \pm 1.1 \cdot 10^{-4}$). This result confirms that the different magnetic field strengths (up to 11 G in the DV) measured with the Hall probe originate mostly from probe instabilities, a result which agrees with the conclusions stated in appendix B.1. Consequently, the maximum field variation observed with the NMR-magnetometer ($\Delta B/B \approx \pm 1.1 \cdot 10^{-4}$) fix an upper limit for the other sources of errors discussed in chapter 5 which, thus, should contribute to the field fluctuations on a lower level.

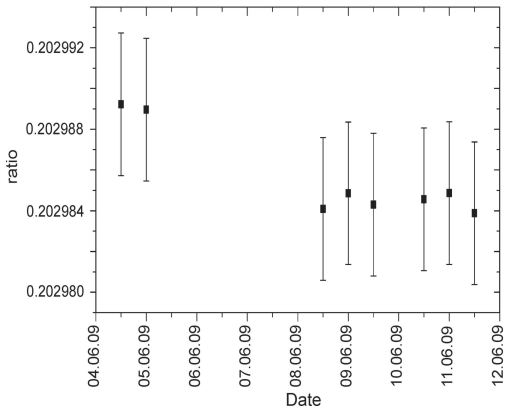

Figure 6.68: Magnetic field ratio reproducibility after several ramping up procedures with beamtime configuration.

As expected, although the absolute value of the magnetic field differs considerably in between ramping up procedures, the relative change in the DV and AP is similar, leading to a constant value of the ratio (see figure 6.68). The dispersion of the values is inside the error bars. As a result, we can affirm that the magnetic field ratio r_B is stable and reproducible at a relative level of $\Delta r_B/r_B = 2 \cdot 10^{-5}$

ratio (r_B)	statistical error	systematical error	$\Delta r_B/r_B$
0.202985	$1.3 \cdot 10^{-6}$	$4 \cdot 10^{-6}$	$1.8 \cdot 10^{-5}$

Table 6.23: Final value of the magnetic field ratio with the setup used during the ILL beamtime.

The final result is presented as the averaged ratio in table 6.23. This is the recommended value as it has been calculated considering stability and reproducibility measurements. However three important points have to further be considered before entering this value into the transmission function (section 3.3):

- The NMR magnetometer measurements have been performed off-axis. Therefore, in order to infer the magnetic field ratio, r_B, within the flux tube, an accurately simulated magnetic field map from the z-axis up to the sample position is indispensable. As it can be seen in table 6.25, the actual magnetic field simulation disagrees with the measurements at the position of the NMR-samples.

- The error due to the lack of calibration of the r.f. generator has not been considered in the present analysis. After an offset measurement and a recalibration of the device, the value of the ratio and its error bars have to be corrected.

- Although the definition of the spectrum center is precise and stable in every measurement, the size of the sample (and therefore the width of the spectrum) and the uncertainty in the sample position, introduce extra errors which have not been considered yet. For a definitive value of the ratio, r_B, these errors have to be taken into account (see appendix C.4), however they are not necessary for a stability and reproducibility study of the ratio. Considering these errors, the systematic error bar

of the ratio would have to be increased to $\approx 2 \cdot 10^{-5}$ which gives a $\Delta r_B / r_B \approx 8 \cdot 10^{-5}$. A relative error of $\Delta r_B / r_B = 8 \cdot 10^{-5}$ introduces an error on the angular correlation coefficient a in the order of $\Delta a/a = 0.07(4)\,\%$, which permits a measurement of the correlation coefficient a with the aimed accuracy $\delta a/a = 0.3\,\%$. Furthermore, this accuracy can be easily improved by reducing the sample size. This has been already tested and is discussed in section 6.5.

Effect on the magnetic field ratio $r_B = 0.202985$	Error	Relative error
NMR- Accuracy (*)	$4 \cdot 10^{-6}$	$1.7 \cdot 10^{-5}$
lack of calibration (**)	$6 \cdot 10^{-7}$ (extra per year)	$3 \cdot 10^{-6}$
width of the samples	$1.6 \cdot 10^{-5}$	$8 \cdot 10^{-5}$

Table 6.24: Magnetic field ratio r_B and uncertainties in beamtime configuration. (*) Considers all the error contributions listed in table 6.19.(**) Refers to the lack of calibration of the r.f. generator. Has to be added per each year without calibration.

At present, the magnetic field simulation is not reliable for the extraction of the ratio r_B on-axis from the measurements off-axis performed with the NMR-Magnetometer.

Position	r_B Hall probe	r_B NMR-magnetometer	r_B Simulation
On-axis (flux tube)	0.2030(2)	—	0.20304
NMR-samples position	—	0.202985(16)	0.20318

Table 6.25: Ratio of the magnetic field, r_B, obtained by three methods: Hall probe measurements (chapter 5), NMR-magnetometer (chapter 6) and magnetic field simulation (appendix C.5). Results on-axis (flux tube) and off-axis at the NMR-sample positions. Measurements with magnet in beamtime configuration. Note that the spectral width has not been considered in the ratio obtained via the NMR-magnetometer.

6.5 Improvements on the NMR-Magnetometer

The NMR-Magnetometer described in this work fulfills the requirements for a precision measurement of the aSPECT magnetic field. It has shown a very good stability and reproducibility as well as the precision required for an accurate magnetic field mapping.

Nevertheless some disadvantages have shown up during the data analysis. Based on their origins, they can be grouped in two categories: detection system and NMR-sample. Both affect the accuracy of the measurement and present difficulties in determining the width of the spectra. Note that to calculate the ratio rigorously the width of the field distribution has to be considered. Furthermore, these disadvantages also affect the data treatment and the later analysis. This makes the analysis a hard task which cannot be completely automatized.

For this reason some improvements on the NMR-Magnetometer have been considered and have been already tested to prove their viability and to demonstrate the increase of

the Magnetometer's performance.

Another disadvantage in the present setup, which has not been presented as it does not affect the data treatment and analysis, is aliasing effect produced when digitalizing the NMR-signal. It affects the detection system and, thus, it is explained next.

6.5.1 Aliasing

Aliasing refers to a distortion of a periodic analog signal due to the process of digitalization. For any sampling interval $\Delta t = \nu_s$, there is a critical frequency $\nu_N = \nu_s/2$, called the Nyquist frequency. If a sine wave of frequency ν is sampled at a frequency $\nu_s >> f$ the wave is completely determined, meanwhile with a sampling frequency equal or lower than ν, the sampled data reproduces a wave with a false aliased frequency, smaller than ν_N (figure 6.69).

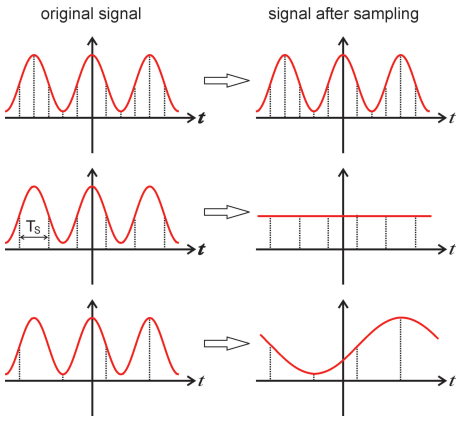

Figure 6.69: Aliasing produced due to an under-sampling of an analog signal. Left, original signal sampled at a frequency $\nu_s = 1/T_s$. Right reconstructed signal for different sampling frequencies.

Mathematically this is known as the sampling theorem: if a continuous function s(t), sampled at a time interval Δt, is bandwidth limited to frequencies smaller than ν_N, then the function s(t) is completely determined by its samples. In the case of working with a bandwidth limited function, the sampling theorem tells us that the entire information content of the signal can be recorded by sampling it at a rate $\nu_s = 1/\Delta t$ equal to twice the maximum frequency of our function. References [76] and [77] contain very complete information about Fourier transforms and their physical applications. Reference [78], *Numerical Recipes on C*, is widely used in this thesis and contains detailed information on Fourier transforms and their implementation in programming.

Furthermore, the act of sampling a signal creates incertitude in the frequency domain which in turn creates "ghost" spectra at both high and lower frequencies (see figure 6.26). The effect of the sampling process on the frequency domain can also be thought of as a partitioning into spectrally similar regions spaced at intervals of $\nu_s/2$. These regions are called Nyquist zones. Each zone contains a copy of the same spectrum. However, rather than being identical copies, the spectrum in each zone is the mirror image of the spectrum in the neighboring zone. A comprehensive explanation of the Nyquist zones applied to

radio frequency can be found in reference [79].

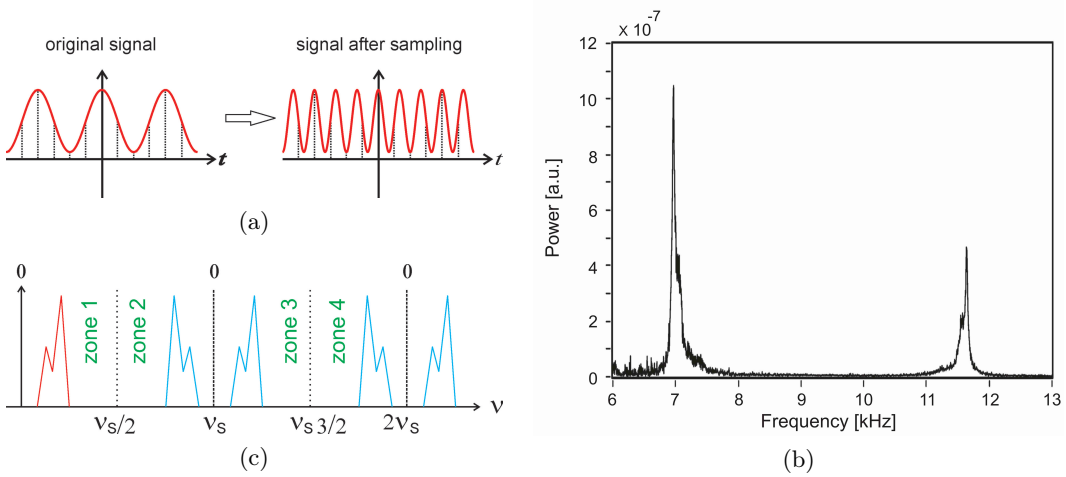

Table 6.26: (a) Reconstruction of a higher frequency signal due to aliasing. (b) Power spectrum measured with the lock-in amplifier. Filter settings: time constant 100 μs, filter slope 6 dB/oct. The spectrum at the right side of the graph is the mirror image of the left one, aliased into the first Nyquist zone. The different amplitude is due to the attenuation filter slope. (c) Nyquist zones created due to aliasing. Each zone contains a copy of the same spectrum where the image is the mirrored spectrum of the neighboring zone.

In our electronic setup, the NMR signal is sampled twice. The first sampling occurs in the lock-in amplifier (see section 6.2.2). According to the manual of the lock-in amplifier, the SR844 multiplies the signal by a (chopped) square wave at the reference frequency. The chopper is used to remove DC offsets and drifts over time and temperature. Unfortunately, the chopper produces spurious responses in the instrument. The ones which concern us are chopping sidebands at $\nu_{sb} = \nu_R \pm 2N \cdot \nu_c$, where ν_c is the chopping frequency and N is an integer. The lock-in amplifier mixes the NMR signal with the reference signal which also contains spurious frequencies, creating mixed signals at frequencies $\nu_M = \nu_{\mathrm{NMR}} - \nu_R$ and $\nu_{M_i} = \nu_{NMR} \pm \nu_{sb}$. As a result, the NMR-signal spectrum appears repeatedly at an interval which depends on the chopper frequency. For instance, the periodicity is about 19 kHz at an input frequency of 14.3 MHz and 23 kHz at 70.4 MHz (see figure 6.26 (b)). Note that the first peak is placed at −7 kHz and mirrored to +7 kHz due to the power spectrum.

However, the major problem is in discriminating between the real reference frequency and one of the side bands. Note that the output signal of the lock-in amplifier tends to 0 Hz when the NMR signal frequency is close to the real reference frequency ($\nu_M = (\nu_{\mathrm{NMR}} - \nu_R) \to 0$ when $\nu_{\mathrm{NMR}} \to \nu_R$) and when it is close to the side bands frequency ($\nu_{M_i} = (\nu_{\mathrm{NMR}} - \nu_{sb}) \to 0$ when $\nu_{\mathrm{NMR}} \to \nu_{sb}$).

The anti-aliasing filter of the lock-in amplifier does not solve this problem since it attenuates signals with high frequencies, but the duplicated spectra at the side bands do not have high frequencies because ν_{M_i} also tends to 0 Hz when $\nu_{\mathrm{NMR}} \to \nu_{sb}$.

Fortunately, the amplitude of the spurious signals is smaller than the amplitude of the real reference signal. Therefore, the height of the spectra will be lower when “sitting”

in a side band than when sitting at the real reference frequency. Figure 6.70 shows the amplitude of the output signal of the lock-in amplifier close to the real reference signal frequency and to the side bands frequency. The shape observed there is a combination of the anti-aliasing filter plus the amplitude of the signals at the side bands.

The only way to distinguish between the spurious spectra and the real spectra is by scanning for a wide range of frequencies in order to find the spectrum with the highest amplitude. Note that since the magnetic field drifts in time (section 6.4.1), the spectrum is shifting and thus this procedure has to be repeated every few days. Also note that in order to compare amplitudes, it is necessary to correct for the decrease of the helium polarization after each measurement.

The shape of this anti-aliasing filter depends on the time constant which is related to the low-pass filter bandwidth, $\Delta\nu_{LP} = 1/(2\pi\tau)$, and to the filter slope; 6 dB/oct, 12 dB/oct... (see figure 6.70). As it can be seen, the attenuation only changes the filter slope but not the position of the secondary resonances. The time constant changes the position and amplitude of the secondary resonance. A filter setting with narrower bands could be used in order to better distinguish the secondary resonances, however, this limits the range of visible frequencies, ν_M. Note that in order to see the complete power spectrum at the DV, which has a width of around 7 kHz, the narrow band of the 1 ms time constant filter is insufficient. The spectrum without filter is the broader one but presents a high level of noise. For this reason, the filter used during the measurements was selected to be 100 μs and 6 dB/oct.

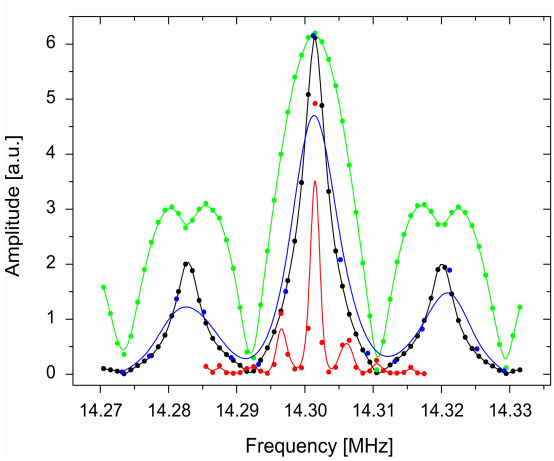

Figure 6.70: Attenuation filter of the lock-in amplifier at the frequency range of the AP for different settings. Green: no filter, black: 100 μs and 6 dB/oct, blue: 100 μs and 12 dB/oct, red: 1 ms and 6 dB/oct. The filter slope has been obtained by measuring the amplitude of the mixed signal (output of the lock-in amplifier) at different values of the reference frequency (for a fixed NMR signal frequency).

Other parameters to consider when selecting the filter are the **update rate** of the output signal and the **delay time** in the response of the lock-in amplifier.

The fastest update rate of the output signal is $48 - 96$ kHz for the 6 dB/oct, 12 dB/oct filter and no filter mode. The update rate is important in order to obtain quality signals from the lock-in amplifier, i.e., mixed signals with high sampling rate.

The instrument has a latency (delay time) of 3 sample periods. As an example, a time constant of 3 s with a filter slope of 12 dB/oct produces a delay of about 5 time constants. The configuration selected for the NMR measurements gives the fastest response and update rate. However, the integration time of the lock-in amplifier plus the residual r.f. pulse seen by the lock-in amplifier, produce the DC-peak discussed in previous sections.

The second aliasing is produced when the output signal of the lock-in amplifier is recorded by the NI-card. In this second aliasing, the situation is simpler. First, there is no attenuation for any range of frequencies (there is no filter). And second, the low frequency of the signal passed to the NI-card, a few kHz, compared to the maximum sampling rate of 250000 samples/s (125000 samples/s if X and Y components are recorded) ensures a complete determination of the spectrum. The aliased spectra are produced far away from the spectrum of interest and thus cannot interfere with it. Finally, the uncertainty between real and aliased peaks does not exist anymore because only the real spectrum will sit at frequencies close to 0 Hz.

We can summarize the negative consequences of the aliasing and spurious signals of the lock-in amplifier:

- In order to distinguish real spectrum from spurious ones, a frequencies scan has to be performed. Since the availability of polarized ^3He is limited, the amount of measurements useful for the determination of the field reduces significantly as does the amplitude of the signal.
- The anti-aliasing filter increases the delay time of the lock-in amplifier response and affects the integration time which, together with the residual r.f. pulse, produces the DC-peak at the beginning of the NMR-signal.

6.5.2 Mixer as a detection system

The lock-in amplifier has proven to be a very useful tool in measuring weak signals removing an enormous amount of noise. However, the aliasing effects and the DC-peak introduce important limitations and make a proper analysis of the magnetic field width at the DV region impossible.

For that reason the lock-in amplifier was substituted by a mixer followed by an amplifier with a low-pass filter (see appendix D.113). The working principle is the same as that of the lock-in amplifier (section 6.2.2). First the NMR-signal is mixed with the reference signal in order to get a mixed signal centered at $\nu_{\text{NMR}} \pm \nu_R$. The high frequency components ($\nu_{\text{NMR}} + \nu_R$) and the high frequency noise are eliminated by the filter with variable band width $\Delta\nu < 100$ kHz. Then the remaining signal, $\nu_{\text{Mixed}} = \nu_{\text{NMR}} - \nu_R$ is amplified.

This procedure does not have the advantages of the lock-in amplifier: better filtering and amplification algorithms, which also correct for offsets. However, since our working requirements are known, the electronics can be customized for our specific needs. The quality of the new electronics can already be seen in figure 6.72. The signal, even with the low thermal polarization of protons compared to the hyperpolarized ^3He, presents a good amplitude and signal to noise ratio: the cleanness of the power spectrum is noteworthy,

(b). Furthermore, the biggest improvement consists of removing the initial DC-peak. The DC-peak is now reduced to a single data point at the origin of the signal. This means that the mixer is also seeing the residual r.f. pulse of the spin flip, but since its duration is only $20\,\mu s$ and the mixer is not integrating, the distortion appears only in the first data point.

A second advantage is in avoiding the aliasing effect and the spurious signals of the lock-in amplifier. In the new electronics setup, the signal is digitalized only by the NI-card and, hence, only one aliasing takes place. Fortunately the sampling rate is so big, 250000 samples/s, that the aliased peaks will not interfere among them. Furthermore, as explained in section 6.5.1, there is no ambiguity in distinguishing the real spectrum from the aliased ones since the real spectrum is the one close to 0 Hz frequencies.

Lastly, the filter can be varied from a bandwidth of $\approx 8\,\text{kHz}$ up to $\approx 100\,\text{kHz}$. This permits one to see the NMR-signal even when scanning at about $\nu_{\text{NMR}} - \nu_R = 90\,\text{kHz}$ off-resonance.

6.5.3 Proton NMR-sample

Polarized ^{3}He is indicated for magnetic field measurements as it produces high amplitude signals with long T_2^*. However, it presents three major disadvantages:

- The biggest inconvenience is the fragility and high cost of the helium filling system. The copper-tube system used to introduce the helium is very fragile at the glass transitions and at the copper bellow. This makes the system very complicated to install and extremely expensive.
- Due to the limited helium supply, the number of measurements is limited to 10-12 measurements (for 1 L of helium at 1 bar) which have to be performed in a time frame of two days.
- The diffusion of the helium atoms gives rise to complex spectra which are also temperature and pressure dependent (see section 6.3.3). Furthermore, the width of the spectrum is especially sensitive to these changes of temperature and pressure (appendix C.4). Therefore, a constant temperature and pressure control and corrections of every measurements would have to be applied in order to use the spectral width to determine the field distribution within the sample cell.

Possible alternatives for the polarized helium are liquids containing protons. Liquids containing protons like water, acetone, alcohols or other chemicals have a high density and therefore thermal polarization occurs enough to produce an easily detectable signal. The use of liquids would result in a cheaper and more robust alternative method that can be used at any time and as much as desired. Furthermore, the self-diffusion coefficient of liquids is by orders of magnitude smaller than for gases. Then, the experimental conditions can be approximated to the static limit and then the estimation of the magnetic field distribution from the spectrum width becomes trivial (see section 6.3.3).

In order to check the feasibility of this method, a test setup was built in Mainz. The pick-up coil (6.71 (b)) was rebuilt to smaller dimensions and shielded inside a non-magnetic

metal box to protect from external noise sources. In order to work with similar frequencies than in the *a*SPECT magnet, the magnetic field was lowered to about 0.34 T. Note that the Larmor frequency depends on the magnetic field and on the gyromagnetic ratio (equation 6.6), which for protons is approximately $\gamma = 42.576\,\mathrm{MHz/T}$. Unfortunately, the available magnet is not able to produce magnetic fields high enough to work in the DV conditions so only the AP frequency was measured. The test setup is shown in figure 6.71 (a).

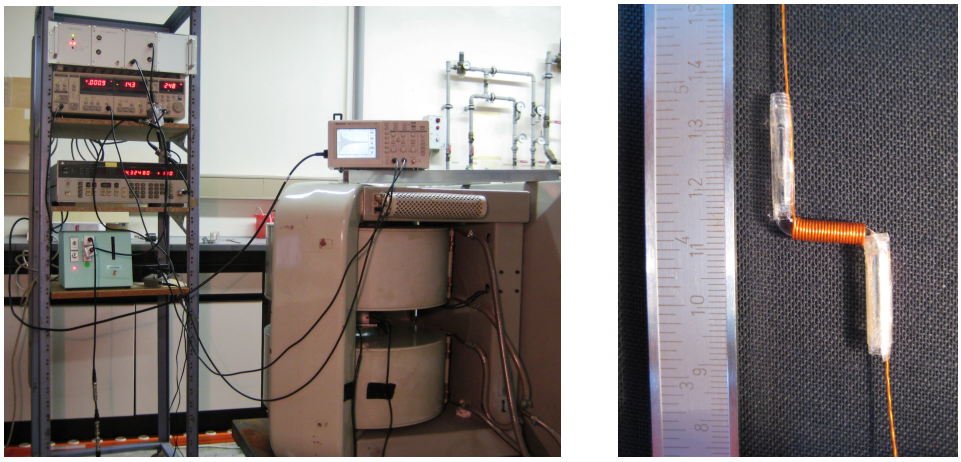

(a) (b)

Figure 6.71: (a) NMR test setup built up at Mainz university. Left, electronics setup, right, nmr magnet with resonant circuit and sample material. (b) NMR sample composed of acetone and ethanol on a ratio of 1:1 inside a Duran cell.

In gases, internuclear dipole-dipole interactions are completely negligible (see section 6.1.3), however, in solids and liquids, dipole-dipole interactions are large and cause a very strong relaxation resulting in a short T_2^*. However, in liquids these interactions are usually averaged out due to the Brownian movement of the particles, resulting in a larger T_2^* than in solids. Consequently, the best option is to find a material which remains in liquid phase at the low temperature range of the spectrometer. Several combinations of alcohols and acetone where tested. Finally, it was found that a mixture of acetone with ethanol in a ratio of 1:1 stays liquid up to 150 K, only 80 K above the estimated temperature inside the bore tube. The strategy is then to use a small sample so the heat load necessary to warm it up to 150 K is small and keeping, at the same time, enough material to produce a signal visible with our electronics.

The sample produced for that purpose is shown in figure 6.71. The cell is made of Duran glass because of its low content of ferromagnetic materials. The shape has been designed in order to give enough place for the pick-up coil, visible in the picture, and a heating wire used to warm up the sample material over its melting point. The third straight section is needed to seal the cell. The sample was filled by introducing the mixture with a syringe and cooling it down in such a way that the liquid is sucked into the sample volume. Afterwards, the air contained in the cell is warmed up in order to expand it and evacuate the cell. To seal the cell, it was cooled down with liquid nitrogen to freeze the mixture and afterwards, the glass was sealed with a torch.

The cable used for the pick-up coil is Kapton wire, suitable for ultra high vacuum. The wire can be reduced in diameter in order to increase the number of turns and therefore

the efficiency of signal reception. Only the precaution of keeping a low resistance has to be taken into account. The specifications of the coil are: L=1.25 cm, N=23 turns and r=0.14cm (inductance $\approx 327\,\mathrm{nH}$). The capacitor has a capacitance of 390pF. The heating wire used was tungsten with a resistance of $100\,\Omega/\mathrm{m}$. Twenty-nine turns presented a resistance of $35.7\,\Omega$ at room temperature. The dimensions of the sample cell are: $\phi = 3\,\mathrm{mm}$ and wall thickness of 0.5 mm.

Similarly to the helium magnetometer, the first amplifier was used at half of its power, the pulse amplitude was fixed to 316 mV (in the r.f. generator) and the flip angle was varied by the length of the pulse. The pulse length corresponding to a spin flip of $\alpha = \pi/2$ was found at $\tau = 2.5\,\mu\mathrm{s}$.

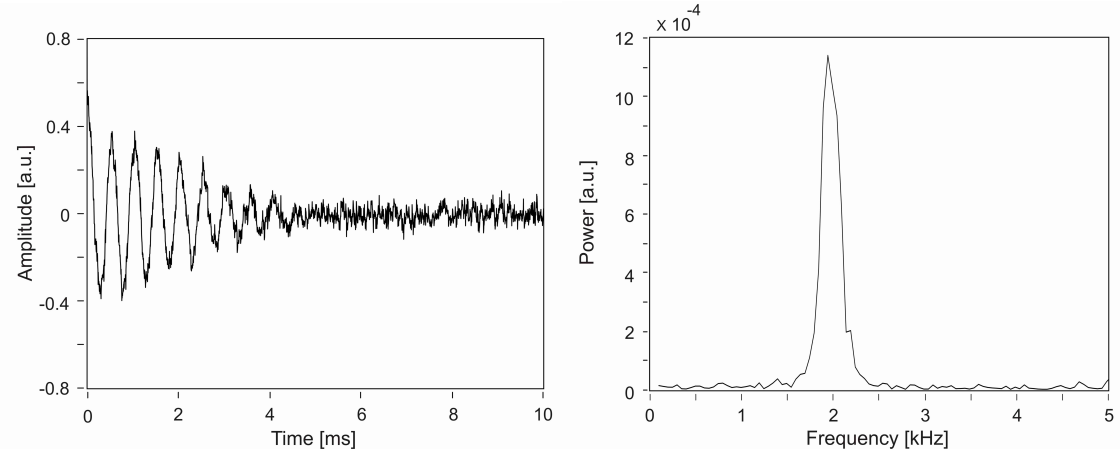

(a) (b)

Figure 6.72: Signal with protons and its power spectrum

The sample was cooled down with liquid nitrogen and afterwards introduced in the magnetic field for a measurement of the NMR-signal. The sample was warming up by heat exchange with the surroundings while the temperature was monitored with a pt 100. The first signal was obtained at a temperature slightly over the 150 K (figure 6.72). The amplitude is considerably reduced compared to the helium but still produces a good signal to noise ratio. The magnetic field homogeneity in the magnet used for the test is slightly better than in aSPECT $< 10^{-4}$. These results allow us to recommend such a NMR-sample for the aSPECT spectrometer.

In order to test the heating up procedure in environmental conditions similar to the inside of the aSPECT spectrometer, the sample was introduced into a glass dewar with a thermometer pt 100 (see figure 6.73). A small amount of liquid nitrogen was introduced inside the dewar and sealed. The sealed dewar was introduced into liquid nitrogen and isolated with aluminium foil. Due to the heat transfer into the system it was not possible to reach the liquid nitrogen temperature. After reaching the minimum equilibrium temperature, a small current was applied to warm up the sample. The system does not simulate the vacuum conditions of the aSPECT spectrometer but is a worst case scenario. In the aSPECT vacuum conditions, the heat transfer through the nitrogen atmosphere is not present so the sample should warm up faster. The measured heat curve is shown in figure 6.73.

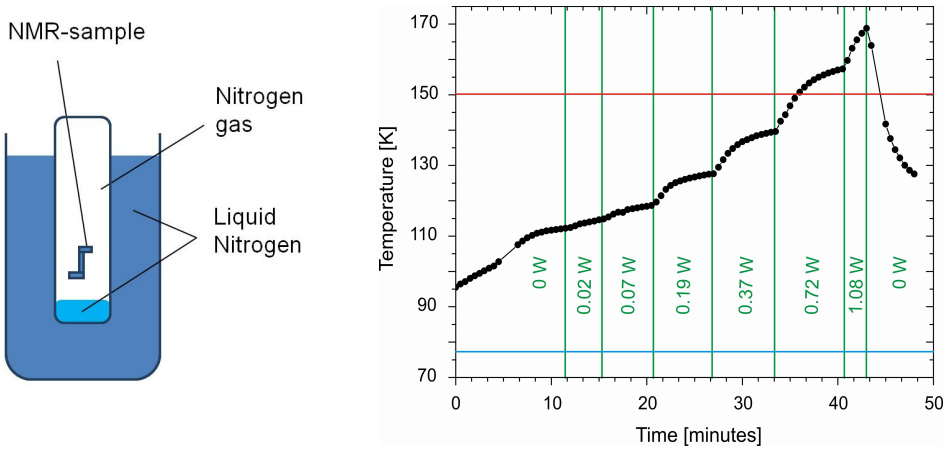

(a) (b)

Figure 6.73: (a) Cooling down system for the warming up test of the proton NMR-sample. (a) Warming up curve of the sample.

6.6 Outlook of the NMR-magnetometer

The NMR-Magnetometer described in this work has shown a very good stability and reproducibility several orders of magnitude better than necessary for our *a*SPECT spectrometer. The accuracy reached is better than required for the determination of the correlation coefficient a with an accuracy $\delta a \approx 3 \cdot 10^{-4}$.

Furthermore, the NMR-magnetometer has been used to measure and characterize the magnetic field ratio of the *a*SPECT magnetic field, r_{B}, off-axis. The drift of the magnetic field has been accurately measured and the result has been used in order to correct the magnetic field mappings performed with the Hall-probe magnetometer (see chapter 5).

The results are summarized next:

- **Magnetic field drift:** $(\Delta B/B)/\Delta t = (-1.292 \cdot 10^{-4} \pm 2 \cdot 10^{-7})\mathrm{day}^{-1}$
- **Ratio stability:** the stability of the ratio has been determined to be $\Delta r_B = 4 \cdot 10^{-6}$ which implies $\Delta r_B / r_B = 1.8 \cdot 10^{-5}$, one order of magnitude better than requirements.
- **Ratio reproducibility:** it has been determined to be $\Delta r_B = 4 \cdot 10^{-6}$, i.e., $\Delta r_B / r_B = 1.8 \cdot 10^{-5}$, one order of magnitude better than required.

  Considering only statistical errors, the ratio can be determined with an accuracy up to $\delta r_B = 1.3 \cdot 10^{-6}$. This value illustrates that the ratio may be determined with higher accuracy just by reducing the systematical errors, mainly reducing the sample size and improving the r.f. generator accuracy.
- The **reproducibility of the absolute magnetic field** is approximately $\Delta B/B = \pm 1.1 \cdot 10^{-4}$ (waiting about 8 hours to stabilize the field before switching to persisten mode).
- **Absolute value of r_B:** if we consider the field distribution within the sample volume as an uncertainty for the absolute B-field value, the error bar would have to be increased to approximately ± 3.7 kHz at the 70 MHz range and to ± 0.8 kHz at the

14 MHz range. This corresponds to a $\Delta r_B \approx 1.6 \cdot 10^{-5}$, giving a relative uncertainty of $\Delta r_\mathrm{B}/r_\mathrm{B} \approx 8 \cdot 10^{-5}$ (see appendix C.4). The error is still better than necessary for the *a*SPECT spectrometer.

The improvements performed in the NMR-magnetometer during this thesis have already increased the accuracy in the absolute magnetic field measurements. On the one hand, the use of the mixer instead of the lock-in amplifier eliminates the problem of the DC-peak (section 6.3.1). Without this artifact, no truncation is necessary and therefore, the complete spectral width can be accurately determined. On the other hand, the sample volume has been already reduced by using protons instead of helium. Therefore, the field distribution within the sample is reduced, which in turn reduces the field uncertainty.

Furthermore, the new NMR-magnetometer setup is cheaper, more robust, easy to install and permits an infinite number of measurements at any time.

The NMR-magnetometer can be used for a precise magnetic field mapping within the DV and AP and to monitor the ratio of the magnetic field during the course of beamtimes. For a complete mapping of the *a*SPECT magnetic field, jointed measurement with the NMR-magnetometer and the Hall probe can be performed.

At present, to relate the ratio or the absolute magnetic field measured off-axis (with the NMR-magnetometer) with the present magnetic field mappings at the DV and AP volumes, an improvement of the magnetic field simulation is required (appendix C.5). This is necessary for trajectory calculations and for the study of different systematics of *a*SPECT (section 3.4).

Chapter 7

*a*SPECT beamtime at ILL

From November 2007 to June 2008, *a*SPECT was set up at the cold neutron beam position PF1b on the H113 guide at the Institute Laue-Langevin (ILL) in Grenoble, France. The activities carried out during this period can be split into three parts:

- From November to December 2007, the complete experiment was set up at PF1B. First test measurements were performed.
- From end 2007 to April 2008 the reactor was shut down for maintenance tasks. This time was used to perform magnetic field measurements and to apply small improvements to the setup.
- The main data collection period took place from April to the end of May 2008.

The main objectives of the beamtime at ILL were to overcome the problems in the *a*SPECT setup found during the beamtime at the FRM-II in 2005/2006 [50] and to study the systematics in the extraction of the parameter a in order to obtain a relative error better than $\frac{\Delta a}{a} \cong 5\,\%$.

In this chapter an overview of the experimental setup of *a*SPECT at the PF1B neutron beam line is given. Also, the data collection process, the analysis and conclusions of the measurements carried out during this period are presented.

7.1 Experimental Setup

The ILL-reactor provides a maximal power of 58.3 MW during 50 days of continuous operation. The neutrons emitted in the fission process of the Uranium are fast neutrons, i.e., have energies of several MeV. Fast neutrons are moderated inside the reactor core by heavy water, D_2O, to thermal energies of about 25 meV. This energy corresponds to neutron velocities of $\mathrm{v} \approx 2200\,\mathrm{m/s}$. The neutrons are further slowed down by a *vertical cold source* located in the reactor core. This source mainly consists of a vessel filled with liquid deuterium at 25 K. A double neutron guide (H113) situated close to the *cold source* extracts the neutrons for fundamental nuclear and particle physics experiments. The average velocity of the *cold neutrons* is approximately of $\mathrm{v} \approx 1000\,\mathrm{m/s}$. Since the number of neutrons decaying within a given volume is inversely proportional to their velocity, the moderation of the thermal neutrons permits to gain statistics in the experiments. Cold neutrons offer the best compromise between probability of decay neutrons and the need

of high counting statistics.

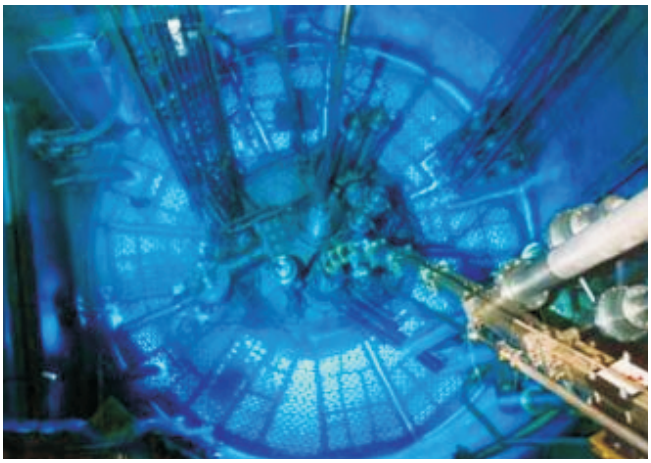

Figure 7.74: Top view of the reactor core with the vertical cold source of the Institut Laue-Langevin, situated in Grenoble/ France. It provides one of the strongest cold neutron beams in the world.

The beam position PF1B [80], in which *a*SPECT was mounted, is a free experimental area at the end of the neutron guide H113 with dimensions of about $10 \times 3\,\mathrm{m}^2$ (wide×length). The PF1B beam-line is one of the most powerful cold neutron sources in the world (beside MEPHISTO at FRM-II in Garching). The capture flux at the end of the guide, measured by gold foil activation, is ϕ_c=1.35·10$^{10}\,\mathrm{cm}^{-2}\,\mathrm{s}^{-1}$ [80], where the capture flux is defined as the particle flux ϕ weighted with the velocity v:

$$\phi_c = \int_v \phi(v)\frac{v_0}{v}dv, \tag{7.1}$$

This is a very important parameter in *a*SPECT since both, the neutron detector used to monitor the neutron flux and the neutron decay rate at the *a*SPECT DV, have a $\frac{1}{v}$ dependence.

The H113 guide is a super-mirror neutron guide with a profile of $60 \times 200\,\mathrm{mm}^2$, and a length of 78 m. The neutron guide is curved in its central part to block direct sight from the exit of the guide into the reactor core. This results in a neutron density distribution at the end of the guide which is not completely left-right symmetric. The H113 beam guide ends in a concrete shielded casemate close to the experimental zone. The distance from the end of the neutron guide to the *a*SPECT spectrometer had to be bridged by extra pieces of neutron guide. A linear neutron shutter made of boron carbide was introduced in the casemate in order to perform systematic tests. The neutron guide was evacuated to a pressure in the order of 10^{-2} mbar to minimize neutron scattering with residual gas. The ultrahigh vacuum of the main vacuum chamber of the spectrometer ($\sim 10^{-9}$ mbar) is separated from the rough vacuum of the neutron guide by a magnesium-aluminum window (MgAl3Zn1) with a thickness of 250 μm. On the other side of the spectrometer a beam dumb acts as an absorber to stop the neutron beam. A sketch of the complete setup at the PF1B position can be seen in figure 7.75.

7.1.1 Beam tailoring

The initial neutron beam coming from the PF1B neutron line has to be optimized in order to fulfill the specific requirements of our experiment. Firstly, since the dimensions of the DV of the spectrometer are smaller than the ones of the initial beam, the beam size has to be reduced to a size of $45 \times 70\,\mathrm{mm}^2$. Inside the spectrometer, the collimation has to be minimal in order to avoid background radiation which cannot be shielded. Similarly, primary or scattered neutrons should not hit the inner walls of the spectrometer. Finally, the resulting beam should have a homogeneous spatial distribution over the width of the DV to minimize the edge effect. The complete collimation system has to also be properly shielded to reduce radiation in the experimental zone. To accomplish these requirements, the neutron beam tailoring was designed on three parts:

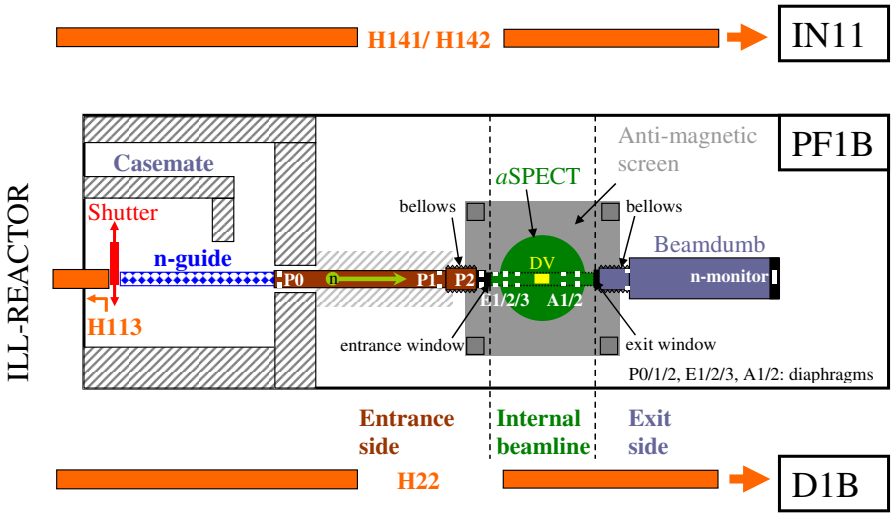

Figure 7.75: Sketch of the PF1B beamline at ILL.

- The entrance side:
  Due to the divergence of the neutron beam at the exit of the PF1B, a long collimation system is needed to ensure an approximately constant and homogeneous beam profile all along the DV of the spectrometer. To achieve that, the neutron beam is collimated in three steps (diaphragms P0, P1 and P2) before reaching the entrance window of the spectrometer.

- The internal beamline:
  The main collimation is produced at the entrance of the spectrometer. It reduces the background products that reach the detector. However, inner collimation system is necessary for fine tuning and to prevent primary neutrons from hitting the inner spectrometer walls. Three diaphragms E1 to E3, are located before the DV. Two other diaphragms, A1 and A2, collimate the neutron beam to enter the beam stop.

- The beamdumb:
  The beamdumb is composed by an aluminum vacuum chamber of dimensions, 150 $\times 50 \times 50\,\mathrm{cm}^3$. It is covered by shielding materials in order to avoid that secondary radiation produced there affects the experiment. A neutron counter was installed at the center of the back wall of the beamdumb for in-situ monitoring of the neutron flux.

The positions and sizes of the different apertures used in the three parts of the collimation system were optimized with two different Monte-Carlo simulation programs [45].

The complete *a*SPECT setup is shown in figure 7.76. Figure 7.76 (a) shows the entrance side whereas the right-side, picture (b), shows the beamdumb. An antimagnetic screen to shield neighboring experiments from our strong magnetic field is visible on both pictures. The blue coils surrounding the cryostat are antihelmholtz coils that modify the field shape at the AP (see chapter 5). In the picture are missing other correction coils (Helmholtz) that were not installed at that moment. On top of the antimagnetic screen it is visible the electronic setup of the detector.

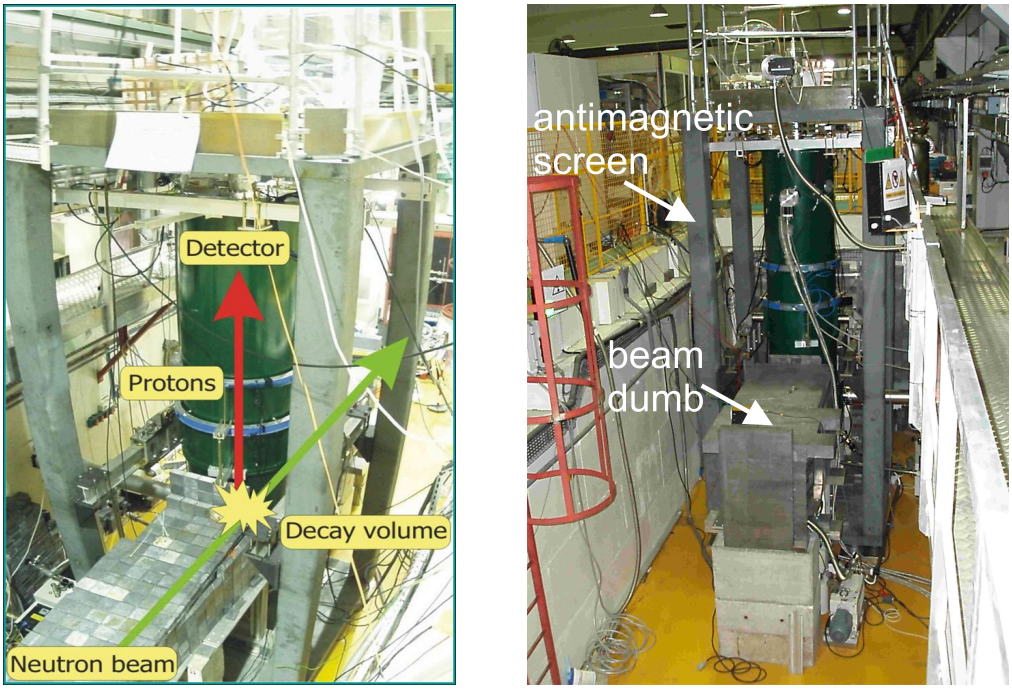

(a) Entrance side.

(b) Exit side with shielded beam dumb.

Figure 7.76: The complete *a*SPECT-Setup mounted at PF1B at ILL.

7.1.2 Neutron beam profiles

Once the magnet was centered and the complete setup aligned with the neutron beam, it is fundamental to image the resulting neutron beam profile inside the spectrometer. For this purpose, copper foil activation was planned in three positions: in front the entrance window, behind the exit window and at the center of the DV. Unfortunately, the lack of

time made impossible the measurement inside the DV so the neutron beam profile there had to be calculated by Monte-Carlo simulations[45]. The information obtained permits to weight the neutron beam profile with the magnetic field, in order to extract the ratio of the magnetic field r_B (chapter 5) and to perform trajectory calculations.

Copper foil activation is a precise procedure to determine the density distribution of a neutron beam. The irradiation of a thin copper foil ($\approx 150\,\mu$m) by neutrons produces the activation of the material. Due to neutron capture the isotopes ^{63}Cu and ^{65}Cu are generated:

$$\begin{aligned} {}^{63}Cu + n &\rightarrow {}^{64}Cu + \gamma \qquad (\tau = 12.7h) \\ {}^{65}Cu + n &\rightarrow {}^{66}Cu + \gamma \qquad (\tau = 5.1min) \end{aligned} \tag{7.2}$$

These isotopes are not stable and decay with the half life indicated in 7.2. After two hours, the activity of the isotope ^{66}Cu is negligible and almost pure ^{64}Cu beta decay is detected. The decay electrons of the ^{64}Cu are detected by a PIN-diode detector shielded with lead and fixed 35 mm over the foil in an external setup. An unique small hole of $\phi = 3.5$ mm on the lead shield determines the area read by the PIN-diode at each position. The detector is moved by an automatized robotic arm which scans automatically the two-dimensional intensity profile on a grid with an step size of 2.5 mm. The total area of 36×48 steps is scanned in about 2.5 h. After one scan is finished, the measurement is repeated in reverse scanning sequence until six scans per copper foil are performed. This provides a first order correction for the exponential decay of the intensity during the time needed for each scan, see figure 7.77.

For systematic studies (e.g, edge effect), different diaphragm widths (diaphragm P2, figure 7.75) were used to collimate the neutron beam. All the neutron beam profiles obtained with different diaphragm widths were measured at the entrance and exit of the spectrometer. The neutron intensity distribution inside the DV was reconstructed from these measurements [45]. The neutron beam profiles obtained with this procedure showed to be sufficient for the determination of the ration r_B with the accuracy necessary for aSPECT, chapter 5.

7.1.3 The Proton detector

The detector used by the aSPECT spectrometer during the ILL beamtime in 2008 was a silicon drift detector (SDD), [81]. A detailed description of the aSPECT proton detector and its electronics can be found in M.Simson [46]. In an earlier beamtime (FRM-II 2005 [50]) a classical semiconductor detector was used (PIN diode detector). It consisted of a thin silicon wafer with a continuous n-doped layer on one side and p-doped strips on the other side. An electrical field in reverse bias mode was used both for depleting the detector and creating the field gradient to collect charges created by penetrating particles. In contrast, the SDD is based on the sidewards depletion principle, see figure 7.78. Instead of using a single field for depletion and for charge separation, two separated fields are applied. Here, the bulk material of the detector is n^- doped silicon, were the superscript $-$ refers to a faint degree of doping. On one side of the SDD a smooth p^+ layer is implemented, whereas the other side has a structure of concentric p^+ rings ("+" refers to s strong degree of doping). The rings on the front side have different potentials from $\sim -15\,V$ on the innermost ring to ~ -230 V on the outermost ring in such a way that

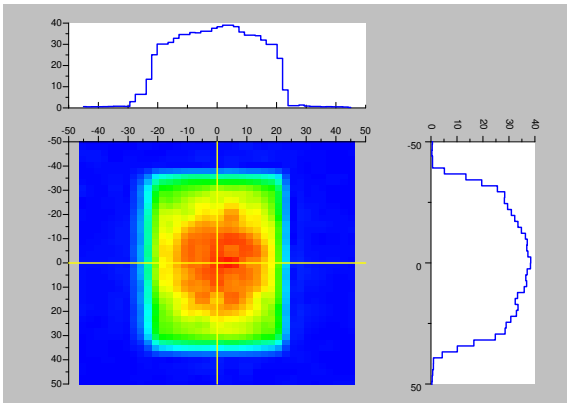

(a) Entrance, full beam

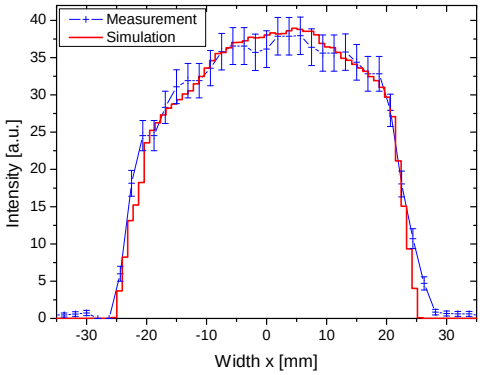

(b) Entrance, full beam: Width (y=z=0)

Figure 7.77: Beam profile measured by copper foil activation. The measurement is plotted in blue and the simulation in red color.

a potential valley is created inside the detector, figure 7.78 (b). Free electrons created by particle impact inside the valley will drift towards the centre of the front side of the detector, where they are collected by a small n^+ doped anode.

A special feature of this detector is the amplifying FET[1] on the detector chip itself. This minimizes the cable length from the detector to the first amplification stage to zero and thus decreases the capacitive noise and the pick-up of external noise. Furthermore, a temperature diode is implemented on the detector chip.

The amount of particles collected depends on the energy of the incident particle, and thus, the amplitude of the generated electrical signal too. This signal is pre-amplified first by the FET and afterwards by the preamplifier board. To reduce the pickup noise, the preamplifier board is directly connected to the detector. After the amplification, the signals are transferred by coaxial cables in the central tube of the detector mechanics to the outside of the spectrometer.

The signals coming from the preamplifier are fed into an adapter board inside the aluminium box on top of the spectrometer. This board shapes the signals and distributes them to the ADC (analog to digital converter). The raw signals from the detector consist of a steep rising part and a long exponentially falling part. The shaper is mostly sensitive to the rising part and shortens the pulse, so it can be treated by the digital electronics.

Digital electronics and the trigger algorithm

The last part of the signal processing electronics is the sADC[2] board. The signals coming from the preamplifier are continuously digitized by a 12 bit ADC. The sampling frequency is 20 MHz, resulting in time bins with a width of 50 ns. The events typically have a length of about 5 μs, so this frequency offers a decent compromise of a good resolution in time while keeping the data volume on a reasonable level.

[1] Field-effect transistor.
[2] Sampling Analogue to Digital Converter.

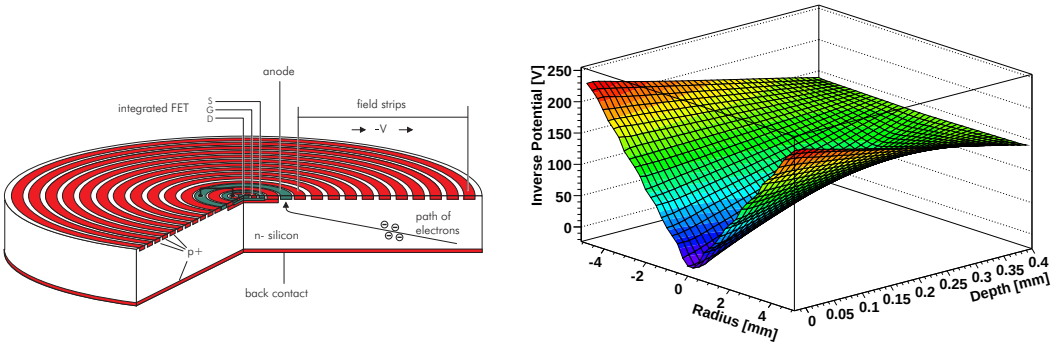

(a) (b)

Figure 7.78: The principle of a silicon drift detector. (a) Scheme of a typical SDD detector [46]. (b) Simulation of the potential inside a SDD detector. Free electrons created within the potential valley drift towards the centre on the front side, where they are collected by the anode.

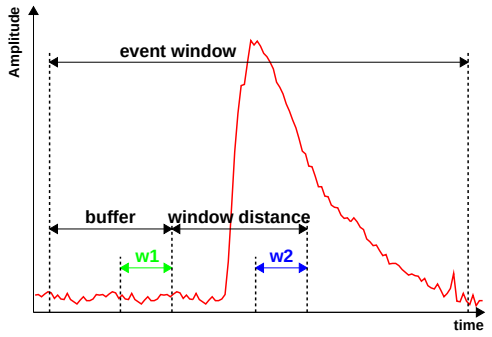

Figure 7.79: Typical proton event. General overview of the average windows and buffer used by the trigger algorithm.

After being digitized, the signals are treated by two field programmable gate arrays (FPGA) which provide data buffering and processing. The full amount of data sampled by the ADCs is far too large to be stored on a conventional personal computer (about 28.6 MB/s per channel), thus the data is analyzed by the two FPGAs with respect to a trigger algorithm.

The data from the ADC is continuously shifted through a register and discarded at the end if no pulse was detected. The general pulse detection algorithm is based on the comparison of two windows within the shift register. If the mean values of those two windows differ by more than an external threshold, the trigger condition is fulfilled.

As it is shown in figure 7.79, window w1 is used to determine the baseline, whereas w2 is separated from w1 by the window distance. If an event is registered by the electronics, the mean value of w2 will be higher than the one of w1 and the threshold condition is fulfilled. An additional parameter in the algorithm, called delay, can be set, so that this threshold condition has to be fulfilled several times in a row before a trigger decision is made. This feature helps to suppress triggers on noise. The exact stored region around the event is determined by the length of the event window and the trigger buffer. This

buffer ensures that a sufficient amount of data before the event is stored.

In the case of the aSPECT electronics, the lengths of the two windows w1 and w2, the trigger buffer, the event window and the delay can be set from the control program. The window distance is fixed to 16 time bins. For most of the measurements during the beam time, both w1 and w2 were set to a length of 16 time bins, the delay was 3, the trigger buffer had a length of 15 time bins, and the event window of 100 time bins.

The data is transferred to a computer via a HOTLINK interface. This allows us to operate the sADC board at the same high voltage as the detector, while the DAQ computer is at earth potential.

7.2 Data Analysis

The data taken with the aSPECT spectrometer has to be first decoded and then analyzed in order to obtain statistical and systematical information of the angular correlation coefficient a. The decoding and analyzing procedure comprises the approximate following steps:

- Decoding of the raw data to a processable format.
- Exclusion of data proceeding from instable periods (e.g., discharges, drifts, etc.).
- Event analysis to determine the energy and type of the detected particle.
- Background subtraction.
- Determination of the proton count rate at every analyzing plane voltage.
- Extraction of the angular correlation coefficient a.

The first point is deeply treated in the PhD thesis of M. Simson [46] and will not be discussed here. The other points are also discussed in [45] and [46]. A summary and a discussion of their content will be further given.

7.2.1 Event Analysis

For every triggered event, a sequence of ADC values with predefined length (usually 100 bins = 5 μs) is written to the PC, see figure 7.79. This sequence is called one event and is the signal produced by the detected particle after being shaped by the shaper board. Due to the shaping, electrons and protons with similar energies are undistinguishable. Further analysis is necessary to determine the energy of the particle and to discriminate between electrons, protons and noise events.

The simplest way to determine the pulse-height of one event, i.e. its energy, is to take the maximum of each event and subtract a fixed baseline. This method is however insensitive to possible baseline fluctuations and noise laying over the pulse maximum. A pulse fitting routine has shown to be a much more reliable procedure and even permit to extract information from events which otherwise would be lost. A comparison of the pulse-height extraction procedures by direct subtraction and with the fitting routine can

be found on [45]. With the fitting routine, an event pulse is described as a mathematical function with 5 parameters:

$$y_{\mathrm{Fit}}(x) = \begin{cases} y_0 & ;\ x \leq x_0 \\ y_0 + A\left(1 - e^{-\frac{x-x_0}{t_1}}\right)^p e^{-\frac{x-x_0}{t_2}} & ;\ x > x_0 \end{cases} , \tag{7.3}$$

where y_0 is the baseline of the pulse, x_0 is the starting point of the pulse and t_1 and t_2 denote the rise and decay time of the pulse, respectively. Parameter p influences the shape of the pulse and parameter A gives its height. t_1, t_2, and p are given by the electronics. Figures 7.80 (a) and (b) show examples of proton and high energetic electron events.

Events sorted as noise events have to be taken also into account because during the time one of these events is produced plus during the time needed by the electronics to recover, no other event can be detected.

Some other events do not produce a satisfactory result on the fit and have to be retreated. Two special cases of unsorted events have to be considered carefully:

1. **Pile-up:** it is produced when a second proton is detected shortly after the triggering of the first one. In this case, the shape of the signal is altered by the rising edge of the second proton, see figure 7.81 left. Consequently the fit function 7.3 does not work.

2. **Proton after electron:** The falling edge of high energetic electrons is longer than the length of one ADC event. Thus, if a proton follows shortly after such an electron, its event will be located on the exponentially decaying edge of the electron (figure 7.81 right). Then, the proton cannot be distinguished by the fit function.

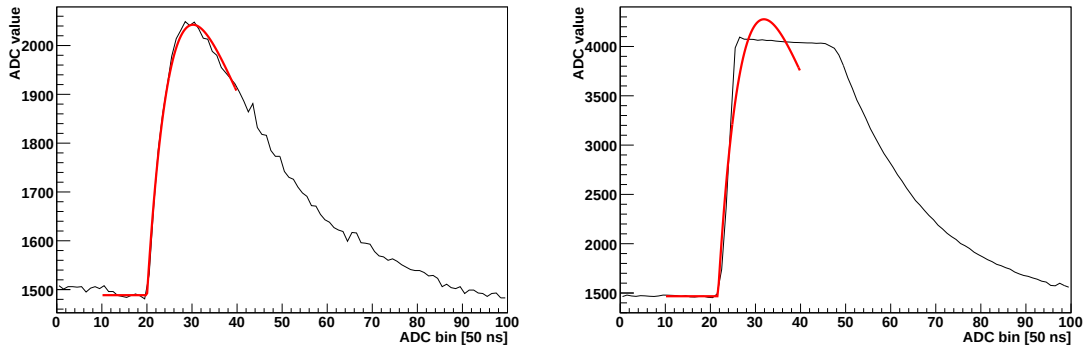

(a) (b)

Figure 7.80: (a) Typical proton event with the resulting fit (red line). (b) A high energetic electron or gamma which is cut off due to the limited maximum amplification of the electronics.

By performing a second derivative to the fit function 7.3, these two specific cases can be distinguished. Then, the second proton of the pile-up case is neglected and enters into the

dead time correction. In the second case (proton after electron) another specific fit routine which delivers a realistic result for the pulse height of the proton events is applied [46].

Dead time correction

Every event has a length of $5\,\mu$s. During this time no other event can be registered. However, due to the nature of the trigger, the next event cannot be detected before a minimum time difference of $5.2\,\mu$s. This fact defines a "non-extendable" dead time [82] which causes a reduction of the count rate which depends on the absolute count rate. To correct for that effect a dead time correction has to be applied. A first order dead time correction can be written as follows:

$$C_{\mathrm{corr}} = \frac{C_{\mathrm{meas}}}{1 - C_{\mathrm{meas}} \cdot T_{\mathrm{dead}}}, \tag{7.4}$$

where $T_{\mathrm{dead}} = 5.2\,\mu$s is the dead time per event. C_{corr} and C_{meas} are the corrected and the measured count rate, respectively. Due to the rather high count rate on one detector pad, the dead time correction has a rather strong impact on the extraction of a. For example, for a count rate of $C_{\mathrm{meas}} = 500\,\mathrm{s}^{-1}$ at $U_{\mathrm{A}} = 0\,\mathrm{V}$, the count rate loss would be $\approx 1.3\,\mathrm{s}^{-1}$. The value of the correction depends on the AP-voltage (APV) settings because of the differences in the measured proton count rates at different AP voltages and therefore it produces an error on the coefficient a: The APV-dependent count rate loss shifts the coefficient a relatively by $\Delta a/a < 4\,\%$. This shift is correctable on a $0.1\,\%$ level but requires an accurate knowledge of the dead time: An uncertainty of $\delta T_{\mathrm{dead}} = \pm 0.2\,\mu$s results in an error $\delta a/a =< 0.04\,\%$. More information can be found in [46].

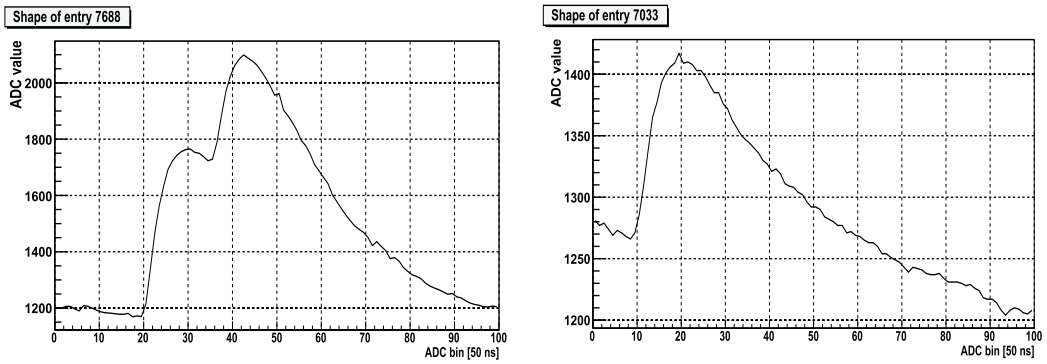

(a) event 7688. (b) event 7033.

Figure 7.81: Left: Pile-up effect on two consecutive protons. Right: electron followed by a proton.

7.2.2 Extraction of the angular correlation coefficient a

After the fitting of the pulses, the value of a has to be extracted from the proton spectra. For that, the information obtained from the fitting rutin is used to build up a pulse-height histogram for every AP voltage. The total count rate at each analyzing plane voltage (including background measurements, i.e., 780 V at APV) can be then extracted by integration over the pulse-height histograms. Finally, the count rate of each measurement is corrected for the dead time of the electronics and the background is subtracted in order

to obtain the pure proton count rate for each AP voltage.

Pulse height histogram

Figure 7.82 (a) shows a typical pulse-height spectrum for different analyzing plane voltages. The uncertainty of each point in the spectra with N counts (per ADC channel) is given by $\sqrt{N}/T$ (statistical error). The left peak corresponds to the thermal noise of the electronics. The peaks centered at about 600 ADC channels are the proton peaks measured at different AP voltages. The proton distribution can be described by a superposition of a Gaussian and an inverted Landau distribution. The tail towards lower ADC channels is caused by protons that are backscattered or loose more energy in the dead layer or close to the surface of the active layer [46]. Therefore, the tail of the proton peak is produced by protons which deposit only small energy in the active area of the detector. This tail reaches to low ADC channels even below the electronic noise peak. The upper end of the proton peak is defined by protons which deposit their maximum energy of 15.75 keV impact energy (for -15 kV detector HV). The small peak visible at about 750 ADC channels was not expected and has been carefully investigated. The pulse shapes in that peak look like ordinary events. Also the count rate under this peak changes at different APV like in the main peak (proton peak). The most probable explanation of this extra peak is a slightly higher amplification in a small spot of the detector [46]. Detailed information about this peak will be given in section 7.2.3. Electrons and gammas present an almost constant distribution all over the energy range of the detector and produce a peak at about ADC channel 2500 where the detector reaches its saturation energy (this peak is not shown in the figures).

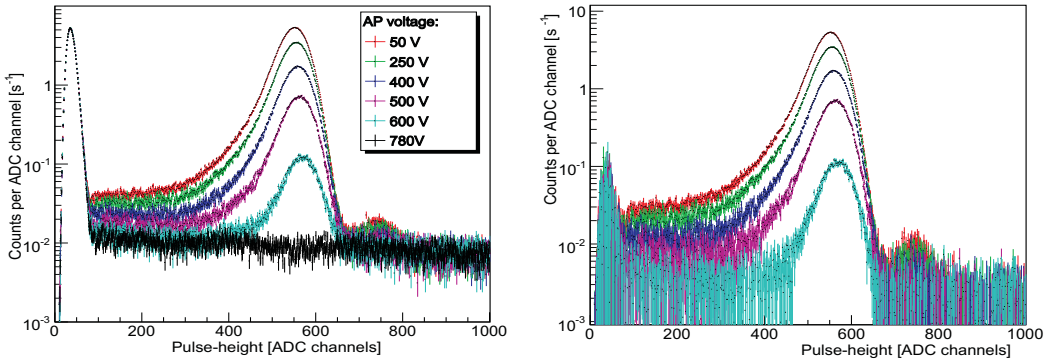

(a) (b)

Figure 7.82: Subtraction of the background: (a) shows the pulse height spectra for different AP voltages. (b) The 780 V measurement (used as background) is subtracted from the other measurements to obtain the pure proton spectra.

Background subtraction

The background is measured by applying 780 V to the analyzing plane electrode to stop all protons from neutron decay (represented by black points in figure 7.82, (a)). It has to be subtracted from the measurements with different analyzing plane voltages in order to obtain the pure proton count rates. This procedure assumes that the background

does not depend on the AP voltage (this point will be discussed in section 7.2.3). The principle of the background subtraction is shown in figure 7.82. The residual peak at low ADC channels visible after background subtraction (figure 7.82, (b)) is due to instabilities of the electronic noise of the detector. There are two possible strategies for the background subtraction:

1. For each single measurement the count rate of the closest background measurement in time is subtracted.

2. The averaged proton count rate for every AP voltage is calculated by summing up all measurements (in a data set[3]) with the respective voltage and making the average. Then, the average background count rate is subtracted.

The first option has the advantage that it corrects short term count rate fluctuations. However, it is difficult to avoid introducing a systematic effect. For example, if some background measurements are used more often than others, the errors become correlated and different weighting of the measurements would be necessary. Also, although the background is measured in a regular pattern in every fourth file, some measurements had to be excluded because of malfunctions of the data taking system. This, again, introduce correlated errors.

Detailed analysis of the background (see [46] and [45]) did not find short term fluctuations (i.e. during a data set) in the background count rate. Therefore, the method of subtraction of averages was chosen for the analysis.

Integration of the count rate

To extract the proton count rate for each analyzing plane voltage, the background-subtracted spectra in figure 7.82 (b) have to be integrated. For that, the optimum integration limits in ADC-channels have to be found. The lower limit is set as close as possible to the electronic noise peak (e.g. ADC channel 80) in order to include the tail of the proton peak at low ADC channels. Too low integration limits have to be avoided in order not to integrate part of the electronic noise which is highly instable. The upper limit of the integration region is set well above the maximum proton impact deposition energy, about channel 1200.

During the data analysis the integration limits were varied in order to find the optimum ones. A dependence of the value of a on the lower integration limit was found, see figure 7.83. Since the analyzing plane potential barrier cuts away the lower part of the proton spectrum (protons with insufficient energy to cross the potential barrier are reflected), for a fixed integration limit, one cuts away more proton counts for the lower AP voltages than for the higher ones. This effect introduces an AP-dependent systematic error which cannot be avoided. However, proton simulations [46] are able to describe this effect correctly and the measured count rates can be corrected. For a lower integration limit of 80 ADC channels, the correction is only $\Delta a = 0.13(9)\,\%$. The error bar is dominated by the statistics of the proton simulations and thus can be lowered by simulating more protons.

[3] A data set consist of several hundred single measurements of 40-120 s measurement time with neutron beam switched "on".

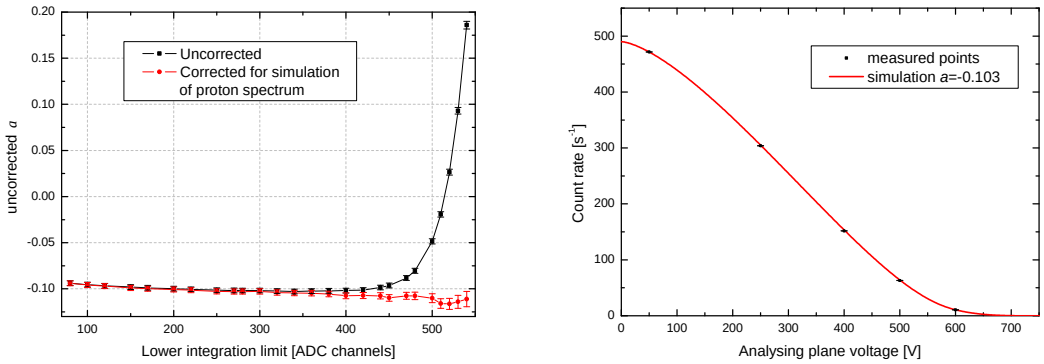

(a) (b)

Figure 7.83: (a) Dependence of a on the lower integration limit. The error bars are purely statistical. The lines between the points are to guide the eye. The values of a shown are result of a blind analysis (uncorrected a), see [46] or [45]. (b) Integral proton spectrum. The error bars of the data points (black) are smaller than the points itself. The red line shows a simulation of the actual PDG-value for the correlation coefficient a. The proton count rates for each AP voltage are fitted using equation 7.5 to obtain a.

The same systematic test was performed for the upper integration limit by fixing the lower and varying the upper limit. No dependence of a on the upper integration limit was found [46] [45].

With the integration of the proton peak in the pulse-height spectrum for a certain AP voltage, a single data point of the integral proton spectrum is obtained (figure 7.83 (b)). For the standard measurement settings we obtain 6 data points which can be plotted as a function of the voltage. These measured points are then fitted by a theoretical function, $N_p(U_A)$, that includes a as a fit parameter. The proton count rate $N_p(U_A)$ at a given APV can be described by [7]:

$$N_p(U_A) = N_{p,0} \int_0^{T_{max}} F_{tr} w_p(T) dT \tag{7.5}$$

with T being the kinetic energy of the decay protons, F_{tr} being the transmission function defined in equation 3.25, and $w_p(T)$ the differential proton spectrum (section 2.2.3). Without Coulomb correction (which takes into account the electromagnetic interaction between electron and proton) and radiative corrections (which takes into account bremsstrahlung), $w_p(T)$ is given by $w_p(T) = g_1(T) + a \cdot g_2(T)$ (with $g_1(T)$ and $g_2(T)$ as defined in equations 2.30 and 2.31). Coulomb and radiative corrections on $w_p(T)$ can be found in [42]. The value of a is then obtained from the fit of the measured points to $N_p(U_A)$ [7]. The measurements with 0 V analyzing plane voltage are not used for the fit of a (see section 3.4.3), thus $N_{p,0}$ (the proton count rate at 0 V) is a free parameter in the fit.

7.2.3 Background studies

During the *a*SPECT beamtime at the FRM-II, background count rate fluctuations turned out to be the major problem in the data analysis and prevented us from giving a definitive value for a. Several changes in the spectrometer setup have been implemented in order to improve the background conditions, which have been already discussed in chapter 4. Another important modification has been the installation of a neutron shutter which permits to study the background shortly after taking measurements with neutron beam. A complete description of the *a*SPECT Background studies can be found in the PhD. thesis of M. Borg[45].

Several systematic investigations to the *a*SPECT experiment have been performed, in which the neutron shutter has been used. For example, to investigate trapping effects, different settings of the voltages on the lower pair of ExB electrodes were used. The neutron shutter permits to observe the evolution of the count rates over the measurement time by comparing them for closed and open shutter position. Figure 7.84 (a) shows the increase of background (measurement at 780 V APV) with the neutron shutter open and for different settings of the lower ExB. For the very low drift potential of $-2.4 \mid 0$ V the count rate starts to fluctuate as soon as the shutter is opened and even after it is closed again, particles still remain trapped for some seconds. Applying $-200 \mid 0$ V the count rate is stable and drops back to the normal background count rate after the shutter is closed (trap P-III, section 4.1.1).

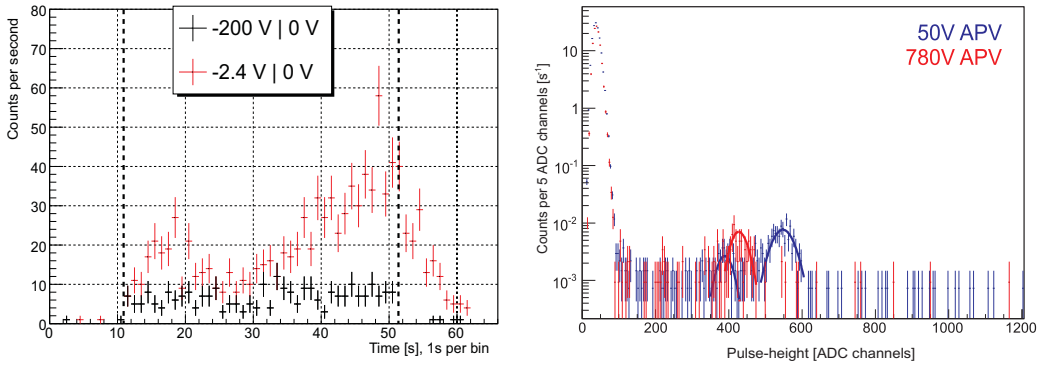

(a) (b)

Figure 7.84: (a) Comparison of measurements with two different settings of the lower $\vec{E} \times \vec{B}$ electrodes. The thick, dashed, black lines denote the opening and closing of the neutron shutter, showing the efficiency of the $\vec{E} \times \vec{B}$ field for removing trapped charged particles. (b) Spectra for closed shutter after measurement. One peak for 780 V and two peaks for 50 V were found in the background analysis. To retrieve visible peaks all measurements from a full run were summed up. The red and blue lines are Gaussian fits to the peaks.

Measurements before, during and after a period with open shutter permit to perform a detailed investigation of the background produced inside the spectrometer. Background can be produced either by the neutron beam, the decay products, or by other sources. Measurements with neutron beam "on" and "off" for different APV voltages and several configurations of the spectrometer (electric and magnetic field configurations) have been analyzed in detail [45].

In summary, the background studies have shown that the background measurements at 780 V APV with neutron beam "on" are not drifting during the data sets(several hours). However, non-statistical contributions to the background count rate at 780 V APV have been observed in the region < 600 ADC channels. This background components are present even at 780 V APV and, furthermore, show an APV-dependence.

In the FRM-II beamtime, the contribution of APV-dependent background was visible as a clear peak in the pulse height spectrum of single measurements at 780 V (with neutron beam "on" and "off"). In contrast, the APV-dependent background can only be observed now by summing the measurements of a complete data set ($\sim 10 - 12$ hours) for a given APV-setting. In the spectra measured with neutron beam "off", shown in figure 7.84 (b), two small peaks are visible. The height of these peaks depends on the AP voltage. The first peak is visible for all AP voltages while Peak 2 appears only for measurements with APV 0 and 50 V.

Detailed studies of the background extra peaks revealed the following information:

Peak 1 (ADC channels 300 to 450) is visible for all analyzing plane voltages, before and after opening the shutter. Its intensity increases minimally with the APV. It is probably caused by particles produced above the analyzing plane by a mechanism coupled to the electron trap between the lower $\vec{E} \times \vec{B}$ electrodes and the negative high voltage at the detector and the upper $\vec{E} \times \vec{B}$ electrodes [45] (trap P-I, section 4.1.1).

Peak 2 (ADC channels 500 to 600) is visible only for 0 and 50 V analyzing plane voltage and its intensity decreases from 0 V to 50 V. Therefore, the origin of the background must be below the analyzing plane. After closing the neutron shutter, the peak decays exponentially with a time constant of 2 to 3 s (for 50 V APV). This long time constant points to a particle production mechanism involving trapped electrons that ionize residual gas molecules [45] (traps P-II and P-IV, section 4.1.1).

These peaks induce a shift on the angular correlation coefficient. The average shift induced by the APV-dependent background peak1 on the coefficient a is $\Delta a/a = -1.14 \pm 0.30\,\%$. The average shift induced by the background peak2 is $\Delta a/a = +2.07 \pm 0.31\,\%$. The coefficient a can be corrected by inversion of that shifts, both corrections together induce a systematic error of $\delta a/a = 0.61\,\%$ [45].

In summary, there are still some background contributions that depend on the AP voltage, but their intensity has been reduced by a factor of 5 to 10 in comparison to the FRM-II beamtime. For future beam times, a further reduction of APV-dependent background is fundamental. The main lines which have to be followed for that purpose are [45]:

(1) The vacuum conditions in aSPECT should be further improved since the probability of residual gas ionization depends on the pressure (see section 3.4.3), for example, using additional SAES getter pumps installed at the side-ports of aSPECT.

(2) A background study with reduced neutron beam width showed that the production of both background peaks is clearly coupled to radiation induced secondary electrons. Therefore, the width of the neutron beam should be reduced gradually below a size, where both background peaks are negligible. This could be done by the implementation of a retractable diaphragm in front of the entrance window.

(3) The lowest APV-setting where the background peak2 disappears has to be determined. This APV should be used as lowest APV-setting (instead of 50 V) in the measurement of the integral proton spectrum.

7.2.4 Dependence of a on the Electrostatic Mirror Potential

During our latest beam time, the mirror potential of electrode e2 was reduced from 1000 V to 820 V. The data analysis has revealed that with decreasing mirror potential the proton count rates drop down by a few hertz and the value for the angular correlation coefficient a is shifted to more negative values[38]. Two possible contributions were studied:

Non-Adiabatic Proton Motion

It is possible that a shifts due to an enhanced energy transfer from transverse to longitudinal motion for $U_{e2} = 1000\,\mathrm{V}$. Decay protons emitted in the negative z-direction are reflected by the electrostatic mirror at the latest at $z = -298.5\,mm$ for $U_{e2} = 1000\,\mathrm{V}$, whereas they are reflected at $z = -318.5\,\mathrm{mm}$ for $U_{e2} = 820\,\mathrm{V}$. As a consequence, protons may experience a excessively large electric field gradient in the case of $U_{e2} = 1000\,\mathrm{V}$ and therefore a breakdown of the adiabatic approximation. However, non-adiabatic motion cannot explain such large shift[38].

Penning Discharges in the Bottom of the Spectrometer

It is also possible that the count rate loss for $U_{e2} = 820\,\mathrm{V}$ is actually a rise in the APV-dependent background for $U_{e2} = 1000\,\mathrm{V}$. The electric field distribution exhibits a saddle point at the electrostatic mirror which is shifted from $z = -364\,\mathrm{mm}$ to $z = -330.5\,\mathrm{mm}$ with increasing mirror. At the same time, the electric potential at the saddle point is increased from about $800to$ 911.5 V, which may be too high to prevent Penning discharges in the bottom part of the spectrometer.

At present, the Monte Carlo (MC) simulations are not precise enough to clarify the problem[38]. Further calculations and investigations on this systematic effect in a future beamtime are necessary.

7.2.5 Correlated events: base line shift and saturation effect

Due to kinematic reasons, only a fraction of the decay electrons ($\sim 1/7$) reaches the detector and can be detected in coincidence with the proton from the same decay. There exist two possibilities: "direct electrons" and "backscattered electrons". About 14.7 % of the electrons emitted into the upper hemisphere reach the detector directly ("direct electrons"). On the other hand, electrons emitted into the lower hemisphere can be backscattered on the grid wires of the mirror electrode or the bottom plate of the electrode system ("backscattered electrons"). According to trajectory simulations, up to 15 % of the electrons emitted into the lower hemisphere are backscattered and may reach the detector [38]. When one of these two circumstances occur and one electron is detected in coincidence with the proton from the same decay, the two events are called "correlated events".

High energetic electrons saturate the detector electronics (i.e, shaper and/or preamplifier board) creating pulse shapes which show a plateau, followed by a tail towards the original baseline value, figure 7.85 (a). However, this baseline is not reached immediately. First, a baseline drift towards lower values is observed before the detector signal relaxes back to the original baseline value. Typically, the baseline height is at about 1500ADC channels and can drop temporary to 1000 ADC channels after a saturating electron pulse.

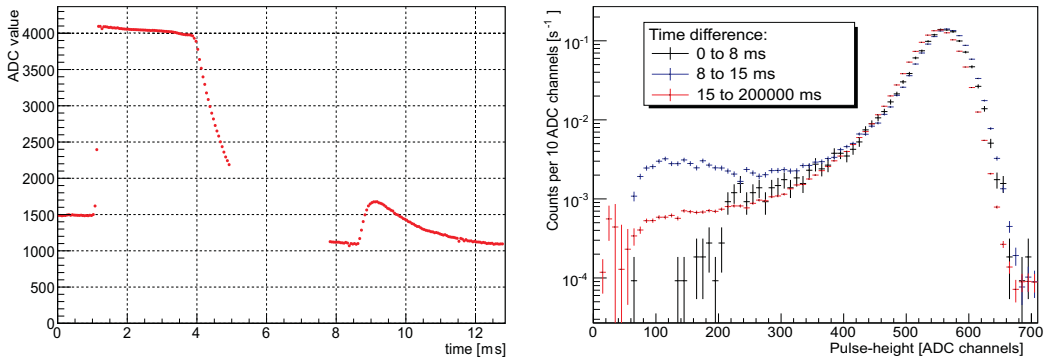

(a) (b)

Figure 7.85: a) An electron followed by a proton. The electron event saturates the electronics and is therefore cut off. After the electron, the baseline drops to ADC values around 1100 and the following proton has a lower and changing baseline. b) Pulse-height spectra for events arriving at the detector in different time ranges after an high energetic electron.

When a coincidence proton pulse is detected shortly after the saturating electron pulse, there is a finite probability that it will be detected on the falling tail of the decaying electron pulse. Figure 7.85 (a) shows a typical example for coincidence events.

The pulse routine permits to extract the pulse height of such events (see section 7.2.1), however, the behavior described above may cause two effects that influence the result of our measurement:

(1) The on-line trigger efficiency of the trigger windows w1 and w2 (see figure 7.79) is lower for protons sitting on the tail of a saturating electron pulse. Due to the baseline drift, the value of window w1 is shifted to higher values compared to the value at the position of window w2. As a result, a proton event will be lost if it has (a) a rather low pulse height and/or (b) if the baseline drift and thus the shift between w1 and w2 is too high.

(2) Pulse height spectra of coincident protons were extracted for different cuts in the coincidence time interval. The "coincidence time interval" or "time difference" between two pulses is the interval between the rising time of both pulses. In the case of cutting correlated events with a time difference larger than 8 μs, there are almost no counts with pulse-heights below 200 ADC channels, see figure 7.85 (b). For time differences between 8 and 15 μs there are more counts with low pulse-height than in any other case. This effect can be explained by a **saturation of the preamplifier**. The principle is shown in figure 7.86. The original pulse given by the detector consists of a short steep rising part and a long decay. The shaper then differentiates and integrates the signal and is mostly sensitive to the rising edge of the signal. The height of the pulse after the shaper is proportional to the change in pulse-height before the shaper.

If an electron deposits so much energy that the preamplifier comes close to saturation or even saturates, an event following after a short time will drive the preamplifier into saturation and cuts off the second peak. After the shaper the peak will have a lower pulse-height as well and will be detected in the low energy tail of the spectrum (figure 7.85 (a) and (b)). This effect turned out to make the dominant impact on a.

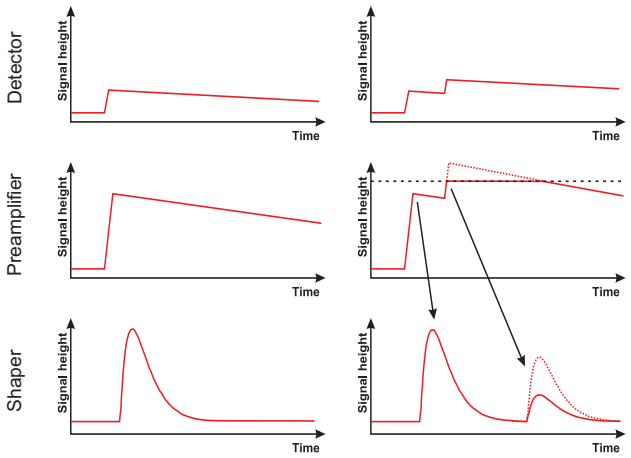

Figure 7.86: Schematic of the preamplifier saturation. Left: Single event. Right: Saturation for subsequent events.

Furthermore, the systematic introduced by these two effects is APV-dependent: due to the high energy and low weight of the decay electrons, they reach the detector much faster than protons. Electrons can be considered instantaneous and thus, the time difference between electrons and protons is essentially the time of flight of the proton from the decay volume to the detector. The protons time of flight (TOF) depends on the settings of the analyzing plane voltage. The proton's minimal TOF correspond to 0 V APV and was calculated to be 6 μs. Therefore, the two mechanism described above have a stronger influence on measurements with low analyzing plane voltages. This effect results in a shift of the coefficient a to more positive values. For example, the relative increase of a when the low integration limit is varied from ADC channel 250 to 100 is $\Delta a/a = +6.4\,\%$ [45]. Note that a decrease of the low integration limit implies to "accept" more low energetic events produced by coincident events.

Correction of the saturation effect

A two steps process may lead to a correction of the data. The idea is to exclude coincidence proton events from the determination of the proton count rates which are used to extract a. The exclusion can be done by assigning an artificial long dead time to each electron event (i.e., even if a proton event was detected in the measurement in this time span, it will be rejected in the analysis). Afterwards, it would be possible to reconstruct the amount of lost proton events by the application of a correction curve obtained from measurements where the saturation effect is simulated.

Increasing the dead time after electrons shifts the value retrieved for a up to $\Delta a/a \approx 100\,\%$ see figure 7.87 (a). The huge shift is caused by the different amount of correlated events that are excluded for each analyzing plane voltage. In order to know the actual value of the coefficient a, this behavior has to be reproduced by the simulations. Several calculations [38] have provided curves which show a behavior comparable with the measurements, figure 7.87 (b). Their shapes depend strongly on several input parameters like the amount of backscattered electrons, the energy and angular distribution of backscat-

tered electrons, the lower energetic limit for the saturation of the preamplifier by decay electrons, etc.

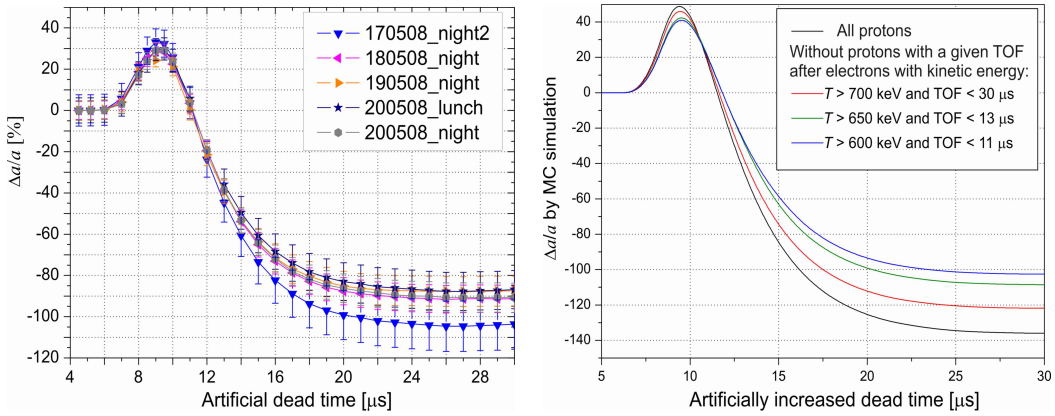

(a) (b)

Figure 7.87: (a) Dependence of $\Delta a/a$ on an artificial dead time after electrons for data sets with settings: upper ExB -2/ -2 kV, lower ExB -1000/ -50 V. (b) Calculated dependence of $\Delta a/a$ on an artificial dead time.

Unfortunately, two main problems showed up during the analysis of the data. On the one hand, it has not been possible to separate electrons that saturate the preamplifier from the rest of the electrons [46]. On the other hand, any correction would have to rely on the simulated time of flight spectra for what it is necessary to know the initial angular and energy-distributions of decay electrons and protons in the DV. In the case of backscattered electrons which are detected in coincidence with their proton, the angular and energy distribution is hard to predict and the accurate count rate of backscattered electrons is not known as well. The backscattering probability of electrons is strongly energy dependent. For example, it can have values between 40 % (for low electron energies) and 25 % (for high electron energies) at the surface of the grid electrode (e1) [38]. Electrons are backscattered on different materials (e.g., stain-less steel, copper, gold) in aSPECT, which possess different backscattering probabilities. Therefore, the accuracy of the TOF-simulations is critically limited by the insufficient knowledge of the energy and angular distribution of backscattered electrons. Consequently, it was not possible to restrict the input parameters of the simulation sufficiently by the dependencies extracted from the measured data sets. Thus, the amount of coincidence proton events which were lost by the saturation effects could not be reliably reconstructed and therefore neither a correction or an estimation of the error due to this effect is possible.

As a result, the destructive impact of the saturation effects frustrated our aim to extract the coefficient a with an error $\Delta a/a < 5\,\%$. However, an upper limit for the error induced by the saturation effects can be extracted from the measured dependencies for low integration limits. Although we cannot present a definitive value of the correlation coefficient a, I would like to present a preliminary value obtained from the analysis of the measurement runs 20_05_08/night and 20_05_08/lunch [38]:

$a = -0.098(\pm 0.003)_{\mathrm{stat}}(\pm 0.016)_{\mathrm{sys}}$

For future beam times, the saturation effects can be suppressed by progressive reduction of the amplification of the detector electronics. The amplitudes of high energetic

electrons have to be decreased below the saturation limit.

7.2.6 Magnetic field tests

Although the magnetic field mappings shown in chapter 5 have to be improved in order to reach the aimed accuracy of the *a*SPECT spectrometer, $\delta a \approx 3 \cdot 10^{-4}$. The present magnetic field measurements permit the determination of a with an accuracy $\Delta a/a < 5\,\%$. Furthermore, it has been demonstrated that the measured neutron beam profiles introduce a completely negligible systematic error. Consequently, the different magnetic field configurations used during the beamtime represent an useful and safe tool for the study of the *a*SPECT systematics.

As explained in chapter 5, the *a*SPECT magnetic field has been designed in a way that permits to study different systematics related to the transmission function and to the working principle of the spectrometer. In this section two important systematic tests carried out during the beamtime are presented.

Different ratio r_B

The influence on the coefficient a of a variation of the magnetic field ratio r_B was tested by applying an additional magnetic field in the AP region. For this test, the magnet was set in beamtime configuration (chapter 5), and the external correction coils c14 and c15 were energized at 50 A in Helmholtz configuration. With this current, the ratio of the magnetic field, r_B, was increased by 1.08 % (from $r_\mathrm{B} = 0.2030(2)$ to $r_\mathrm{B} = 0.2052(2)$, see section 5.4.5 and appendix B.2).

From our simulations, we expect a shift in the angular correlation coefficient a of $\Delta a/a = (-10 \pm 4)\,\%$ when using the standard ratio $r_\mathrm{B} = 0.2030(2)$ for the analysis of the data with the increased ratio $r_\mathrm{B} = 0.2052(2)$. The first error proceeds from fitting 7.5 to the simulated proton count rates and the latter one from the uncertainty in the magnetic field ratios.

Figure 7.88 shows the value of a obtained from data set "200508_lunch", measured with the standard ratio, and from data set "200508_night", measured with the modified ratio but otherwise entirely the same parameter settings. The resulting a agrees in both cases within the error bars (see table 7.27). However, analyzing the data set "200508_night" with the standard r_B value ($r_\mathrm{B} = 0.2030(2)$), the a-value differs by about $\Delta a_{exp}/a_{exp} = (-13 \pm 5)\,\%$. This illustrates the high impact of r_B on the transmission function and confirms that the procedure to extract a is reliable within the present error bars.

However, our statistics were too low to draw further conclusions. High-precision measurements with different magnetic field ratios may also be used in order to study possible angular-dependent detection efficiency of our spectrometer.

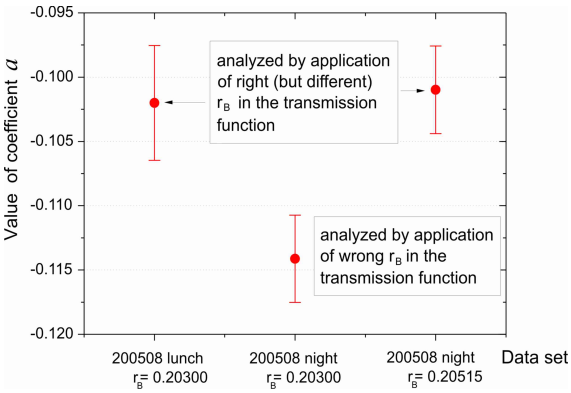

Figure 7.88: Influence of magnetic field ratio r_{B} on a. Data set "200508_lunch" was measured with the standard value of r_{B} while data set "200508_night" was measured with a magnetic field ratio increased in a 1.08 %. By analyzing the data set "200508_night" with the standard value of r_{B} the a-value differs by about 13 % from the data set "200508_lunch". When applying the corresponding ratio the a-values are statistically consistent.

a_{exp}	ratio used for the calculation	ratio used for the measurement
$-0.1020(45)$	$r_{\mathrm{B}} = 0.2030(2)$	$r_{\mathrm{B}} = 0.2030(2)$
$-0.1141(33)$	$r_{\mathrm{B}} = 0.2030(2)$	$r_{\mathrm{B}} = 0.2052(2)$
$-0.1009(34)$	$r_{\mathrm{B}} = 0.2052(2)$	$r_{\mathrm{B}} = 0.2052(2)$

Table 7.27: Angular correlation coefficient a calculated for different magnetic field ratios r_B.

Reduced field

As it was explained in section 5.4.5, a low magnetic field configuration permits to study important systematics. On the one hand, a low magnetic field increases the uncertainty in a due to the fact that the adiabatic approximation does not hold anymore (section 3.4.2). On the other hand, the lower magnetic field produces an increase of the gyration radius (equation 4.4) which translates into larger effective flux tube diameter (equation 4.1). The increase of the diameter of the effective flux tube has three consequences:

- The size of the DV gets increased being more sensitive to the potential created by the charging of the collimation system 4.2.
- The bigger diameter of the flux tube also translates into higher count rate and therefore a larger impact of the saturation effect in the detector preamplifier (see section 7.2.5).
- The area of the neutron beam "seen" by the detector is bigger as well as the region where edge effect may occur (section 3.4.4). This produce an increase of the impact of the edge effect on a .

Measurements with a reduced magnetic field were performed in order to study these systematics (see section 5.4.5 and appendix B.2). The currents applied to the coils were scaled down to a main current of 30 A. This configuration produces the same magnetic

field profile than the one measured with beamtime configuration but with lower absolute fields: $B_0 \approx 0.9326\,\mathrm{T}$ and $B_A \approx 0.1893\,\mathrm{T}$. The resulting ratio $r_\mathrm{B} = 0.2030(2)$ agrees with the ratio measured in beamtime configuration. Therefore, no substantial effect on a is expected from the magnetic field ratio.

Such a low magnetic field increases the uncertainty in a due to the fact that the adiabatic approximation does not hold anymore. From the MC simulations (see section 3.4), we expect a shift of a of $0.5\,\% \ll \Delta a/a < 4\,\%$ due to non-adiabatic effects. With the reduced field configuration it was observed a relative shift of the correlation coefficient a of $\Delta a_\mathrm{exp}/a_\mathrm{exp} = (+32 \pm 4)\,\%$ from $a_\mathrm{exp} = -0.1025(28)$ for $B_0 = 2.177\,\mathrm{T}$ to $a_\mathrm{exp} = -0.0697(38)$ for $B_0 = 0.933\,\mathrm{T}$ (21_05_08/night).

Such a variation of the coefficient a cannot be explained only with the non-adiabatic effects. To the effect of the non-adiabatic proton motion we have to add the effects produced by the changed diameter of the effective flux tube. The most important contributions are summarized in table 7.28. The values are taken from [38].

Effect on the angular correlation coefficient a	Relative shift [%]	Relative error [%]
Edge effect (2D simulation) (*)	−23	1
Non-adiabatic motion (*)	+16	4
Preamplifier saturation (**)	−21	9
Charging collimation (**)	+19	12

Table 7.28: Most relevant shifts and uncertainties on the antineutrino-electron angular correlation coefficient a in the case of low field measurement. (*) Calculated for $I_\mathrm{main} = 30\,\mathrm{A}$. (**) Calculated for $I_\mathrm{main} = 70\,\mathrm{A}$. The preamplifier saturation shift is only valid for a lower integration limit of 80 ADC channels. Note that the preamplifier saturation is also considering the shift due to electron backscattering.

Note that the shift of a due to the charging of the collimation system is underestimated since for $I_\mathrm{main} = 30\,\mathrm{A}$ the effective flux tube is larger and therefore reaches closer to the collimation system. The saturation of the preamplifier for the case of $I_\mathrm{main} = 70\,\mathrm{A}$ is slightly higher than for the case of $I_\mathrm{main} = 30\,\mathrm{A}$ and therefore can be consider as an overestimation[38]. Unfortunately, we do not have exact calculations of these effects for the case of $I_\mathrm{main} = 30\,\mathrm{A}$ at the moment.

The large error bars do not permit us to make clear statements. Averaging these effects, a relative shift of $\Delta a/a = -9\,\% \pm 16\,\%$ may occur due to the combination of the different systematics. This theoretical prediction is only 2.4σ from the experimental result. However, these calculations are a rough estimation which is not actually considering all the factors which may influence this low field measurement. Therefore, it is not possible to distinguish the dominant uncertainty or to extract a precise correction for the coefficient a. Further calculations with higher accuracy are necessary.

Chapter 8

Summary and Outlook

The aSPECT spectrometer has been build up to perform accurate measurements of the proton recoil spectrum in the decay of free unpolarized neutrons. Its design allows to determine the angular correlation coefficient a with an accuracy of at least $\delta a = 3 \cdot 10^{-4}$.

During this PhD thesis, the spectrometer was set up at the cold neutron beam position PF1b on the H113 guide at the Institute Laue-Langevin (ILL) in Grenoble, France. The main objective was to perform a precise measurement of the coefficient a with an accuracy comparable to existing results, i.e., $\delta a/a < 5\,\%$ and to study systematic effects for a final accuracy of $\delta a/a = 0.3\,\%$ in future beamtimes.

The experience gained during the first aSPECT beamtime[50] at the Forschungs- Neutronenquelle Heinz Maier- Leibnitz in Munich, Germany (2005-2006), permitted to identify the fundamental improvements necessary for this beamtime:

The aSPECT PIN-Diode proton detector was exchanged for a silicon drift detector. This detector delivers a much better separation of signal and noise even with low acceleration voltages. With the **new proton detector**, the acceleration voltage was reduced by a factor two down to -15 kV. This solved the problem of electrical breakdowns [46].

Modifications in the electrode system, **detector high voltages electrodes** and a considerable **improvement of the vacuum** conditions (chapter 4) permitted to lower the background count rate by a factor of 5 to 10. Also the fluctuating contributions to the background were reduced to a very low level, indicating a minimization of particle traps (section 7.2.3). Several components of the background were systematically studied [45].

The aSPECT **magnetic field was readjusted** (chapter 5 and 4) to match the requirements of the new proton detector and to provide a more suitable profile for the determination of a. Important **systematics related to the transmission function** (section 7.2.6) were studied by applying specific magnetic field configurations during the beamtime. The strong effort on the magnetic field measurements provided accurate aSPECT **magnetic field maps**. In spite of the serious limitations on the prove stability and accuracy, it was possible to measure the magnetic field with an accuracy sufficient for a 5 % accuracy measurement of a. For the target of $\delta a/a = 0.3\,\%$, the accuracy of the measurements has to be improved.

To overcome this limitations a **high accuracy NMR-magnetometer** was developed

(chapter 6). Its special design makes the magnetometer ultrahigh vacuum compatible and suitable for magnetic field measurements in a temperature working range from approximately 10 K to 400 K. With this magnetometer, the stability and reproducibility of the magnetic field and its ratio r_B were determined to be better than required for a precise a measurement (see table 6.24). This magnetometer also demonstrated to be suitable for a measurement of the magnetic field ratio r_B with an accuracy of $\delta r_B/r_B < 10^{-4}$, necessary for a measurement of a with an accuracy of 0.3 %. Further improvements on the magnetometer have been already tested. These improvements provide us with a higher accuracy and a much more stable, reliable and confortable measurement procedure and data analysis.

Many other systematic effects were studied during this beamtime and are now well understood leading to rather small corrections and systematic errors[38][45]. The most important systematics related to the transmission function are listed in table 8.29. A complete list of systematics can be found in [38].

Effect on the angular correlation coefficient a	Relative correction [%]	Relative error [%]	Relative error (MC) [%]
longitudinal B field gradient (chapter 5)	0.001		0.05
radial B field gradient (chapter 5)		0.3	0.1
B field ratio (chapter 5)		0.3	0.1
B field ratio (with calibration error) (chapter 5)		0.9	0.2
Barrier Voltage U_A [38]	0.09		0.11
WF inhomogeneities [38]	-0.03	$^{+1.9}_{-1.6}$	0.18
Non-adiabatic proton motion [38] (*)	-0.014	$^{+0.013}_{-0.03}$	
Charging collimation [38]	-19	12	

Table 8.29: Corrections and uncertainties on the antineutrino-electron angular correlation coefficient a related to the transmission function. (*) The correction due to the non-adiabatic proton motion considers only the effect of the lower ExB potential (section 3.4.2). The values related to the magnetic field correspond to the Hall probe measurements.

During the data analysis several different systematic effects were investigated. Exhaustive Monte Carlo simulations were performed to compute a variety of systematic corrections[38]. The dominant systematic uncertainties on the neutrino-electron correlation coefficient a were found to be a possible charging of the collimation system[38] (section 4.2), potential Penning discharges in the bottom of the spectrometer (section 7.2.4), and a violation of the condition for adiabatic transport[38] (section 7.2.4). However, an **energy dependent saturation effect** of the preamplifier prevented the extraction of a value of a with a reasonable error bar[46].

The knowledge acquired during the studies of the electromagnetic field of the aSPECT

spectrometer, the results of the beamtime, and the Monte Carlo simulations, provide important information which has be used in order to propose fundamental improvements for **future *a*SPECT beamtimes**:

Proton detector

The **saturation effect** can be avoided taking several measures: the amplification of the preamplifier has to be reduced by about a factor two, which still keeps the pulse-height of the protons on a reasonable level. Furthermore, the shaper has to be modified in order to remove the undershoot of the baseline after high energetic electrons and to shorten the shaping time which will reduce the event length and therefore the probability of pile-ups. New mechanics moveable in the horizontal plane will allow to position the detector in the center of the beam profile, thereby minimizing the edge effect[46].

Background

Regarding the background components, it is advisable to continue improving the vacuum conditions to reduce the probability of rest gas ionization (and thus the amount of uncorrelated background) and to reduce the electrostatic mirror potential, to prevent Penning discharges in the bottom part of the spectrometer[38]. From the background analysis it is possible to conclude that longer measurements with closed shutter are necessary to study the AP voltage dependent background. Additionally, the lowest AP voltage setting from which on peak 2 disappears has to be determined. Also the stability of the neutron beam monitor has to be improved[45].

Transmission function

In respect to the transmission function, it is necessary to further improve the quality of the surfaces of the electrodes and to extend the surfaces studies with the Kelvin probe. Three measures are remarkable:

- to coat the surfaces of the collimation system with a layer of conductive material in order to prevent a charging of the collimation system.
- to increase the volume of the DV and to reduce the influence of work function inhomogeneities in the effective proton flux.
- re-polish and subsequently re-coat the inner surfaces of the analyzing plane (AP) electrode e14, in order to reduce the influence of work function inhomogeneities.

The *a*SPECT magnetic field fulfils its design requirements (chapter 5), however, two fundamental improvements regarding the magnetic field measurement are necessary. On the one hand, the magnetic field mapping has to be performed with higher accuracy for the extraction of the ratio r_{B} (weighted with the neutron beam profile) and for trajectory calculations (chapter 5). On the other hand, an on-line monitor during beamtimes is necessary to check, in-situ, the field stability and to determine the absolute magnetic field value for trajectory calculations (chapter 6).

An accurate mapping of the magnetic field within the DV and AP regions and a constant magnetic field monitoring are possible with the NMR-magnetometer developed

during this thesis. Further, joint measurements with the Hall probe and the NMR magnetometer would permit accurate magnetic field measurements within the complete spectrometer.

A monochromatic ion source is also recommendable for a joint study of the electric and magnetic field which enters the transmission function.

Simulations

Several MC simulations have to be improved[38]. The most important tasks are:

- re-examine the influence of non-adiabatic proton motion, in particular with regard to the height of the main magnetic field (section 7.2.6).
- increase the quality of the simulations of the edge effect. For that it is also necessary to measure the neutron beam profile directly in the DV with improved accuracy.

Appendix A

Electrode System and Cryostat

A.1 Cleaning of the Electrode System and Vacuum improvements

Two main reasons demand a proper treatment and cleaning of the *a*SPECT electrodes: a highly homogeneous work function and good ultra high vacuum conditions (chapter 4).

Gold coating prevents the copper to oxidize and provides a homogeneous work function. Polishing and coating procedures have been improved with respect to the FRM-II *a*SPECT beamtime (2005-2006) in order to obtain better surfaces with a more constant work function (section 4.3). The good result of the new treatment can be seen in figure A.89. Studies of electrodes surface of samples from the FRM-II *a*SPECT beamtime are discussed in section 4.3.

Dust or residues (like industrial oils, or chemicals from the coating bath) can remain on the surface of the electrode affecting the homogeneity of the work function. They can also evaporate contaminating the UHV necessary for our spectrometer. In order to minimize these effects, an improved cleaning procedure which preserves the surfaces quality has been developed for the ILL beam-time.

The complete electrode has been cleaned piece by piece in a bath of distilled water and Mucasol[1]. This solution is very effective to remove dirtiness, residual industrial oils or of the electrolytic bath used for the coating. Afterwards, it is submerged in distilled water to remove rests of the bath. Finally, it is cleaned in a bath of pure isopropanol and again with distilled water. The clean electrodes, still wet, are introduced into a vacuum oven at 90° during two or three hours (higher temperatures have to be avoided because they may accelerate the diffusing process of gold into copper). This procedure permits to dry the water on the surfaces and avoid to catch carbon atoms from the air. The high temperature together with the vacuum also increases the outgassing of the surfaces.

Every clean piece is introduced into plastic bags and filled with pure nitrogen in order to keep a clean atmosphere. Other pieces like Macor insulators and titanium screws are cleaned following the same procedure but inside an ultrasonic bath which removes

[1] Mucasol laboratory detergent is an alkaline, high-performance liquid concentrate for wiping down lab surfaces and cleaning labware in immersion and ultrasonic baths.

molecules stuck on the surfaces. After all the pieces have been cleaned and protected in bags with nitrogen atmosphere, the electrode system is build up inside a gray room [2]. After cleaning, the complete electrode system was built up and wired in approximately two days. Finally, it was introduced inside the cryostat and pumped down to approximately 10^{-5} mbar. Protected inside the main vacuum chamber of the spectrometer it was transported to the ILL reactor.

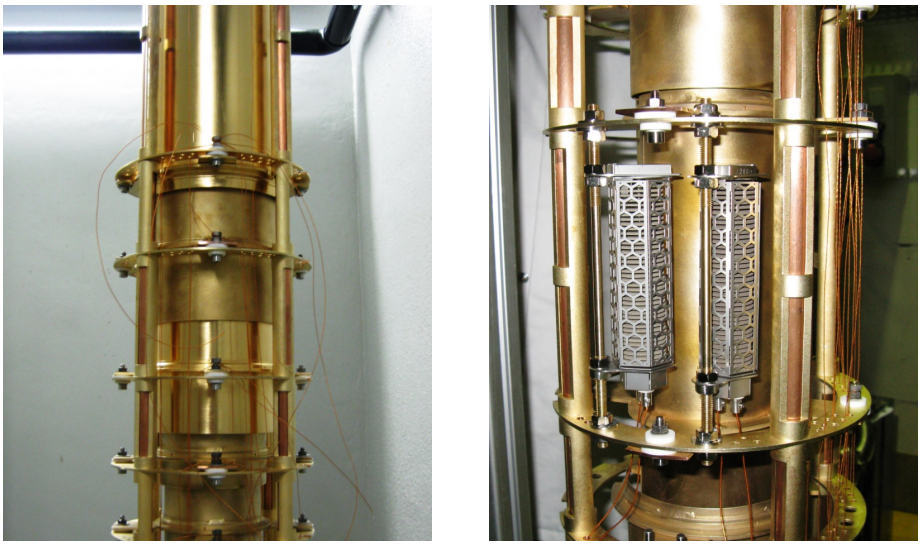

(a) Coating and surface treatment. (b) SAES getter pumps.

Figure A.89: (a) View of electrodes e14 and e12. The new electrodes e12 and 14 can be compared with the original electrodes used during the FRMII beamtime. The bad quality of the surfaces of those electrodes which were not retreated for the ILL beamtime is not an inconvenience since they do not enter in the transmission function. (b) Set of two SAES getter pump cartridges installed to improve the vacuum quality. A total of four pumps were installed in pairs of two at electrodes e2 and e9.

Further evacuation of the main vacuum chamber increases the cleanliness of the electrodes. The cooling down of the system makes the electrodes, and every cold surface, to act as cryo-pumps. Molecules inside the vacuum chamber are caught by cold surfaces when collision occurs. This effect increases the quality of the vacuum, but damages the purity of the surfaces. Therefore, cooling down has to be done only after a good vacuum has been reached. For the beamtime at the ILL reactor, the cooling down process was started at a vacuum of about 1×10^{-7} mbar. Better vacuum would have been achievable, however, the lack of time made it impossible to extend the evacuation period. After the cooling down, the vacuum was much better than 1×10^{-8} mbar. The vacuum sensor was

[2] A clean room is designed to have a low level of environmental pollutants such as dust, airborne microbes, aerosol particles and chemical vapors. A clean room has a controlled level of contamination that is specified by the number of particles per cubic meter at a specified particle size. The ambient air outside in a typical urban environment contains about 35.000.000 particles per cubic meter with a size of 0.5 μm and larger. In clean rooms in which the standards of air contamination are not very rigorous the content of particles can be from several orders of magnitude less, going down to tens of particles for the best ones. The gray room is the intermediate stage which separates normal conditions from the clean room so the pureness of the air is orders of magnitude worst than inside the clean area.

placed at the very bottom of the spectrometer and connected to it via a long vacuum tube which placed the sensor outside of the antimagnetic screen. In this region the magnetic field is very low and thus monitoring of the vacuum is possible while the superconducting magnet is working. The vacuum at this position is much worse than in the volume of the electrode system. Thus, the values measured there have to be considered an overestimation. The vacuum at the region of interest, main vacuum chamber, is estimated to be sufficient for a precision measurement of a [19] and it is also considerably improved respect to the FRM-II beamtime (at the FRM-II, a vacuum of 2×10^{-8} mbar was measured close to the main vacuum chamber).

This improved level of vacuum was possible thanks to the addition of four getter pumps and the improved treatment of the surfaces. The getter pumps were directly installed in the electrode system in pairs of two at different heights, figure A.89 (b). The getter pumps used were SAES CapaciTorr -D 400-2 Pumps. Getter cartridges have to be activated to develop their pumping characteristics. This activation process consists of a heating procedure up to a temperature of about 500 °C for 60 minutes. The heat treatment diffuses the thin protective layer into the bulk and makes the surface clean and able to sorb the gas molecules. The efficiency of this activation process is related to the diffusion coefficient of the material which depends on an exponential function of the temperature and on the square root of time. Due to the proximity of the getters to the superconducting coil, a high temperature increase is not recommendable since an elevated temperature can deform the superconducting coils affecting thus the field characteristics. To avoid it, the getters were activated in several steps to keep the coil temperature on a reasonable level (about 10-15 °C over room temperature). With a temperature lower than the recommended 500 °C but longer activation time, the complete activation can be reached. Heating and waiting periods were alternated till the vacuum showed no improvement any more. This process took about three hours.

A.2 Cryostat and coil system design

The cryogenic magnet was manufactured by Cryogenics Inc. It consists of a set of nine superconducting coils of NbTi. The coils are connected in series in such a way that the ratio of the field is kept constant independently of the intensity of the introduced current or its possible fluctuations. The number of windings differs from one coil to another to create the field profile described in chapter 5. Trim coils c5 and c6 are used to modify the shape of the magnetic field at the DV and for systematic checks. The external correction coils, c12 to c15, were added *a posteriori* to modify the shape of the field at the AP to the desired configuration. The locations and characteristics of the internal coils are shown in table A.30.

In the first column are listed the different coils with the numeration used in figure 4.14. Coils c2 and c4 are manufactured in three parts (a, b, and c) made with different kind of wires, see figure A.90. Each type of wire is indicated with a different index, i_w:

$i_w = 6$: $dz = 0.65$ mm, $dr = 0.6$ mm.
$i_w = 7$: $dz = 0.75$ mm, $dr = 0.7$ mm.
$i_w = 8$: $dz = 0.85$ mm, $dr = 0.8$ mm.

coil	i_w	r_{min} [cm]	r_{max} [cm]	z_{min} [cm]	z_{max} [cm]	turns	n_r	n_z
1	6	12.900	13.380	-42.940	-14.280	3529.0	8.0	440.9
2a	8	25.480	27.080	-13.700	-6.550	1680.0	20.0	84.1
2b	7	27.080	27.780	-13.700	-6.550	950.0	10.0	95.3
2c	6	27.780	30.402	-13.700	-6.550	4808.0	43.7	110.0
3	6	13.130	13.550	-11.780	-11.325	49.0	7.0	7.0
4a	8	24.280	26.040	6.730	11.410	1210.0	22.0	55.1
4b	7	26.040	27.300	6.730	11.410	1116.0	18.0	62.4
4c	6	27.300	30.780	6.730	11.410	4176.0	58.0	72.0
5	6	13.130	13.550	11.320	11.775	49.0	7.0	7.0
6	6	14.080	14.560	13.960	27.930	1720.0	8.0	214.9
7	6	15.000	15.780	29.540	47.350	3562.0	13.0	274.0
8	6	15.000	15.900	47.410	79.000	7290.0	15.0	486.0
9	6	19.280	19.460	99.060	165.950	3087.0	3.0	1029.1
10	6	12.000	13.980	190.000	220.290	15378.0	33.0	466.0
11	6	12.000	14.700	220.290	235.310	10395.0	45.0	231.1

Table A.30: Coil geometry data.

where dz and dr are the the dimensions defined in figure A.90. Considering the critical current density for superconducting wires and the cross-section of the wires, 0.39 mm^2, a maximum current of 100 A is permitted. The current density is defined as 100 turn/cc (A/cm^2), where $cc = (z_{max} - z_{min}) \cdot (r_{max} - r_{min})$ The origin of the coordinate system has been set at the center of the DV, see figure 4.14. The number of wire layers varies from one coil to another in order obtains the desired magnetic field. For each coil the number of layers in axial and radial coordinate is given by n_z and n_r respectively:

n_z: number of wire layers in axial coordinate.
n_r: number of wire layers in radial coordinate.

The two split pair coils c2 and c4 have been designed approximately as Helmholtz coils in order to create a high and homogeneous magnetic field and to permit, at the same time, the neutrons to fly across the DV region. Coils c5 and c6 are powered separately. They produce a magnetic field gradient along the z-axis up to 1% of the main field. This gradient permits to change the homogeneity of the magnetic field and to create a linear gradient with its maximum well below the DV. In this way proton traps are avoided and several systematic checks are possible, see section 3.4 and chapter 5.

The coils, with the exception of c12 to c15, are placed inside a cylindrical cryostat of three meters height and seventy centimeters of diameter, see figure 4.14 and A.91.

The cryostat contains a twenty centimeter diameter axially centered bore tube kept at a temperature of about 50-70 K. This bore tube defines the main vacuum chamber, i.e.,

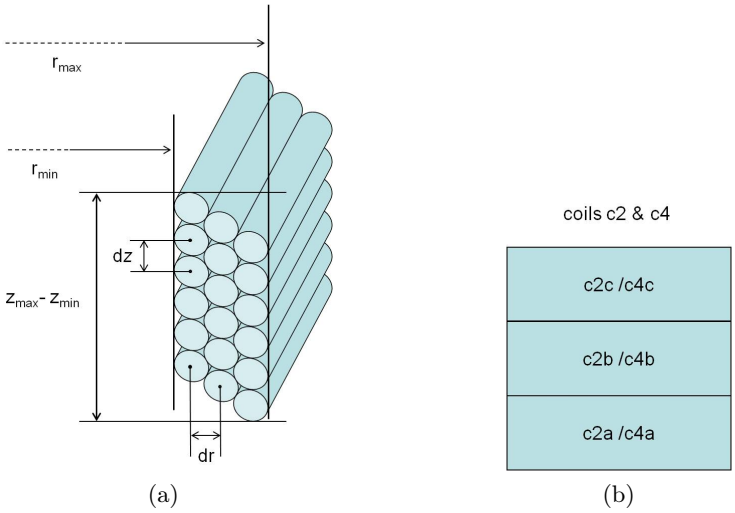

Figure A.90: (a) Packing of the wires and definition of the coils parameters. (b) Design of the internal correction coils c2 and c4.

the chamber where the electrode system is installed. The pressure in the main vacuum chamber is about 10^{-9} mbar in operating conditions. This high level of vacuum is necessary in order to suppress background and collisions of protons with rest gas, see section 3.4.

The superconducting coils are placed at the outer side of the bore tube, in what is called the insulating vacuum chamber. This chamber is thermally insulated to keep the superconducting coils at about 4 K. The insulation vacuum in this cavity is of about 10^{-4} mbar.

There are six openings providing access to the main vacuum chamber. Four of them are around the decay volume level and are used for the vacuum pumping system and as entrance and exit for the neutron beam. The other two accesses to the main vacuum are at the top and bottom extremes of the bore tube. The upper entrance is used to introduce the proton detector into the spectrometer whereas the electrode system is placed into the main vacuum through the lower entrance. The electrode system is designed to have the central part of the DV electrodes at the height of the two windows which give access to the neutron beam.

A.2.1 Cooling down and ramping up

The cryostat is cooled down by two cryocoolers of type Sumitomo RDK408D. Each cryocooler has a cooling power of 35 W at the first stage (of about 70 K) and of 1 W at the second stage (of about 4 K). The temperature at the coils and bore tube is continually controlled by 20 temperature sensors located along the spectrometer.

Before powering up the magnet, the insulating vacuum has to be evacuated to a pressure of about 10^{-4} mbar and the main vacuum to a pressure of at least 1×10^{-7} mbar. This process requires about 6 days of vacuum pumping. Once the main vacuum has reached the suitable pressure, the system can be cooled down. The cooling process takes about 120 hours. Using liquid nitrogen for pre-cooling, the overall cool down time can be reduced to less than 80 hours. The liquid nitrogen is introduced through a nitrogen line

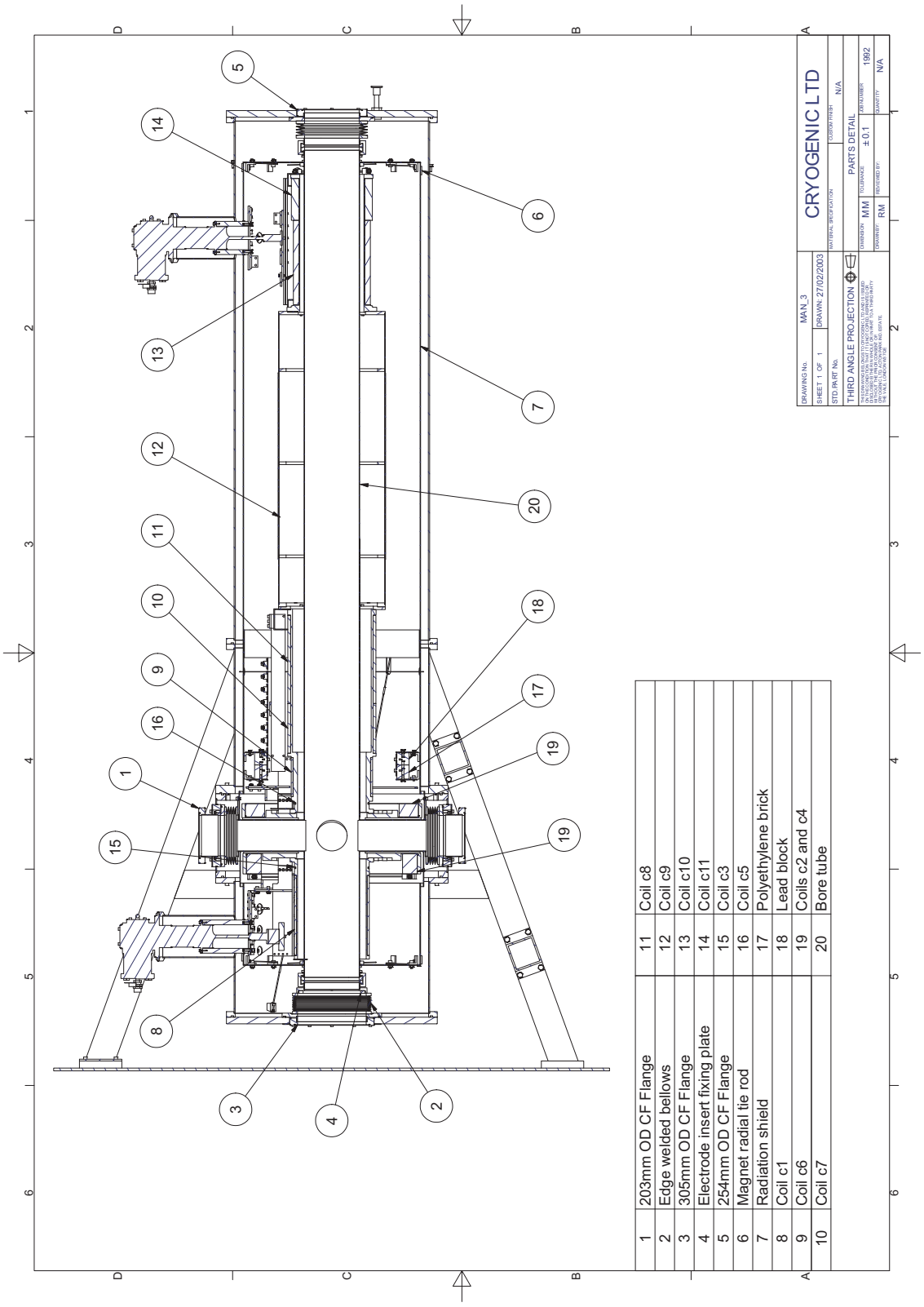

Figure A.91: Technical drawing of the system assembly. The coils are indicated and named according to the scheme shown on figure 4.14.

with accesses on top of the cryostat. The nitrogen line is a tube which travels through the insulating vacuum to fasten up the cool down process up to the liquid nitrogen temperature. Once the temperature gets close to this limit, the line has to be evacuated with dry clean gas and pumped to an insulating vacuum. Once the cooling down process is completed, about 3 hours are needed to ramp up the coils to 70 A. The time needed to ramp up the coils depends on the critical temperature at which the transition from superconducting to conductive states happens. The critical temperature is a function of the magnetic field. When the magnetic field increases, the critical temperature decreases. Therefore, the higher the field, the lower the ramping speed has to be in order to keep the temperature of the superconducting coils on a safe level below the critical temperature. The process of warming up takes approximately 5 days. In an emergency case, this period can be reduced to 2 days by inserting a clean gas inside the insulating vacuum chamber. Prior to the opening of any of the two vacuum chambers, nitrogen gas is introduced in order to create a protective layer over the surfaces which will help to avoid other gasses to stick there.

A.2.2 External Correction coils

External correction coils c12 to c15 were added a posteriori to modify the position of the local maximum of the AP, see section 5.1.2 and for systematic checks. Coils c12 and c13, see figure 4.14, are set as anti-Helmholtz coils whereas coils c14 and c15 are set in Helmholtz configuration. The pair of coils c12 and c13 create a gradient which permits to shift the position of the local maximum of the magnetic field at the AP, to the height of the electric potential maximum created by the AP electrode, see [44] for more details. This is necessary due to our definition of the transmission function, see section 3.3. The second pair of coils, c14 and c15, create a homogenous field which changes the ratio of the magnetic field, r_b, for systematic tests of the transmission function. The dimensions and positions of the coils c12 and c13 are:

- Inner and the outer radius of the coils: $R_{\text{in}} = 37\,\text{cm}$ and $R_{\text{out}} = 41\,\text{cm}$, respectively.

- Position in the z-axis: $z_{c12} = 104.5\,\text{cm}$ and $z_{c13} = 159.0\,\text{cm}$. Width of the coils $\Delta z = 6.0\,\text{cm}$. z_i is the position of the center of the coil measured from the decay volume.

- Area of the wires $A = 10\,\text{mm}^2$ ($\phi \approx 3.56\,\text{mm}$), resistance $180\,\text{m}\Omega/100\,\text{m}$.

- Number of turns $n = 32$. Total length $\sim 80\,\text{m}$

For 25.5 A of current used for most of the beam time the consumed power is $\sim 150\,\text{W}$. Therefore, for a safe powering of the coils a cooling system is necessary. In the final setup, the coils were built up with 32 turns in 4 layers of 8 turns each. A layer of plastic festo tubes with 6 windings surrounding the conductive cable was enough for an effective temperature stabilization. The field produced by the coils with a current of 25.5 A has a maximum value of about 12 Gauss. This represent a 0.3% of the main field at the AP.

To calculate the current necessary to shift the local maximum of the AP magnetic field to the most homogeneous region of the electric field, we proceed as follows: after adapting

the simulation to fit with the magnetic field measurements with only main field we add the effect of the anti-Helmholtz coils, c14 and c15, and calculate, then, the necessary current to shift the maximum position to the correct height. With 70 A main field and 25.5 A, the measurements of the magnetic field on- and off-axis showed that the position of the maximum is placed at the most homogeneous region of the electric field according to the electric field simulations at $z = 132\,\mathrm{cm}$.

The coils c14 and c15 have the same characteristics as the previous correction coils, c12 and c13, but with 40 windings and in helmholtz configuration in order to produce a variation on the order of 1 % of the main field, with 70A main field and 50A at the correction coils. The position of these coils is: $z_{c14} = 112.0\,\mathrm{cm}$ and $z_{c15} = 151.0\,\mathrm{cm}$.

Appendix B

Additional magnetic Field checks

B.1 Reproducibility of the field

In addition to the accuracy and stability of the Hall probe (sections 5.2.1 and 5.2.3) to measure the magnetic field and the external factors discussed in section 5.3, also the reproducibility of the field it self has to be considered. Several factors influence the field reached after the ramping up procedure of the magnet. One of the biggest is due to the stabilization of the current once the power supply reaches its selected value, see figure B.92. Region I corresponds to the time when the power supply reaches its selected value. Still it takes six hours more (region II) to reach a considerably field stability (region III). The change of the field during that time is still about 30 G at the DV. Since this change happens proportionally at the AP too, the ratio of the main field remains unaltered. Nevertheless, the additional correction coils are powered always at the same current (field) independently of the actual value of the main field. This affects the ratio of the total field the same way than the drift of the main field, see section 5.2.1. A difference in the main field of 30 G affects the ratio r_B on a relative level smaller than $6 \cdot 10^{-5}$ and is therefore only a small problem for the calculation of the ratio. But it represents approximately 0.14 % of the field and thus has to be considered for trajectory calculations [38].

The point marked as "Jump" is an artefact related to the instability of the hall probe. The heater for the persistent mode was switched off at about 9:30. Afterwards, a small decrease of the field was observed until the field recovered stability. This small change of the field of about 1 G is negligible. At about 10:30 the power supplies were ramped down.

Other factors influencing the reproducibility of the field have been discussed in section 5.3. These effects may lead to slightly different magnetic fields after every ramping up procedure and are not easily calculable with the accuracy necessary for aSPECT. Consequently, measurements after several different ramping up procedures are advisable in order to estimate the reproducibility of the field in situ.

The magnetic field has been ramped up several times with a previous warming up procedure in order to remove hysteresis effects. After every ramping up, the field was measured and the ratio r_B has been calculated. The ramping up procedure was always carried out at night and the persistent mode switched on the next morning. In this way, the power supply had the complete night to stabilize, see figure B.92.

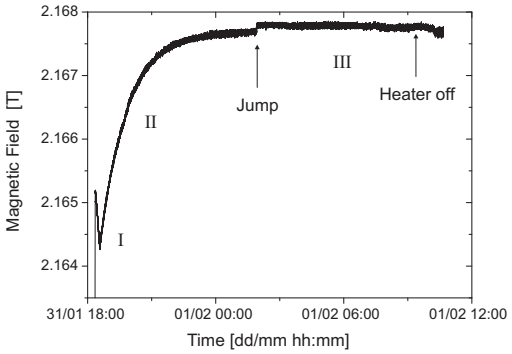

Figure B.92: Magnetic field measured with the MPT-141 Hall probe at the DV while ramping up the current energizing the main coils. The moment where the jump is produced corresponds to the time when the power supply reaches its selected value. Still takes six hours more to reach a considerably stable field. The change during this time is about 30 G.

The maximum difference observed in the absolute value of the magnetic field after different ramping up procedures was 11 G at the DV. The fluctuations between measurements taken in different days, figure 5.37, are also in the same order, $\sim$ 8 G. Therefore, this difference of 11 G can be explained by the probe uncertainty plus a slightly different field.

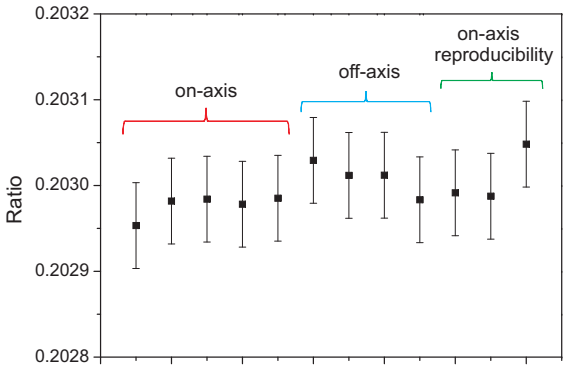

Figure B.93: Stability and reproducibility of the magnetic field ratio r_B. The ratio has been calculated from every scan along the $z-axis$ with total error bar. The last three values correspond to measurements on-axis after ramping up the field for reproducibility tests.

During the course of the beamtime the superconducting magnet had a quench due to a failure in a water-cooling circuit. Therefore, it was necessary to repeat the magnetic field measurements at the end of the official beamtime at ILL in order to check the effect of the quench on the magnetic field profile.

The magnetic field profile measured after the quench was found to fit perfectly with the previous measurements. The ratios calculated from all the measurements (before and after the quench) give approximately the same value, see figure B.93. In conclusion, the ratio is reproducible after every ramping up and measurable with a relative accuracy of $3 \cdot 10^{-4}$. The final value given for the ratio r_B, in table B.31, is the average of all the ratios from figure B.93.

Calibration error	Ratio	$\Delta r_B / r_B$	Relative error on a $\Delta a/a$ [%]
No	0.20300(5)	$\pm 3 \cdot 10^{-4}$	± 0.3
Yes	0.2030(2)	$\pm 1.5 \cdot 10^{-3}$	± 0.9

Table B.31: Ratio of the magnetic field r_B obtained averaging the result of table B.31 with the ratios measured for the reproducibility tests.

B.2 Magnetic Field configurations for systematic tests on a

Different magnetic field configurations aimed to perform systematic tests were also measured.

the aSPECT magnetic field has been designed in a way that permits to study different systematics related to the transmission function and to the working principle of the spectrometer. In this section two important systematic tests carried out during the beamtime are presented.
Several systematic tests are necessary in order to calibrate our spectrometer for an accurate measurement of the correlation coefficient a (see section 3.4). Two fundamental systematic tests with different magnetic field configurations are presented next.

Low field configuration

A field configuration with low magnetic field values permits to study two important systematics of the aSPECT spectrometer. On the one hand, a low magnetic field increases the uncertainty in a due to the fact that the adiabatic approximation does not hold anymore (see section 3.4.2). On the second hand, although the ratio of the magnetic field B_{det}/B_0 is conserved (see chapter 5), the lower B field produces an increase of the gyration radius (equation 4.4). This translates into a larger effective flux tube diameter and, thus, in an increase of the impact of the edge effect on a (section 3.4.4). The study of proton spectra measurements with low field configuration brings helpful information to understand and calculate the influence of both systematics on a (see section 7.2.6).

After the beamtime, the magnetic field profile was measured with low magnetic field configuration. For that, the standard magnetic field configuration (I(main)=70 A, $I(c3)$ = 35 A, $I(c5)$ = 15 A, $I(cc)$ = 25.5 A) was scaled down to I(main)=30 A, $I(c3)$ = 15 A, $I(c5)$ = 6.4 A, $I(cc)$ = 11 A. The result was an identical magnetic field profile (within the error bars) with the same magnetic field gradient and ratio. Figure B.94 shows a magnetic

field measurement with beamtime configuration (blue) together with a measurement with low magnetic field configuration (black) scaled to 70 A in order to fit in the same graph.

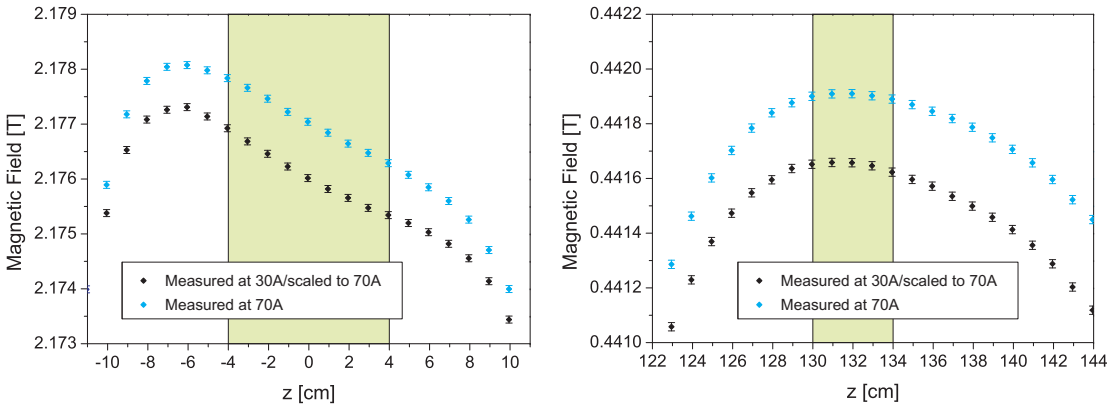

(a) DV (b) AP

Figure B.94: Magnetic field measurements at the DV and AP, (a) and (b) respectively, with beamtime configuration and low field configuration (I(main)=30 A, $I(c3)$ = 15 A, $I(c5)$ = 6.4 A, $I(cc)$ = 11 A) scaled to 70 A in order to fit in the same graph. The measurements are corrected with first and second correction. The error bars correspond to the stability error. The size of the error bars in the AP measurement are smaller than the size of the points.

The magnetic field ratio r_B obtained after averaging the magnetic field at the DV with the neutron beam profile is presented in table B.32. Note that the curvature present in the DV in the low field configuration is approximately symmetric around 0 cm and therefore it does not affect the field ratio in a considerable level (see section 5.1.5). The result coincides, within the error bars, with the measurements performed with beamtime configuration, table B.31.

Ratio	Systematic Error
0.20296	$\pm 5 \cdot 10^{-5}$

Table B.32: Ratio of the magnetic field r_B for low field configuration: I(main)=30 A, $I(c3)$ = 15 A, $I(c5)$ = 6.4 A, $I(cc)$ = 11 A.

Increased magnetic field ratio (r_B)

A different magnetic field ratio r_B permits to test the influence on the coefficient a of a possible error on the determination of r_B.

For that test, the external Helmholtz coils c14 and c15 were energized with a current intensity of 50 A[1] while the magnet was set in beamtime configuration. This produces an increase of the magnetic field at the AP region of about 1 %, see figure B.95. The ratio of the field was increased by 1.01 % (table B.33).

[1]Coils c14 and c15 are referred to as HC

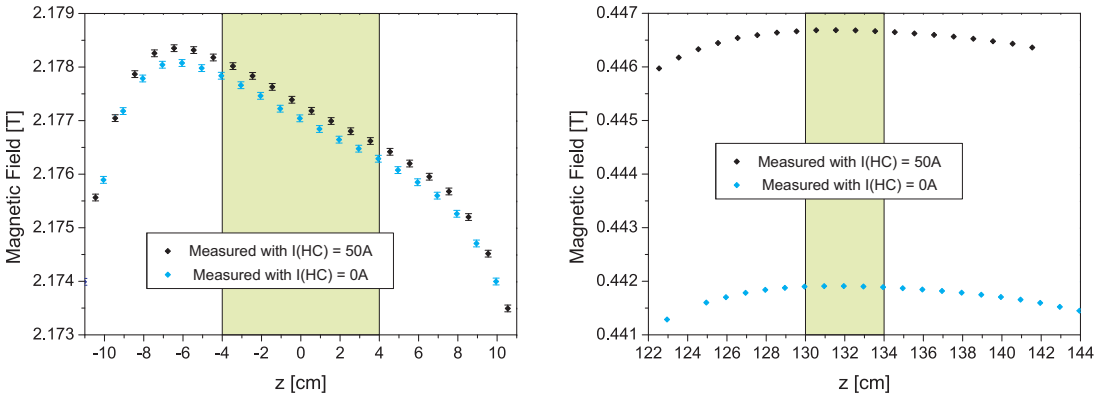

(a) (b)

Figure B.95: Magnetic field measurements at the DV and AP, (a) and (b) respectively, with beam-time configuration and increased magnetic field ratio configuration (I(main)=70 A, $I(c3) = 35$ A, $I(c5) = 15$ A, $I(cc) = 25.5$ A, $I(HC) = 50$ A. The measurements are corrected with first and second correction. The error bars correspond to the stability error.

Ratio	Systematic Error
0.20515	$\pm 5 \cdot 10^{-5}$

Table B.33: Ratio of the magnetic field r_{B} for the field configuration with increased ratio: I(main)=70 A, $I(c3) = 35$ A, $I(c5) = 15$ A, $I(cc) = 25.5$ A, $I(HC) = 50$ A.

Appendix C

NMR-Magnetometer calculations

C.1 Longitudinal relaxation of polarized ^3He

The longitudinal relaxation time of the polarized ^{3}He, T_1, limits the time for measurements at the DV- or AP-sample. Although the ^{3}He is hyperpolarized to high polarization rates (more than 70%), already significant amounts of polarization are destroyed during filling of the Helium into the system, mainly due to passing through strong field changes, see section 6.1.3. In addition, it gets in contact with different types of material surfaces with different amount of para- and ferromagnetic impurities. Probably the highest contribution to the depolarization is due to wall relaxation inside the copper tube system. Due to its fragility and length a proper cleaning procedure was not possible.

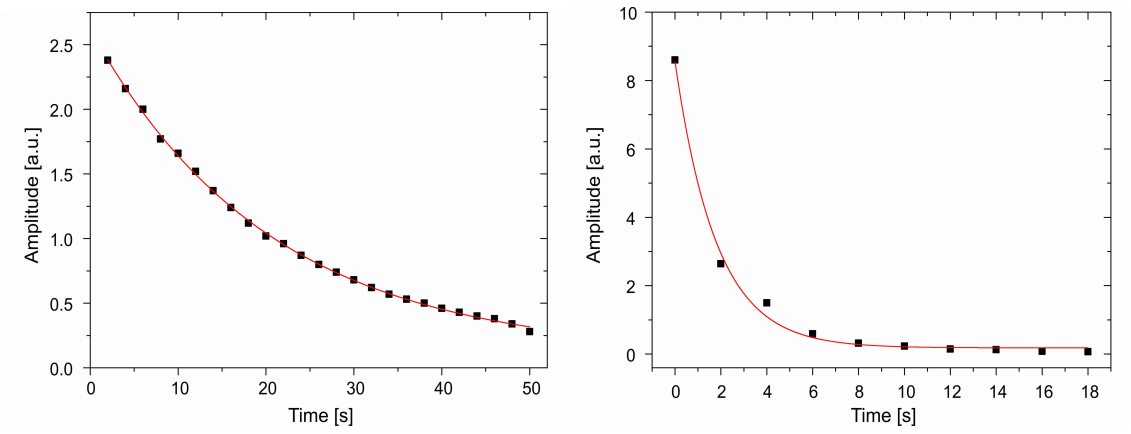

(a) (b)

Figure C.96: Estimation of the longitudinal relaxation time, T_1, from the decay of the signal amplitude on each new measurement. (a) and (b) measurements with main configuration at DV and AP respectively.

Once the helium is introduced into the system, it can move freely from the copper tube-system to the glass NMR-samples, or reverse. Form a rough estimate of the self-diffusion coefficient of the ^{3}He (appendix C.2), we find that the helium atoms can move several centimeters per second. Consequently, a prediction of T_1 inside the system would have to include large magnetic field gradients and several uncharacterized surfaces. Similar to the calculation of the depolarization rate, the calculation of T_1 is not possible.

However, T_1 can be estimated from the decay of the signal amplitude on each measurement of a set. Although, the r.f. pulse partially destroys the polarization, the mobility of the helium ensures that it will be replaced by unexcited helium before the next measurement.

In order to characterize the value of T_1, the decay of the amplitude of the signal after each measurement has been fitted to an exponential decay, see figure C.96. The polarization destroyed with every NMR-measurement is considered negligible compared to the big amount of helium which remains unaffected.

The results show a similar value of T_1 (table C.34) for both configurations, main field and beamtime configuration, however it is much smaller at the AP than at the DV-sample. The different values of T_1 between both regions are probably due to a different surface contamination on the copper-tube surface or on the glass NMR cell (the AP-sample cell was visibly dirtier than the DV-sample cell). The short T_1 values measured indicate that the polarization is rapidly lost and only a few measurements can be acquired with each helium filling.

$T_1(s)$		
	DV	AP
Main field configuration	20.3(4)	1.81(12)
Beamtime configuration	15.3(2)	1.25(12)

Table C.34: Experimental T_1 values. The error bars are obtained from the fit to an exponential decay.

C.2 Self-diffusion coefficient and Edge Enhancement

C.2.1 Chapman and Enskog theory

Chapman and Enskog presented a detailed theory, named after them [70], which makes use of the Kinetic Theory of Gases in order to build up a model to calculate transport coefficients. A good and complete description of this theory can be found in the book of J.O. Hirschfelder et al. [83].

Hirschfelder defines the diffusion as a transport phenomenon where the physical property which is transported is the mass. For the calculation of the transport coefficients applies a classical treatment of kinetic theory of dilute monoatomic gases and mixtures (the Chapman-Enskog theory). The final result for the transport coefficients can be then expressed in terms of the collision integrals, $\Omega^{(l,s)\star}$, which depend on T^*. The omega integrals involve the dynamics of a molecular encounter and hence the intermolecular force. The integrals can be found tabulated in the book from Hirschfelder for the Lennard-Jones Potential. The coefficient of diffusion for a single component, the self-diffusion coefficient $[D]_1$ in cm^2/s, is presented as:

$$[D]_1 = 0.0026280 \frac{\sqrt{T^3/M}}{p\sigma^2 \Omega^{(1,1)\star} T^*} \tag{C.1}$$

given in m^2/s were p is the pressure in atmospheres, T the temperature in Kelvin, M the molecular weight and $T^* = kT/\epsilon$ is the reduced temperature. σ and ϵ are the energy parameters of the molecular potential, the Lennard-Jones Potential, in Å and K, which can be found tabulated in ref. [83]. The subindex 1 indicates a first order approximation. The higher approximations for the coefficient of self diffusion are given by:

$$[D]_k = [D]_1 f_D^{(k)} \tag{C.2}$$

where $f_D^{(2)}$ is a function of the reduced temperature, for which the expression can be found in appendix A of ref. [83].

An exhaustive study of the diffusion coefficient of Helium and Xenon by NMR and molecular dynamics simulations can be found in [84].

C.2.2 Calculation of the self-diffusion coefficient

Temperature and pressure conditions within the NMR samples affect the ^{3}He self-diffusion coefficient (equation C.1) and therefore the signal characteristics, see section 6.3.3. These parameters were not under control during the experiment and thus have to be estimated.

Regarding the pressure conditions, the polarized ^3He is stored in a 1 L reservoir at about 1 atm. For a set of magnetic field measurement, a valve is opened to allow the helium to fill the evacuated NMR-sample volume. Every new helium filling results in lower equilibrium pressure, varying from approximately 850 mbar down to an end pressure of about 150 mbar in the last useful measurement (i.e., with enough density to produce a visible signal). Due to the decrease of the pressure, the thermal conductivity of the gas (and, thus, the time to reach the equilibrium temperature) also varies in each measurement .

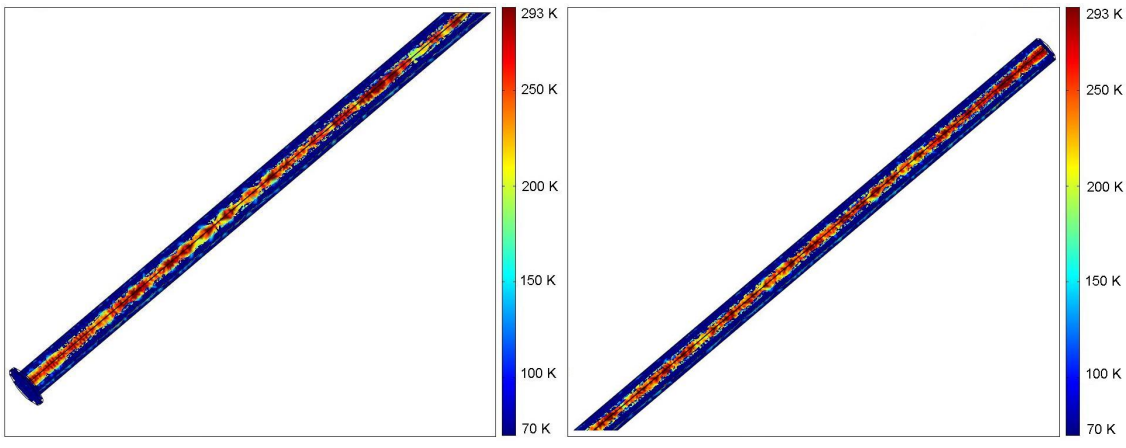

(a) (b)

Figure C.97: Simulation via COMSOL Multiphysics of the temperature evolution of the polarized ^3He inside the copper-tube system after 30 s. (a) Image of the lowest $\sim$ 10 cm of the tube. (b) Image of the highest $\sim$ 10 cm of the tube. Both pictures show a transversal cut at around 2 mm off-axis

$D\ [cm^2/s]$	293 K	200 K
850 mbar	2.15	1.14
150 mbar	12.17	6.48

Table C.35: Diffusion coefficient, D, as a function of temperature and pressure.

The temperature evolution of the polarized ^{3}He has been estimated via COMSOL MULTIPHYSICS, see figure C.97. The copper-tube system has been idealized as a cylinder of diameter $OD = 4$ mm and $ID = 3$ mm (the one of the actual system), and a length of 1.5 m, corresponding to the part of the tube completely inside of the bore tube of the cryostat (see figure 6.45). The boundary conditions have been chosen as thermally isolated (in order to simulate the UHV conditions within the bore tube) with thermal contact to a cold source around 70 K, at the bottom of the tube (to consider the thermal contact of the cooper-tube system with the electrode system). The initial conditions have been chosen as 70 K for the copper and 293 K for the helium. The helium thermal properties had to be set as constant (in temperature and pressure) due to limitations in the program. The pressure has been fixed as worst case, i.e., 1 atm. Note that the thermal conductivity is independent of the pressure [69] and the heat capacity decreases with decreasing pressure. The simulation is not considering convection effects which would contribute to fasten up the cool down process. However, the helium is free to flow from regions at room temperature to the NMR-samples, transferring a big heat load. Both effects should partially cancel. With these conditions, the result obtained with COMSOL show a very slow cooling down in comparison to the duration of the measurement sets[1]: about 200 K after 30 s.

The self-diffusion coefficient of ^3He has been calculated for the complete range of pressures and temperatures estimated above. With the initial conditions of 293 K and 850 mbar, the result shows a coefficient of self-diffusion $\approx 2.15\, cm^2/s$. This result is of the same order as the value of $1.85\, cm^2/s$ measured for ^{3}He at room temperature and atmosphere pressure by ref. [84].

C.2.3 Edge enhancement

The diffusion coefficient calculated previously permits to estimate the ratio l_s/l_g in order to determine the dominant contribution to the spectra: motional narrowing or edge enhancement (see section 6.1.5). For that, it is necessary to determine the length scales defined in section 6.1.5 at the variable experimental conditions of the DV and AP samples. The value of l_s/l_g at the initial conditions of the first measurement, of the first set, carried out with a new cell of polarized ^{3}He, is given in table C.36. The magnetic field gradient, g, has been estimated from magnetic field simulations (section C.5). It differs considerably between main field (MF) and beamtime (BT) configurations in the DV-sample. Therefore, two l_s/l_g values are given. In the AP-sample, both configurations have similar field gradient and, thus, only one value of l_g is presented.

[1] The measurement set has a maximum duration of about 30 seconds due to the short longitudinal relaxation time, T_1, see appendix C.1. This reduces the maximum number of measurements to approximately twelve measurements per helium filling, with a time interval of 2 seconds between measurements.

	l_g cm	l_s cm	l_s/l_g
DV (MF)	0.08	0.6	7.5
DV (BT)	0.07	0.6	9.1
AP	0.01	0.6	5.5

Table C.36: Calculation of the ratio l_s/l_g as a function of the field gradient, at the initial conditions: 293 K and 850 mbar.

Note that the length scale l_s corresponds to the cell diameter since along the longitudinal cell axis, the nearest wall is too far away to produce a significative effect on the NMR-signal (see figure 6.46). Consequently, g is calculated considering the radial field gradients: $g = \left(\frac{\partial B_z}{\partial r}\right)$.

Table C.37 shows the variation of the ratio l_s/l_g from the first helium filling to the last one and for the temperature variation produced once the helium has been introduced into the NMR-samples.

l_s/l_g	293 K	200 K
850 mbar	7.5/9.1 (5.5)	9.3/11.2 (6.8)
150 mbar	4.2/5.1 (3.1)	4.8/5.9 (3.8)

Table C.37: Ratio l_s/l_g calculated for different temperatures and pressures. The first two values are the ratio calculated at the DV for main field and beam time configuration, respectively. In brackets, the ratio calculated at the AP for both configurations is shown.

The range of ratios l_s/l_g obtained for different temperatures and pressures indicates a combination of motional narrowing and edge enhancement. Since the quotient l_s/l_g is larger at the DV than at the AP, higher motional narrowing occurs in the AP-sample, thus, leading to narrower spectra. According to the results given in table C.37, the edge enhancement effect is larger at high pressures whereas motional narrowing increases as the pressure goes down. This translates into a narrowing of the spectra. From equation 6.34 we know that:

$$\frac{1}{T_2^*} \propto \frac{1}{D} \tag{C.3}$$

If we consider the case of fast exchange limit, i.e., pure motional narrowing, figure 6.57 (c) shows that the spectrum is a Lorentzian and its width is given by:

$$\frac{1}{T_2^*} \approx \Delta\omega_0 \tag{C.4}$$

Combining C.3 and C.4 we obtain $\Delta\omega_0 \propto 1/D$ and therefore $\frac{\Delta\omega_2}{\Delta\omega_1} = \frac{D_1}{D_2}$.

Consequently, an increase of the diffusion coefficient (as the NMR samples cool down) produces a narrowing of the spectral width by the same factor. However, in our actual situation, the spectrum is composed of the sum of several Lorentzian peaks (figure 6.57 (b)). The number and width of these individual spectra decreases when D increases, i.e., when the pressure goes down. Thus, the width of the complete spectrum gets also narrowed but not in the same proportion as the individual peaks.

As a result, the decrease of the pressure narrows the individual peaks but not the complete spectral width which is affected at a much smaller level. This effect explains the fact that an increase of the diffusion coefficient at a factor 6 (table C.35) produces a spectrum narrowing of only a factor 1/1.4 instead of the factor 1/6 expected in a single Lorentzian spectrum (see figure C.104).

C.3 Calculation of the signal induced by a magnetic field distribution

In an ideal experiment, the signal induced in the pick-up coils by a precessing magnetization which decays exponentially (FID) can be written as:

$$U_{ind} \propto M_{\perp} e^{\frac{-t}{T_2^*}} \cos(\omega_0 t) \tag{C.5}$$

In a real experiment, the detected signal is the sum of several frequency components (section 6.3.3). This signal can be approximately calculated if the size of the coils and the magnetic field distribution are known. Although our experimental conditions are in between fast and the slow exchange regimes, in order to simplify the calculation, the motion of the Helium atoms will be considered slow compared to the duration of the experiment so they can be considered static during the acquisition time.

Since a real scenario has to consider a field distribution over the NMR sample, the induced signal has to be constructed as a sum of all the frequency components present on the volume of the sample. For that, the induced signal has to be calculated integrating over the complete frequency distribution, $f(\omega)$:

$$U_{ind} \propto M_{\perp} e^{\frac{-t}{T_2^*}} \int_{-\infty}^{+\infty} f(\omega) \cos(\omega t) d\omega \tag{C.6}$$

Here we have simplified considering a global T_2^* for the complete signal which, then, depends on the complete range of frequencies inside the volume. A more detailed analysis would consider different T_2^* for the various frequency components of the signal.

Since the magnetic field distribution at the region of the sample is unknown, we have to chose a realistic guess for the frequency distribution. For example, a linear magnetic field gradient produces a rectangular shaped frequency distribution:

$$f(\omega) = \begin{cases} 0 & \text{if } |\omega| > \frac{\Delta\omega_0}{2} \\ 1/2 & \text{if } |\omega| = \frac{\Delta\omega_0}{2} \\ 1 & \text{if } |\omega| < \frac{\Delta\omega_0}{2} \end{cases} \tag{C.7}$$

In other words, a linear gradient translates into an interval of frequencies with the same weights for each of them. Then, the integral for the induced signals results:

$$U_{ind} \propto M_{\perp} e^{\frac{-t}{T_2^*}} \int_{\omega_0 - \frac{\Delta\omega_0}{2}}^{\omega_0 + \frac{\Delta\omega_0}{2}} \cos(\omega t) d\omega \tag{C.8}$$

and therefore:

$$U_{ind} \propto M_{\perp} e^{\frac{-t}{T_2^*}} \frac{\sin\left(\frac{\Delta\omega_0}{2} t\right)}{\frac{\Delta\omega_0}{2} t} \cos(\omega_0 t) \tag{C.9}$$

Figure C.98 shows the signal represented by the previous equation as well as its power spectrum. Since a fit of equation C.9 to the measured data does not converges, the parameters used for the plot have been chosen manually in order to produce a signal with similar characteristics than that of figure 6.60. However, these values are completely contradictory to experimental results. Hence, although the result is correctly addressed and it shows how the inhomogeneity of the field reproduces similar profiles than measured, the wrong results forces to search for a more refined frequency distribution

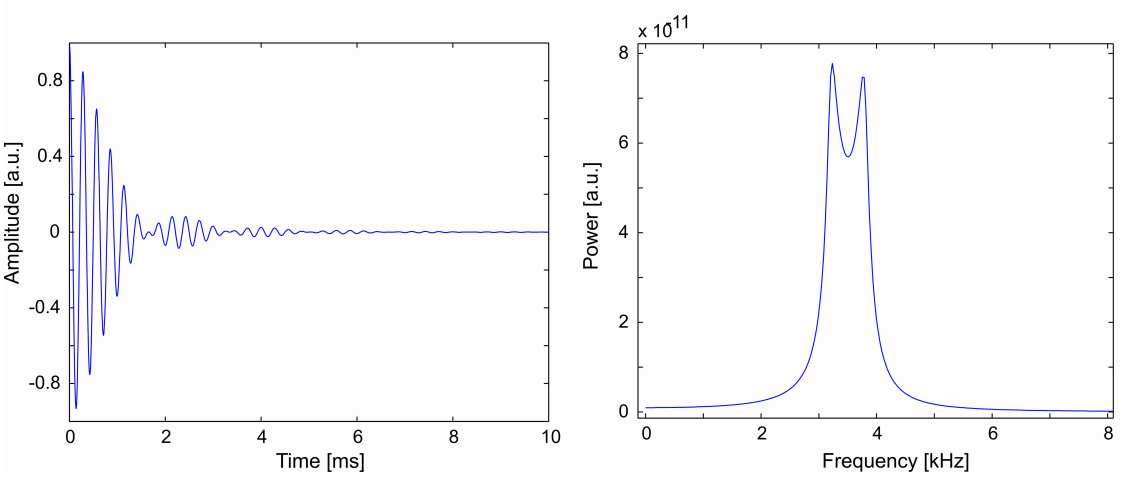

(a) (b)

Figure C.98: Signal induced by a rectangular shaped frequency distribution, equation C.9, with parameters: $\omega/2\pi = 3.5\,\text{kHz}$, $T_2 = 2.5\,\text{ms}$ and $\Delta\omega/2\pi = 0.6\,\text{kHz}$. (a) Induced signal. (b) Power spectrum.

A more refined model can be obtained considering a more realistic frequency distribution. In order to take into account a lower sensitivity of the pick-up coils at the edges it is reasonable to propose a Gaussian function as frequency distribution. However, the signal obtained and its power spectrum does not reproduce the measured data.

Considering the shape of the power spectrum of figure 6.60, we can construct a signal composed of two main frequency components, broadened approximately to Lorentzian curves due to a frequency distribution around each of them. Then, the power spectrum is the addition of two Lorentzians centered each of them around the respective central

frequency. With these considerations, the measured signal shown in C.99 has been fitted to the following function:

$$U_{ind} \propto M_1 e^{-t\lambda_1} \frac{\sin\left(\frac{\Delta\omega_1}{2}t\right)}{\frac{\Delta\omega_1}{2}t} \cos(\omega_1 t) + M_2 e^{-t\lambda_2} \frac{\sin\left(\frac{\Delta\omega_2}{2}t\right)}{\frac{\Delta\omega_1}{2}t} \cos(\omega_2 t) \tag{C.10}$$

where $\lambda = \frac{1}{T_2^*} \approx \gamma\Delta B = \Delta\omega_0$. In summary, we are using the result obtained in equation C.10, centering the decaying waves at two near frequencies. This shows clearly that the frequency distribution is the responsible of the exponential decay and of the modulation with the sinc function. The complete width of the spectrum is then defined as the addition of half of the width of the Lorentzians plus the distance between them. This permits to estimate the complete T_2^* of the signal from $\Delta\omega_i$. The result obtained for figure C.99 is a power spectrum with a width of 1200 Hz which correspond to a T_2^* of 0.8 ms. This result agrees with the expectations obtained from other approaches, see section 6.3.3.2

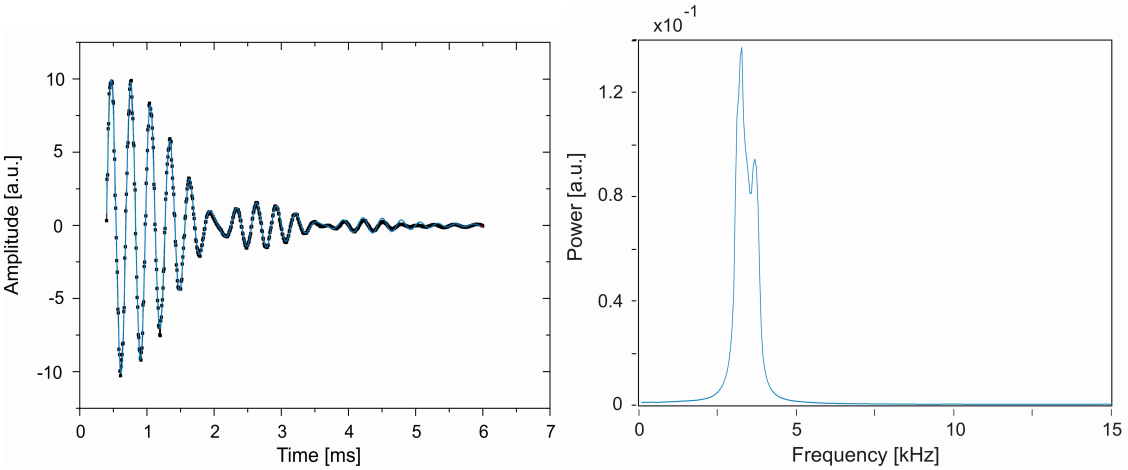

(a) (b)

Figure C.99: (a) NMR signal generated at the AP region with beam-time configuration. (b) Power spectrum of the signal on (a)

C.4 Width of the magnetic field distribution

Due to the double peak structure of the power spectra measured in the AP-sample, the spectra are fitted to the sum of two Lorentzian functions and the spectral width is defined as the full width at half maximum of the individual peaks plus the distance between peaks (section 6.3.3.2). However, a periodic variation of the spectral width as the truncation length increases has been observed, figure 6.63. If we study separately the position of the two peaks maxima and the individual widths, figure C.100, we observe that the width of the two peaks remains approximately constant and the effect of the variable width is observed on the distance between maxima.

Theoretically, in the absence of fast decaying components (as occurs in the AP NMR-signals (section 6.3.3.2)) the spectra width should be constant even for large truncation

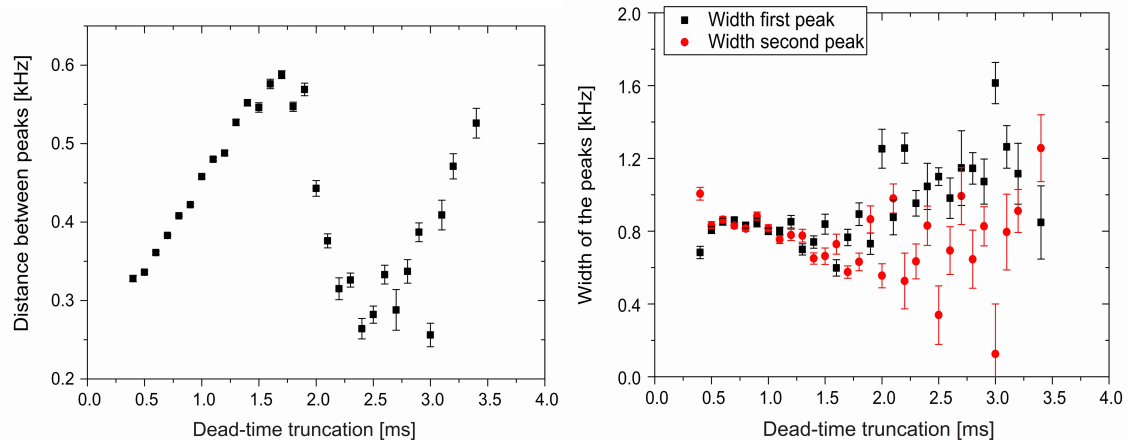

(a) Distance between maxima (b) Width of the two spectrum peaks

Figure C.100: Distance between maxima and width of the individual peaks of the power spectrum as a function of the truncation length.

times. This explains the phenomenon observed in figure C.100 (b). The variation of the width observed in figure C.100 (a) has to be explained as a mathematical artifact due to the combination of the power spectrum and the dead-time truncation.

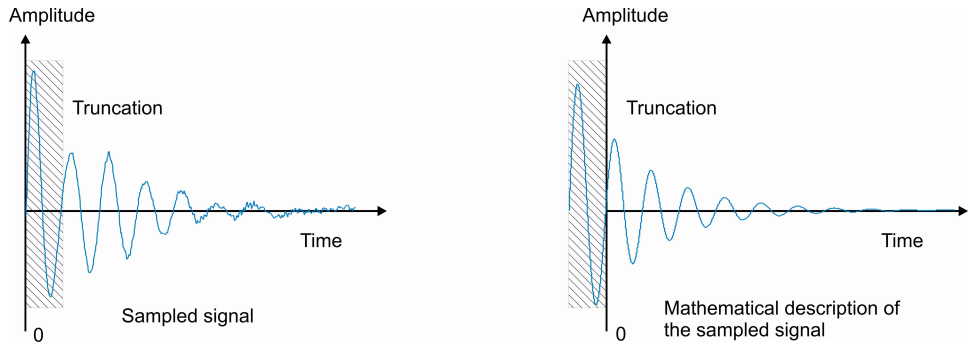

Figure C.101: Comparison of the result of the FT with a complete signal and a truncated signal. (a) Complete NMR signal. (b) Power spectrum of signal (a).

In a sampled NMR-signal, the truncation can be performed by just removing a certain number of data points, see figures C.101, 6.52 (c) and equation 6.47. However, in a mathematical description of the sampled, signal the truncation has to be done by means of a time shift, t_0, and limiting the integration interval from 0 to ∞, see figure C.101. As explained in section 6.3.1, in a single frequency component signal (e.g., $s(t) = Ae^{-t/T_2^*}e^{i\omega_0 t} = e^{-t/T_2^*}[\cos(\omega_0 t) + i\sin(\omega_0 t))$, the time shift converts into an amplitude change and a phase shift which cancels when calculating the power spectrum:

$$s(t+t_0) = Ae^{-t_0/T_2^*}e^{-t/T_2^*}e^{i\omega_0 t}e^{i\omega_0 t_0} = AA'e^{-t/T_2^*}e^{i\omega_0 t}e^{i\varphi_0} = A'e^{i\varphi_0}s(t) \tag{C.11}$$

$$|\mathcal{F}(s(t+t_0))|^2 = |A'e^{i\varphi_0}\mathcal{F}(s(t))|^2 = A'^2|\mathcal{F}(s(t))|^2 \tag{C.12}$$

However, if the signal is composed of two sinusoidal waves with different frequency:

$$s(t) = Ae^{-t/T_2^*}\left[e^{i\omega_1 t} + e^{i\omega_2 t}\right] \tag{C.13}$$

the time shift also makes to appear two different phases which dependent on the truncation length:

$$s(t+t_0) \quad = \quad Ae^{-t_0/T_2^*}e^{-t/T_2^*}\left[e^{i\omega_1 t}e^{i\varphi_1} + e^{i\omega_2 t}e^{i\varphi_2}\right] \tag{C.14}$$

where $\varphi_1 = \omega_1 t_0$ and $\varphi_2 = \omega_2 t_0$. Then, the Fourier transform results in:

$$\mathcal{F}(s(t+t_0)) = Ae^{-t_0/T_2^*}\left[\frac{e^{i\varphi_1}}{\frac{1}{T_2^*} + i(\omega-\omega_1)} + \frac{e^{i\varphi_2}}{\frac{1}{T_2^*} + i(\omega-\omega_2)}\right] \tag{C.15}$$

Consequently, the phases do not cancel when calculating the power spectrum but a mixing term containing φ_1, φ_2, $(\omega-\omega_1)$ and $(\omega-\omega_1)$ appears. This mixing term produces a deformation of the power spectrum in such a way that the resulting spectrum is not just the simple addition of two Lorentzians. Nevertheless, a fit of the power spectrum to two Lorentzians adjusts well enough to the measured spectrum (section 6.3.3) and permits to determine the complete width of the spectrum. The problem arises from the dependency of the power spectrum with the truncation length, t_0, throughout φ_1, φ_2, and explains the observed dependence of the peak distance on the truncation lengths.

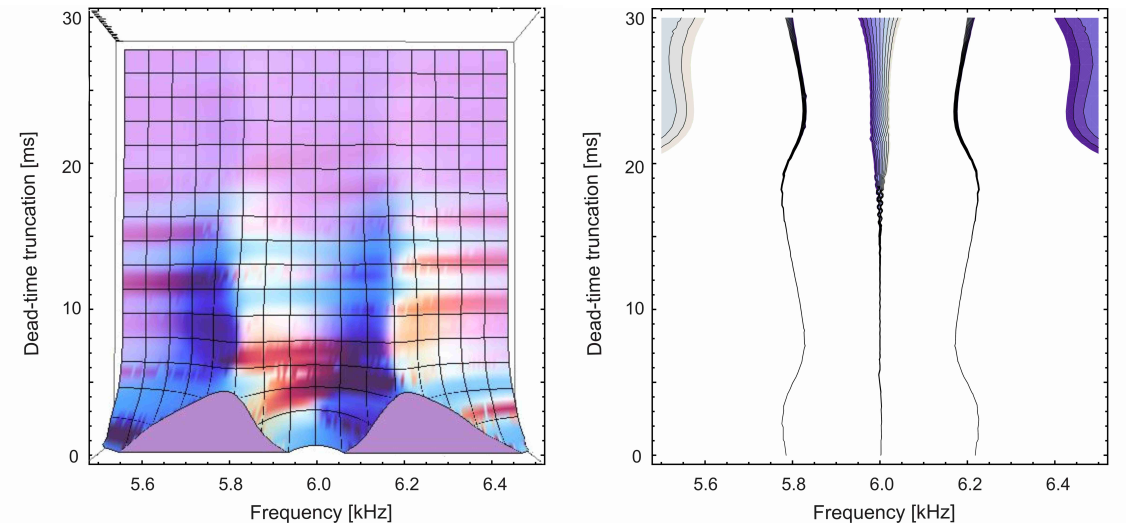

Figure C.102: (a) Power spectrum of equation C.14 as a function of the truncation length, t_0. (b) Position of the power spectrum maxima of equation C.14 as a function of the truncation length, t_0.

To see that effect mathematically, we proceed to calculate the power spectrum of equation C.14 via Mathematica. The position of the maxima is obtained by calculating the

derivative and finding the zero crossing. The result of the power spectrum maxima as a function of the truncation length is presented in figure C.102. The parameters used for the plots are: $\omega_1 = 5800\,\text{Hz}$, $\omega_2 = 6200\,\text{Hz}$ and $T_2 = 10\,\text{ms}$. The reason for not using the typical values of ω_i and T_2^* is the poor resolution on the calculation for such a short values of T_2^*. For this reason, the periodicity in the change of the maxima and width is not comparable to the actual measurements (section 6.3.4).

Figure C.102 (a) shows the variation of the total spectral width. Due to the short T_2^* it is not possible to see the effect for large truncation lengths. This is because the truncation reduces the area under the peaks making it difficult to distinguish the real spectral width. Note that the width of the spectrum has to be calculated as the full width at half maximum. Therefore, in order to observe the spectral width, a cut at different amplitude heights for different truncation length should be performed. Hence, it is not easy to distinguish (in this picture) how much a possible variation of the individual peak width and how much the distance between peaks contributes to this value. Figure C.102 (b) shows that the variation of the total width can be properly explained by the variation of the distance between peaks. This effect can be corrected in order to determine the actual spectral width.

Dead-time Correction

If no truncation is applied ($t_0 = 0$), the two phases defined in equation C.14, φ_i, are equal to zero, $\varphi_1 = \varphi_2 = 0$. Then, the mixing term of the power spectrum depends only on $(\omega - \omega_1)$ and $(\omega - \omega_1)$ and the actual spectral width can be extracted. In some measurements at the AP-sample, the amplitude of the NMR-signal is high enough (much higher than the DC-peak) that no truncation is needed. In such cases the actual width is directly obtained from the fit of the spectrum to two Lorentzians.

In measurements were a truncation is necessary, the actual spectral width can be determined via a simple correction. All the measurements at the AP-sample present exactly the same dependency with the truncation length. For short truncation lengths, this dependence can be approximated to be linear (see figure C.103).

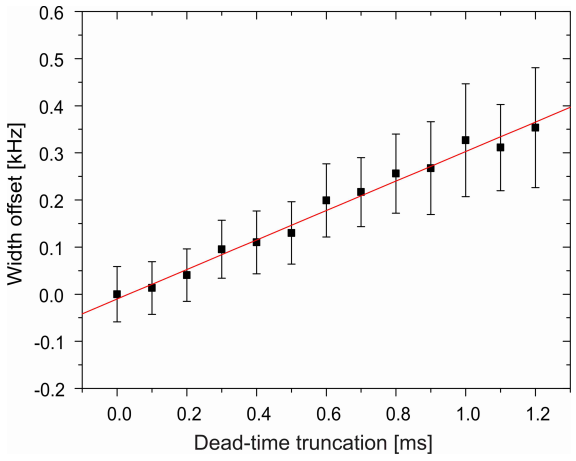

Figure C.103: Offset of the width of the spectrum versus the truncation length, t_0, for several measurements at the AP.

Figure C.103 has been obtained by averaging the spectral width of a large number of high amplitude measurements for different truncation lengths. The error bars in the plot are only statistical. The offset and its error for the most common truncation lengths is shown in table C.38.

truncation length (t_0) [ms]	0.5	0.6	0.7	0.8	0.9	1.0
offset [Hz]	130	200	220	260	270	330
error [Hz]	±130	±150	±160	±170	±200	±240

Table C.38: Offset correction for the width of the spectrum at the AP.

Results

Figure C.104, shows the spectral width of the AP-sample measurements. White background indicates measurements were carried out with the magnetic field in main field configuration. The measurements performed with magnet in beamtime configuration are shown with a green and blue background. Green corresponds to the set of measurements intended to check the stability (from 02.06.09 to 05.06.09) and blue to the measurements for the reproducibility of the ratio r_B (from 05.06.09 to 12.06.09).

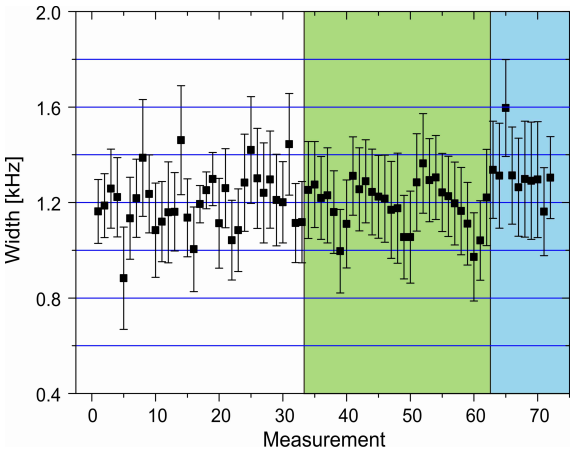

Figure C.104: Width of the spectra of every measurement at the AP. The measurements are drawn with their total error bars. White background indicates measurements with main field configuration. Green and blue background are for the measurements with beamtime configuration, being green the long measurement intended to check the stability (from 02.06.09 to 05.06.09) and blue the measurements for the reproducibility of the ratio (from 05.06.09 to 12.06.09).

The narrowing of the width for decreasing pressures predicted in section 6.3.3, is clearly visible at the measurements with beam-time configuration (green area). During these measurements, the large supply of polarized helium permitted to take a considerable number of measurements at an established configuration with decreasing helium pressure. Thanks to that, it is possible to observe the direct dependence of the spectral width with respect to the pressure, $\Delta\omega_0 \approx \frac{1}{T_2^*} \propto \frac{1}{D} \propto p$ (see appendix C.2).

Measurements displayed in the blue area, i.e. reproducibility test, correspond mostly

to high pressure measurements. At this time, the first measurements performed with a new cell of polarized helium were used to measure the magnetic field whereas the remaining helium was used for systematic checks. Hence, these measurements have the broadest spectral width. Note that the actual spectral width/field distribution has to be considered as the one measured at high pressure. Under these conditions motional narrowing is minimal and therefore the actual field distribution can be observed.

During the set of measurements with main field configuration (white area) the limited supply of polarized helium forced us to save helium from one day to another for time stability checks. Therefore, only short sets of measurements are available and half of them have been performed with low polarization. The values with higher error bars and higher distance to the average value correspond to those measurements with low polarization (low signal to noise ratio).

As explained in section 6.3.3, the small amount of measurements at the DV with an amplitude high enough to study the width does not permit a similar analysis. With the limited statistics and the high noise level, the results are obtained with big error bars. Nevertheless, they agree satisfactorily with the expected value (see appendix C.5). A summary of the width at DV and AP for the two configurations used is shown in table C.43.

	Spectral Width [kHz]
DV /main field	6.8(5)
DV /beam time setup	6.9(5)
AP /main field	1.3(3)
AP /beam time setup	1.3(3)

Table C.39: spectral width at DV and AP.

C.5 Magnetic field simulation

The aSPECT magnetic field is a fundamental component of the MAC-E filter and, thus, has to be properly characterized (chapter 5. Magnetic field mappings at the DV and AP regions, weighted with the neutron beam profile, permit to calculate the ratio r_B with an accuracy which allows a measurement of the coefficient a on a 0.3 % level. Additionally, trajectory calculations for systematic studies require an accurate knowledge of the magnetic field distribution within the complete spectrometer. A magnetic field simulation able to reproduce the magnetic field measurements would permit to render the aSPECT magnetic field in any region of the spectrometer with a grid as detailed as necessary for precise calculations. Furthermore, such a grid would allow us to relate the measurements within the flux tube (hall-probe) with the NMR-magnetometer. This would lead to a better knowledge of the exact magnetic field during beamtimes monitored with the NMR-magnetometer.

The position and characteristics of the superconducting coils which generate the aSPECT magnetic field are known due to the specifications of the manufacturing company. Using

those parameters a magnetic field simulation has been programmed[38] and compared to the measurements discussed in chapters 5 and 6. Unfortunately, the magnetic field simulation does not fit properly to the measurements at the AP region [44]. To correct for this effect, the currents of the superconducting coils which generate the AP magnetic field have been varied in order to adjust the simulation to the measurements.

The magnetic field simulation along the z-axis of the spectrometer is properly fitting at the DV region but it differs considerably at the AP-region (see figure 5.38). However, it provides a magnetic field ratio which agrees with the Hall-probe measurements (table 6.25) and a maximum position shifted from the real one by only $\approx 0.5\,\mathrm{cm}$.

A transversal cut of the simulated magnetic field at the height of the NMR-samples ($z = +132.4\,\mathrm{cm}$ at the AP and $z = +0.4\,\mathrm{cm}$ at the DV) is displayed in figure C.105. The figure shows the simulated magnetic field for the complete radius of the bore tube. The samples are shifted $+4\,\mathrm{mm}$ from the desired position while keeping the correct distances between them. This shift implies that the ratio measured with the NMR can be different from the ratio at $z = 0\,\mathrm{cm}$ and $z = +132\,\mathrm{cm}$. Nevertheless, because the relative homogeneity of the field is better then 1×10^{-4} per centimeter, the error induced on the ratio r_B due to that shift is negligible (see chapter 5).

The glass cells containing polarized ^{3}He have an inner diameter of 6 mm and an "effective" length (see section 6.3.3) which has been defined as the length of the pick-up coil, $\approx 15\,\mathrm{mm}$. The position of the samples in a Cartesian reference frame, with origin in the center of the DV (with z along the symmetry axis of the spectrometer and x in the neutron beam direction), is:

	DV	AP
x	$-12\,\mathrm{mm}$	$-12\,\mathrm{mm}$
y	$+79\,\mathrm{mm}$	$+80\,\mathrm{mm}$
z	$+4\,\mathrm{mm}$	$+132.4\,\mathrm{mm}$

Table C.40: NMR-samples position in a Cartesian reference frame with its origin at the center of the DV and with z along the symmetry axis of the spectrometer and x in the neutron beam direction.

The values of the magnetic field ratio, r_B, obtained from the measurements with the Hall probe and the NMR-magnetometer are summarized in table C.41. Where both measurements show the same ratio (within error bars) on- and off-axis. This is a very good result for aSPECT since it permits to use the same transmission function independently of the proton emission position (chapter 5). The values obtained from the simulated field do agree with the measured value at the axis of the spectrometer. However, they overestimate the ratio off-axis, i.e., at the NMR-samples position. To clarify this discrepancy it is necessary to proceed in two ways. On the one hand, measurements on- and off-axis with the same measurement probe need to be performed in order to ensure a proper comparison of the results. On the other hand, the quality of the magnetic field simulation has to be improved, and measurements off-axis at the NMR-samples position have to be also used, in order to obtain a reliable field simulation which reproduces the measurements all over

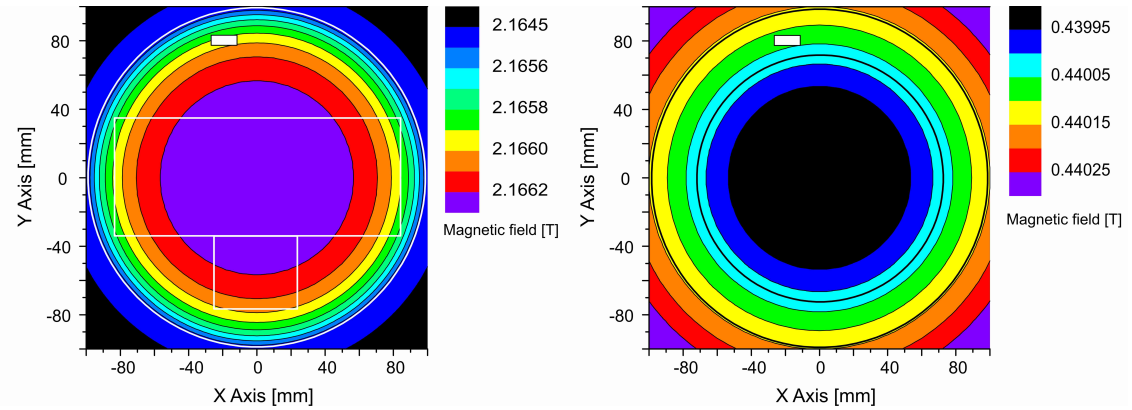

(a) (b)

Figure C.105: Simulation of the magnetic field in beamtime configuration. (a) Transversal cut of the simulated magnetic field at +0.4 cm, DV. Position of the NMR-cell, bore tube and DV represented in white. (b) Transversal cut of the simulated magnetic field at +132.4 cm, AP. Position of the bore tube and AP electrode represented in black, NMR-cell in white.

the spectrometer volume.

Position	r_B Hall probe	r_B NMR-magnetometer	r_B Simulation
On-axis (flux tube)	0.2030(2)	—	0.20304
NMR-samples position	—	0.202985(16)	0.20318

Table C.41: Ratio of the magnetic field, r_B, obtained with three methods: Hall probe measurements (chapter 5), NMR-magnetometer, and magnetic field simulation (appendix C.5). Results on-axis (flux tube) and off-axis at the NMR-sample positions. Measurements with magnet in beamtime configuration. Note that the spectral width has been considered as error in the ratio obtained via the NMR-magnetometer.

The magnetic field simulation also permit us to check the estimation of the magnetic field distribution within the NMR-samples as obtained from the spectra (only B_z). The values of the magnetic field inhomogeneity are summarized in table C.42. Only the z component of the magnetic field B_z contributes to the NMR-spectra and to the decay of the NMR-signal (T_2^*). Due to that and to the small contribution of radial components to the absolute value of the field within the DV and AP regions (chapter 5 and 6), the radial field component is not treated in this work. For the study of different systematics via trajectory calculations, the complete magnetic field vector is needed. This topic is treated in detail in the PhD. thesis of Gertrud Konrad [38].

DV	main field config. [kHz]	beam-time config. [kHz]
Simulation	4.2	7.5
spectral width	6.8(5)	6.9(5)
T_2^* (signal fit)	6.3	6.7

AP	main field [kHz]	beam-time [kHz]
Simulation	1.4	1.4
Fourier Analysis	1.3(3)	1.3(3)
T_2, signal fit	1.2	1.2

Table C.43: Inhomogeneity of the magnetic field, in terms of frequency, at the NMR-sample positions, calculated by three different methods.

	DV	AP
main field configuration	1.3 Gauss	0.43 Gauss
beam-time configuration	2.3 Gauss	0.43 Gauss

Table C.42: Inhomogeneity of the magnetic field over the NMR-sample volume obtained from the magnetic field simulation (only B_z).

Tables C.43 summarize the inhomogeneity of the field (in terms of frequency) within the NMR-samples, obtained by the different methods. The only values presented with error bars are the ones obtained from the width of the spectra. The values obtained from the fit of the signals to obtain the T_2^* are only intended as a proof of the consistency of the spectrum analysis and therefore, only a few measurements have been analyzed. The tables show a very good agreement for the two analysis procedures and the simulation at the AP region. However, the values at the DV region show a larger difference. This indicates that the magnetic field simulation needs improvement.

Appendix D

NMR-Magnetometer electronic details

D.1 Q factor of a LC circuit

The quality factor, Q factor, is a dimensionless parameter that describes how strongly damped an oscillator or resonator is. It characterizes a resonator's bandwidth relative to its center frequency, see equation D.1. Low Q circuits are therefore damped and lossy and high Q circuits are underdamped. In respect to the bandwidth; low Q circuits are broad band and high Q circuits are narrow band.

$$Q = \frac{\omega_0}{\Delta\omega} \tag{D.1}$$

Additionally, the higher the Q, the higher the voltage which which can be stared in the circuit, the a more sensitive a receiver is. In terms of the components of an LCR-circuit the Q factor is written:

$$Q = \frac{1}{R}\sqrt{\frac{L}{C}} \tag{D.2}$$

The values of R, L and C have to be selected in order to get a large Q with a sufficient bandwidth at the Larmor frequency, ω_0, of the corresponding nuclei. The Q factor of the resonant circuits of the aSPECT NMR-samples, table D.44, are large enough to provide a more than sufficient sensitivity together with a broad bandwidth which permits to vary considerably the settings of the aSPECT magnetic field for systematic checks on the determination of the correlation coefficient a.

	Q	Bandwidth $\Delta\omega$ (MHz)
DV	26	2.5
AP	24	0.6

Table D.44: Q factor of the LC circuits to pick up the FID-signal of the aSPECT NMR-samples.

D.2 Electronic sketch of the custom Power Amplifier.

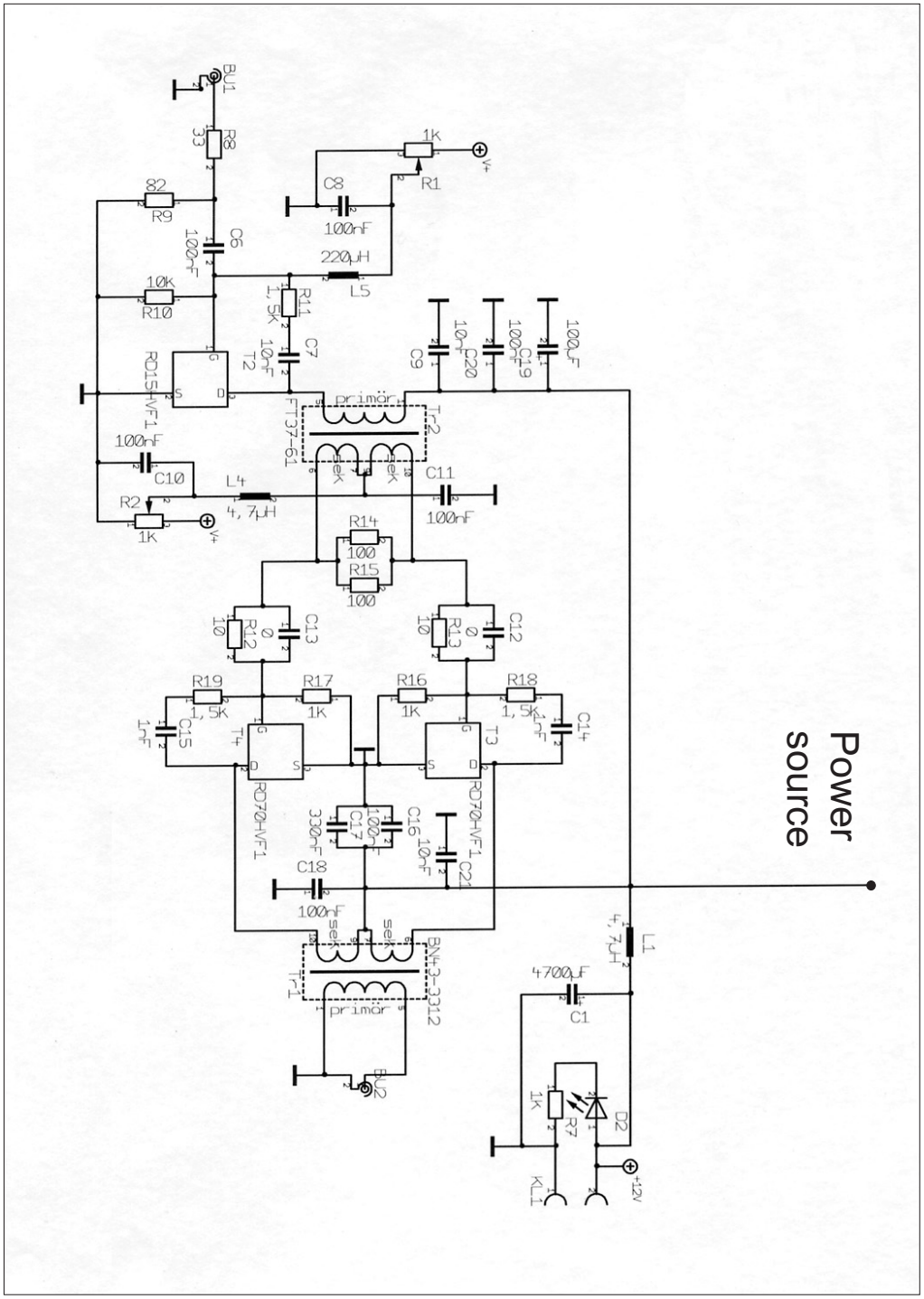

Figure D.106: Sketch of the custom Power Amplifier.

D.3 NMR-electronics spectra

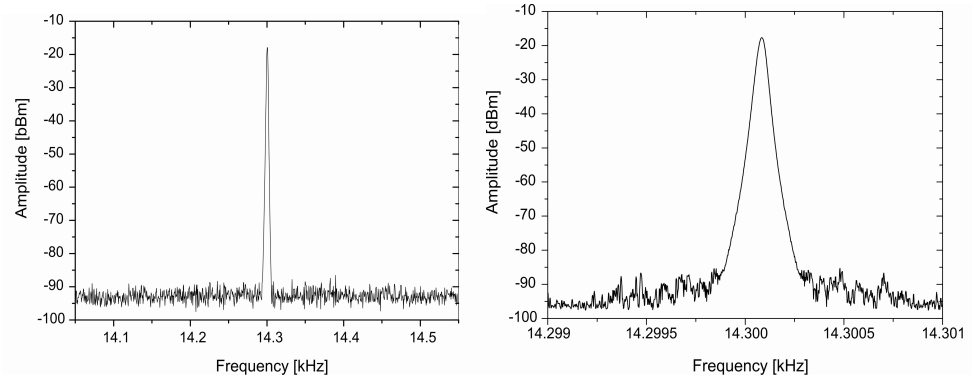

(a) (b)

Figure D.107: Spectra of the HP 8656B r.f. generator at around 14.3 MHz with a signal amplitude of 316,mV

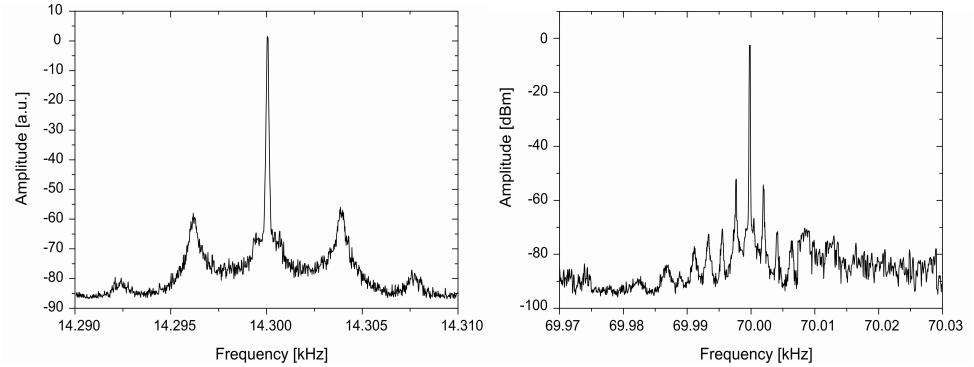

(a) (b)

Figure D.108: Spectra after measured after the custom MPI-power amplifier with an input signal amplitude of 158,mV

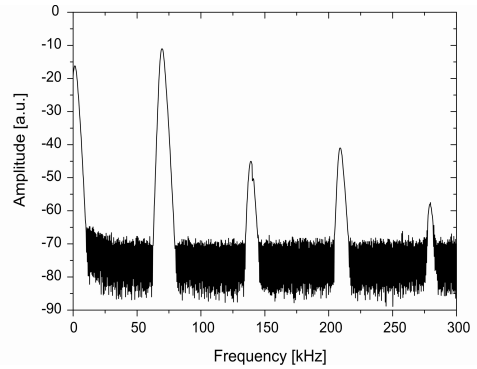

Figure D.109: Spectrum measured after the custom MPI-power amplifier (at 70.0 MHz) with an input signal amplitude of 158,mV. The scale is selected to show the harmonics.

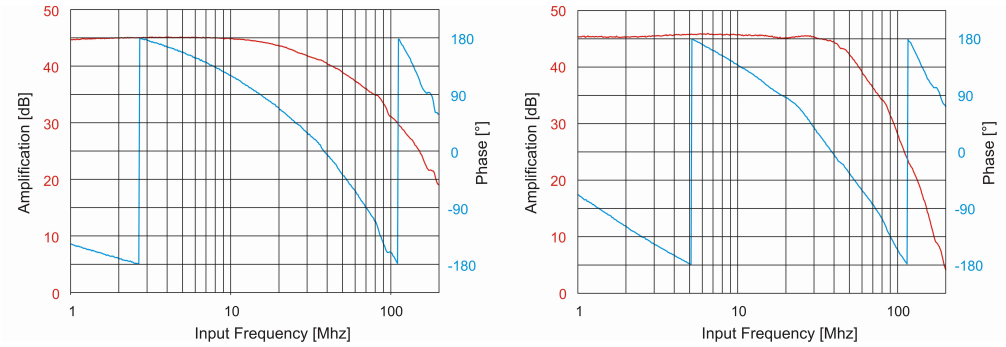

(a) (b)

Figure D.110: Gain spectra of the custom MPI-power amplifiers.

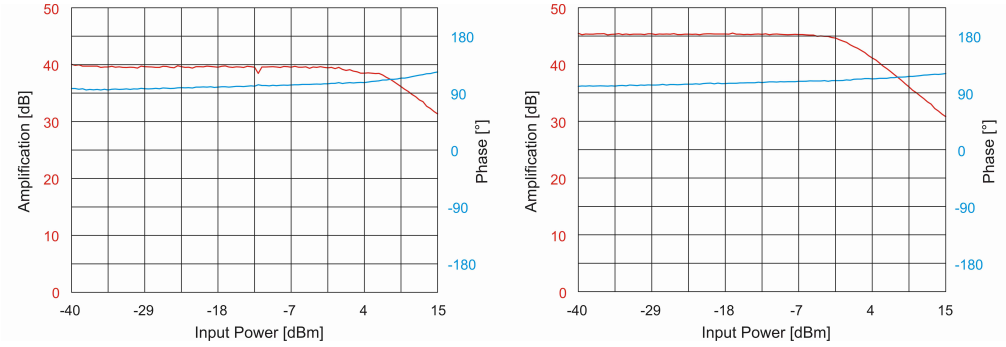

(a) (b)

Figure D.111: Gain versus amplitude of the input signal of the custom MPI-power amplifiers

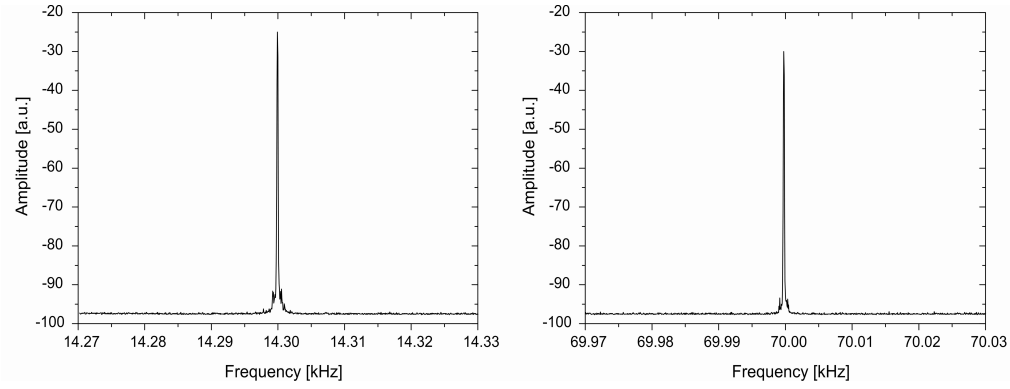

(a) (b)

Figure D.112: Spectra measured after the MITEQ power amplifier with an input signal amplitude of 316,mV.

D.4 Electronic setup of the improved *a*SPECT NMR - Magnetometer

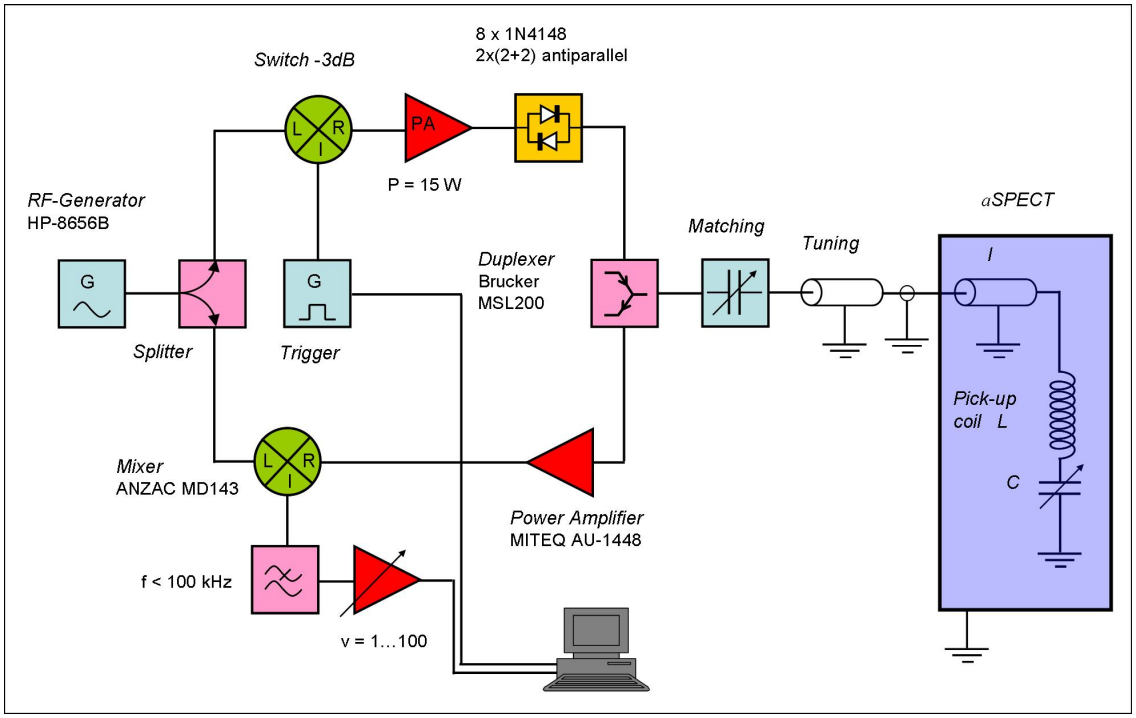

Figure D.113: Sketch of the electronics setup of the *a*SPECT NMR-Magnetometer with a mixer instead of the lock-in amplifier. The spectrometer is represented in blue on the right side of the picture.

Bibliography

[1] N. Severijns, M. Beck, and O. Naviliat-Čunčić, *Rev. Mod. Phys.* **78**, 991 (2006). (Cited on pages 1, 2, 5, 7, 8, 9, 11, 13, and 14.)

[2] C. Amsler et al., *Phys. Lett. B* **667**, 1 (2008), and 2009 partial update for the 2010 edition (URL: http://pdg.lbl.gov). (Cited on pages 2, 3, 6, 10, 11, 13, 14, and 15.)

[3] A. P. Serebrov et al., *Phys. Lett. B* **605**, 72 (2005). (Cited on pages 2 and 14.)

[4] A. P. et al., *Phys. Lett. B* **693**, 221 (2010). (Cited on pages 2 and 14.)

[5] H. Abele, *Prog. Part. Nucl. Phys.* **60**, 1 (2008). (Cited on pages 2, 5, 11, 13, and 14.)

[6] J. D. Jackson, S. B. Treiman, and H. W. Wyld, *Phys. Rev.* **106**, 517 (1957). (Cited on pages 2, 7, and 12.)

[7] S. Baessler et al., *Eur. Phys. J. A* **38**, 17 (2008). (Cited on pages 2, 3, 5, 38, and 147.)

[8] f. t. K. c. P. de Simon, *Journal of Physics: Conference Series* **171**, 012051 (2009). (Cited on page 3.)

[9] E. Goudzovski, *Journal of Physics: Conference Series* **110**, 052019 (2008). (Cited on page 3.)

[10] K. Varvell, *Flavor Physics and CP Violation Conference, Vancouver* **15**, 772 (2006). (Cited on page 3.)

[11] C. Stratowa, R. Dobrozemsky, and P. Weinzierl, *Phys. Rev. D* **18**, 3970 (1978). (Cited on pages 3 and 13.)

[12] J. Byrne et al., *J. Phys. G: Nucl. Part. Phys.* **28** (2002). (Cited on pages 3 and 13.)

[13] T. Hsu and J. L. Hirshfield, *Rev. Sci. Instrum.* **47**, 236 (1976). (Cited on pages 3 and 18.)

[14] G. Beamson, H. Q. Porter, and D. W. Turner, *J. Phys. E* **13**, 64 (1980). (Cited on pages 3 and 18.)

[15] P-Kruit and F. H. Read, *J. Phys. E* **16**, 313 (1983). (Cited on pages 3 and 18.)

[16] C. Kraus et al., *Eur. Phys. J. C* **40**, 447 (2005). (Cited on pages 3 and 18.)

[17] J. Angrik et al., *FZKA Scientific Report* **7090** (2004), http://bibliothek.fzk.de/zb/berichte/FZKA7090.pdf. (Cited on pages 3 and 18.)

[18] C. W. E.W. Otten, *Rep. Prog. Phys.* **71**, 086201 (2008). (Cited on pages 3 and 18.)

[19] F. Glück et al., *Eur. Phys. J. A* **23**, 135 (2005). (Cited on pages 5, 23, 25, 26, 31, 35, 36, 38, 39, 40, 44, 50, 51, 52, 70, 71, and 163.)

[20] O. Zimmer et al., *Nucl. Instr. and Meth. A* **440**, 548 (2000). (Cited on pages 5, 52, and 53.)

[21] J. D. Bjorken and S. D. Drell, *Relativistic Quantum Mechanics*, McGraw-Hill, New York, 1963. (Cited on page 6.)

[22] T. D. Lee and C. N. Yang, *Phys. Rev.* **104**, 254 (1956). (Cited on page 7.)

[23] C. S. Wu et al., *Phys. Rev.* **105**, 1413 (1957). (Cited on page 7.)

[24] G. Gamow and E. Teller, *Phys. Rev.* **49(12)**, 895 (1936). (Cited on page 8.)

[25] F. Glück, J. Joó, and J. Last, *Nucl. Phys. A* **593**, 125 (1995). (Cited on pages 8, 12, 13, and 20.)

[26] S. L. Glashow, *Nucl. Phys.* **22**, 579 (1961). (Cited on page 10.)

[27] S. Weinberg, *Phys. Rev. Lett.* **19**, 1264 (1967). (Cited on page 10.)

[28] A. Salam, *Elementary Particle Theory: Relativistic Groups and Analyticity*, Almqvist and wiksell, stockholm edition, 1968. (Cited on page 10.)

[29] N. Cabibbo, *Phys. Rev. Lett.* **10**, 531 (1963). (Cited on page 11.)

[30] M. Kobayashi and T. Maskawa, *Prog. Theor. Phys.* **49**, 652 (1973). (Cited on page 11.)

[31] D. Dubbers, *Prog. Part. Nucl. Phys.* **26**, 173 (1991). (Cited on page 11.)

[32] J. Byrne, *Neutrons, Nuclei and Matter*, Institute of Physics Publ., Bristol, 1995. (Cited on page 11.)

[33] W. S. Wilburn, *J. Res. Natl. Inst. Stand. Technol.* **110**, 389 (2005). (Cited on page 13.)

[34] V. K. Grigor'ev et al., *Sov. J. Nucl. Phys.* **6**, 239 (1968). (Cited on page 13.)

[35] F. E. Wietfeldt et al., *Nucl. Instr. and Meth. A* **545**, 181 (2005). (Cited on page 13.)

[36] F. E. Wietfeldt et al., *Nucl. Instr. and Meth. A* (2009). (Cited on page 13.)

[37] D. H. Wilkinson, *Nucl. Phys. A* **377**, 474 (1982). (Cited on page 13.)

[38] G. Konrad, PhD thesis, Johannes Gutenberg-Universität Mainz, 2011. (Cited on pages 13, 24, 27, 29, 36, 40, 44, 45, 48, 52, 60, 70, 74, 75, 150, 152, 153, 156, 158, 159, 160, 169, 188, and 189.)

[39] O. Nachtmann, *Z. Phys.* **215**, 505 (1968), note a correction of a sign error in Eq. (4.5), found by C. Habeck, PhD Thesis, University of Sussex (1997). (Cited on page 14.)

[40] C. Habeck, PhD thesis, University of Sussex, 1997. (Cited on page 14.)

[41] P. G. Dawber et al., *Nucl. Instr. and Meth. A* **440**, 543 (2000). (Cited on page 14.)

[42] F. Glück, *Phys. Rev. D* **47**, 2840 (1993). (Cited on pages 15 and 147.)

[43] J. D. Jackson, *Classical Electrodynamics*, John Wiley & Sons, 3rd edition, 1975. (Cited on page 19.)

[44] F. Ayala Guardia, First Tests of the neutron decay spectrometer *a*SPECT, 2005. (Cited on pages 20, 61, 70, 75, 167, and 188.)

[45] M. Borg, PhD thesis, Johannes Gutenberg-Universität Mainz, 2011. (Cited on pages 24, 28, 38, 42, 48, 138, 139, 142, 143, 146, 147, 148, 149, 152, 157, 158, and 159.)

[46] M. Simson, PhD thesis, Technische Universität München, 20010. (Cited on pages 24, 29, 30, 38, 44, 45, 71, 139, 141, 142, 144, 145, 146, 147, 153, 157, 158, and 159.)

[47] T. G. Northrop, *The Adiabatic Motion of Charged Particles*, Interscience Publ., 1963. (Cited on page 26.)

[48] P. C. Clemmow and J. P. Dougherty, *Electrodynamics of Particles and Plasmas*, Addison-Wesley Publ. Comp., 1969. (Cited on page 26.)

[49] R. Dendy, editor, *Plasma Physics: An Introductional Course*, Cambridge University Press, 1993. (Cited on page 26.)

[50] R. Muñoz Horta, in *Proceedings of the XIV International Seminar on Interaction of Neutrons with Nuclei, Dubna, 2007*, 2007. (Cited on pages 28, 31, 32, 35, 36, 40, 44, 47, 70, 135, 139, and 157.)

[51] F. M. Penning, *Physica (Utrecht)* **3**, 873 (1936). (Cited on page 32.)

[52] H. G. Dehmelt, *Adv. At. Mol. Phys.* **3**, 53 (1967). (Cited on page 32.)

[53] R. H. Fowler and L. Nordheim, *Proc. Soc.* **A 119**, 173 (1928). (Cited on page 32.)

[54] F. Glück, (2007), http://fuzzy.fzk.de/bscw/bscw.cgi/d354775/The_Penning _discharge_(F._Glueck).pdf. (Cited on page 32.)

[55] G. Konrad et al., Design of an Anti-Magnetic Screen for the Neutron Decay Spectrometer *a*SPECT, in *Proceedings of the European Comsol Conference, Grenoble, 2007*, p. 241, 2007. (Cited on page 38.)

[56] T. P. Sheahen, *Introduction to high-temperature superconductivity*, Springer, 1994. (Cited on page 66.)

[57] G. B. Scott, M. Springford, and J. R. Stockton, *Journal of Physics E: Scientific Instruments* **1**, 925 (1968). (Cited on page 66.)

[58] C. P. Slichter, *Principles of Magnetic Resonance*, Springer-Verlag Berlin Heidelberg New York, 2nd edition, 1978. (Cited on page 81.)

[59] M. Levitt, *Spin Dynamics: basics of nuclear magnetic resonance*, John Wiley and Sons, Ltd., 2001. (Cited on page 81.)

[60] P. Callaghan, *Principles of Nuclear Magnetic Resonance Microscopy*, Oxford Science Publication, 1991. (Cited on pages 81, 91, 104, and 107.)

[61] R.R.Ernst, G.Bodenhausen, and A.Wokaun, *Principles of Nuclear Magnetic Resonance in One and Two Dimensions*, Clarendon Press, Oxford, 1987. (Cited on page 81.)

[62] L. A. Pedrós, R. Acosta, P. Blümler, and H. Spiess, *Journal of Magnetic Resonance* **197**, 56 (2009). (Cited on pages 86 and 91.)

[63] R. Gamblin and T. Carver, *Phys. Rev. A* **138**, 946 (1965). (Cited on page 86.)

[64] L. Schearer and G. Walters, *Phys. Rev. A* **139**, 1398 (1965). (Cited on page 86.)

[65] G. Cates, S. Schaefer, and W. Happer, *Phys. Rev. A* **37**, 2877 (1988). (Cited on pages 86 and 89.)

[66] D. D. McGregor, *Phys. Rev. A* **41**, 2631 (1990). (Cited on page 89.)

[67] M.A.Bouchiat, T.R.Carver, and C.M.Varnum, *Physical Review Letters* **5**, 373 (1960). (Cited on page 90.)

[68] F.D.Colegrove, L.D.Schearer, and G.K.Walters, *Phys. Rev. A* **132**, 2561 (1963). (Cited on page 90.)

[69] P. Atkins and J. de Paula, *Physical Chemistry*, Oxford University Press, 2002. (Cited on pages 90 and 178.)

[70] S. Chapman and T. Cowling, *The mathematical theory of non-uniform gases*, Cambridge university press, 3rd edition, 1970. (Cited on pages 91 and 176.)

[71] B. Putz, D. Barsky, and K. Schulten, *Journal of Magnetic Resonance* **97**, 27 (1992). (Cited on page 91.)

[72] W. B. Hyslop and P. C. Lauterbur, *Journal of Magnetic Resonance* **94**, 501 (1991). (Cited on page 91.)

[73] P. Callaghan, A. Coy, L. Forde, and C. Rofe, *Journal of Magnetic Resonance* **A101**, 347 (1993). (Cited on page 91.)

[74] B. Saam, N. Drukker, and W. Happer, *Chemical Physics Letters* **263**, 481 (1996). (Cited on page 91.)

[75] T. M. de Swiet, *Journal of Magnetic Resonance* **B 109**, 12 (1995). (Cited on pages 91 and 92.)

[76] D. C. Champeney, *Fourier Transforms and their Physical Applications*, Academic Press, Inc., 2nd edition, 1973. (Cited on page 126.)

[77] R. N. Bracewell, *The Fourier Transform and its Applications*, McGraw-Hill, Inc., 2nd edition, 1986. (Cited on page 126.)

[78] W. H. Press et al., *Numerical Recipes: The Art of Scientific Computing*, Cambridge University Press, 3rd edition, 2007. (Cited on page 126.)

[79] J. H. Reed, *Software radio: a modern approach to radio engineering*, Prentice Hall, 2002. (Cited on page 127.)

[80] H. Abele et al., *Nucl. Instr. and Meth. A* **562**, 407 (2006). (Cited on page 136.)

[81] E. Gatti and P. Rehak, *Nucl. Instr. and Meth. A* **225**, 608 (1984). (Cited on page 139.)

[82] W. Leo, *Techniques for Nuclear and Particle Physics Experiments*, Springer, Berlin, Heidelberg, New York, 2st edition, 1994. (Cited on page 144.)

[83] J. Hirschfelder, C. Curtis, and R. Bird, *Molecular theory of gases and liquids*, John Wiley & Sons, 1965. (Cited on pages 176 and 177.)

[84] R. Acosta, P. Blümler, L. A. Pedrós, S. Komin, D. Sebastiani, and H. Spiess, *Physical Chemistry Chemical Physics* **8**, 4182 (2006). (Cited on pages 177 and 178.)

Curriculum Vitæ

Name	Fidel Ayala Guardia
Birthday	January 28th, 1978
Birthplace	Valencia, Spain
Since 25/09/2006	PhD student at the Johannes Gutenberg-University of Mainz in the group of Prof. Dr. Werner Heil
02/2006 - 06/2011	"Wissenschaftler Mitarbeiter" at the Johannes Gutenberg-University of Mainz in the group of Prof. Dr. Werner Heil
2004 - 2005	Diploma thesis in neutrons physics at the Johannes Gutenberg-University of Mainz in the group of Prof. Dr. Werner Heil Title: "First test of the neutron decay spectrometer aSPECT"
1997 - 2004	Diploma in physics at the University of Valencia
1996 - 1997	Student in mathematics at the University of Valencia
09/1996	"Selectividad" (A level) at the Instituto San Vicente Ferrer, Valencia, Spain
1987 - 1996	High school, Instituto San Vicente Ferrer, Valencia, Spain
1983 - 1987	Primary school, Liceo Corbí, Valencia, Spain